7-2020

Development of High-Density Propulsion System Technologies for Interplanetary Small Satellites and CubeSats

Morgan Andrew Roddy
University of Arkansas, Fayetteville

Development of High-Density Propulsion System Technologies for Interplanetary Small Satellites and CubeSats

A dissertation submitted in partial fulfillment
of the requirements for the degree of
Doctor of Philosophy in Microelectronics-Photonics

by

Morgan Andrew Roddy
Rose-Hulman Institute of Technology
Bachelor of Science in Engineering Physics, 2010
University of Arkansas
Master of Science in Microelectronics-Photonics, 2012

July 2020
University of Arkansas

This dissertation is approved for recommendation to the Graduate Council.

_____
Po-Hao Adam Huang, Ph.D.
Dissertation Director

_____
Larry Roe, Ph.D.
Committee Member

_____
Ingrid Fritsch, Ph.D.
Committee Member

_____
Silke Spiesshoefer, Ph.D.
Committee Member

_____
Rick Wise, Ph.D.
Ex Officio Committee Member

The following signatories attest that all software used in this dissertation was legally licensed for use by Morgan Roddy for research purposes and publication.

Mr. Morgan Roddy, Student	Dr. Adam Huang, Dissertation Director

This dissertation was submitted to http://www.turnitin.com for plagiarism review by the TurnItIn company's software. The signatories have examined the report on this dissertation that was returned by TurnItIn and attest that, in their opinion, the items highlighted by the software are incidental to common usage and are not plagiarized material.

Dr. Rick Wise, Program Director	Dr. Adam Huang, Dissertation Director

Abstract

The goal of this research was to support the development of a novel propulsion system for small satellites (<180 kg) and CubeSats. This was pursued by conducting a collection of studies that were designed to provide engineering data that would be critical in designing a functional prototype. The novel propulsion system was conceived by the author to provide best-in-class performance for the small satellite and CubeSat families of spacecraft. This context presents specific design requirements that the presented technology attempts to satisfy. The most critical among these is high density; the propellant was designed to be stored with high density and the thruster was designed to be as compact as possible. The propulsion system is composed of two primary elements, a propellant generator and a thruster. The propellant generator works by sublimating a solid crystal into vapor and then using this vapor to etch a dense metal. The resulting gaseous byproducts of this reaction are the propellant. This dissertation used xenon difluoride (XeF_2) vapor to etch tungsten (W) which react to form xenon gas (Xe) and tungsten hexafluoride (WF_6). This approach gave a theoretical propellant storage density 5.40 g/cm^3; and 5.17 g/cm^3 was demonstrated. The sublimation dynamics of the XeF_2 were studied as a function of surface area and temperature and it was found to be suitable for the intended application due to its high effluence rate; that is, it sublimates fast enough to be useful. The sublimation rates are on the order of 10's of µg/s. The etch rate of XeF_2 on W was also studied and found to be suitably fast to provide useful amounts of reactants for use as a propellant, again on the order of 1's of µg/s. The thruster is an electrostatic radio frequency (RF) ion thruster design and is manufactured with Low Temperature Co-Fired Ceramic (LTCC) materials system and manufacturing technology. Manufacturing samples of the thruster were built at the University of Arkansas in July 2015 and tested at NASA's Marshall Space Flight Center in May 2018. Testing validated the viability of the

LTCC thruster and provided valuable information on how to improve the thruster's design.

Acknowledgements

I would like to take this opportunity to thank the people who have supported my academic and professional pursuits over the past fifteen years.

First and foremost, I want to thank my wife, Denise Beike, for all of her love, support, advice, encouragement, and strength over the last decade. I wouldn't have made it without you!

Thanks go out to my parents, Kurt and Lisa Roddy, who through their love and support have helped me fulfil many life-long dreams, thank you from the bottom of my heart.

Thanks go out to Adam Huang for being a mentor and friend over the last five years. I have learned and grown tremendously under your guidance and I owe you a debt of gratitude. Thanks go out to my lab mates for your friendship and comradery: John Lee and Josh Pennington.

Thanks go out to my many mentors and friends who over the years have helped me stay the course: Ken Vickers, Rick Wise, Scott Kirkpatrick, Elaine Kirkpatrick, Marij Sayed, Azad Siahmakoun, Donald Richards, Jeff Brown, Linea Hess, Karen Hulsebosch, Kipp Kraus, Chris Jose, Mike Horn, Ramzi Zahreddine, Katie Kraigh, Jeff Beckman, Alice Forehand, Chris Leibs, Jeremy Holm, and Bruce Masse.

Thanks to my committee, Larry Roe, Ingrid Fritsch, Silke Spiesshoefer, and Rick Wise, for your time and guidance.

This work was supported by a generous Walton Foundation Doctoral Academy Fellowship award. The research was also supported by NASA's Marshall Space Flight Center (MSFC) Cooperative Agreement Notice-Dual Use Technology Development grant at MSFC NNM17AA15A.

Cheers,

Morgan Roddy

Table of Contents

List of Figures

List of Tables

List of Published Papers Used in this Dissertation.

Part of Chapter 4 was originally published as: “Characterization of LTCC-Manufactured Electrostatic Thruster (LTCC-ET) – Close-out Report”, P.-H. A. Huang, K. M. Polzin, M. A. Roddy, NASA/TM-2019–220136, M-1487, M19-7371, NASA Document ID: 20190027344, Published Jun 1, 2019

1. Background

The goal of this research was to study and develop a selection of technologies to form an understanding of the materials and processes that together may be applied to propulsion technology for small spacecraft. The vision of this work is that small satellites could be enabled to conduct significant interplanetary operations on their own. The mission of this work was to provide a technological basis for this and to provide a roadmap for how enabling technologies could be developed. The motivation of this research comes from an observation that there exists a capability gap in propulsion technologies available to small satellites. Small satellite propulsion has unique challenges and constraints that are less impactful in larger systems. The technical solution that has been hypothesized to address this gap was conceived as a result of the experiential knowledge of the author and established literature. The solution employed materials systems and processes that were familiar to the semiconductor and electronic industries. This innovation is a result of the author's experience in semiconductor materials, devices, and manufacturing, and RF systems engineering, materials, and processes. The basis technologies, processes, and materials that this work draws from are not traditionally associated with propulsion or even space technologies. The innovation of this work was to bring together several disparate existing subjects to realize a technological basis for a novel propulsion concept. The concepts that will be presented in this dissertation are a new propellant and propellant storage methodology as well as a new architecture for a thruster. The result of this dissertation is a successful demonstration that these disparate subjects can be applied to the development a novel propulsion system and a hypothetical roadmap of the required future activities to reach the stated goal.

1.1. Small Satellite Technologies

The space era was ushered in with the first two artificial satellites put into orbit by the USSR and the USA in 1957 and 1958, respectively. Both satellites were both 'small satellites' as

Sputnik 1 weighed 83.6 kg and Explorer 1 weighed 13.97 kg [1]. These satellites' masses were limited by the capability of launch vehicles of the 1950's era and not the ambition of their creators. The next few decades realized the creation of heavy launch vehicles. Many new launch vehicles were created and the heaviest and most capable of these was the Saturn V, which could place as much as 140,000 kg into low earth orbit (LEO) [2]. The ever growing launch capacity kicked off by the space race led to the deployment of thousands of satellites for commercial, scientific, and national defense applications. The pinnacle of satellite technology, the International Space Station (ISS) which weighs ~420,000 kg, began construction in 1998, is still growing to this day, and has had its funding tentatively extended until 2030 [3]. Today's standard commercial communication satellites and flagship scientific missions such as the James Webb Telescope weigh in around 5,800 – 6,700 kg [4, 5, 6, 7].

The trend of increasing spacecraft size has in the past two decades given way to the re-emergence of smaller spacecraft. This shift was facilitated by miniaturization of electronics and computing resources. Today the term 'small satellite' is defined by NASA as a spacecraft that is less than 180 kg in mass [8, 9].

Small satellites offer several key advantages over their larger cousins: cost, ease of access to space, and risk tolerance. There are three primary costs involved in operating a satellite: design / construction, launch, and operation. Small satellites are typically cheaper to design and build because they are simpler than their larger cousins. Their size constraints mean that they can integrate fewer systems which makes them more cost effective. However, this does not mean that they are 'cheap' as a 10 kg small satellite (CubeSat) developed by NASA can still cost in excess of $10M. Small satellites typically do not have the service life of larger satellites. They are typically designed to operate for months or years and then are retired due to lack of radiation

hardness and orbital decay due to atmospheric drag. The missions they conduct are therefore more succinct. This is partially due to the fact they do not have as robust hardware, and thus as long lifetimes, as larger missions. The most significant cost savings of small satellites are their launch cost.

Large launch vehicles designed to place large payloads, such as communication satellites, into orbit always have mass margin. Mass margin is the extra mass that a launcher could bring to the target orbit which is in excess of the mass of the primary payload. Mass margin is typically sold to small spacecraft operators who fly their hardware as secondary payload. This has the downside that the secondary payload can only be placed in the orbit of the primary payload (or an intermediate orbit). However, there is a substantial savings in launch cost afforded by the choice to be a secondary payload. Small satellites enjoy easier access to space as government agencies such as NASA and the DoD regularly buy up mass margin on launch vehicles and distribute this among a range of customers. Private organizations also use this approach for their access to space.

Small satellite programs can be more risk tolerant because of their cost and this allows for greater technical innovation. The lower relative cost compared to large flagship state-sponsored missions means that there is less monetary risk which allows for more technological or mission profile risks to be taken. For example, small satellites regularly fly unproven hardware for technology demonstration purposes while large missions would not typically employ any critical components that are not flight proven (with the exception of flight test programs). All these considerations have helped popularize the small satellite ecosystem over the past 2 – 3 decades and realized a space industry that no longer ignores the value that small satellites can provide.

A small satellite form factor has emerged that leverages the aforementioned values by introducing a standardized form factor, the CubeSat. CubeSats enjoy standardization because their

geometry is fixed to be integer multiples of 10 cm x 10 cm x 10 cm cubes. Each cube is referred to by the unit of 'U' which has a volume of 1 L. This definition has led to the development of standard satellite deployment mechanisms, called launchers, which further reduce launch costs. Costs are reduced by significantly simplifying the process of integrating a satellite with a launch vehicle and the process of deploying the satellite. The most popular CubeSat deployment systems are the Poly Picosat Orbital Deployer (P-POD), developed at the California Polytechnic Institute [10], and the NanoRacks CubeSat Deployer (NRCSD) developed by a private launch services company, NanoRacks [11]. Both devices, very simply put, contain CubeSats in a box during launch and then deploy them by opening a hatch on the box and pushing the satellites out via a large spring. The simplicity of these deployment mechanisms, coupled with the relatively low cost of development, has led to an explosion in the adoption of the CubeSat form factor in academic, government, and commercial sectors. Since CubeSats were first flown in 2003, approximately 1150 have been launched, according to an international organization who tracks their use [12]. This popularity has led to the rapid growth of commercially available space hardware which is scaled down the development costs of small satellites, and especially CubeSats, and further propelled their popularity.

1.2. Propulsion System Fundamentals and Tradeoffs

The propulsion technologies available to CubeSat designers has only recently become mature enough for significant adoption. NASA is currently tracking the development and maturation of a wide range of technologies under development and being marketed by a range of organizations [9]. A discussion of propulsion fundamentals is an important prerequisite to delving into the breadth of propulsion systems currently in existence.

Propulsion systems have one specific job, to impart momentum on a spacecraft. This is

always achieved via the principles of conservation of momentum and is stated in its most general form in Equation 1.2.1.

$$\dot{\boldsymbol{P}} = \sum \boldsymbol{F} + \sum \dot{m}\boldsymbol{v} \qquad \text{(Equation 1.2.1)}$$

Stated in words, the time rate of change of momentum of a system is equal to the sum of the forces acting on the system plus the sum of the mass fluxes times their velocities into the system. Devices exist which provide a change in momentum without a mass flux and these rely on solar radiation pressure, photon momentum, from the sun. These devices are referred to as 'solar sails' but are not germane to this discussion. All other propulsion systems rely on ejecting mass to change the momentum of a spacecraft.

The most important figures of merit for a propulsion system are delta-V, that amount of velocity change the system can impart, and thrust, which determines how fast the delta-V can be achieved. These performance metrics cannot be simultaneously maximized for reasons that will be discussed. The designer of a propulsion system would have to optimize a design based on the needs of a mission and the relative cost for a tradeoff between delta-V and thrust.

The total delta-V a spacecraft can achieve is dependent on the mass of propellant, the mass of the spacecraft, and the efficiency of the propulsion system, or specific impulse (I_{sp}). The relationship between these variables is known as the Tsiolkowski equation or the 'rocket equation' [1]. This equation is derived by integrating the acceleration of a spacecraft based on the thrust of the propulsion system and spacecraft mass, and considers the fact that the spacecraft becomes lighter as propellant is consumed. The rocket equation is shown in Equation 1.2.2.

$$\Delta V = g I_{sp} ln\left({}^{m_i}/_{m_f}\right) \qquad \text{(Equation 1.2.2)}$$

In this expression, I_{sp} is the specific impulse of the propulsion system, a measure of thruster efficiency, g is acceleration due to gravity on Earth, m_i is the initial mass of the vehicle and m_f is

the final mass of the vehicle after propellant has been expended. This can also be expressed in terms of vehicle 'dry mass', that is the mass of the vehicle without propellant (m_d), and propellant mass (m_p), shown in Equation 1.2.3.

$$\Delta V = g I_{sp} ln\left({m_d + m_p}/{m_d}\right) \quad \text{(Equation 1.2.3)}$$

From this equation it can clearly be seen that to maximize the delta-V of a propulsion system, one should maximize specific impulse and propellant mass, and minimize vehicle mass.

The specific impulse is the factor that measures the efficiency of a propulsion system. This can be expressed in a number of ways, but the most meaningful way is shown in Equation 1.2.4.

$$I_{sp} = {v_{exit}}/{g} \quad \text{(Equation 1.2.4)}$$

Equation 1.2.4 shows that the efficiency is directly proportional to the exit velocity of the propellant. This definition assumes that the mass flux of propellant is perfectly columnated which is not realistic. However, this level of analysis is sufficient for this discussion so exhaust plume divergence and velocity distribution of propellant will not be addressed. Deeper analyses would result in finding a lower specific impulse than the ideal value defined by Equation 1.2.4 if these considerations were accounted for.

The second most important metric for a propulsion system is thrust. Spacecraft design principles assume that the vehicle is already in space which means that thrust to weight ratio is far less important than for a launch vehicle that must lift off the surface of earth. The thrust is important because it determines how rapidly the propulsion system can affect its total delta-V. Thrust can be expressed a number of ways, but the most germane definition is shown in Equation 1.2.5.

$$T = \dot{m}_p v_{exit} \quad \text{(Equation 1.2.5)}$$

This states that thrust is equal to the mass flux of propellant times the exit velocity of the propellant. Again, this assumes a columnated propellant flux which is a simplification.

Another important consideration for a propulsion system is the time it takes to achieve its specified delta-V. This is important for how orbital mechanics are calculated. In traditional chemical propulsion systems, the delta-V is effectively imparted instantaneously. This is not physically true, but it is a useful assumption to simplify the calculations of how an orbit changes after a propulsion event. Low-thrust propulsion systems on the other hand can take days, weeks, or months to perform a delta-V maneuver which complicates the orbital calculations. Therefore, the time of propulsion is important to consider. The time of thrust can simply be calculated by taking the ratio of propellant mass to propellant mass flux, according to Equation 1.2.6.

$$t_{thrus} = {}^{m_p}/_{\dot{m}_p} \qquad \text{(Equation 1.2.6)}$$

The thruster that is considered in this dissertation is an electrostatic thruster and will be described in further detail in a later section. The key thrust metric of this type of system is the effective accelerating voltage. This quantity is an integration of the electric field along the path a propellant ion travels. This should not be confused with the voltage applied to accelerating grids. The relationship between applied voltage and effective voltage is dependent on several factors including thruster geometry, thruster grid design, plasma density, and others. The transfer function between these variables can either be simulated or physically measured. This transfer function was considered to be outside the scope of this dissertation. Therefore, when accelerating voltage is mentioned, it is the effective voltage, not the grid voltage. The accelerating voltage, V_a, can be related to some quantities already presented. The kinetic energy of a single propellant species (assuming single ionization) can be written in terms of accelerating voltage as in Equation 1.2.7. This can be further described in terms of a specific propellant species, shown in Equation 1.2.8, where q_e is the charge of an electron, M_p is the molar mass of a propellant species, and N_a is Avogadro's number. The exit velocity can be solved for equating the accelerated ion energy to the

kinetic energy as in Equation 1.2.9. From this analysis we can then write exit velocity, specific impulse, and thrust in terms of system level variables in Equations 1.2.9 – 1.2.11 [1].

$$E = V_a q_e \quad \text{(Equation 1.2.7)}$$

$$M_p v_{exit}^2 \Big/ 2N_A = E = V_a q_e \quad \text{(Equation 1.2.8)}$$

$$v_{exit} = \sqrt{2N_A V_a q_e \Big/ M_p} \quad \text{(Equation 1.2.9)}$$

$$I_{sp} = \frac{1}{g}\sqrt{2N_A V_a q_e \Big/ M_p} \quad \text{(Equation 1.2.10)}$$

$$T = \dot{m}_p \sqrt{2N_A V_a q_e \Big/ M_p} \quad \text{(Equation 1.2.11)}$$

From Equation 1.2.10 and Equation 1.2.11, it would seem that the most efficient and quickest way to achieve a delta-V would be to maximize accelerating voltage and minimize propellant molar mass. However, there is a tradeoff space that comes to bear because the total thruster power must be considered. Propellant current can be calculated from the propellant mass flux, the molar mass, Avagadro's number, and the electron charge, shown in Equation 1.2.12. Spacecraft that use electric propulsion are power limited with regards to how they operate the propulsion system. Given the fact that beam current is a deterministic value, Equation 1.2.12 can be solved for the propellant mass flux and is shown in Equation 1.2.13.

$$I_p = \dot{m}_p N_A q_e \Big/ M_p \quad \text{(Equation 1.2.12)}$$

$$\dot{m}_p = I_p M_p \Big/ N_A q_e \quad \text{(Equation 1.2.13)}$$

The effective propellant beam power can be calculated from current and voltage and is shown in Equation 1.2.13. It is important to note that this is not the total power required to operate the thruster because there are other elements in the system that dissipate energy. This power calculation

is simply the power the propulsion system must impart on the mass flux. Total power would be significantly higher than this, however this is a useful framework to describe the tradeoff space of a thruster.

$$P = I_p V_a \qquad \text{(Equation 1.2.14)}$$

Finally, the propellant mass flux can be solved for in terms of deterministic values and independent variables and is shown in Equation 1.2.15.

$$\dot{m}_p = {PM_p}\Big/{V_a N_A q_e} \qquad \text{(Equation 1.2.15)}$$

The factor other than specific impulse that must be optimized to maximize delta-V is propellant mass. There are two ways to achieve this in practice. Typically, the mass of propellant is determined by the mass budget of a spacecraft. Therefore delta-V would be limited by efficiency and the fraction of a spacecraft's initial mass that was allocated to propellant. The mass budget is driven by the capability of the launch vehicle in traditional large satellites. However, the small satellite ecosystem, and especially CubeSats, have another more important factor to consider, volume. This is because small satellites and CubeSats are secondary payloads and are volume limited. The masses of this class of satellite are already small in comparison to the primary payload, by definition. The challenge to optimize propellant mass becomes one of how to store it efficiently. This brings up the primary thesis of this dissertation: It is advantageous for small satellites to have their propellant stored in as dense of a manner as possible to maximize propellant mass and minimize propellant volume.

The most important propulsion system metrics to maximize, delta-V and thrust, can be expressed in terms of design variables that can be affected by a system level design. These variables include propellant molar mass, propellant density, spacecraft dry mass, accelerating voltage, and total thruster beam power. Equations 1.2.16 and 1.2.17 do just this. These equations

remove all deterministic variables from the equation leaving a clear view of how design decisions affect system performance. The new variables introduced in Equation 1.2.16 are propellant storage volume, V_p, and propellant storage density, ρ_p.

$$\Delta V = \sqrt{2N_A V_a q_e / M_p}\, ln\left(m_d + V_p \rho_p / m_d\right) \qquad \text{(Equation 1.2.16)}$$

$$T = P\sqrt{2M_p / V_a q_e N_A} \qquad \text{(Equation 1.2.17)}$$

These two equations give a clear picture of how to improve system performance as well as the tradeoff space between independent variables. First, increasing thrust can be done by increasing power, without introducing a penalty on delta-V. Likewise, increasing propellant density has a direct benefit to delta-V for a fixed volume propellant system but no penalty on thrust. These two variables should always be maximized for small satellite / CubeSat propulsion systems. The mass of a spacecraft and the volume allocated to propellant are not typical design variables that are available to a propulsion system designer so they are not discussed. The accelerating voltage (only applicable for electrostatic thrusters) and the molar mass of propellant affect both thrust and delta-V but not in the same way. Given a fixed power, increasing accelerating voltage will increase delta-V but decrease thrust. Alternately, increasing molar mass of propellant will increase thrust but decrease delta-V. These last two variables are the two that must be appropriately balanced to meet mission demands.

The above tradeoff space for small satellites and CubeSats elucidates the logical progression for propulsion system optimization. The propellant molar mass is inextricably intertwined with propellant density and so these are collectively determined by propellant choice. The tradeoff space between molar mass and accelerating voltage is then determined by mission context. The process for system level design optimization would be to select a propellant and then

determine the necessary accelerating voltage needed to balance thrust versus delta-V considerations. Overall performance can be increased by increasing propellant storage volume or propulsion system power. This dissertation seeks to expand the bounds of possible combinations of propellant selection and storage density by presenting a novel propellant and thruster architecture. The choices made by the author will be described in the section on the proposed propulsion system architecture.

1.3 Xenon Difluoride and Tungsten

Xenon difluoride (XeF_2) is a solid crystalline compound that sublimates at room temperature. The compound, along with its sister compound xenon tetrafluoride (XeF_4), were first synthesized at Oak Ridge National Laboratory in the 1960's and were the first known noble gas compounds [13, 14]. The two compounds' chemical and physical properties were studied for the next several years for the purpose of refining nuclear materials for atomic weapons [15, 16, 17, 18]. The compounds were thought to be useful for this purpose because they react with heavy metal ions to form gaseous fluorides. These fluorides would then be easier to separate from other ore materials for subsequent elemental and isotopic refinement. The literature is not clear how about how successful or useful this method was for the ostensible reason of national security and strategic knowledge confinement. The literature does, however, present some useful information on the nature of these compounds. Physical properties including vapor pressure, density, and heat of sublimation are reported. Two different synthesis methods are also reported. XeF_2 did not find a substantial commercial application until the maturation of the semiconductor industry [19, 20, 21] (there is no noteworthy literature on commercial applications of XeF_4). This was due to the fact that vapor phase XeF_2 aggressively etches certain relevant materials with high selectivity over oxides, including: silicon, tantalum, molybdenum, tungsten, and others [22, 23, 24, 25, 26, 27].

XeF_2 is a very effective etchant of any material that readily forms volatile fluorides. This is because of the etching mechanism of XeF_2 which will be discussed in depth in Chapter 3.

1.4 Low Temperature Co-Fired Ceramics

Low Temperature Co-fired Ceramics (LTCC) is a manufacturing technology analogous to printed circuit board (PCB) technology but uses ceramic structural / dielectric layers instead of glass-epoxy laminates [28]. Additionally, it doesn't use laminated copper sheets on the dielectric which are then etched, as in PCB, but rather uses a silk screen method to deposit conductors as a sinterable paste. LTCC is typically used to create packaging solutions for electronic components, like PCB, but is suited to much more extreme conditions. The technology can also incorporate more advanced structural elements such as cavities and thick-films which are not found in PCBs. These capabilities can be used to form embedded circuit components such as resistors, inductors, capacitors, and RF waveguides.

LTCC technology is orders of magnitude more expensive than PCB technology so it has only been adopted for extreme-use applications. The ceramic material has a very low dielectric loss tangent of 0.001 – 0.0014 which makes it excellent in RF applications with frequencies above 10 GHz where dielectric loss is a significant issue. LTCC is chemically stable and non-reactive so it is useful in harsh environments with high humidity or chemical exposure. LTCC ceramic has a breakdown voltage in excess of $4 \text{ X } 10^{10}$ V/m making it suitable for high-voltage applications. Additionally, the structural and electrical properties of LTCC don't degrade until high temperatures are reached, >500 °C, at which point virtually any electrical component would have failed. These material properties make LTCC technology an excellent choice for exotic applications where PCB would not have acceptable survivability or performance.

LTCC devices are built akin to PCB as previously stated. Designs are created by stacking

individual layers of soft ceramic-polymer thick films called ‘green tape’. These typically range between 0.005” – 0.020” thick and are typically processed as an 8” x 8” square sheet. Each layer can have vertical interconnects (vias), much like PCBs, which are punched out of the green tape with a die then filled with electrically conductive and sinterable paste. Lateral conductors are made of the same paste and are applied with a silkscreen process. Voids can also be punched or milled into the green tape. Once each layer is completed, they are stacked together and subjected to high pressures ranging from 2000 – 4000 psi to laminate the layers together. The entire stack is then co-fired at 850 – 1000 °C to fuse all the layers together, burn off the polymer binders, and result in a single monolithic structure.

1.5 Current State of the Art in CubeSat / Small Satellite Propulsion

Propulsion systems are divided into several sub-genres. The first genre is chemical propulsion, the second is thermodynamic propulsion, and the third electric propulsion. Chemical propulsion relies on a chemical reaction or decomposition process to increase the enthalpy of a gas which is then expelled through a nozzle. Chemical propulsion comes in two common variants: monopropellant or bipropellant. Monopropellants rely on chemical decomposition in a catalyst reaction chamber and bipropellants rely on a chemical reaction between two chemicals that meet in a combustion chamber. Thermodynamic propulsion techniques rely on a propellant to have energy in its stored state that is transformed when the propellant is used. The classic example of this is a cold gas thruster that works by releasing compressed gas through a nozzle. Thermodynamic thrusters can also include devices such as a resistojet which works similar to the cold gas thruster with the addition of a heating element in the propellant expansion path. Electric propulsion, sometimes called solar electric propulsion, derives its name from the fact that electricity, typically generated from solar panels, is used to accelerate propellant. This is achieved

by using electric or magnetic forces and the selection of which force is employed determines the sub-genre of electric propulsion.

The current state of the art for propulsion that can be used for CubeSat and small satellites is best summarized in NASA's 2018 report on the ecosystem of small satellite technologies [9, 29, 30]. This document is updated every several years to serve as a benchmark for the academia, industry, and governmental agencies. Table 1.1 is taken from this report and will be described in detail. The table is organized by technology area, 'Product', thrust, specific impulse, and 'TRL Status'. TRL stands for Technology Readiness Level and is a 9-point scale used by the aerospace

Table 1.1: Summary of the current state of the art for small satellite propulsion systems [9].

Propulsion System Types for Small Spacecraft			
Product	Thrust	Specific Impulse (s)	TRL Status
Hydrazine	0.5 - 30.7 N	200 - 235	9
Cold Gas	10 mN - 10 N	40 - 70	GN2/Butane/R236fa 9
Alternative (Green) Propulsion	0.1 - 27 N	190 - 250	HAN 6, ADN 9
Pulsed Plasma and Vacuum Arc Thrusters	1 - 1300 μN	500 - 3000	Teflon 7, Titanium 7
Electrospray Propulsion	10 - 120 μN	500 - 5000	7
Hall Effect Thrusters	10 - 50 μN	1000 - 2000	Xenon 7, Iodine 3
Ion Engines	1 - 10 mN	1000 - 3500	Xenon 7, Iodine 4

industry to describe the maturity of a technology [31]. These range from principle of operation scientifically valid to fully flight-ready and mature technologies. The TRL definitions are shown in Table 1.2.

Table 1.2: Technology Readiness Level definitions.

TRL Definitions	
TRL 1	Basic principles observed and reported

TRL 2	Technology concept and/or application formulated
TRL 3	Analytical and experimental critical function and/or characteristic proof-of-concept
TRL4	Component/subsystem validation in laboratory environment
TRL5	System/subsystem/component validation in relevant environment
TRL 6	System/subsystem model or prototyping demonstration in a relevant end-to-end environment (ground or space)
TRL 7	System prototyping demonstration in an operational environment (ground or space)
TRL 8	Actual system completed and "mission qualified" through test and demonstration in an operational environment (ground or space)
TRL 9	Actual system "mission proven" through successful mission operations (ground or space)

Hydrazine is a special kind of propellant called a 'monopropellant'. It is called this because its decomposition products react with each other and do not need to be mixed with anything to function. Hydrazine's chemical structure consists of two nitrogen atoms bonded together by a single bond and each having two dangling hydrogen atoms. Hydrazine's chemical formula is N_2H_4 and is a highly toxic and unstable liquid at room temperature [1]. Operation of a hydrazine thruster is performed by flowing it over a catalyst bed, which is typically heated to hundreds of degrees Celsius, and then the gaseous result is expanded out a nozzle. The hydrazine spontaneously decomposes under these conditions to create a propellant stream of hot gas.

Propulsion systems of this design are typically used for attitude control on larger spacecraft and are attractive because of their relative simplicity. Their wide adoption means that they are a mature technology with a diverse range of product offerings. The challenge of using hydrazine thrusters is that it is difficult to miniaturize the support equipment they require, namely redundant valving systems. Additionally, high delta-V maneuvers are not practical due to low storage density. Hydrazine thrusters are generally characterized as having good thrust, specific impulse, and have a high TRL. An example of a CubeSat-targeted commercial hydrazine propulsion system is the CubeSat High-impulse Adaptable Monopropellant Propulsion System (CHAMPS) developed by Aerojet Rocketdyne that is a 1 U system that carries up to 360 g of propellant, has a thrust of 0.24

– 2.9 N, dissipates ~ 2 W of power, and has a specific impulse of 215 s [32].

A new type of monopropellants, sometimes referred to as 'green propellants', have gained traction over the last decade. They have been developed to address the toxicity concerns of hydrazine. This makes it easier for a green propellant thruster to be integrated on small satellites or CubeSats. Green propellants are like hydrazine in that they are a monopropellant which is an advantage for simplicity. The challenge with green propellant systems is that they have low specific impulse, low storage density, and have miniaturization challenges. These systems are not suitable for high delta-V maneuvers for the same reasons that other monopropellant technologies fall short, but they are an ever maturing technology. The most mature example is the Busek BGT-X5 thruster which boasts 10% higher specific impulse and 45% greater storage density over hydrazine when using a proprietary green propellant (AF-M315E). This system takes up 1 U of volume and can provide 500 mN of thrust at a specific impulse of 220 – 225 s while dissipating 20 W of power during operation [33]. Other noteworthy examples are the Busek BGT-X1 with 100 mN of thrust and a specific impulse of 214 s [34], the Aerojet Rocketdyne MPS-130 CHAMPS with 1.5 mN of thrust and specific impulse of 240 s [35], the Aerojet Rocketdyne GPIM Propulsion System with 400 – 1100 mN of thrust and a specific impulse of 235 s [36], and the ECAPS HPGP thruster with 1000 mN of thrust and a specific impulse of 232 s [37].

Cold gas thrusters are the simplest kind of thruster. They produce thrust by simply releasing compressed gas through a nozzle. This technology is very mature and the most common propulsion system used on small satellite missions. The limitation of cold gas thrusters is that they are inherently low specific impulse because of the thermodynamics of an expanding gas. This limits their usefulness to being only good for attitude control, reaction wheel desaturation, and minor station keeping maneuvers. They are not useful for significant delta-V maneuvering. Cold gas

thrusters are generally characterized as having good thrust, low specific impulse, and have a high TRL. One of the most technologically mature cold gas thrusters for CubeSats is the VACCO Micro CubeSat Propulsion System that flew on two interplanetary missions that were launched on May 5, 2018. These were the MarCO A and MarCO B CubeSats which performed flybys of Mars in November 2018. The propulsion system provided a total impulse of 755 N-s with a thrust of 25 mN and specific impulse of 25 s [38]. Other noteworthy examples are the SSTL SNAP 1 thruster with 50 mN of thrust and a specific impulse of 43 s [39], the UTIAS-SSFL CNAPS thruster with 40 mN of thrust and a specific impulse of 35 s [40], Microspace Rapid POPSAT-HIPI thruster with 1 mN of thrust and a specific impulse of 43 s [41], the GOMSpace MEMS Cold Gas thruster with 1 mN of thrust and a specific impulse of 50 – 75 s [42], and the VACCO Industries CPOD with 25 mN of thrust and a specific impulse of 40 s [43].

There is a class of thrusters that are based on the cold gas thruster with one addition, the resistojet thruster. This thruster architecture uses a resistive heater placed in the propellant stream to add thermal energy to propellant. This increases the enthalpy of the gas and, in turn, this increases exit velocity of the propellant giving a boost in specific impulse. This approach increases efficiency at the expense of having greater power demands of the spacecraft. An example of this technology flown on a small satellite mission was NovaSAR in 2012 which used a xenon-based resistojet thruster for attitude control. The LPR thruster was manufactured by SSTL and had a thrust of 18 mN and a specific impulse of 48 s and dissipated 30 W of power [44]. Other noteworthy resistojet examples are the CU Aerospace PUC thruster with 5.4 mN of thrust and a specific impulse of 65 s [45], CU Aerospace CHIPS thruster with 30 mN of thrust and a specific impulse of 82 s [46], the Busek AMR thruster with 10 mN of thrust and a specific impulse of 150 s [47], and the University of Southern California's FMMR thruster with 0.13 mN of thrust and a specific

impulse of 79 s [48].

Pulsed plasma thrusters or vacuum arc thrusters are a promising type of propulsion due to their very high specific impulse. These thrusters operate by using an arc discharge from a high voltage source to vaporize a very small amount of propellant through ablation. This process can eject propellent at very high velocity which is why the specific impulse can be so high. The challenge with this propulsion method is that the propellant is stored and used as a solid. This makes it very difficult to manage the process of delivering more propellant to the arc discharge region, especially in low gravity. A common design is to use a cylindrical slug of propellant, such as Teflon, which is pushed through a tube to the discharge section of the thruster by a spring. This method is limited by the travel of the spring. This technology can be useful as a reaction control thruster or to desaturate reaction wheels but not for high delta-V maneuvers because propellant mass is extremely limited. The most mature commercial offering of this technology is the Busek BmP-220 Micro-Pulsed Plasma Thruster. This system is a compact device weighing only 0.5 kg which provides 175 N-s total impulse, a system volume of 0.375 L, a total dissipated power of 3 W, a thrust of 0.14 mN, and a specific impulse of 536 s [49]. Other noteworthy examples include the Busek MPACS thruster with 0.14 mN of thrust and a specific impulse of 830 s [50], Primex Aerospace EO-1 PPT thruster with 0.14 mN of thrust and a specific impulse of 1150 s [51], George Washington University μCAT thruster with 0.02 mN of thrust and a specific impulse of 3000 s [52], Würzburg University UWE4 Arc Thruster with 0.01 mN of thrust and a specific impulse of 1100 s [53].

Electrospray thrusters are a promising technology that has been maturing over the last 15 years. The operation principle is to use an accelerating grid to accelerate an ionic fluid that is a liquid in the vacuum of space. This process is similar to an electrostatic thruster but does not

require generating a plasma to form ions. Rather, the ionic fluid is atomized with a jet spray and then accelerated with electrostatic forces. The most notable example of this technology is the Scalable ionic Electrospray Propulsion System (S-iESP) thruster developed at MIT. This method is limited in its usefulness because the propellant storage is difficult to scale up. The technology is, however, relatively mature at TRL 7 and flew on the AeroCube-8 mission in 2016 [54]. The system boasts a very compact size of 96 X 96 X 21 mm, low mass of 95 g, low power dissipation of 1.5 W, thrust of 74 – 82 μN, and a specific impulse of 1717 s [55]. Other noteworthy electrospray propulsion systems include the Accion Systems TILE 5000 thruster with 1.5 mN of thrust and a specific impulse of 1800 s [56], the Busek BET-1mN with 0.7 mN of thrust and a specific impulse of 800 s [57], and the Busek BET-100 with 0.1 mN of thrust and a specific impulse of 1800s [30].

The final two thruster architectures are Hall effect and electrostatic thrusters. These two types of thrusters are the two most mature electric propulsion technologies and both design paradigms have flown on missions dating back to the 1970s. Both thrusters rely on the basic process of ionizing a gaseous propellant by electrical means and then using electrodynamic and electrostatic forces in the case of the Hall effect thruster or only electrostatic forces in the case of the Ion Engine to accelerate the propellant. The method by which plasma is generated differs among commercial designs but they typically use electric arc discharge or an RF antenna to generate plasma. The TRL level of these thrusters is reported to range widely and based on propellant type. The current state of the thrusters is that they are actively being developed for small satellites and CubeSats by academia, government, and industry.

Hall effect thrusters are characterized by having a cylindrical toroidal plasma cavity with an axial electric field and a radial magnetic fields. Propellant is flowed into the base of the toroid where it is ionized to form a plasma. The ions are then accelerated by electrostatic fields created

by an anode in the base of the thruster and a cathode at the outlet of the toroid. The applied radial magnetic field serves to confine propellent ions from bombarding the cathode during operation and eliminates the need for an accelerating grid, a feature of ion engines. This helps to reduce the system complexity and improve thruster lifetime. The final requisite element of the hall thruster is a neutralizing spray. This is simply an electron gun that is aimed into the exhaust plume to neutralize the propellant and keep the spacecraft charge neutral. The absence of this element would quickly lead to charge buildup on the spacecraft which would lead to two poor outcomes. First, the exhausted propellant would be attracted back to the spacecraft due to its high charge and would return and stick to the spacecraft, bringing its momentum with it and rendering the thruster useless. Second, the high charge on the spacecraft could lead to catastrophic electrical failures throughout the vehicle. Hall effect thrusters are typically high-power devices though some have been scaled down to sizes suitable for small satellites and CubeSats. The most noteworthy example is the MIT MHT-9 Hall thruster. This device operated with power input ranging from 20 – 500 W, an accelerating voltage of 100 – 300 V, produced 1 – 18 mN of thrust, and had a maximum specific impulse of 2000 s [58]. Other noteworthy Hall thruster examples are the Busek BHT-200 thruster with 12.8 mN of thrust and a specific impulse of 1390 s [59], the Busek BHT-600 with 39.1 mN of thrust and a specific impulse of 1530 s [59], the Sitael Aerospace HT100 thruster with 50 mN of thrust and a specific impulse of 1100 s [60], the Sitael Aerospace HT400 thruster with 50 mN of thrust and a specific impulse of 1750 s [61], and the UTIAS-SFL CHT thruster with 1 – 10 mN of thrust and a specific impulse of 1139 s [62].

The thruster architecture presented in this dissertation is based on the Radio Frequency Ion Engine architecture, or simply put, an electrostatic thruster. Although the operating principle of an electrostatic thruster is straightforward, the actual device can be quite complex [63, 64, 65, 66, 67,

68]. There are three primary elements: a plasma cavity, an excitation source, and a set of grid electrodes. First, a cavity contains a gaseous propellant which is ionized to form a plasma. Second, an RF antenna of some type, which differs depending on the specific example, provides the energy to create the plasma. Some designs rely on arc discharge to ignite plasmas but this is atypical [63]. Third, there is a set of gridded electrodes which are perforated with holes to allow propellant to leak out of the cavity. The first electrode closest to the plasma chamber, the screen electrode, serves as an RF ground and helps define the plasma cavity in the electrical sense. The second electrode on the thruster's exterior, the accelerating electrode, is arranged outside of the screen electrode and is charged to a high DC voltage. As ionized gas leaks out of the cavity and past the screen electrode, the electric field from the accelerating electrode applies a force on the ions and accelerates them out of the system to provide thrust. The typical electrostatic thruster also includes a neutralizing spray device to keep the exhaust plume and spacecraft charge neutral. A schematic of this design is shown in Figure 1.1.

Significant efforts have been made in the past to develop electrostatic thrusters for small

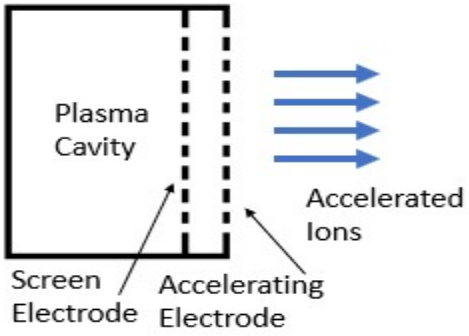

Figure 1.1: Architectural schematic of an electrostatic thruster.

satellites and CubeSats. The Busek BIT-3 is a 56 – 80 W thruster with 1.15 – 1.25 mN of thrust and a specific impulse of up to 2300 - 3500 s, depending on its operating conditions [9, 29, 30,

69]. This thruster has passed design reviews to fly on two upcoming 6 U CubeSat missions, LunaH-MAP and IceCube, two lunar missions that will fly in 2020 or 2021 (dependent on the launch of NASA's first Space Launch System rocket) [29, 30, 70]. Busek also has another electrostatic thruster product offering, the BIT-1 which is a smaller version of the BIT-3 and has a thrust of 0.18 mN and a specific impulse of 2150 – 3500 s [29, 30, 69]. Airbus has a range of electrostatic product offerings including the RIT-μX with 0.05 – 0.5 mN of thrust and specific impulse ranging over 300 – 3000 s, and three variants of the RIT 10 EVO thruster with thrust levels of 5, 15, and 25 mN, respectively, each having specific impulses of 1900, 3000, 3200 s, respectively [29, 71, 72]. The University of Tokyo has designed, built, tested, and flown the I-COUPS thruster witch has 0.3 mN of thrust and a specific impulse of 1000 s [9, 72]. The final significant thruster is the Enpulsion IFM Nano Thruster with 0.01 – 0.4 mN of thrust and a specific impulse ranging from 3000 – 6000 s [9, 73]. All of the aforementioned thrusters are either flight proven, or have been demonstrated under realistic conditions (in vacuum).

A graphical summary of the thrust and specific impulse of all the above-mentioned thrusters is shown in Figure 1.2. The noteworthy takeaway of the plot is that electrostatic thrusters are best-in-class when considering both specific impulse and thrust and therefore the electrostatic architecture was selected as the basis of this dissertation's thruster component.

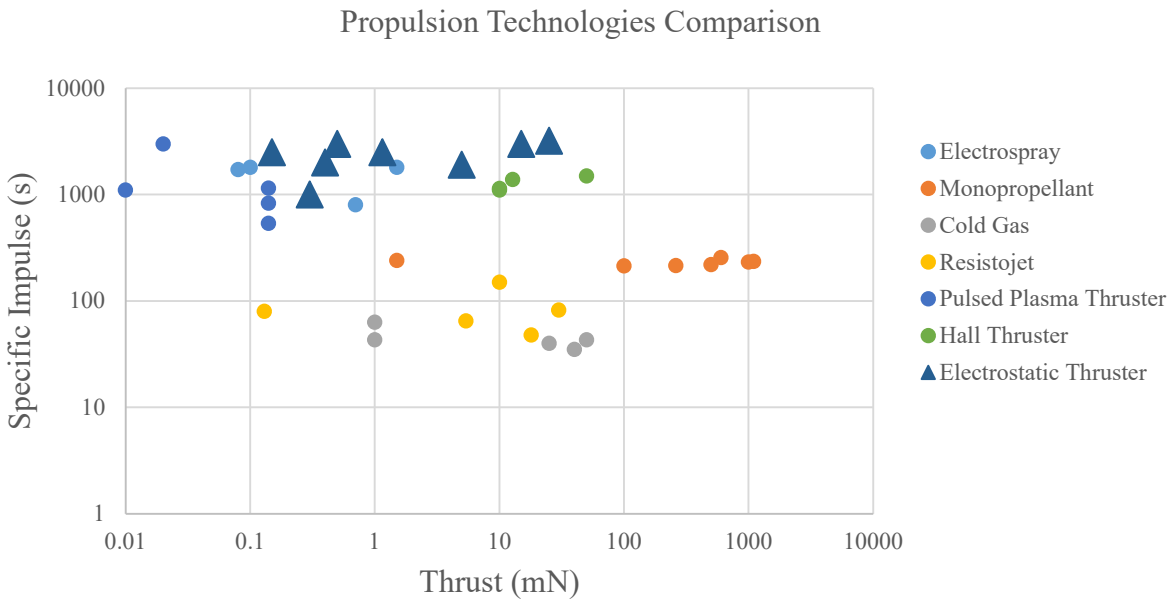

Figure 1.2: Summary plot of the current state of the art of small satellite propulsion systems.

This research did seek to innovate on the fundamental form of the electrostatic thruster. Rather, the goal was to seek a new way of combining all the requisite elements of the thruster in a new way so as to be optimized for application on CubeSats. This effort required understanding the important figures of merit for a thruster and how they relate to the application ecosystem. The previous discussion of the tradeoff space of propulsion systems gave rise to optimizing several factors. First, an ideal thruster would occupy minimal volume. Again, this is driven by the fact that CubeSats are a volume constrained satellite architecture, so volume is at the highest premium. Second, an ideal thruster could be operated at maximally high accelerating voltages too for the best specific impulse and thrust. The tradeoff between thrust and specific impulse is still important but that is pertinent to a thruster's operation, not physical design. Third, the thruster must have maximally long grid lifetime. The burn time of a thruster is determined by how it is operated and the total amount of fuel available, but it is limited by how long the grids last before they erode away. Again, operational factors relate to how the thruster is used, not how it is designed so it is

important to design to worst case scenarios, i.e. very long burn times. Therefore, the three most important design qualities that will be addressed by the thruster design presented in this dissertation are: compactness, high-voltage tolerance, and resistance to corrosion/erosion. All three of these issues are directly addressed by the selection of materials and techniques that was employed in this work.

1.6 Proposed Propulsion System Architecture

A propulsion system architecture is proposed in this dissertation. The intent of the work was to explore the feasibility of this proposal and to carry out fundamental research to provide engineering data that can be used to build a prototype of the system, or at least identify key areas that need further investigation before prototyping. The intent of the proposed architecture was to fill a hypothetical need based on an intended 'use-case'. The proposed architecture is illustrated in Figure 1.3.

The proposed propulsion system is a heavy metal subliming electrostatic propulsion system. This architecture is novel and no such system has been found in the literature. The proposed system is novel because of the propellant generation paradigm and a new type of thruster

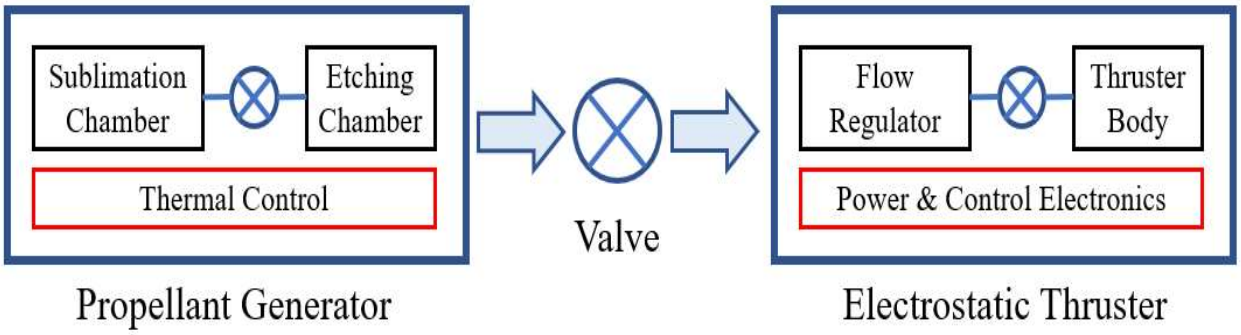

Figure 1.3: Schematic of the proposed propulsion system.

manufacturing technology. The system operates by subliming a corrosive material that etches a heavy metal. The corrosive material is stored in a subliming chamber and the heavy metal is stored in an etching chamber. Both chambers' temperatures are regulated by a thermal control system and separated by a valve. These components together make up the propellant generator. The purpose of this arrangement is to be able to store propellant in a maximally dense form which, as has been shown theoretically, helps to optimize the achievable delta-V that the system can provide.

The corrosive material that will be explored in this dissertation is XeF_2 and the heavy metal is W. These materials react to form a stream of Xe and WF_6 gases and this flow of gas is used as propellant. The process would also work using XeF_4 and W as reactants and could theoretically achieve slightly better performance. This approach allows for the highest propellant storage density that has ever been reported. The theoretical maximum propellant storage density is 5.44 g/cm^3 for XeF_2 and W and 5.70 g/cm^3 for XeF_4 and W. XeF_4 was not explored in this research because it is not readily available commercially.

The propellant generator is separated from an electrostatic thruster by a valve. The electrostatic thruster is composed of a gas flow regulator, power and control electronics, and a thruster body. The flow regulator controls the mass flow rate of propellant entering the thruster body which is a critical operational parameter for any propulsion system. The electronics coordinate valves, flow control, and DC and RF power delivery to the thruster. The thruster body is the component that ionizes propellant and accelerates it to produce thrust. The thruster is based on a classical thruster design, the electrostatic RF ion thruster, but is manufactured with an entirely new technique, the LTCC process and materials system. An advantage of using LTCC is that the electrodes can be embedded in a tough and chemically resistant ceramic material which enhances grid lifetime. Additionally, the manufacturing technique allows for a very efficient packing of

functional elements of the thruster to improve how compact it can be produced. The ceramic material also allows for the thruster to be capable of very high voltages and temperatures, limited only by the drive electronics or other ancillary equipment. This research focused on studying the behavior of the three novel elements of this propulsion system, the sublimation chamber, etching chamber, and thruster body. The heaters, valves, flow control, and electronics are well understood engineering components and are not academically interesting in this context.

The intended use-case for the proposed propulsion system provided context so that performance targets were not arbitrary. The hypothetical use-case was an interplanetary 3 U CubeSat mission that needs a delta-V in excess of 1000 m/s. The design was further constrained by placing a 10 W power limit for propellant beam power and a propellant storage volume of only 0.1 L. This mission profile was selected in 2014 based on the assertion that would have been exceedingly difficult with the technology of the day. The only technology that could compete was an iodine propellant based propulsion which was in development at the time [71, 9]. That mission has been delayed due to propulsion system development challenges stemming from propellant corrosion. It was originally intended to be capable of a 200 m/s delta-V maneuver to lower its orbit from a 600 km circular orbit to a 300 km circular orbit.

The method of defining a tradeoff space, as described by Equation 1.2.16 and Equation 1.2.17, was investigated for the above use-case. Again, this method involved determining the intended power, propellant, and propellant storage volume. This method assumed that the application was a power limited and volume constrained spacecraft such as a CubeSat. The propellant selection that was made determined the average propellant storage density as well as the average propellant molar mass. From these parameters, the thrust and specific impulse as a function of effective accelerating voltage were calculated. A plot showing this relationship is

shown in Figure 1.4. These calculations determined that an accelerating voltage of 318 V would result in a delta-V of 1000 m/s and net a thrust of 106 μN. This delta-V would take ~112 days to achieve on the use-case CubeSat. This represents the performance target of this work.

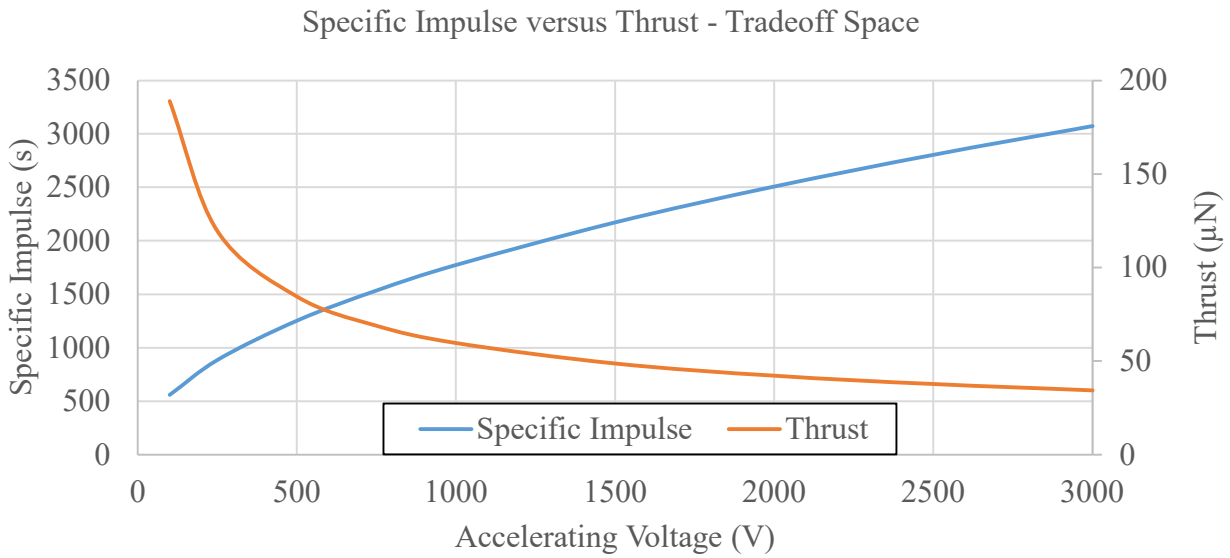

Figure 1.4: Thrust versus delta-V tradeoff space for the intended use-case CubeSat fitted with the proposed propulsion system.

The sublimation of XeF_2 was studied as a function of its surface area and temperature and this work is presented in Chapter 2. The etching behavior of XeF_2 on W was studied, and this work is presented in Chapter 3. The design, fabrication, and testing of the LTCC electrostatic thruster was performed and is presented in Chapter 4. The conclusions of this work and a discussion of future work and potential lines of research stemming from this dissertation are discussed in Chapter 5.

2. Sublimation Dynamics of Xenon Difluoride

The most important element of this research was to understand the sublimation dynamics of xenon difluoride. This substance was well known to have a vapor pressure in the single to double digit torr range at room temperature and elevated temperatures [13, 14, 15, 16, 17]. It is typically used in etching systems by subliming solid crystals under vacuum to provide gas phase reactants [25, 19, 26, 27]. The literature describing the use of XeF_2 focused on its reactability for use in etching or in chemical synthesis of other compounds. However, there was no previous work that described the fundamental behavior of how the phase change from solid to gas occurs. There were still gaps in the behavior of XeF_2 that had to be explored in order to use it in the intended use case. Namely, the sublimation dynamics had to be studied.

The central idea of this dissertation was that high-density propellant storage can be achieved for use in small satellite propulsion systems. XeF_2 is a solid crystal with a higher density than any compressed gas propellant. Furthermore, its reactive properties opened the door for the etching of high-density metals to turn them into gaseous compounds that could be used as propellant. It was not critical to have precise etching products because the products were intended to be used in an electric propulsion system. In this operation, nearly any gas can be ionized and then accelerated by electric and magnetic forces to generate thrust. This is in contrast to a chemical propulsion system wherein the propellant must have precise chemical concentrations and compositions for proper use. The far more important quantities that must be understood in an electric propulsion application are the mass flow rate and pressure of propellants. The first piece of the hypothesized high-density propulsion system that had to be understood was the generation of XeF_2 gas for use in a propulsion system. The studies proposed and conducted for this research have sought to empirically determine the relationship between effluence, that is the mass flowrate of a subliming sample of XeF_2, and the pressure, temperature, and surface area of the crystal.

2.1 Methodology and Experimental Apparatus to Study Sublimation Dynamics of XeF_2

An experimental apparatus and procedure to investigate the sublimation dynamics was proposed by the author and approved by the committee. A schematic of the physical test apparatus is shown in Figure 2.1. The apparatus consisted of a vacuum chamber, a crystal sample holder, a pressure transducer, a pneumatic vacuum vent valve, and an in-situ thermocouple probe to measure the interior of the vacuum chamber. The vacuum chamber was a custom designed piece of

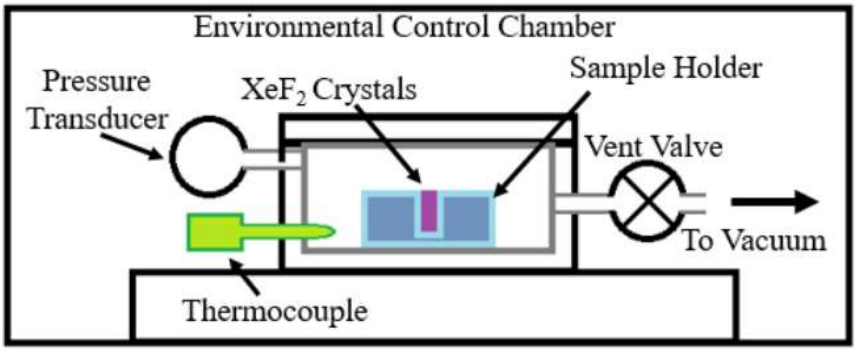

Figure 2.1: Schematic of the sublimation dynamics experimental setup.

hardware that was fabricated in-house. The body of the vacuum chamber consisted of a large block of 6061-T6 aluminum, which provided a mounting-points for a vacuum line, valves, and pressure transducers, as well as a large thermal mass to improve thermal stability during operation. This block had a pocket milled into it to form the interior cavity of the chamber. A lid, also made of 6061-T6 aluminum, was designed to be bolted to the body of the chamber via eight ¼”-28 socket head cap screws and had double o-ring face seals to seal to the chamber body.

The large number of high thread-pitch bolts meant that the lid could be clamped very tightly without having to worry about galling the threads over numerous cycles of opening and closing and to ensure that a good o-ring seal cold be made. All other vacuum connections were either 1/8”

NPT or 1/4" compression (Swagelock^{tm} style) fittings which have excellent vacuum sealing properties due to their tapered design. The eight bolts provided ~4000 lbs of clamping pressure on dual o-rings in the face of the chamber lid which, in conjunction with the other sealing faces, provided an excellent vacuum chamber with leak rates in the µtorr/second range. The crystal holder was a 0.5" X 0.9" X 0.9" piece of aluminum with four holes drilled all the way through. The nominal sizes of these holes were 0.050", 0.075", 0.100", and 0.125". These varying hole sizes were selected to provide varying XeF_2 crystal surface area. During experimentation, only one of the four holes would be filled with crystals in order to provide different levels of surface area in the design of experiments. The internal volume of the vacuum chamber, including dead space in the transducers was estimated to be 44.8 cm^3 based on precise CAD models.

Pressure measurements were provided by one of two Baritron^{tm} pressure transducers. Two transducers were used to have a wide dynamic range of measurement. The first transducer had a maximum range of 10 torr and an accuracy of ± 0.001 torr. The second transducer had a maximum range of 100 torr and an accuracy of ± 0.010 torr. These devices consisted of a calibrated Inconel diaphragm fitted with a factory calibrated strain gauge. Pressure was determined by the manufacturers proprietary calibration curves based on pressure dependent deflection of the Inconel diaphragm. The pressure was given read out by a MKS 651B transducer controller. The pneumatic vent valve was a normally off valve that opened when provided 1 – 3 bar of air pressure. The supply air was provided by a solenoid valve plumbed to house air which was driven by high power op-amp voltage follower and an analog output from the data acquisition hardware (DAQ). The thermocouple was included for real-time in-situ temperature measurements and was a type-K thermocouple. The thermocouple was measured by an AD595 hermetic thermocouple driver with internal temperature compensation. The device's output was a voltage proportional to temperature

with a 10 mV/°C slope. Additional hardware involved in the sublimation dynamics setup was a vacuum pump and an environmental control chamber.

The environmental control chamber's role was to establish and maintain the temperature of each experiment. The thermocouple driver and the solenoid op-amp were powered with ±15 V by a pair of voltage regulators (LV7815 and LV7819) which in turn were powered by a benchtop power supply. The experiment was controlled by a custom LabView computer program that was written for this research. The software controlled the valve, and read the thermocouple temperature via a USB DAQ, the NI USB-6216. The pressure transducer was powered and read by the MKS 651B controller which had a serial interface connected to the computer hosting the LabView code. A photograph of the sublimation dynamics experimental setup is shown in Figure 2.2.

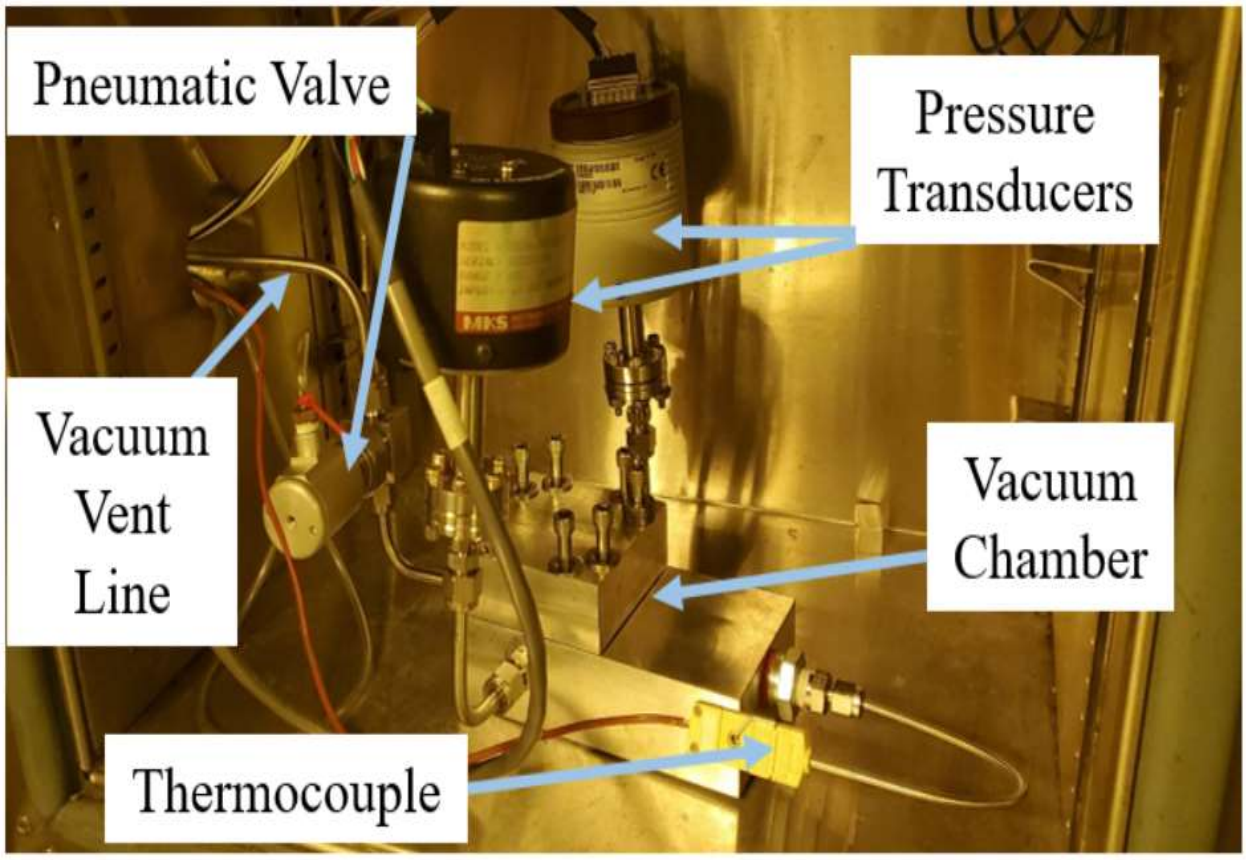

Figure 2.2: Photograph of the sublimation dynamics experimental setup inside the environmental control chamber.

2.2 Pilot Data and Initial Observations

An effort to validate the experimental test apparatus, procedure, electronics, and software was undertaken before the test campaign commenced in earnest. This process brought up a number of concerns that had to be addressed before moving on. The first three attempts to conduct a sublimation test, Trials 1 – 3, failed due to data corruption. The LabView™ code was fixed so that data was properly stored. Trials 4 – 7 successfully produced clean data that show no signs of having errors due to instrumentation or software. These trials were serially analyzed and modifications to the test setup and experimental method were implemented based on the analysis. The completion of Trials 4 – 7 yielded a vetted experimental method and test setup.

The experimental method used for Trial 4 began with loading ~75 mg of XeF_2 into the 0.075" hole in the crystal holder and tamping it down with a 0.075" drill rod (stock from which drill bits are ground; had a precise diameter which was ground and polished and made of hardened tool steel). The crystal holder had a piece of Kapton^{tm} tape covering the bottom of the hole to keep the crystals from falling out during handling. The crystal holder was then placed in the vacuum chamber and the entire apparatus sealed and pumped down. The software controlled the experiment in the following manner. First, the vacuum vent valve was opened until an experiment start pressure threshold was reached, 0.3 torr, at which point the valve was closed and the pressure and temperature were recorded as a function of time for 10 minutes at a sampling frequency of ~10 Hz. After the 10 minute experiment collection time was reached, the sampled data was stored in an Excel^{tm} file. This is referred to as a sublimation cycle. After the first cycle, the process was repeated by opening the vacuum vent valve until the experiment start pressure was reached and again the vent was closed and pressure and temperature data taken. This process lasted for 50

cycles. This number of cycles was not required but ensured that all the XeF_2 was consumed during the trial. The aforementioned process was the basis for all future sublimation experimental procedures and the final procedure only had simple modifications from the original.

The results from Trial 4 were simultaneously interesting and concerning. Thirty-five of the 50 cycles sampled had sufficient XeF_2 mass to sublime until the calculated vapor pressure was reached or exceeded (these raw time-based pressure traces are only shown for trial 4 and not again because they are exemplary of all subsequent data collected in form and overall behavior). The first issue was that every cycle had a max pressure that was higher than the calculated vapor pressure. Figure 2.3 shows the maximum pressure reached as well as the calculated vapor pressure based on the average temperature [16]. The second issue was that the time constant for sublimation was not constant but increased with time. This quantity, τ_s, was determined by finding the time it took to reach 95% of the calculated vapor pressure and dividing that time by three. This approach assumed that the sublimation dynamics follow a first order reaction rate where change in pressure over time was proportional to the pressure. The time constant for sublimation is shown in Figure 2.4. The third issue was the pressure traces did not have asymptotic behavior as was expected. In the most basic theory of sublimation, the pressure should stabilize at a pressure equal to the vapor pressure; therefore, a plot of pressure versus time should approach a horizontal asymptote. The fourth issue was that the max pressure reached was not constant and decreased with time. Not only was it larger than the expected value (vapor pressure) but it was not constant. Lastly, Cycle 1 had curious behavior and didn't follow a smooth curve like all of the other pressure traces did. The pressure traces from cycles 1 – 5 are shown in Figure 2.5 and pressure traces from cycles 1 – 35 are shown in Figure 2.6.

The chief goal in analyzing the data from Trial 4 was to determine if the observed effects

described above were real and reflecting the true sublimation dynamics of XeF_2 or if there were issues with the method or apparatus which led to unexpected results. The analysis below led to introducing three modifications to the experimental method and are described in detail in the next several paragraphs.

The first modification was to address pressure overshoot, the behavior of pressure rising significantly higher than the calculated vapor pressure (Figure 2.3). This effect was hypothesized

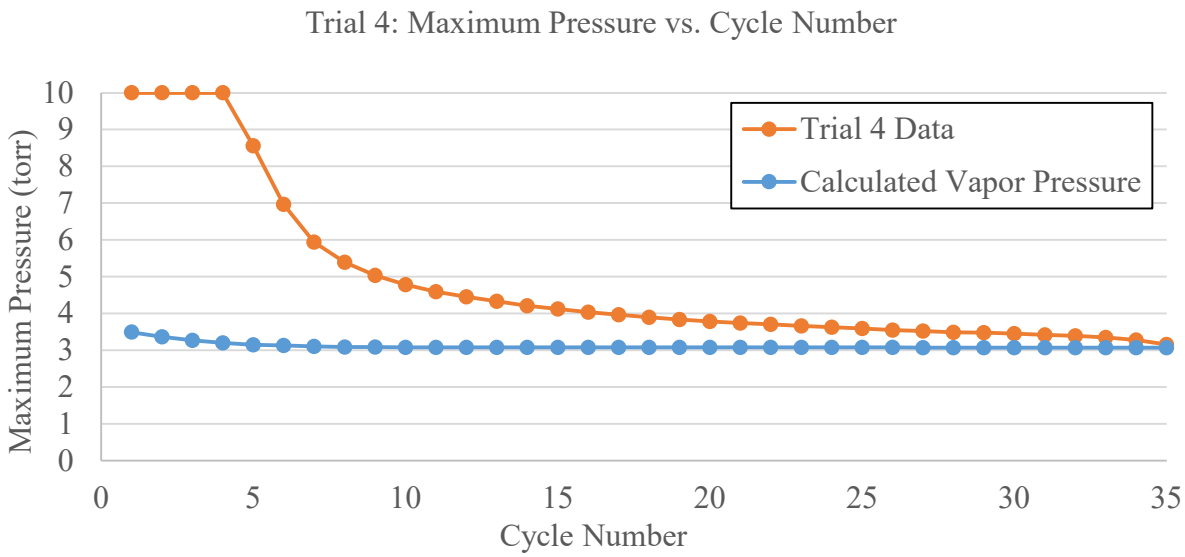

Figure 2.3: Maximum pressure compared to the calculated vapor pressure of XeF_2 for Trial 4.

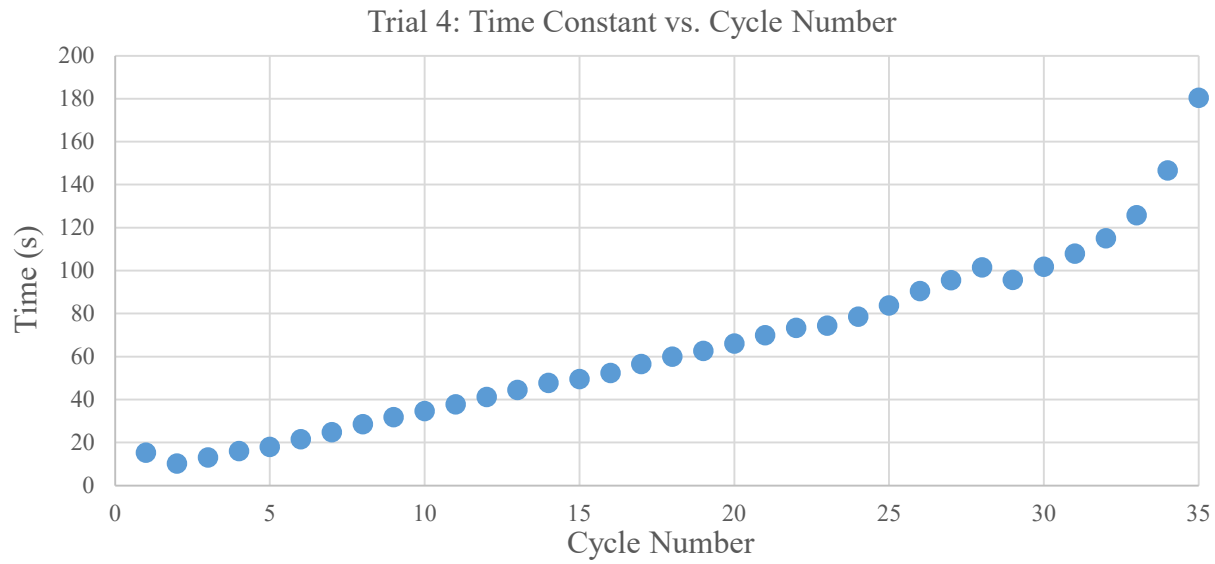

Figure 2.4: Time constant of sublimation for Trial 4 over 35 cycles.

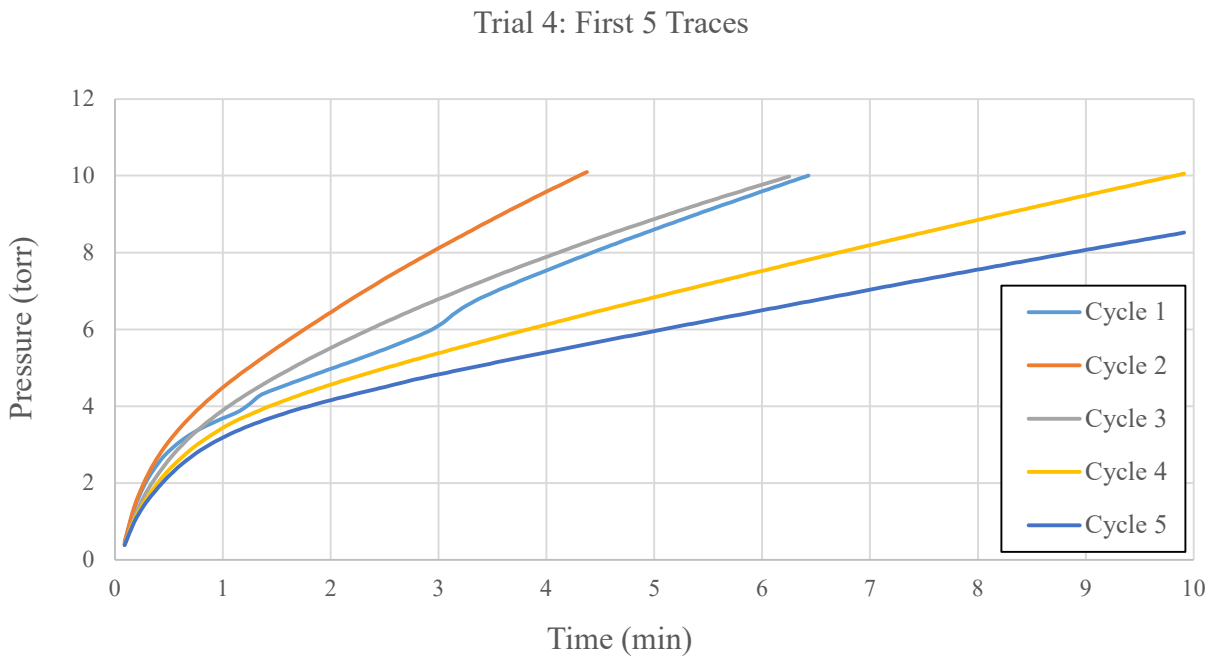

Figure 2.5: Pressure traces from sublimation cycles 1 – 5 for Trial 4.

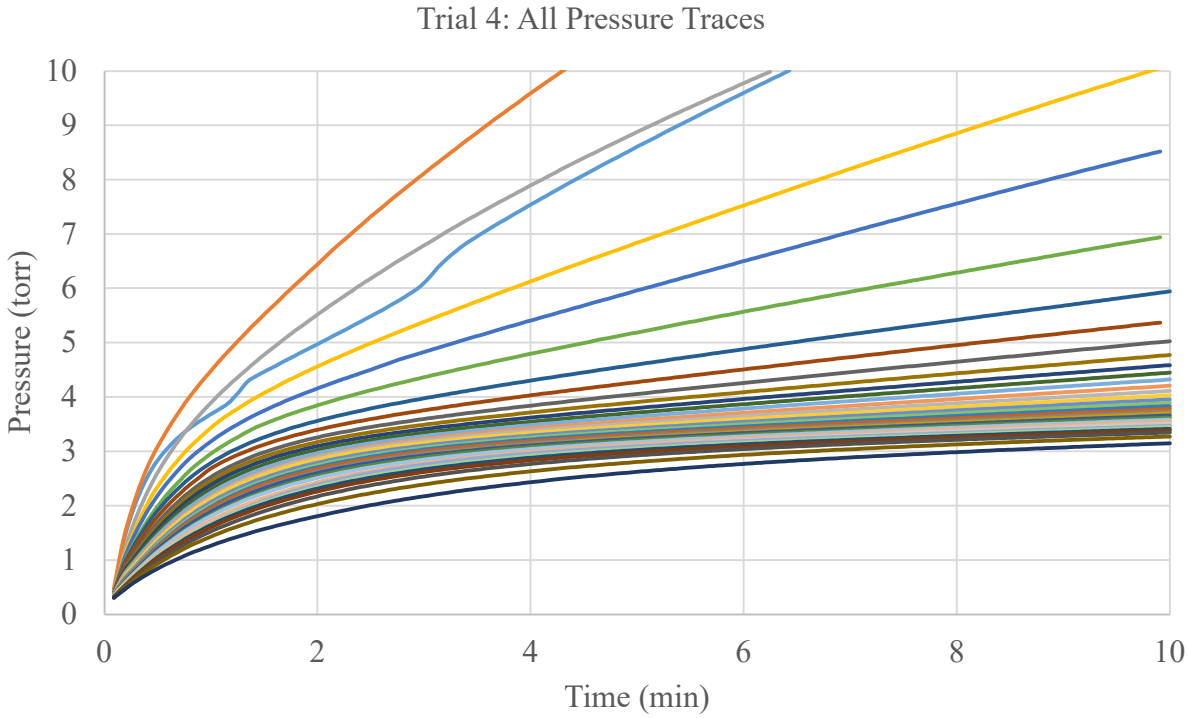

Figure 2.6: Pressure traces from sublimation cycles 1 – 35 for Trial 4.

to be caused by outgassing of absorbed water inside the vacuum chamber. Additionally, the oddities of Trial 4, Cycle 1 (Figure 2.5) were hypothesized to be a similar transient behavior. Both of these issues were addressed by introducing a 'bake-out' step before Trial 5 was attempted. This process involved heating the environmental control chamber to 60 °C for 8 hours to drive off any absorbed moisture. The chamber was capable of higher temperatures but there was a fear that damage to the pressure transducers could occur and an abundance of caution was taken to avoid damage. The implementation of the bake-out eliminated the odd behavior of Cycle 1 but had no noticeable effect on the issue of pressure overshoot.

The second modification was to address the increasing time constant of sublimation (Figure 2.4). This effect was hypothesized to be due to changes in the microscale surface area of the XeF_2 crystals. The process of loading the crystals into the sample holder involved tamping down the

crystals with a drill rod. The crystals were mechanically weak and so some crystals were pulverized to a very fine size while others remain in larger pieces. This can only be described qualitatively because there was no way to measure actual distribution of crystal size in-situ.

An analogy of this process would be to envision what would happen if you took all of the dishes in your home and randomly placed them into a large box. If one took a large flat board and uniformly compressed the top of the stack of dishes, it stands to reason that some would break and some would not. The dishes (crystals) may all start out with a certain size distribution but would certainly end up with a size distribution populated with pieces of dishes (crystals) that are significantly smaller than what were originally present as well as some dishes that are in the original size distribution. This is the understanding of what is happening with the crystal packing in the sample holder and is important because of the hypothesized behavior of sublimation dynamics.

Sublimation is the process that takes place to balance the equilibrium between the solid and gas phases of a material that is colder than its triple point (deposition is the complementary process). Sublimation is dependent on surface area because this is the interface for the sublimation / deposition dynamic equilibrium. The experiment has sample surface area as an independent variable by virtue of having different crystal holder hole sizes because surface area affects sublimation dynamics. The important thing to keep in mind, however, is that surface area is important at the macro and micro scale. The hypothesis for why the time constant for sublimation was shorter for earlier cycles and longer for higher cycles was that it was caused by a changing size distribution of crystals. The earliest cycles had a crystal size distribution that included much smaller crystal sizes than the later cycles. The understanding was that the smallest crystals were the first to sublimate and do so more rapidly than the larger crystals (due to their greater surface

to volume ratio) which meant that crystal size distribution was not constant over the experiment and was an uncontrolled and unmeasurable variable that affects the results of the experiment. This effect was ultimately seen in every single experimental trial conducted for the entirety of this research.

This realization was important in understanding and interpreting the results of the sublimation dynamics experiment and is a very important takeaway and conclusion of the experiment; size distribution of crystals was a critical factor in the sublimation dynamics of XeF_2. It was considered that the depth of the holes in the sample holder could be a contributing factor to the variance in sublimation time constant. The idea was that as crystals sublimate, the surface of the crystals becomes farther and farther down the hole of the sample holder. For this to contribute to the observed change in time constant, the flow of gas from the crystal surface to the vacuum chamber would have to be choked by the hole in the sample holder. This was ruled out because the change in geometry that this process would introduce was negligible compared to the relatively far more tortuous paths for expansion and diffusion of gas throughout the experimental setup. The conclusion of these thought experiments was that the time constant for sublimation changed based on the size distribution of the XeF_2 crystals and a random variable within this study. This was a modification of how to interpret the data rather than a modification of the experimental process or setup.

The third modification was to address the absence of asymptotic behavior in the pressure versus time traces (Figure 2.5 and Figure 2.6). This effect was initially thought to be a combination of outgassing of absorbed water and a leak in the experimental setup that was introducing air from the outside. Instead of an asymptotic behavior, the pressure traces exhibited a linear pressure rise over time after transient changes in sublimation during the first ~4 minutes of the experiment. The

major concern was that the pressure did not stabilize to a fixed vapor pressure in accordance with the initial hypothesis of this work. The outgassing issue was addressed already and the bake out step was introduced in the experimental method to combat the issue. The leak issue was investigated and was determined to be insignificant.

The pressure rise rate of Trial 4, Cycle 50 was calculated to determine the leak rate of the system. This cycle was chosen to represent the leak rate since the XeF_2 crystals had be exhausted ~15 cycles prior. The estimate of the leak rate of the system was found to be ~9 mtorr/min. Over a 10 minute experimental cycle time, this would lead to a change in pressure of the system of ~0.09 torr due to air leaks. However, the linear rate of pressure rise for the first 35 trials (last 6 minutes of experiment, after transient behavior) ranged between 0.1 – 1.2 torr/min and can be seen in Figure 2.7. Clearly, the leak rate could not account for lack of asymptotic behavior during the experiment and there was something else that was causing the pressure to rise steadily. It was hoped that the bake out procedure could improve this behavior. In conclusion, the final modification to the experimental method was to increase the cycle time for sublimation from 10 to 15 minutes in order to capture more data to see if a horizontal asymptote cold be reached by simply observing the sublimation over a longer time.

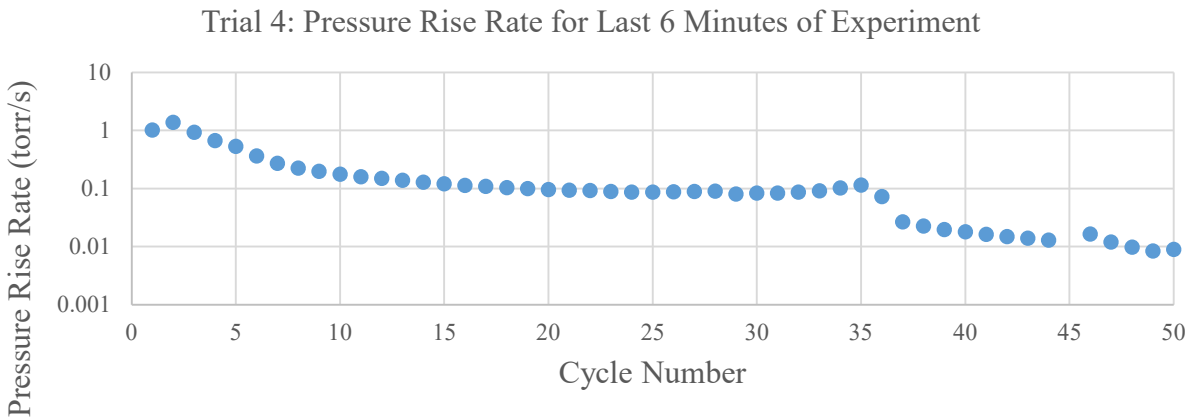

Figure 2.7: Pressure rise rate calculated for the last 6 minutes of each cycle of Trial 4.

The steadily decreasing maximum pressure reached on each cycle was hypothesized to be due to a temperature decrease in the XeF_2 crystals due to latent heat cooling. The idea was that subliming crystals drew heat out of the remaining crystals and the sample holder over the course of the experiment. This heat depressed the temperature of the crystals and, therefore, reduced the predicted vapor pressure. The vapor pressure observed was still greater than the predicted vapor pressure but there still was a trend that higher cycle numbers had lower maximum pressure. This hypothesized thermal issue was addressed in two ways. First, a five minute thermal stabilization period was added between the completion of a data collection and the venting process. It was theorized that if there was a temperature depression due to latent heat loss, this heat could be replaced by letting the system sit idle for extra time. Second, the Kapton™ tape on the bottom of the crystal holder was removed to promote a good thermal contact between crystal holder and the thermally massive vacuum chamber, thereby connecting the crystals to the large thermal mass of the experimental setup.

In summary, the Trial 4 experiment showed behavior that could possibly indicate shortcomings in the experimental method or setup. The maximum pressure reached was much higher than predicted and this was thought to be due to outgassing. This was addressed by adding a bake out step. The sublimation time constant was not a constant and this was believed to be a result of changing microscale surface area of the XeF_2 crystals over the course of the experiment. This was an effect that could not be directly measured or controlled in-situ and was understood to contribute to systematic error. The pressure traces did not exhibit horizontally asymptotic behavior as was expected. This was determined to not be due to a leak and needed further investigation. The experimental time was increased to see if simply more time was needed to reach an equilibrium.

The decreasing maximum pressure reached was not constant and decreased with cycle number. This was theorized to be due to thermal effects and a thermal soak and improved thermal contact of the sample holder was implemented to try to alleviate this issue.

The aforementioned modifications were implemented for Trial 5. The result of trial 5 was very similar to Trial 4 and exhibited the same general behavior. The erratic pressure plot from Trial 4, Cycle 1 was not observed and the change was attributed to the inclusion of the bake out step. The time constant for sublimation again increased over cycle number but this was again believed to be due to the microscale surface area of XeF_2 crystals. Again, the maximum pressure was much larger than the predicted vapor pressure, no horizontal asymptote was observed, and the pressure continuously kept rising even after the vapor pressure was reached. Figure 2.8 shows the maximum pressure reached for Trial 5 as well as the calculated vapor pressure based on the average temperature. The time constant for sublimation of Trial 5 is shown in Figure 2.9. The Trial 5 pressure traces for cycles 1 – 20 are shown in Figure 2.10.

Trial 5 led to observations similar to those in Trial 4, namely, pressure overshoot, lack of asymptotic behavior, and decreasing maximum pressure. It was hypothesized that the pressure

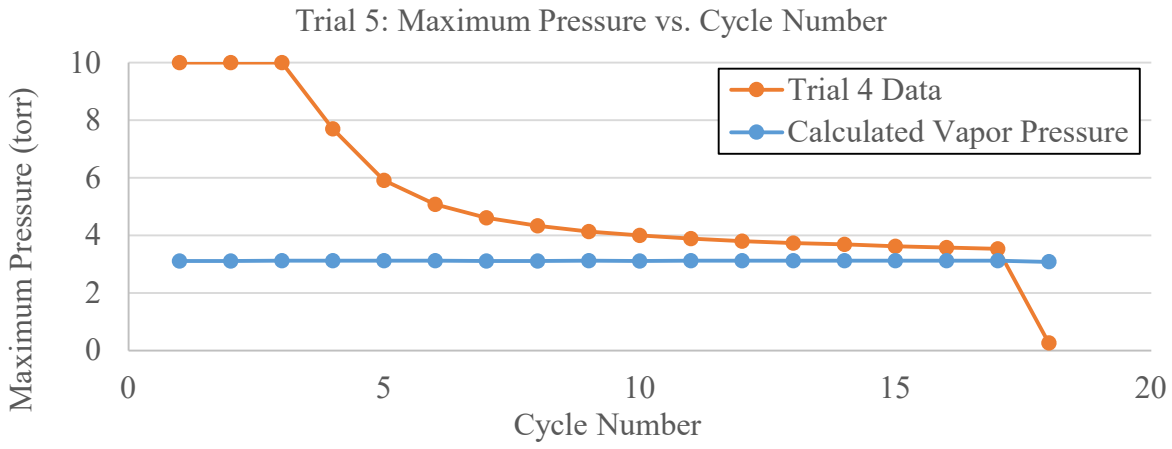

Figure 2.8: Maximum pressure compared to the calculated vapor pressure of XeF2 for Trial 5.

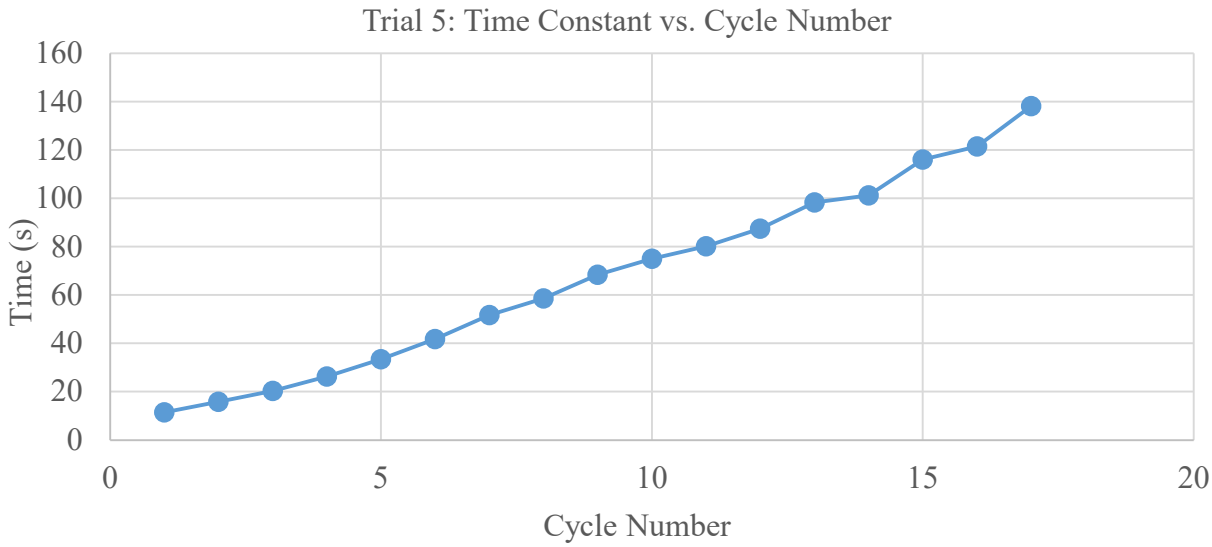

Figure 2.9: Time constant of sublimation for Trial 5 over 17 cycles.

transducer had a significant error so it was checked against a known good transducer that used a fundamentally different method for measuring pressure, the Convectron^{tm} gauge. This sensor uses a feedback loop to keep a hot filament at constant temperature. The air pressure is related to the heat transfer from the filament. At higher pressures, the filament draws more current to maintain its temperature than at low pressure. This relationship is factory calibrated and very stable when

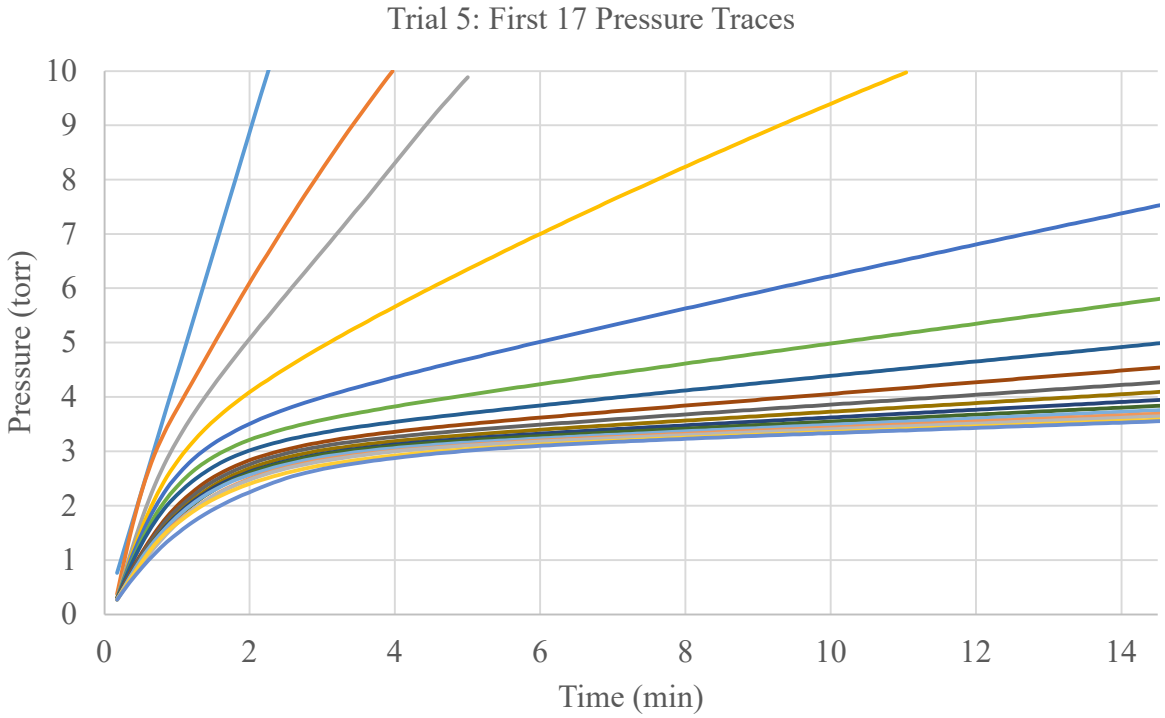

Figure 2.10: Pressure traces from sublimation cycles 1 – 17 for Trial 5.

measuring air pressure. The sensor is not suitable for measuring pressure for the sublimation dynamics experiment because the thermal conduction properties of XeF_2 vapor are not known and therefore there is no factory calibration curve for this gas. The transducer check showed that the two sensors (Baritron^{tm} and Convectron^{tm}) had better than 1% agreement. Therefore, it was determined that the pressure measurement technique was not erroneous. A second hypothesis for the steady increase in pressure and absence of a horizontal asymptote was that the XeF_2 vapor was etching the buna-N o-ring material. The idea was that the pressure continued to steadily rise when there was XeF_2 present from etching but there was no pressure rise when the XeF_2 was exhausted because there was no leak. This was addressed by replacing the o-rings with PET o-rings which are very resistant to fluorine gas as it is a fluorinated polymer.

The o-ring substitution was included in Trial 6 which was conducted with the same nominal

parameters (etch time, thermal soak, bake out, etc.) as Trial 5. The results from Trial 6 were again very similar to Trial 5 and showed the pressure overshoot, the increasing sublimation time constant, the decreasing maximum pressure, and the lack of asymptotic behavior that was previously observed.

The last hypothesis about what could be a cause of the unpredicted behavior was that perhaps the aluminum chamber was being etched by the XeF_2. This was considered to be very unlikely as the literature reports that XeF_2 does not etch aluminum. In an effort to replicate the results of Trial 6, a final pilot trial was undertaken. The chamber was loaded with 78.1 mg of XeF_2 and a small piece of aluminum foil weighing 31.8 mg. The results from Trial 7 were again very similar to Trials 5 and 6 and displayed the same issues of pressure overshoot, the increasing sublimation time constant, the decreasing maximum pressure, and lack of asymptotic behavior. The mass of the aluminum foil did not change during the experiment to the accuracy of the analytical balance used for mass measurements. (0.0001 g resolution).

Trials 4 – 7 showed behavior that was not expected. However, the most obvious factors that could lead to this were investigated; including: thermal instability, leaks, etching of sealing materials, etching of chamber materials, and insufficient experimental time. It was concluded that the sublimation behavior of the XeF_2 crystals that was observed was real and not merely an artifact of the instrumentation, test apparatus, or experimental method.

There were four inconsistencies with a theoretical first order sublimation process. First, the maximum pressure for each cycle and, thus, the measure of vapor pressure of XeF_2 was not constant. Second, apparent vapor pressure of XeF_2 was significantly higher than what it was calculated to be, given the temperature. Third, the pressure continued to rise after the initial rapid sublimation from vacuum to the vapor pressure was achieved. Fourth, the time constant for

sublimation increased with time. Trials 4 – 7 were conducted to understand the fundamental behavior of the XeF_2 material under the experimental conditions and to try to rule out systematic errors or issues with the experimental methodology or setup. The conclusion of these experiments was that the behavior was real and attributed to the nature of the experiment and not due to confounding factors. The first three inconsistencies were believed to be related to each other and a result of the nature of XeF_2. The fourth inconsistency was believed to be due to the microscale crystal size distribution of the XeF_2 as described in detail above.

The chemistry of XeF_2 and the way it is synthesized points to an explanation of why the pressure rises were higher than the calculated vapor pressure and no asymptotic behavior was observed. The compound XeF_2 is created by mixing Xe and F gas together at 400 – 500 °C in a nickel reaction vessel. The nickel acts as a catalyst which leads to liquid phase XeF_2 (and XeF_4) to condense on the surface of the reaction vessel [13, 14]. The liquid XeF_2 then drains down into a U-trap (U-shaped section of tubing). After the reaction, Xe and F have been consumed, the U-trap is chilled to room temperature where the collected XeF_2 can solidify and then be harvested and purified.

The important thing to note is that mixing Xe and F gas at room temperature will not lead to the formation of XeF_2, this only happens at high temperature and in the presence of a catalyst. At room temperature XeF_2 is below its triple point so the only phase changes that can take place are from solid to gas or gas to solid (sublimation or deposition). The second factor is that XeF_2 is not a stable compound and can disassociate into its constituent gases [14]. Given the thermodynamic nature of sublimation and deposition, if a gas / solid combination of material is left alone, the pressure of the gas should approach the vapor pressure of the material over time. This is well understood physics and the most exemplary case is that of CO_2. The difference

between CO_2 and XeF_2 is the stability of these molecules. When CO_2 sublimates, the molecule does not dissociate and is available to return to the solid phase to maintain thermodynamic equilibrium. XeF_2 can also return to the solid phase from the gas phase but if any of it dissociates into Xe and F gas, these will not return to the solid phase because the gases on their own will not form XeF_2 without high temperatures and a nickel catalyst.

This dissociation changes the equilibrium physics for sublimation / deposition of XeF_2. In the case of CO_2, the rate of mass changing from the solid to the gas phase will be equal to the rate of mass changing from the gas phase to the solid phase when at equilibrium. For XeF_2, the rate of mass changing from the solid to the gas phase and the rate of mass changing from gas to solid will be proportional to the difference between the pressure and the vapor pressure. However, Xe and F_2 will also be produced in the gas phase at a rate proportional to the pressure of XeF_2 due to the disassociation of the molecule, which is a one directional reaction at the temperatures considered. This extra reaction leads to a partial pressure of Xe and F_2 in the gas phase. A solid mass of XeF_2 placed in vacuum and confined to a defined volume will sublimate and lead the pressure of said volume to rise. The gaseous XeF_2 that is produced by sublimation will change into one of two things. It will either deposit and return to the solid phase or it will dissociate and form Xe and F_2 gas.

According to the above analysis, the pressure should have increased over time until such a point was reached that the solid XeF_2 stopped subliming and the gas phase was entirely composed of Xe and F_2 gas. However, the pressure of the gas was not necessarily equal to the vapor pressure. Consider a different situation that was not experimentally created. Suppose a mass of solid XeF_2 was placed in a volume that also had gaseous XeF_2 at a pressure equal to the vapor pressure. This initially would have sublimation and deposition rates that are equal. This would represent the

thermodynamic equilibrium state for most other materials and is referred to as the first order equilibrium case. However, in this example, the gaseous XeF_2 would slowly form Xe and F_2 gas and cause the pressure rise above the vapor pressure. The sublimation would slow to a rate lower than what would exist at the first order equilibrium condition since the pressure exceeds the vapor pressure. However, this sublimation would not be balanced by deposition because the concentration of gaseous XeF_2 would decrease with time from dissociation. Ultimately, the only thing to stop sublimation would be the partial pressures of Xe and F_2 gas. The result was that a steadily increasing pressure was observed (in the pressure ranges investigated by this research) even after the vapor pressure was reached because sublimation was not balanced by deposition due to dissociation and there was a steady pressure generation. To verify this theory, a study would need to be conducted to measure the in-situ gas phase composition over time. This, however, was outside the scope of this work. However, the analysis and hypothesis was supported by literature. In conclusion, the dissociation of XeF_2 was believed to be the root cause of the interesting effects observed in the sublimation dynamics pilot studies. It should be stated that the deviation from the hypothesized behavior does not impact the potential for XeF_2 to be used as intended.

In Trials 4 – 7, it was hypothesized that the pressure was higher than the temperature-based vapor pressure reported in literature due to the formation of Xe and F_2 gas. A given mass of XeF_2 gas will have a lower pressure than the same mass of Xe and F_2 in an equivalent stoichiometric ratio. As the XeF_2 sublimated the pressure rose to the vapor pressure but this pressure was overshot and could not be recovered by the thermodynamic equilibrium of sublimation / deposition. The difference in maximum pressure rise between experimental cycles was due to the fact that the initial sublimation rate was different between cycles. The dissociation of XeF_2 was part of this issue, but the crystal size distribution consideration is also germane. The early cycles with a wider

distribution of crystal sizes had higher initial sublimation rates which lead to more rapidly forming XeF_2 gas. Since the rate of Xe and F_2 generation was dependent on XeF_2 pressure, the early cycles hit a higher pressure because there was more XeF_2 present during the experiment. The later cycles which had a smaller distribution of crystal sizes had XeF_2 generated more slowly and so there was less Xe and F_2 formed during the 15 minute experimental cycle time. This led to the result that maximum pressure reduced from cycle to cycle. The pressure continued to rise after the calculated vapor pressure was reached again due to XeF_2 dissociation.

A deeper analysis of the dissociation phenomena was undertaken to try to understand if this was a realistic explanation for the steady pressure rise. The moles of XeF_2 gas in the chamber was calculated according to the Ideal Gas law assuming the pressure was the vapor pressure of XeF_2 at the measured temperature. An assumption was made that this amount of XeF_2 would eventually dissociate into Xe and F_2 gas. This would result in the same number of moles of Xe and F_2 gas as there was moles of XeF_2. The partial pressure of each gas was then calculated and summed to find the final chamber pressure assuming complete dissociation. The vapor pressure of the XeF_2 was calculated to be 3.12 torr based on literature [16] at a temperature of 20 °C, and the corresponding total pressure of Xe and F_2 was calculated to be 17.93 torr. This calculation implies that if sublimation occurred until the vapor pressure of the crystals was reached and then, subsequently, the entire volume of gas dissociated, the pressure should eventually reach 17.93 torr. This process can be modeled by a simple double-exponential expression as shown in Equation 2.2.1 where P is the chamber pressure, t is time, P_v is the vapor pressure of the crystals, P_{dis} is the pressure of the dissociated gas, τ_{sub} is the time constant for sublimation, τ_{dis} is the time constant for dissociation, and t_o is a time offset. A plot of the modeled data and the raw data of a pressure trace from Trial 6 is shown in Figure 2.11. The error between the model and raw data is shown in

Figure 2.12 for visual clarity. The coefficients produced by the curve fitting software are in Table 2.1.

$$P = P_v * \left(1 - e^{-\frac{(t+t_o)}{\tau_{sub}}}\right) + (P_{dis} - P_v) * \left(1 - e^{-\frac{(t+t_o)}{\tau_{dis}}}\right) \qquad \text{(Equation 2.2.1)}$$

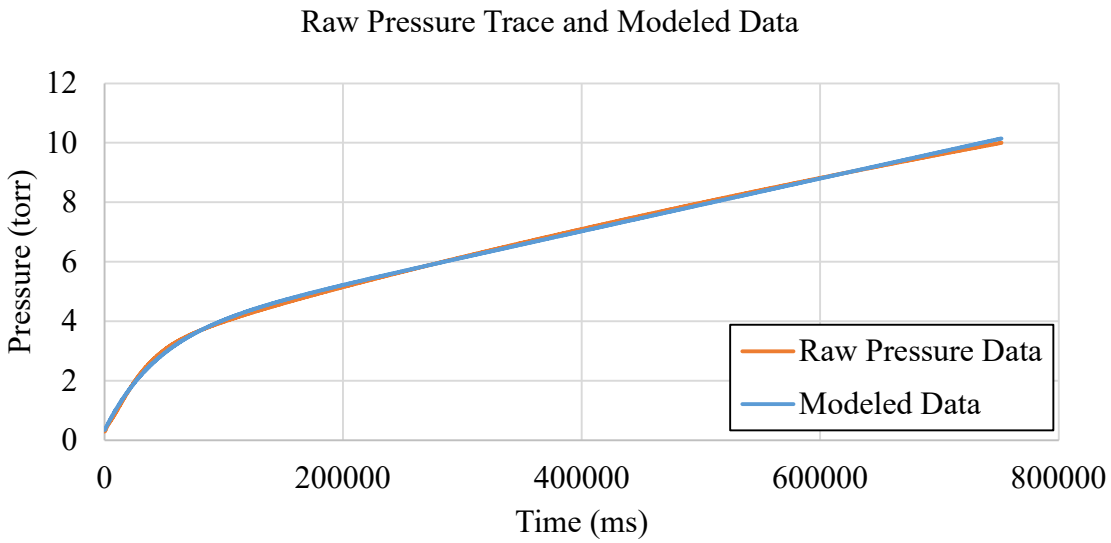

Figure 2.11: Raw pressure data with fitted model.

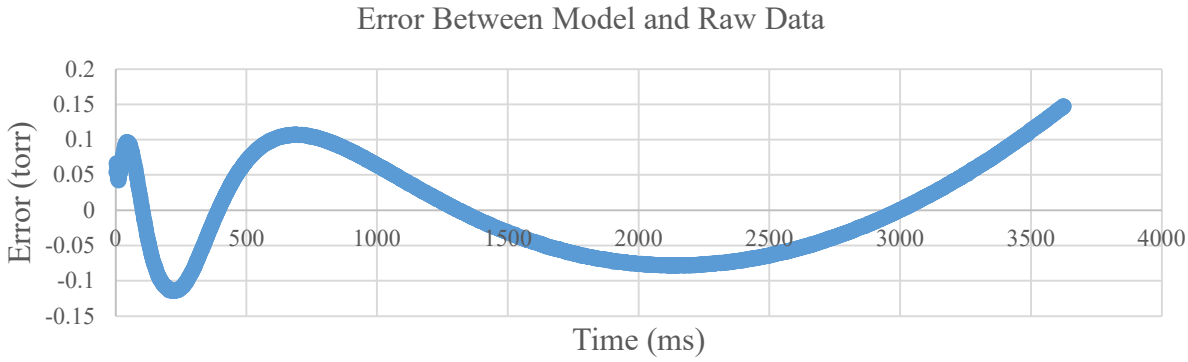

Figure 2.12: Error between raw data and model.

Table 2.1: Fitting coefficients for Equation 2.2.1.

P_v (torr)	P_{diss} (torr)	τ_{sub} (s)	τ_{dis} (s)	t_o (s)
2.75	18.25	27.8	1223	2.13

Equation 2.2.1 fitted the data that was modeled very well. The model implied that as time approaches infinity, the pressure should approach P_{diss}. The fitted value of this was 18.25 torr while the calculated theoretical pressure after full dissociation, according to the assumptions the model makes, was 17.93 torr. This model and the data support the analysis that the pressure rise was in fact due to the dissociation of XeF_2 into Xe and F_2 gases. The time constant for the dissociation component of the model, τ_{diss}, was 1223 s and full dissociation would be expected to be achieved in ~5 time constants, or ~102 minutes. This claim can be further confirmed with additional studies.

The dissociation analysis was undertaken at the request of the dissertation committee members. This extra analysis was conducted after the rest of the dissertation was completed and it was determined that the value of this analysis, namely, calculation of the dissociation time for all experiments conducted, was not impactful on the conclusions of this work or the feasibility of applying the work to the intended use case. Therefore, this analysis was not conducted on the data in the following section.

In conclusion, the differences between a simple first order sublimation reaction and what was observed was due to the tendency of XeF_2 to dissociate into Xe and F_2 and the fact that crystal size distribution was not constant from cycle to cycle of the experiment. These two factors explained all the interesting repeatable effects of the sublimation dynamics study. Other factors have been systematically ruled out and the conclusion is supported by literature and fundamental physics. The conclusion of the pilot studies was that the effects seen were real and not artifacts of erroneous methodology or faulty equipment. The product of the pilot studies was an understanding of the behavior of the XeF_2, an explanation of why the observations do not follow a basic first

order description, and a process that can be used to systematically study the sublimation dynamics of XeF_2 as a function of temperature and macroscale surface area.

2.3 Sublimation Dynamics Full Factorial Study

The pilot studies qualified the experimental method and apparatus that was used to study the sublimation dynamics of XeF_2. A full factorial study of sublimation dynamics was conducted with the independent variables of temperature and macroscale surface area (crystal holder size). The first factor in the study was temperatures ranging from 20 – 50 °C in 10 °C steps. The second factor in the study was crystal holder in diameters ranging from 0.050" – 0.125" in 0.025" steps. Each combination of factors (16 in total) was studied by loading the crystal holder with XeF_2 and conducting a sublimation dynamics study in accordance with the guidelines provided by the pilot study. Table 2.2 shows the nominal values of the independent variables.

Table 2.2: Table of nominal independent variable values for the 16 trials in the sublimation dynamics experiment.

Trial Number	Temperature (°C)	Sample Holder Diameter ($x10^{-3}$ in)
1	20	50
2	20	75
3	20	100
4	20	125
5	30	50
6	30	75
7	30	100
8	30	125
9	40	50
10	40	75
11	40	100
12	40	125
13	50	50
14	50	75
15	50	100

16	50	125

The most important dependent variable that was sought was the effluence of XeF_2, that is the mass flow rate of sublimation. Each experimental trial received the same analytical treatment as the pilot trials. The maximum pressure was plotted and the time constant for sublimation was calculated. Additional analyses were conducted to calculate the vapor pressure and effluence from the pressure traces for each cycle for each trial. The vapor pressure was also estimated in two different ways and the effluence rate as a function of chamber pressure was calculated in four ways. The maximum pressure, time constant, vapor pressure, and estimates of effluence were plotted versus the independent variables, temperature and sample holder diameter.

The most impactful result of the sublimation dynamics study was an estimate of the effluence as a function of chamber pressure. Two separate models were created to predict this as a function of temperature. Effluence was found to not be significantly dependent on sample holder diameter. This was germane to the overall goal of this research because of the intended use case for subliming XeF_2. The mass flowrate of propellant was critical to understand in a propulsion system because it directly affects thrust. The effluence of XeF_2 represents part of the mass flowrate of propellant and, therefore, it must be known over reasonable range of parameters. Effluence was found to be dependent on chamber pressure and temperature.

The experimental process used for the sublimation dynamics experiment is described here. The environmental control chamber would first be set to the nominal temperature of a trial. The system would be allowed to come to temperature over several hours. The pressure transducer was calibrated at each temperature. This involved pumping down the chamber to a base pressure below the threshold of sensitivity of the pressure transducer and then nulling the pressure controller

readout. This process was conducted in accordance with the transducer manufacturer's recommendations. Next, the sample holder was removed from the setup and filled with XeF2 crystals in the appropriate sample hole for the trial. The mass of crystal was recorded. The sample holder was then placed in the test chamber and allowed to reach a thermal equilibrium. The vacuum was then turned on and the software configured for a run. The nominal setpoints for the experiment were as follows: a cycle time of 15 minutes, a thermal stabilization wait time between cycles of 5 minutes, and the total number of cycles to be performed set to 50. The number of cycles that was used was greater than what was needed to sublimate all the XeF_2 crystals used in any to ensure efficient use of the crystals. Each cycle the pressure, temperature, and time were recorded at a collection rate of 20 Hz. The data from every cycle was then stored in its own Excel™ file for further processing. The data was analyzed by a custom MatLab™ code that extracted the maximum pressure, time constant for sublimation, and the calculated values for vapor pressure and effluence. The code also produced a down-sampled data set of every pressure versus time plot for each cycle. This was done because each cycle had ~15,000 data points which would be very cumbersome to graph in its entirety. The down-sampled pressure traces had ~300 data points which still produced a very smooth plot that didn't show any aliasing.

The first result calculated was the time constant for sublimation. The time constant was calculated by finding the time at which the pressure was equal to 95% of the calculated vapor pressure and dividing this time by 3. This approach assumed that the sublimation dynamic was a first order reaction which, as was previously discussed, is not entirely correct. This approach did, however, provide a reasonable estimate of the time constant. The results of the sublimation time constant investigation are presented according temperature for all trials in four plots. Each plot contains all results from every cycle and sample holder diameter that were at a given temperature.

Every plot of time constant as a function of cycle number, the sequential index of the experiment's progression, shows that the time constant of sublimation increases with cycle number. Figure 2.13 through Figure 2.16 shows the results from the trials conducted at 20 °C, 30 °C, 40 °C, and 50 °C, respectively. The average time constant for each trial is shown in Figure 2.17. The time constant data is shown in Table 2.3.

The time constant for sublimation was a situation specific result. The time constant first

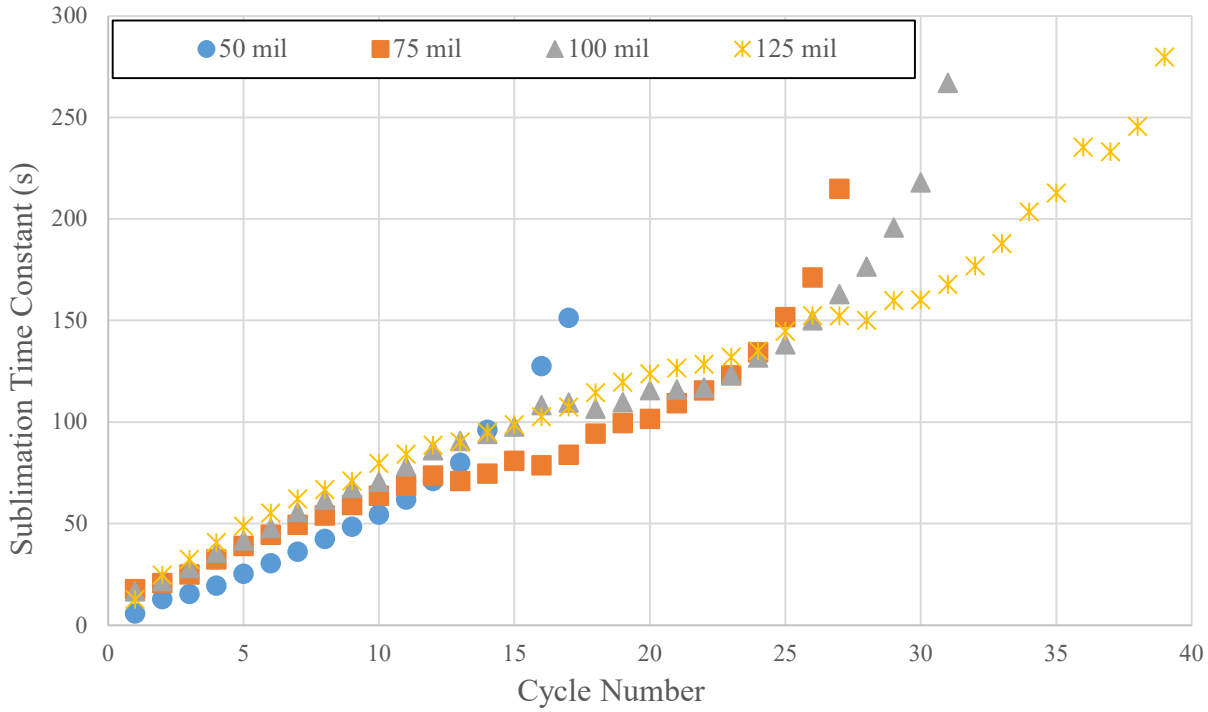

Figure 2.13: Time constant of sublimation for trials conducted at 20℃ for four different sample holder diameters.

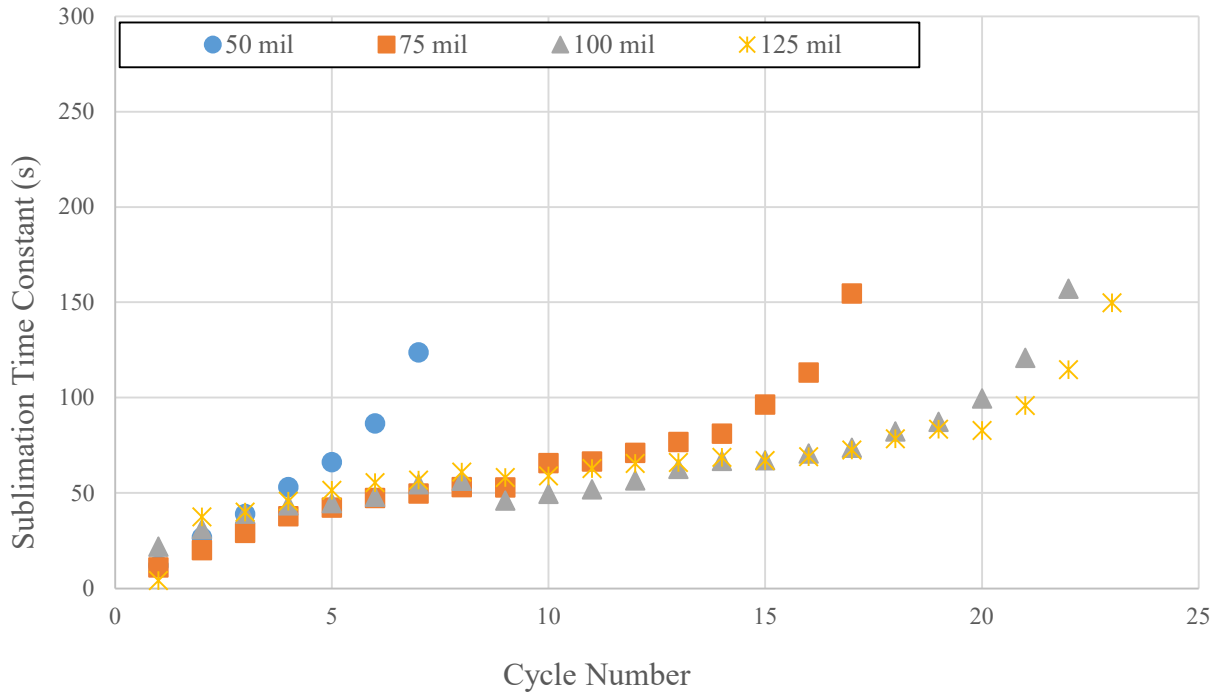

Figure 2.14: Time constant of sublimation for trials conducted at 30℃ for four different sample holder diameters.

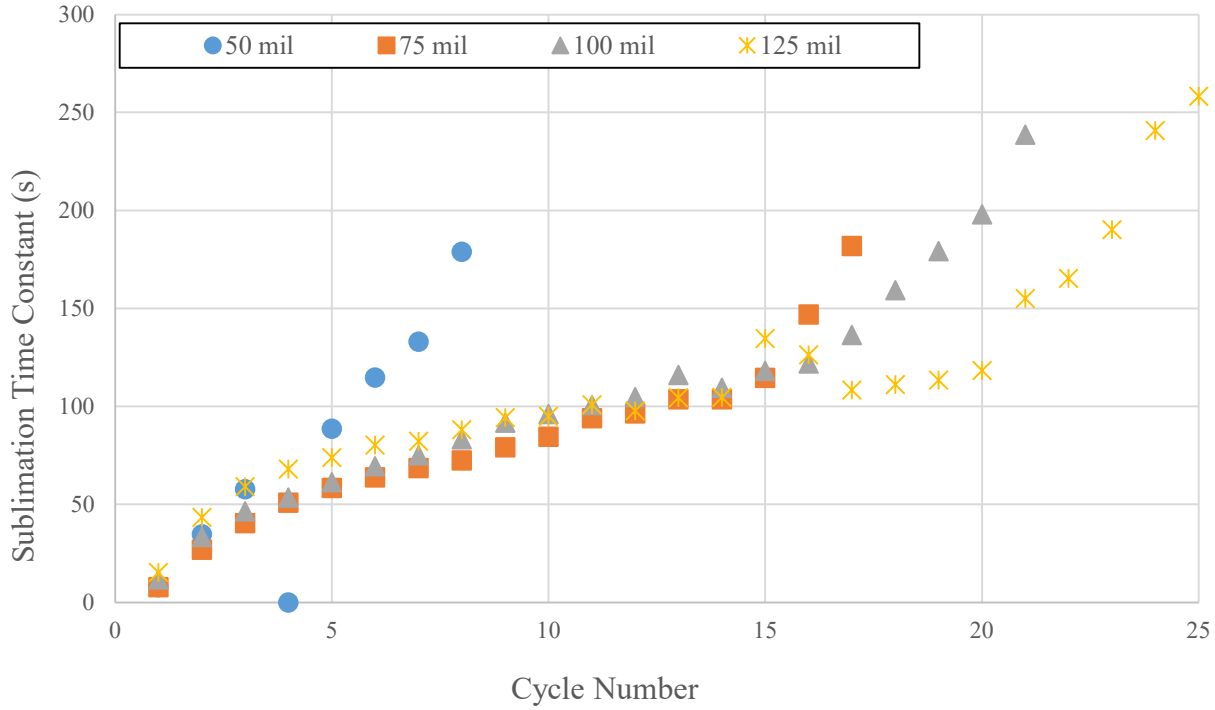

Figure 2.15: Time constant of sublimation for trials conducted at 40℃ for four different sample holder diameters.

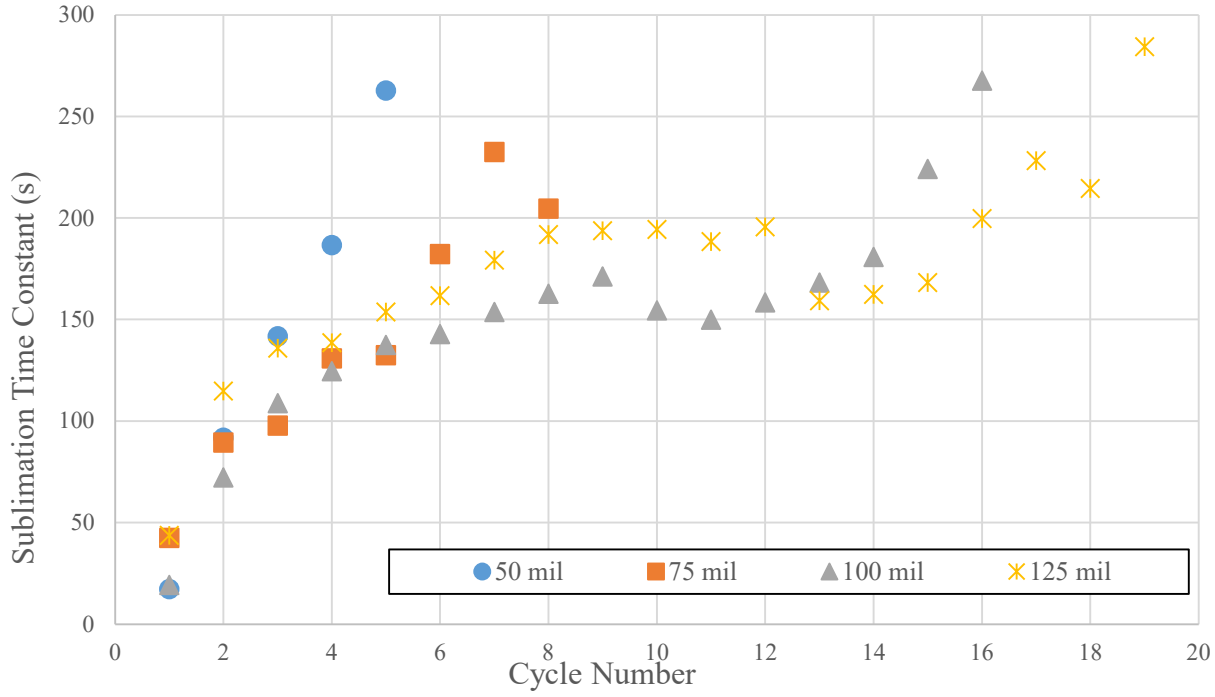

Figure 2.16: Time constant of sublimation for trials conducted at 50℃ for four different sample holder diameters.

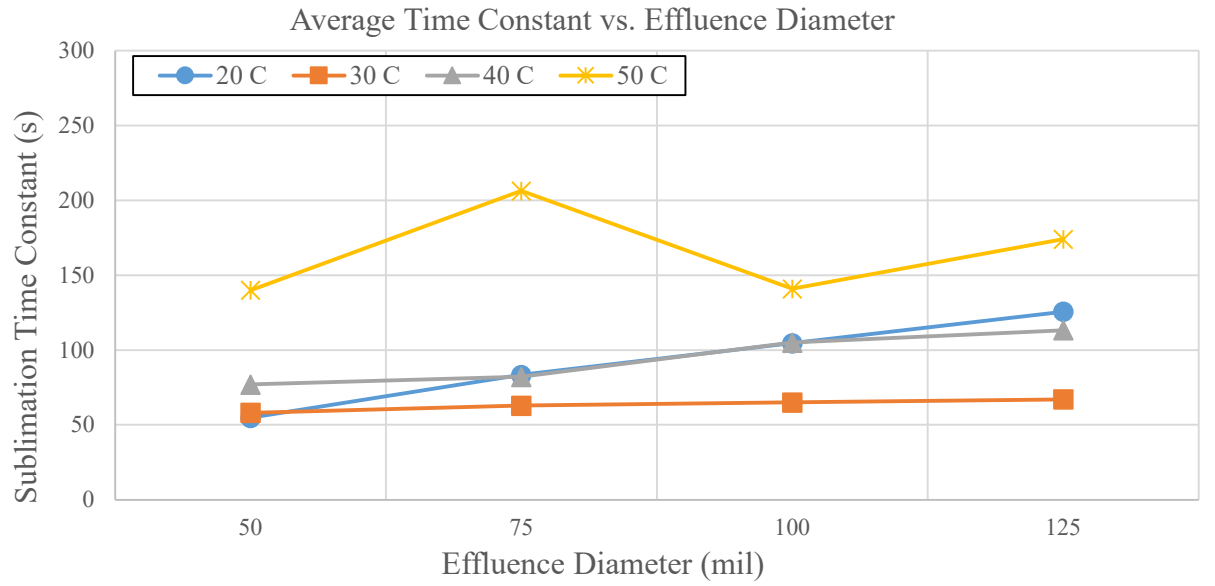

Figure 2.17: Average time constant of sublimation as a function of sample holder diameter at four different temperatures.

Table 2.3: Summary of all time constant of sublimation data.

Temperature (°C)	Effluence Diameter (mil)	Effluence Area (in^2)	Mass of XeF_2 (mg)	Average Time Constant (s)
20	50	1.96E-03	42.0	54.9
20	75	4.42E-03	111.8	83.4
20	100	7.85E-03	100.9	104.5
20	125	1.23E-02	140.4	125.7
30	50	1.96E-03	41.3	58.1
30	75	4.42E-03	146.1	62.8
30	100	7.85E-03	130.0	65.1
30	125	1.23E-02	140.2	67.2
40	50	1.96E-03	58.0	77.0
40	75	4.42E-03	141.0	82.1
40	100	7.85E-03	188.9	105.1
40	125	1.23E-02	253.0	113.3
50	50	1.96E-03	57.6	140.0
50	75	4.42E-03	138.6	206.4
50	100	7.85E-03	243.0	149.8
50	125	1.23E-02	335.0	174.1

assumes that the sublimation dynamics were a first order process which was understood to be incorrect. Furthermore, the time constant was only germane to the context of filling the experimental test chamber which had an estimated volume of 44.8 cm^3 based on a detailed CAD model. This time was, however, relevant to the end use case of XeF_2 sublimation because it gave a sense of how long it might take for a XeF_2 propellant storage vessel to pressurize after being vented. In the context of spacecraft operations, the time constant was likely negligible because a thruster that would use this propellant would most likely be in operation for hours, days, or weeks at a time.

This was due to the fact that the intended use case propulsion system was inherently low thrust so it would take a great deal of time to develop a meaningful change in velocity. The estimate of time constant for sublimation should scale linearly with the volume of a propellant vessel and

be temperature dependent. This implied that a reasonable estimate for the specific time constant of sublimation for a generic propellant vessel volume would be 2000 – 3600 s/L over the range of temperatures measured. This was calculated by taking the ratio of average time constant of sublimation and the chamber volume. The time it would take for a vented propellant vessel to return to the calculated vapor pressure of XeF_2 would be ~3 times the time constant and would result in a pressurization time of 1.7 – 3.1 hr/L. This rate could be impactful depending on whether the sublimated gas is being consumed in a continuous or pulsed configuration, as well as the required propellant mass flowrate.

The second result from the sublimation dynamics study related to how the maximum pressure differs from the calculated value data which was used to estimate the vapor pressure of the XeF_2 [16]. Each trial (combination of cycle number and sample holder diameter) had a maximum pressure associated. Plots of maximum pressure as a function of cycle number show that the pressure reached in a trial tends to decrease as cycle number increases. These maximum pressure plots are shown for each temperature investigated and for each different sample holder diameter. The theoretical vapor pressure as determined by the temperature is included in these plots to serve as a reference. The maximum pressure reached for each cycle in the trials is shown in Figure 2.18 through Figure 2.21 at the temperatures of 20 °C, 30 °C 40 °C and 50 °C, respectively. Each figure has the results from using all four sample holder diameters.

An estimate of vapor pressure for each temperature that was agnostic to cycle number or sample holder was conducted in two ways. The first way was to average the maximum pressure reached for each cycle which had sufficient XeF_2 remaining to observe a significant pressure rise. The second way was to again average the peak pressure but to also truncate the data to eliminate the first two cycles which were then treated as outliers. This was done because the first two cycles

had significantly higher peak pressure than the rest of the cycles due to transient effects. The transient effects were a combination of absorbed water from the air out-gassing and the significantly higher sublimation rate due to the widest distribution of crystal sizes being present during those two trials. The relative effect of these two transients was unknown but it was

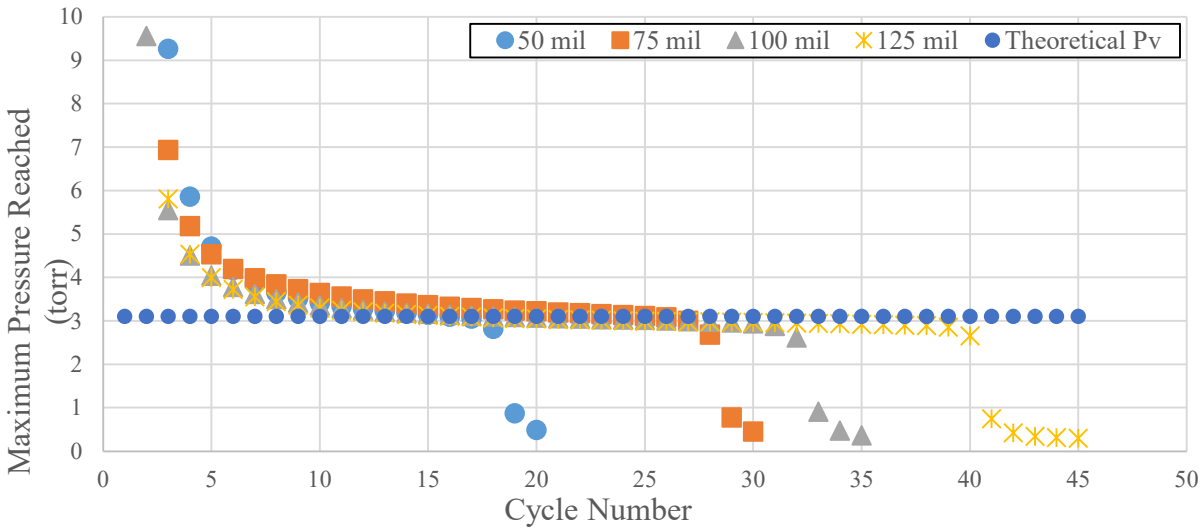

Figure 2.18: Maximum pressure reached at trials conducted at 20℃ for four different sample holder diameters; theoretical vapor pressure of XeF_2 at 20℃.

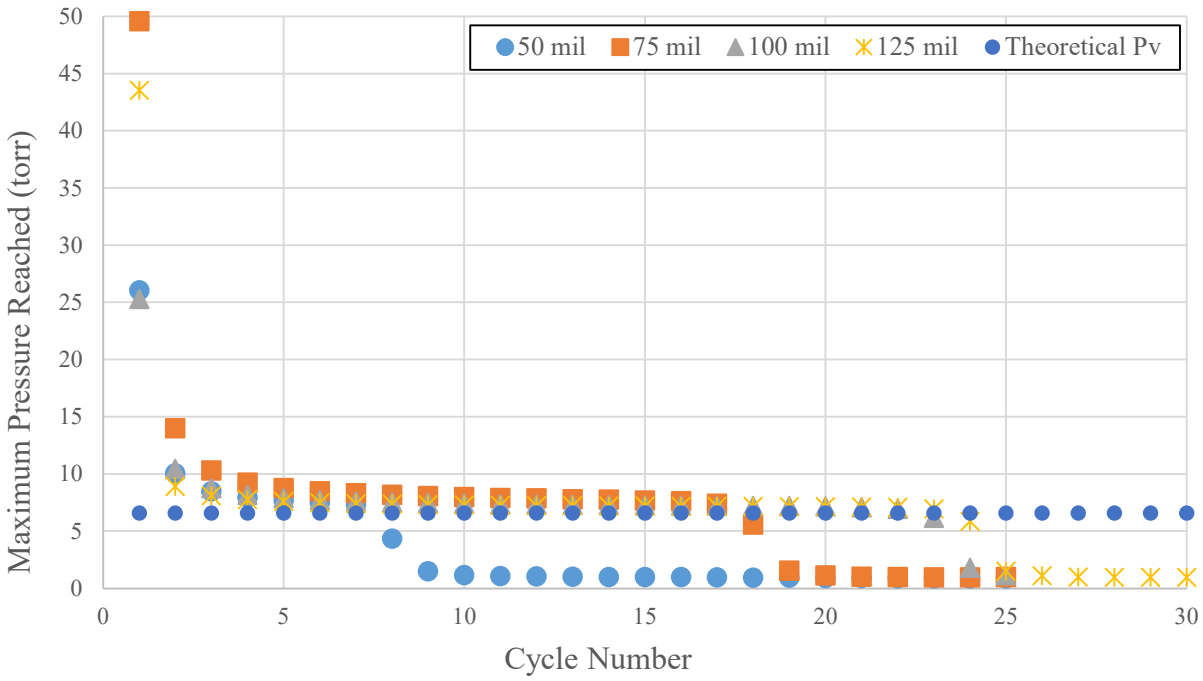

Figure 2.19: Maximum pressure reached at trials conducted at 30℃ for four different sample holder diameters; theoretical vapor pressure of XeF_2 at 30℃.

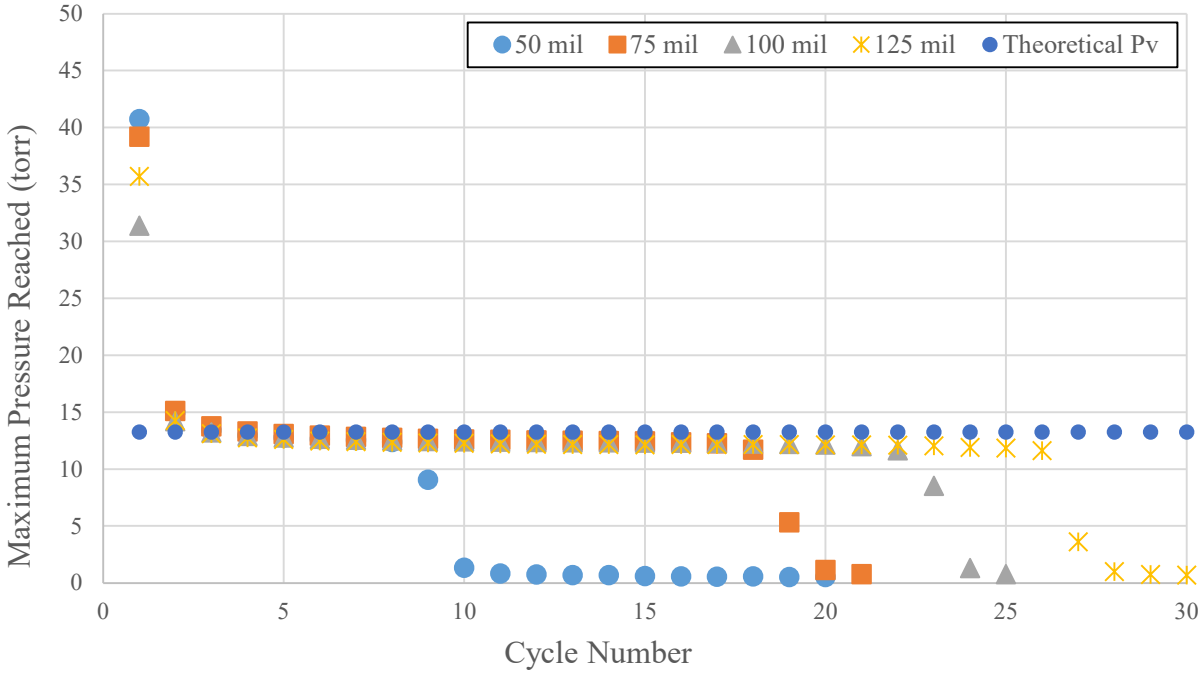

Figure 2.20: Maximum pressure reached at trials conducted at 40℃ for four different sample holder

diameters; theoretical vapor pressure of XeF_2 at 40℃.

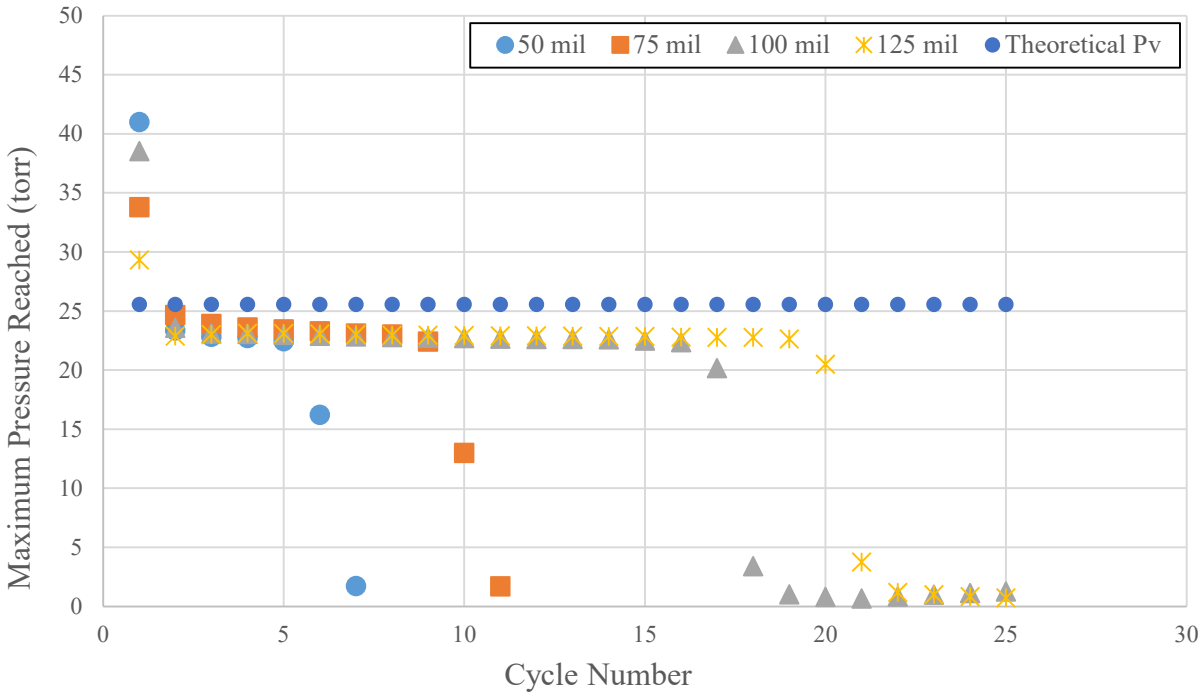

Figure 2.21: Maximum pressure reached at trials conducted at 50℃ for four different sample holder diameters; theoretical vapor pressure of XeF_2 at 50℃.

hypothesized that the crystal size distribution was the stronger effect than outgassing. This outlier behavior became very clear when examining the plots of maximum pressure versus cycle number. The first estimate of vapor pressure was referred to as the 'average vapor pressure' and the second estimate was referred to as the 'truncated average vapor pressure'. The average vapor pressure, truncated average vapor pressure, and calculated vapor pressure are plotted versus temperature in Figure 2.22. The results of the vapor pressure estimates are summarized in Table 2.4.

The vapor pressure measurements of this research were important for two reasons. First, it was important for comparison to literature. The second reason was that the vapor pressure represents an estimate of the maximum operating pressure of a propellant vessel that may be encountered in the desired use case of this work. The propellant pressure was an important factor

in the design and operation of a propulsion system because it is head pressure that causes propellant

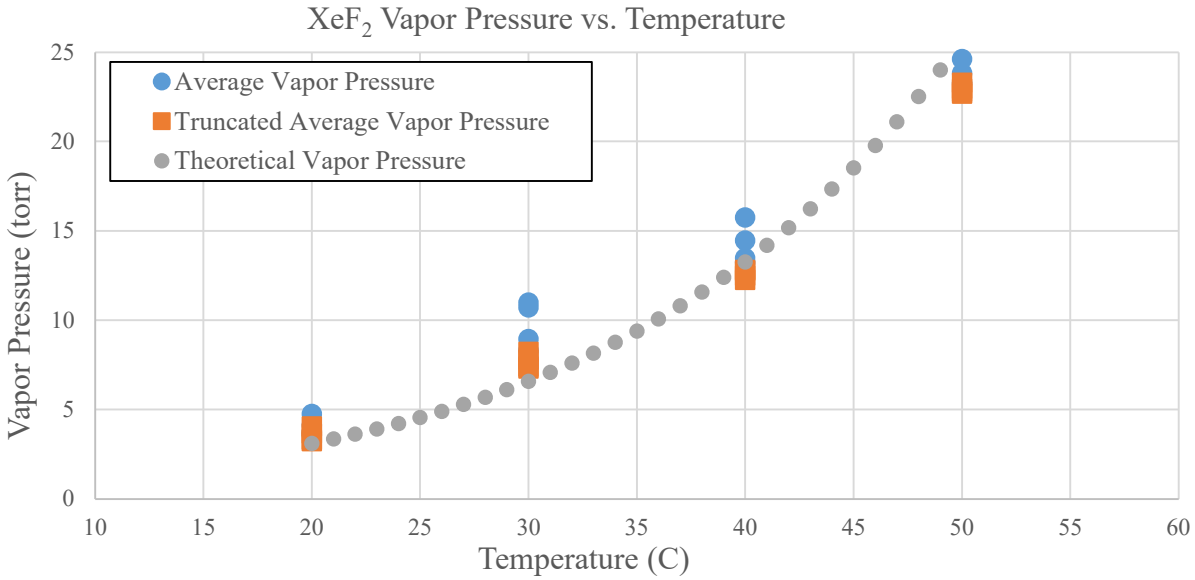

Figure 2.22: Plot of estimated and calculated vapor pressures as a function of temperature.

Table 2.4: Summary of the vapor pressure results for all trials conducted.

Temperature (℃)	Effluence Diameter (mil)	Average Vapor Pressure (torr)	Truncated Average Vapor Pressure (torr)	Theoretical Vapor Pressure (torr)
0	50	4.75	4.05	3.10
20	75	4.13	3.66	3.10
20	100	3.74	3.32	3.10
20	125	3.57	3.22	3.10
30	50	10.72	7.79	6.58
30	75	10.99	8.22	6.58
30	100	8.31	7.40	6.58
30	125	8.94	7.30	6.58
40	50	15.75	12.81	13.27
40	75	14.46	12.76	13.27
40	100	13.47	12.48	13.27
40	125	13.23	12.25	13.27
50	50	26.49	22.68	25.59
50	75	24.61	23.28	25.59

50	100	23.82	22.78	25.59
50	125	23.27	22.94	25.59

to flow through a thruster. The required head pressure is typically low for electric propulsion systems (less than 1 bar) and is typically regulated by a mass flow controller. The controller would simply regulate mass flowrate, but its job would fundamentally be to regulate propellant pressure head to a system that would lead to the desired flowrate. Pressure head is not a typical consideration in propulsion systems as most electric propulsion systems use compressed gas which is stored at hundreds or thousands of psi and so it is always assumed that there is no shortage of pressure head to develop a desirable mass flowrate of propellant. Designers of a use case propulsion system can use the calculated values of XeF_2 vapor pressure as a function of temperature to determine the temperature needed to provide sufficient pressure head for proper thruster operation.

The third and most important result of the sublimation dynamics experiment was the measurements of effluence as a function of chamber pressure. The intended use case of sublimating XeF_2 for a propellant stream will have two requirements from a sublimation vessel. It would first require propellant at a specified flowrate and second at a required pressure. The sublimation dynamics experiment's most important result was exactly this. The results of experimentation have provided data relating mass flowrate of propellant as a function of sublimation vessel pressure, temperature, and sublimation surface area (sample holder diameter in this case). This data will give designers of use case propellant delivery systems the ability to engineer a sublimation vessel that can provide the proper flowrate and pressure of XeF_2. Lastly, the work described here presents two models to estimate flowrate as a function of chamber pressure and crystal temperature.

Producing effluence versus chamber pressure data involved processing every raw pressure trace. There were hundreds of these traces and they are not presented in this chapter in graphical form because there were no obvious visible conclusions to be drawn from them. The pressure

traces from the pilot are representative of the families of pressure traces from each experiment. The first data analysis method used to study the traces was to take the time derivative of the pressure curves. However, simply differentiating the time resolved pressure data would have led to a very noisy resulting dataset and so other numerical techniques were employed and are described below.

The first method of effluence analysis involved using a form of ensemble averaging. The fundamental reason that this approach was employed was because it was desired to have a time independent description of the effluence. The goal was to take each trial with its numerous cycles and combine them into a single plot relating effluence to chamber pressure. This was necessary due to the variance between cycles and the large amount of data to process (each cycle had ~16,000 data points of time and pressure). The ensemble averaging was achieved by binning each pressure curve (pressure versus time curve for a single cycle of any one trial) into data subsets and then analyzing them individually. The first step was to find a subset of each curve where the pressure was between a start pressure and an end pressure. For example, all of the time and pressure point pairs that fell between 0.25 and 0.35 torr were selected from the entire curve. This data subset was then treated as a linear data set and the slope of the data points was found. This slope was then reported as the time derivative of pressure at 0.25 torr. This averaging process is described as a piecewise linearization process. The effluence was then calculated from the pressure derivatives by using the time derivative of the Ideal Gas law. This is expressed mathematically in Equation 2.3.1.

$$dm/dt = \dot{m} = dp/dt * V/RT \qquad \text{(Equation 2.3.1)}$$

The derivative of pressure was multiplied by a factor that was dependent on the temperature, ideal gas constant, and chamber volume, and resulted in a measurement of the effluence in μg/s at a

pressure given in torr. This process was repeated for every 0.1 torr for the entire pressure curve which yielded an effluence curve for a single cycle. This effluence calculation was repeated for every cycle in a trial and the average effluence at each pressure level was calculated. In order to have confidence in the averaged effluence rate, an average was only calculated if there were at least five cycles that had an effluence estimate at any given pressure level. Furthermore, it was determined that the first two cycles would be truncated from the data entirely as they were extreme outliers for the same reasons as described in the vapor pressure measurements. Again, the first two cycles had significant transient effects due to crystal size distribution and adsorbed water. The first results of the effluence study then were referred to as the truncated average effluence curves. The truncated average effluence as a function of chamber pressure for all trials are shown in Figure 2.23 through Figure 2.26 for the temperatures of 20 °C, 30 °C, 40 °C, and 50 °C, respectively.

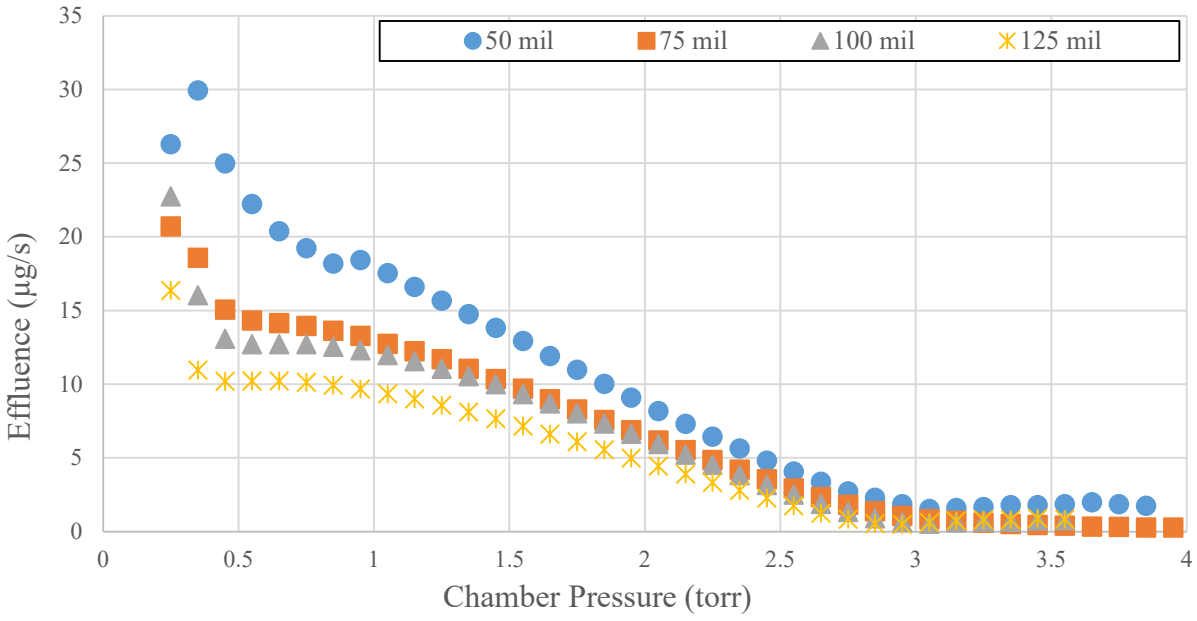

Figure 2.23: Truncated average effluence curves for trials at 20℃.

There were several noteworthy features of the truncated average effluence plots that should be discussed. These features were based on pressure. The first feature was the low-pressure effluence. The second feature was the mid-range linear effluence region. The third feature was the high-pressure effluence. Each of these regions have interesting explanations that help the data

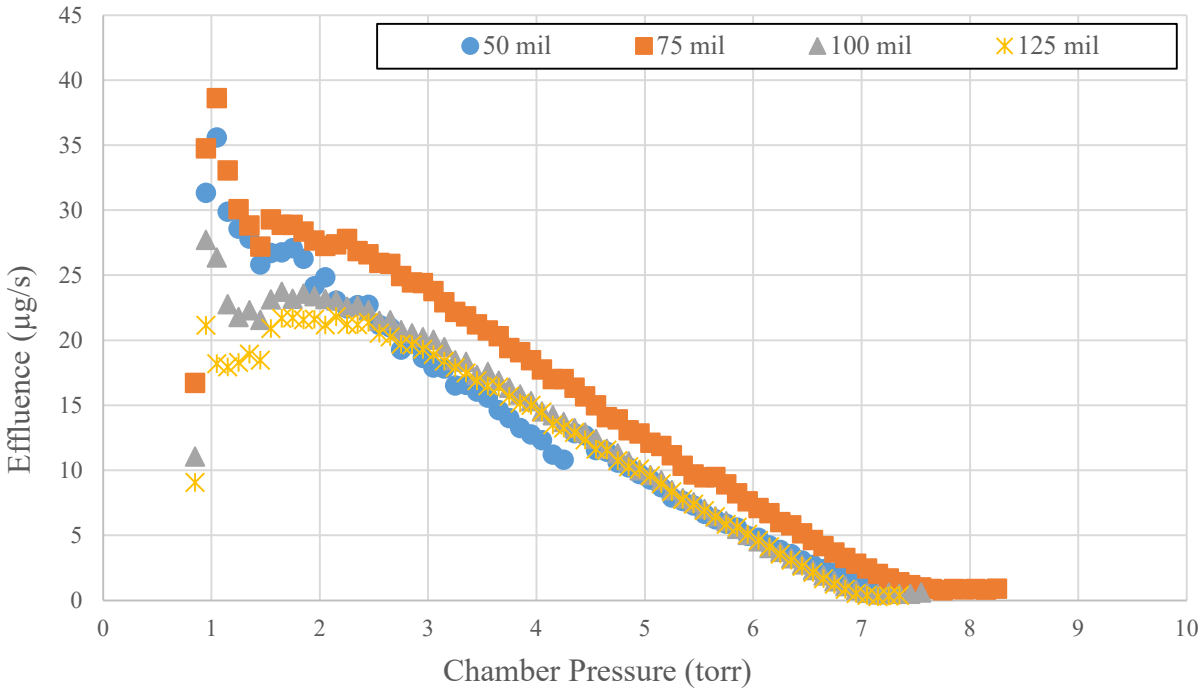

Figure 2.24: Truncated average effluence curves for trials at 30℃.

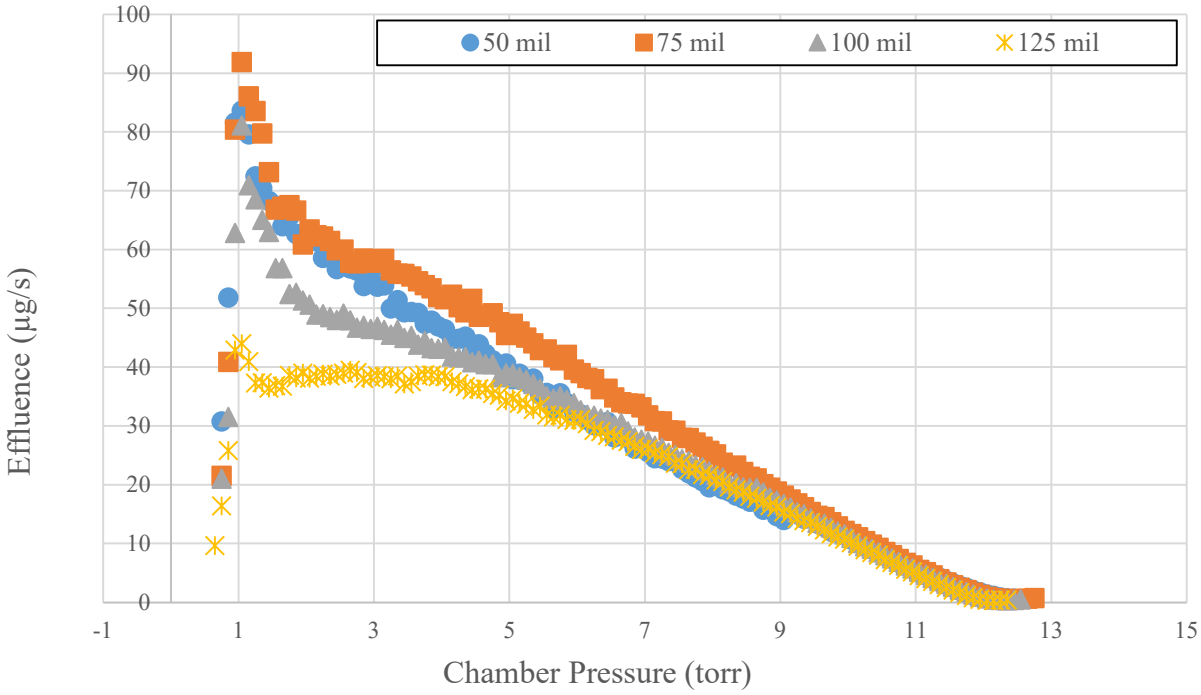

Figure 2.25: Truncated average effluence curves for trials at 40℃.

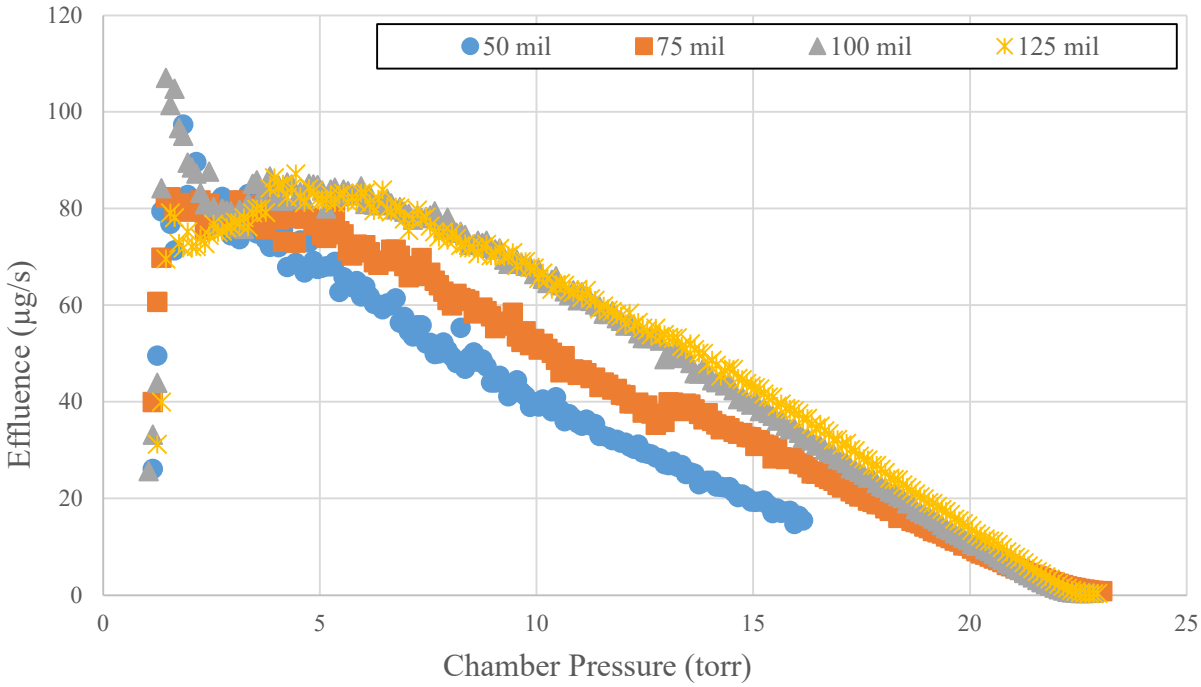

Figure 2.26: Truncated average effluence curves for trials at 50℃.

to one who would use the data for a use case application.

The low-pressure effluence region showed the greatest amount of variability between different sample holder diameters and had the highest effluence. The variability between different sample holder diameters was interesting because it did not appear to be a significant indicator of effluence in the higher pressure ranges but did at low pressure. However, the effect was not consistent. For example, the highest effluence was observed at 20℃ for the 0.050" sample holder, at 30℃ and 40℃ for the 0.075" sample holder, and at 50℃ for the 0.100" sample holder. At higher pressures, the impact of sample holder diameter was less significant. The high effluence in the low-pressure region was logical because one would expect that effluence to be greatest when there was the least amount of chamber pressure to limit sublimation.

The mid-range linear region was the most useful portion of the data set because it was well behaved and could be relevant in a use case application. The linear region could give a designer a stable operating mode for good control of effluence for a propulsion system application. The most noteworthy aspect of the linear region was that there was not a strong dependence on the crystal holder size. This was useful because the surface area of XeF_2 crystals would not need to be controlled in order to get predictable effluence and, thus, propellant flowrate. This linear region was also useful to generate a model of effluence based on temperature and pressure, the most valuable result of this study.

The high-pressure region had low effluence, as would be expected. This was the region where sublimation was still occurring but at a slow rate. This was the same behavior seen in the pilot data where a horizontal asymptote was not reached. The effluence was more variable than the linear region due to the cycle dependent crystal size distribution. Additionally, the high pressures of this region were not actually reached by all of the cycles.

Further analysis of the effluence data was undertaken to refine the usefulness of the data for a use case application. A potential designer would need to have a model of mass flowrate of propellant as a function of temperature and chamber pressure. This knowledge was already represented in the data in this chapter. However, it would be beneficial to have a simplified model that makes some assumptions for rough calculations. It was therefore desirable to create a linearized model of the effluence data.

The linearized effluence model made two assumptions. First, it assumed that the XeF_2 sublimation was occurring in the linear region of the relationship between effluence and chamber pressure. This was the 'well behaved' region of the data and had minimal transient or edge effects driven by crystal size distribution changes or adsorbed water outgassing. The second assumption was that the macroscale surface area was not a good predictor of effluence. This assumption eliminated an independent variable of sample holder size thereby yielding a simpler model of effluence.

The process for creating the linear effluence model was empirical and numerical in nature and it should be noted that this model ought to be qualified with a hypothesis test before deployment by a system designer. The process involved taking each of the 16 trials and truncating the portion of the data that was not linear. By doing this the model effectively ignored the high and low pressure regions of the sublimation data. Each 'linearized' trial was then curve fit and modeled as a linear curve. The slope and intercept of these 16 linear fits was then analyzed. The linearized and curve fit trials conducted are shown in Figure 2.27 through Figure 2.30 at 20℃, 30℃, 40℃, and 50℃, respectively. A summary of the fitting parameters for all trials is shown in Table 2.5.

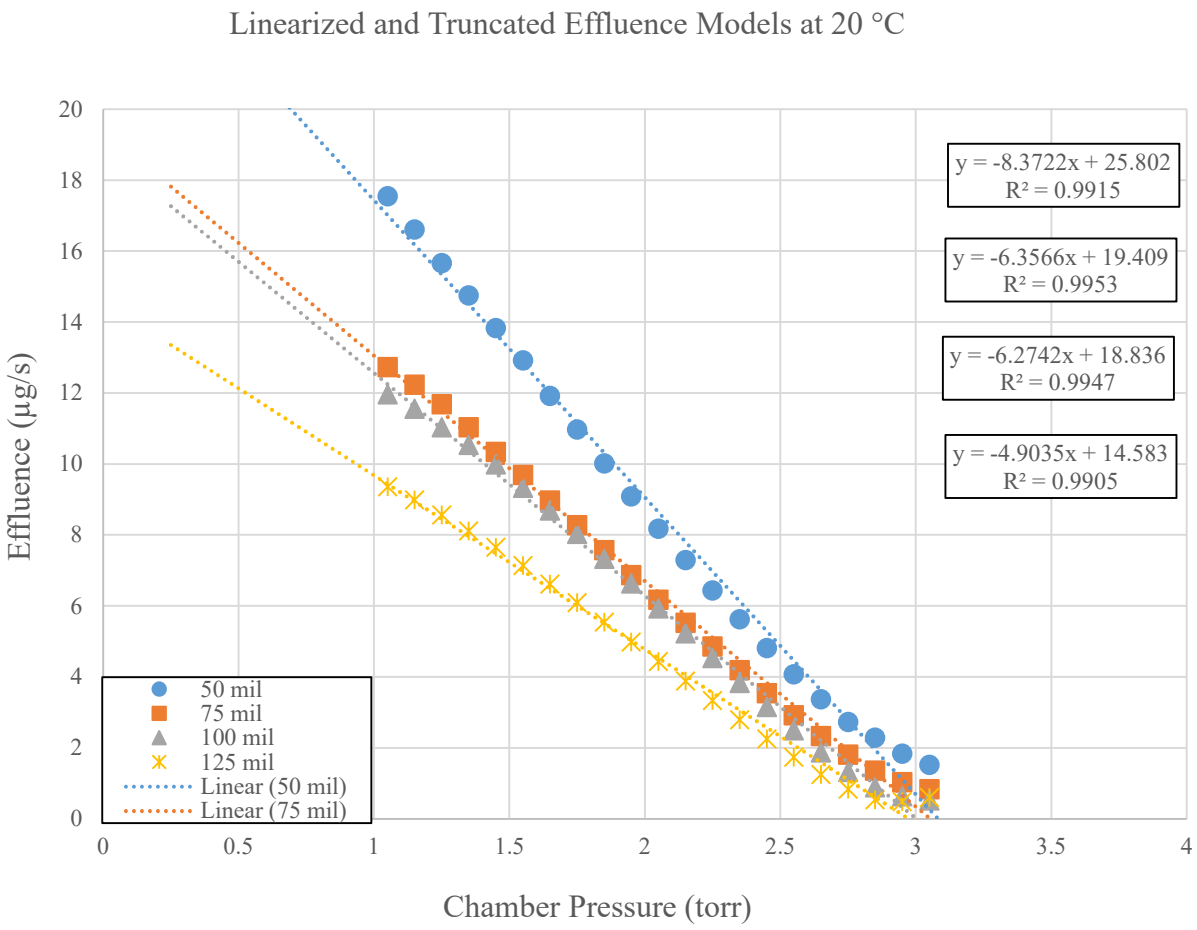

Figure 2.27: Linearized and curve fit truncated average effluence curves for trials at 20℃.

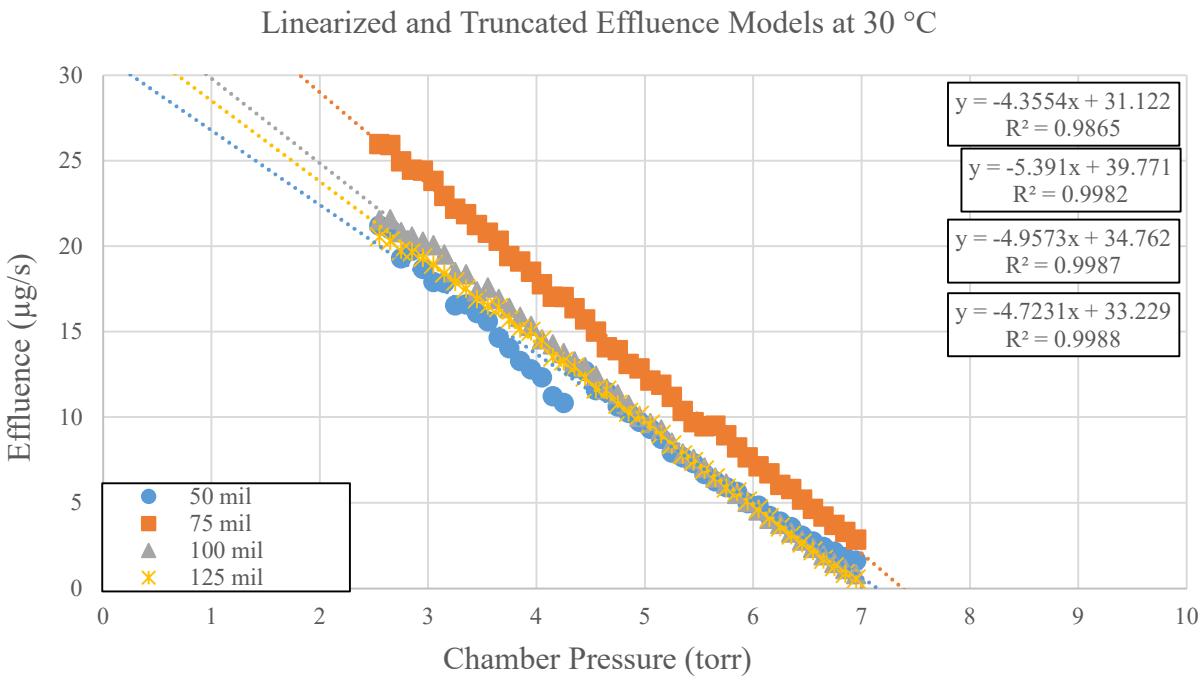

Figure 2.28: Linearized and curve fit truncated average effluence curves for trials at 30℃.

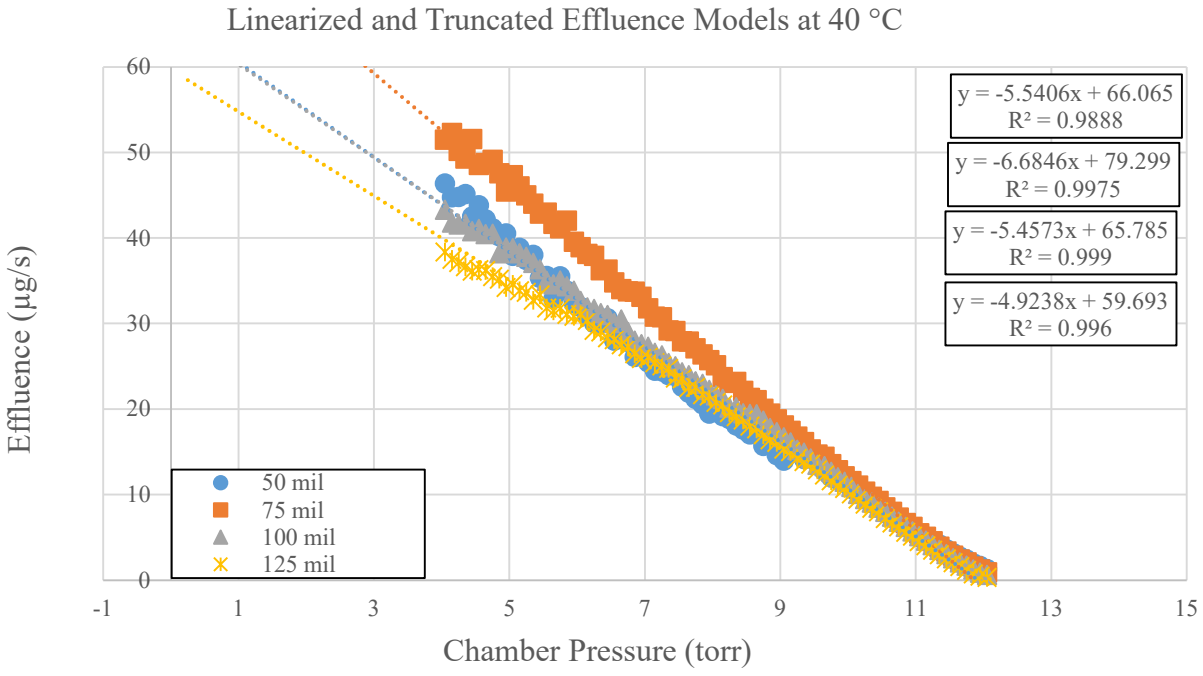

Figure 2.29: Linearized and curve fit truncated average effluence curves for trials at 40℃.

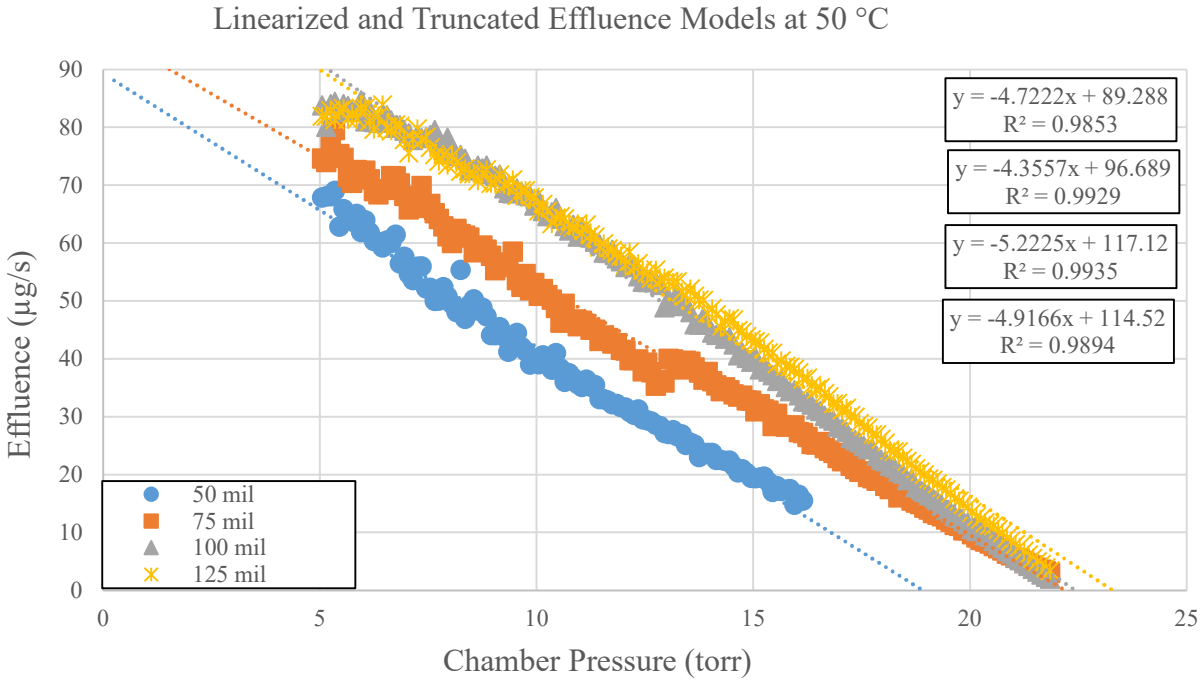

Figure 2.30: Linearized and curve fit truncated average effluence curves for trials at 50℃.

The summary of the slopes, intercepts, and R^2 values showed that the linear fit of each trial were all quite good. This was a product of two things. Firstly, it was indicative of the clarity of the sublimation curves in their linear ranges. The second driving factor was that the truncation of the effluence data was judiciously executed. Table 2.5 was compiled and examined to determine the correlation, between the independent variables of temperature and effluence diameter (sample holder diameter). Plots of the linearized and truncated average effluence slopes versus temperature and effluence diameter are shown in Figure 2.31 and Figure 2.32, respectively. Plots of the linearized and truncated average effluence intercepts versus temperature and effluence diameter are shown in Figure 2.33 and Figure 2.34, respectively.

The correlational studies revealed what was already qualitatively described from the effluence plots. First, its showed that there was not significant correlation between sample holder

Table 2.5: Summary of the slope and intercepts of the linearized truncated effluence curves.

Temperature (°C)	Effluence Diameter (mil)	Slope (µg/s torr)	Y-intercept (µg/s)	R^2
20	50	-8.3722	25.802	0.9915
20	75	-6.3566	19.409	0.9953
20	100	-6.2742	18.836	0.9947
20	125	-4.9035	14.583	0.9905
30	50	-4.3554	31.122	0.9865
30	75	-5.391	39.771	0.9982
30	100	-4.9573	34.762	0.9987
30	125	-4.7231	33.229	0.9988
40	50	-5.5406	66.065	0.9888
40	75	-6.6846	79.299	0.9975
40	100	-5.4573	68.785	0.999
40	125	-4.9238	59.693	0.996
50	50	-4.7222	89.288	0.9853
50	75	-4.3557	96.689	0.9929
50	100	-5.2225	117.12	0.9935
50	125	-4.9166	117.12	0.9894
		Average		
		-5.447	56.973	0.9935

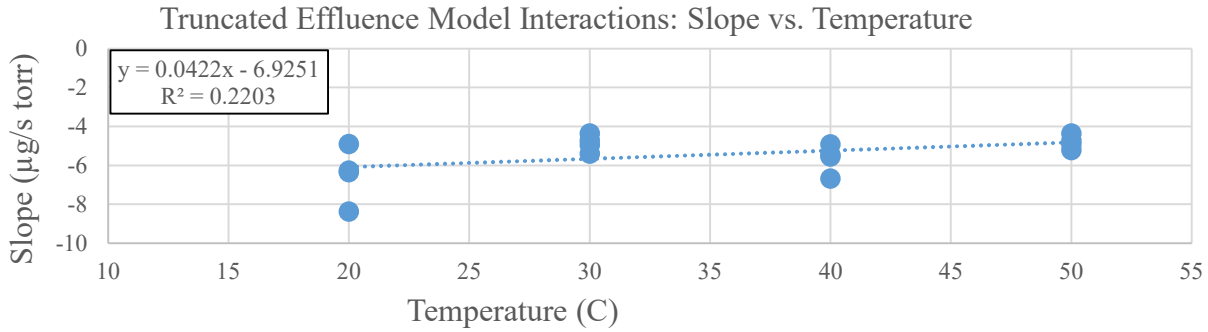

Figure 2.31: Slope versus temperature for all linearized and truncated average effluence plots.

diameter and effluence. The slopes and intercepts of the linear models of effluence (16 in total, one for each of the 16 trials) were not predicted by effluence diameter. This agrees with the findings of effluence analysis. A very interesting observation was that the temperature did not have a significant impact on the slope of the linearized effluence versus chamber pressure plots. The only correlation that was found in the linearized effluence curve fits was between the intercept and

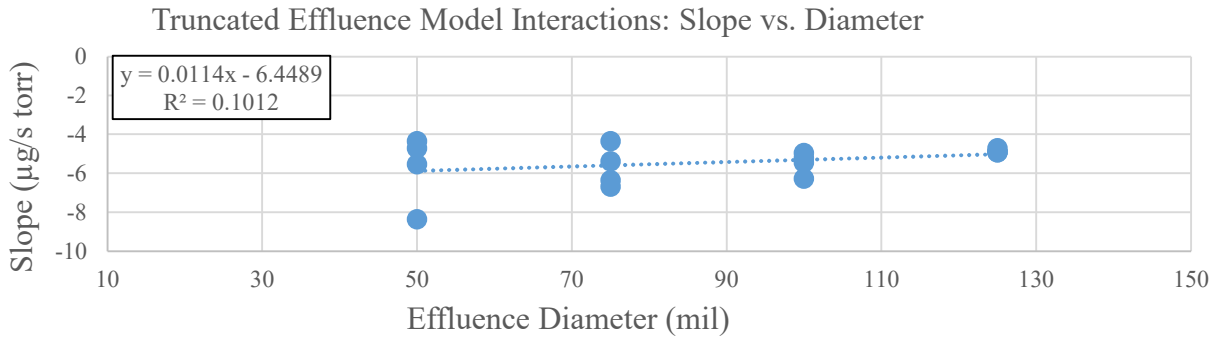

Figure 2.32: Slope versus effluence diameter for all linearized and truncated average effluence plots.

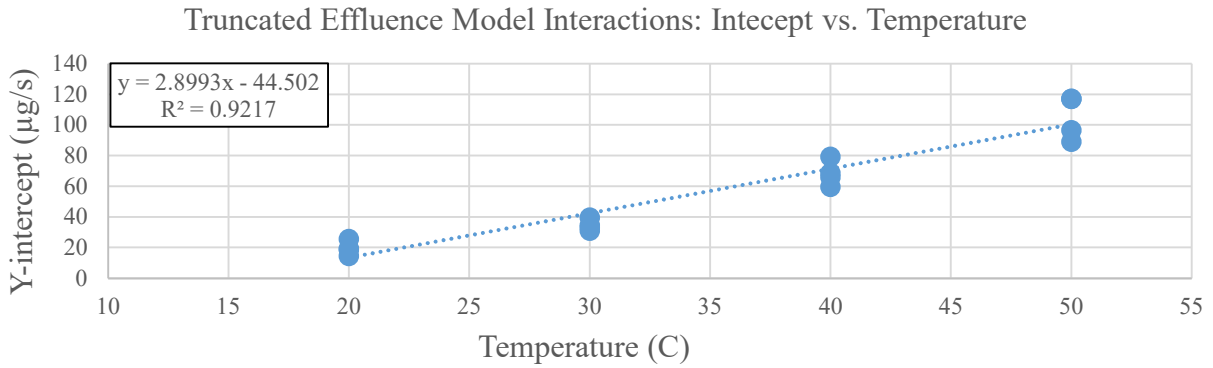

Figure 2.33: Intercept versus temperature for all linearized and truncated average effluence plots.

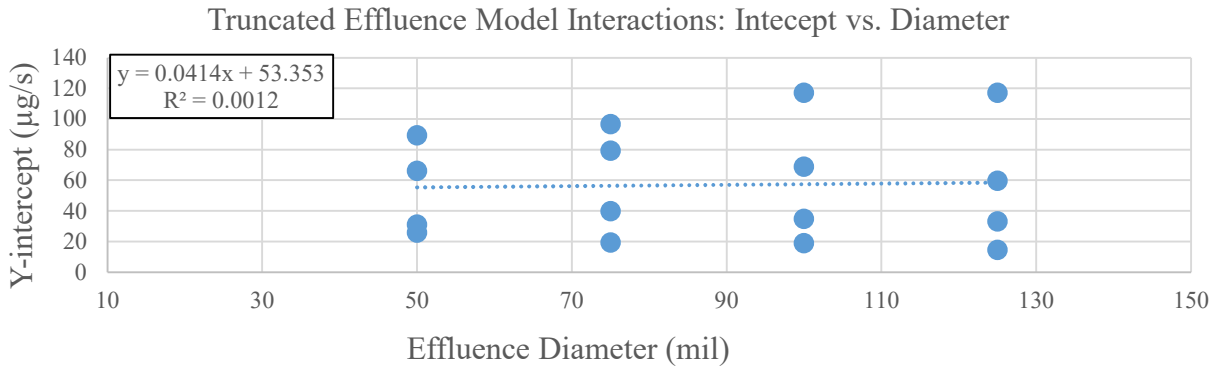

Figure 2.34: Intercept versus effluence diameter for all linearized and truncated average effluence plots.

temperature. A table summarizing the correlational models relating the slopes and intercepts of the

linearized truncated average effluence curves to temperature and effluence diameter is shown in Table 2.6.

Table 2.6: Summary the correlational models relating the slopes and intercepts of the linearized truncated average effluence curves to temperature and effluence diameter.

Plot	Slope	Intercept	R^2
Slope versus Temperature	0.0422	-6.9251	0.2203
Slope versus Effluence Diameter	0.0114	-6.4489	0.1012
Intercept versus Temperature	2.8993	-44.502	0.9217
Intercept versus Effluence Diameter	0.0414	53.353	0.0012

The most important conclusion was that there was independence between the effect of temperature and chamber pressure on effluence. The only predictor of the 16 linear curves features (slopes or intercepts) was temperature. The temperature predicts the y-intercept of the 16 linear curves. The slopes of these curves were not impacted by temperature or effluence area and an average value of all 16 curves can be taken to be the slope of an overall model. The intercept of an effluence versus chamber pressure model was therefore calculated based on temperature. The slope of the effluence versus chamber pressure was calculated based on the average slope all 16 linear models. Therefore, a model of effluence was formulated that has two independent predictors, temperature and chamber pressure. The result of this analysis is shown in Equation 2.3.2. This model has limitations on its usefulness because it was based on the linear region of the effluence versus chamber pressure data. A plot of the upper and lower bounds of temperature and pressures for which the model is valid is shown in Figure 2.35.

Effluence (µg/s) = -5.447 (µg/s torr) * P (torr) + 2.8993 (µg/s℃) * T (℃) – 44.502 (µg/s)

(Equation 2.3.2)

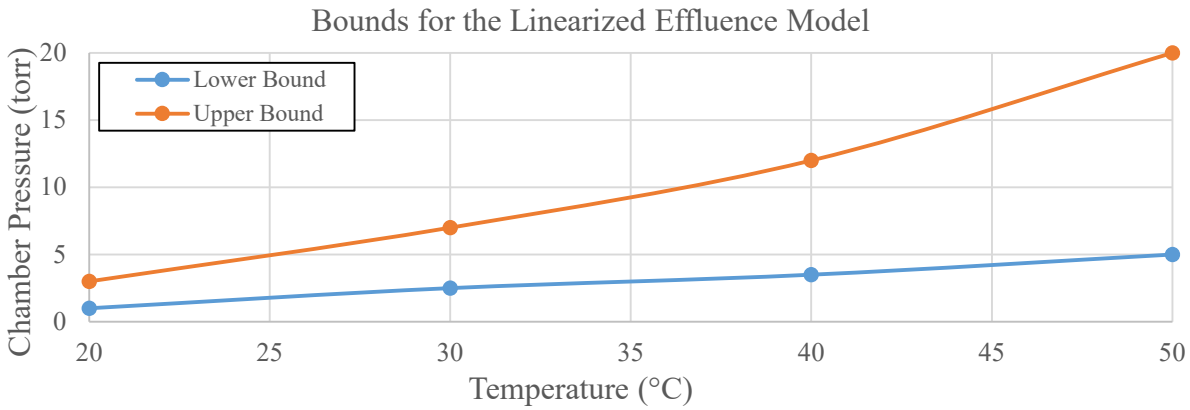

Figure 2.35: Upper and lower bounds of the temperatures and chamber pressures for which the effluence model is valid.

2.4 Sublimation Dynamics Conclusions

The conclusion of the sublimation dynamics experiment was that the effluence of XeF_2 can be predicted by a model if the operating conditions are within the linear range. This range was defined by the upper and lower bounds shown in Figure 2.35. Furthermore, the nature of the factors that can affect effluence rate have been identified. The most important factor that can affect effluence was the size distribution of XeF_2 crystals. More broadly, microscale crystal surface area had significant impacts on effluence. The macroscale surface area was not found to be significant because the microscale surface area was a dominant effect. Another finding was that sublimation does not stop once the vapor pressure of XeF_2 has been reached due to the dissociation of the molecule into Xe and F_2 gases.

The goal of this study was to provide an understanding of the dynamics of the sublimation of XeF_2 for the use case application of creating a propellant delivery device. XeF_2 is used commercially as a subliming etchant in the electronics industry but XeF_2 was never studied in the depth presented here nor for the proposed application. Present applications don't rely on the

specific XeF_2 sublimation dynamics because systems use a timed dosing scheme which are tuned until good etching results are obtained. The process was entirely empirical and was based on the specifics of a single etching tool or process. The data presented in this dissertation is the only study ever conducted that empirically examined the nuance of how XeF_2 sublimates. It is believed that the data contained in this dissertation will be valuable to future designers of the use-case propellant delivery system for small satellites.

3. Tungsten Etching with Xenon Difluoride Vapor

The goal of the W etching experiments was to determine if the material could be etched fast enough to be useful as a propellant stream in an electric propulsion system, and if the process could be done with sufficient efficiency to out-perform the current state-of-the-art in terms of propellant storage density. In order to answer this question several things were investigated. First, the etching efficiency of XeF_2 was sought, that is the ratio between the mass of W etched and the theoretical mass W that should be etched if the stoichiometry of the etching was ideal. Second, the average etch rate over time of W was sought. Third, the conditions under which good etch efficiency and sufficient etch rates can occur were sought. These three subjects were empirically investigated. The results of the investigation showed that W could be etched at sufficient rates to be useful as a propellant stream under the conditions explored, and that it could surpass the current state-of-the-art in terms of propellant storage density.

The etching experiments were conducted in first a dynamic fashion and then in a static fashion. The first dynamic etch experiment immediately revealed that the mass flowrate of W being etched was more than sufficient to be useful in an electric propulsion system. However, the etching efficiency of this process was ~37%. The etch dynamics experimental setup was modified by decreasing the flow channel depth in order to see if the efficiency could be improved but it decreased to 11%. This led to a conclusion that the dynamic etch experiment was not a good approach to study etching due to uncontrolled factors. The static etch experiments were then undertaken and these revealed some interesting findings and demonstrated that the etch efficiency could be high enough to yield a propellant whose solid storage density was superior to the state-of-the-art (more dense than iodine). In the end, the conclusion of the etch experiments was that the chemical reaction of XeF_2 etching W could be useful for the use case scenario of creating a high-density propellant stream, however the experiments were not up to task to fully characterize the

etch rate for reasons that will be discussed.

3.1 Overview of Etching Chemistry

The first discussion of W etching by gas phase XeF_2 must start with the chemical reaction that occurs at the surface of the W. The first fundamental question that was considered was what is the overall final chemical reaction that takes place to etch W. The nature of Xe and F individually are quite contrasting. Fluorine is the most electronegative element and in a diatomic gaseous form it is extremely reactive. This is in stark contrast to Xe which is a noble gas and is one of the least reactive elements. When gas phase XeF_2 reacts with anything, it is the F that will react and attach to other atoms or molecules, leaving the Xe as a monatomic gas. This is no different in the case of XeF_2 reacting with W. The reaction produced Xe gas and tungsten hexafluoride, WF_6. The commercial production of WF_6 gave an initial picture of the stable reaction products of W and XeF_2. Tungsten hexafluoride is formed by flowing F_2 gas over a powder bed of W in a vessel that has been purged of air (leaving only F_2 and W to react). This reaction forms WF_6 which condenses into a liquid at ~17℃. This liquid can then be harvested using a U-trap or some other gravity driven method to tap off the condensed WF_6. It was of note that the production of WF_6 does not involve additional purification steps unless there was oxygen contaminates in the system, in which case WOF_4 could be formed. This meant that under the conditions that this research would be exploring, it was expected that no reaction products other than Xe and WF_6 would be formed. This was because the lesser fluorides of tungsten are not volatile and do not readily form gasous compunds. The conclusion then is that the reaction that is expected during XeF_2 etching of W is the following.

$$3\ XeF_2 + W \rightarrow 3\ Xe + WF_6$$

This conclusion was further supported by an in-depth study of the process of XeF_2 etching W [22, 23] which gave a clear picture of the intermediate reaction products as well as the final

chemical formula. The study worked with three different samples of W, an annealed crystalline (100) sample, an ion damaged crystalline (100) sample, and a polycrystalline sputter-deposited thin-film sample. These samples were exposed to an environment of XeF_2 gas at 4 X 10^{-6} torr for 200 s. The surface of the W was studied in-situ with x-ray photoelectron spectroscopy over time to observe the evolution of etching products over time. The spectroscopy studies identified the presence of WF and no other WF_x species on the annealed polycrystalline sample. The first conclusion of this study was that defect sites or grain boundaries are the locations at which etching occurs. The reaction between XeF_2 and W did not progress to create WF on the surface of the W if it was monocrystalline because defects are required for further uptake of fluorine. The spectroscopy studies identified the presence of WF, WF_2, WF_3, and WF_4 on the surface of the ion damaged crystalline and polycrystalline samples and no WF_5 or WF_6 was observed on either sample. The explanation for this is that the compound WF_5 is not stable and will not be formed on the surface of the tungsten [23]. The presence of WF_6 was not observed on the surface of the W samples because this species has a boiling point of 17℃ at atmospheric pressure and will evaporate from the sample's surface under the conditions of the experiment. The authors concluded that the overall chemical reaction for etching is by the following formulae.

$$XeF_2\ (gas) + 2\ W\ (solid) \rightarrow Xe\ (gas) + 2\ WF\ (solid)$$

$$XeF_2\ (gas) + 2\ WF\ (solid) \rightarrow Xe\ (gas) + 2\ WF_2\ (solid)$$

$$XeF_2\ (gas) + 2\ WF_2\ (solid) \rightarrow Xe\ (gas) + 2\ WF_3\ (solid)$$

$$XeF_2\ (gas) + 2\ WF_3\ (solid) \rightarrow Xe\ (gas) + 2\ WF_4\ (solid)$$

$$XeF_2\ (gas) + WF_4\ (solid) \rightarrow Xe\ (gas) + WF_6\ (gas)$$

The rate of etching was limited by the final step in the above reactions. This was due to the probabilities involved with the reaction [19]. The probability of a XeF_2 coming near enough to a

W atom on the surface of the sample was dependent on the pressure and temperature of the gaseous XeF_2. When this happened, a F atom would leave its molecular form and attach to a W atom with some probability. The probability of a XeF_2 contributing a F atom to WF to form WF_2 had a similar probability based on temperature and pressure. This could also be said for the formation of WF_3 and WF_4. The probability for forming WF_6 was different, however, because there was no stable intermediate species of WF_5 that was formed. In order to transition from WF_4 to WF_6, two fluorine atoms had to simultaneously bind to the WF_4 which meant two F atoms must be in the same region at the same time. The probability of this occurring was relatively less than that of a single F meeting a surface WF_x site. Therefore, the etching of W by XeF_2 was limited by the reaction of WF_4 reacting with two F atoms. This analysis also supported the argument outlined previously of the conclusion that etching of W by XeF_2 has only one stable tungsten fluoride as a gaseous reaction product.

The ideal mass ratio for efficient etching was calculated based on the molar mass of XeF_2 and W. The above analysis has concluded that it takes three XeF_2 molecules (169.29 g/mol) to liberate a single W atom (183.84 gm/mol). Therefore, the ideal mass ratio for perfect etch efficiency was calculated and this equates to 2.76 g of XeF_2 being needed to perfectly etch 1 g of W. The term 'efficiency' was used in this study and was evaluated by dividing the ideal mass ratio by the measured mass ratio of XeF_2 to W. This can also be calculated for the case of higher fluorides of xenon namely xenon tetrafluoride (XeF_4) and xenon hexafluoride (XeF_6) and are shown below. These two compounds are not commercially available but have been synthesized and are known to be somewhat stable compounds [16]. These compounds would in theory etch W by the exact same process as XeF_2 with the obvious modifications to the stoichiometry

$$\frac{3*169.28\frac{g}{mol}Xe_{\ 2}}{183.84\frac{g}{mol}W} = 2.76\ \frac{g\ XeF_2}{g\ W} \qquad \text{(Equation 3.1.1)}$$

$$\frac{3*207.80\frac{g}{mol}XeF_4}{2*183.84\frac{g}{mol}W} = 1.70\ \frac{g\ Xe\ _4}{g\ W} \qquad \text{(Equation 3.1.2)}$$

$$\frac{254.28\frac{g}{mol}Xe\ _2}{183.84\frac{g}{mol}W} = 1.38\ \frac{g\ XeF_2}{g\ W} \qquad \text{(Equation 3.1.3)}$$

The storage density of XeF_2 and W in the ideal stoichiometric ratios for ideal reaction was an important metric. The metric that represents state-of-the art was also important. The state-of-the-art in high density propellant storage is crystalline iodine which has a density of 4.933 g/cm^3. The actual storage density that can be achieved based on observed etch efficiency was what has been compared to the ideal value. The storage density of the combination of reactants (XeF_2 and W, XeF_4 and W, or XeF_6 and W) have be calculated as a function of etch efficiency. This data is plotted in Figure 3.1 along with the density of iodine. The efficiency needed to match the storage density for iodine is 52. 7%, 50.4%, and 71.7% for XeF_2, XeF_4, and XeF_6, respectively.

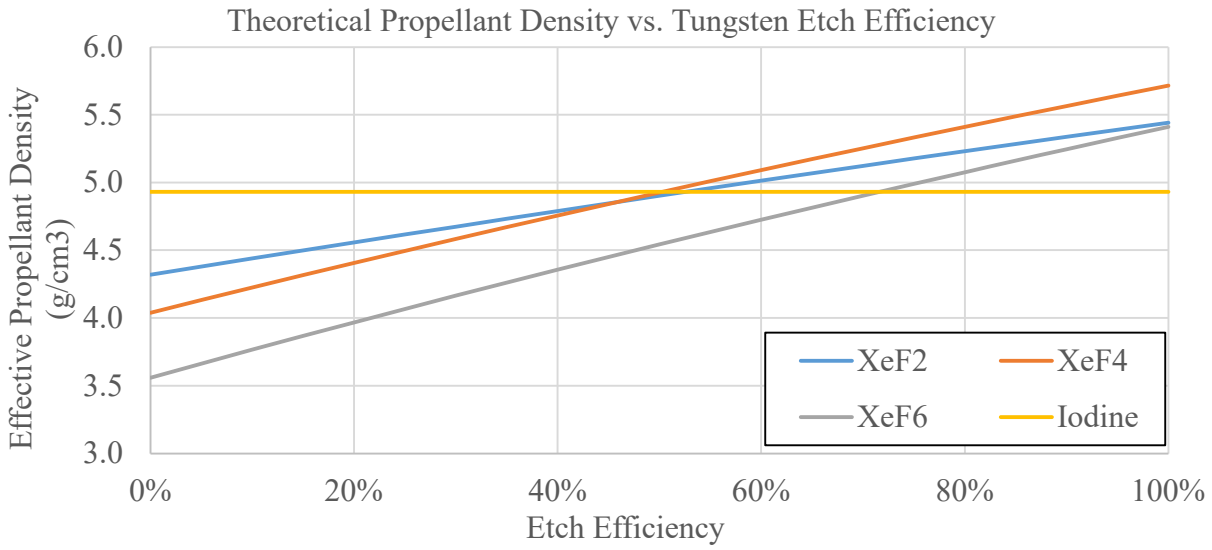

Figure 3.1: Theoretical propellant density as a function of etch efficiency for xenon fluorides and tungsten.

3.2 The Dynamic Etch Experiment

The key question that was addressed by the dynamic etch experiments was is it possible to achieve sufficient etch rates of W to produce a propellant stream that would be useful for an electric propulsion system. The baseline mass flowrate that was sought was 1 μg/s of mass flow rate of W. This is a typical value for a micropropulsion system operating on a small satellite bus. The etch rate of W by XeF_2 vapor is reported in literature to be 80 nm/min (~1.3 nm/s) [27]. This was achieved in a 'homemade' XeF_2 etching tool at UC Berkeley. This tool was designed to be analogous to the commercial Xetch® system manufactured by Orbotech (formerly Xactix) or Samco International. These devices sublimate crystalline XeF_2 and deliver the vapor to an etching target via a pulsed paradigm. A dose of XeF_2 is sent to the etching chamber at a pressure of 2.6 torr and let sit for 10 – 60 s long etch pulse. The etch chamber is then vented and the process repeated. The depth of etch is controlled by manipulating the number and length of the etch pulses. The commercial etching systems claim to be able to etch materials that can form volatile fluorides such as Si, Ta, Ti, Mo, and W. The etch rate described in literature would imply that only a small surface area of W is needed to produce the target mass flowrate of 1 μg/s. The required area for this flowrate and at the reported etch rate of W was calculated to be 0.65 mm^2. This was good news for the desired use case because an appreciable mass of W that might be used for propellant would have a much larger surface area. Therefore, it was expected that an etching reaction should not be surface area limited.

The physical layout of the dynamic etch experiment was designed to be able to measure the etch rate of a ribbon of W in-situ while it was being etched. The ribbon used for testing measured 8" long, 0.100" wide, and 0.001" thick, and was manufactured by Scientific Instrument Services (PN W342). The ribbon was placed in a flow channel that was 0.110" wide and 0.040"

deep. The flow experiment was comprised of a stack of four acrylic sheets that had features laser cut and machined into them. The four acrylic parts were sealed together by a o-rings between the layers. The top layer, the lid, contained holes for sixteen spring loaded gold pins which made contact with the ribbon. The second layer had passthrough holes for the pins as well as the actual flow channel cut into it. The third layer, the ribbon holder, served as the substrate to which the ribbon was affixed and had holes through which to pass the tails of the ribbon. These holes also served as the inlet and outlet ports for gas flow. The final layer of acrylic served as a base to hold the stack together and had a flat surface to mate against o-rings in an aluminum fixture. The aluminum fixture was comprised of two halves that were bolted together in a clam-shell arrangement. The acrylic stack was slid into a channel in the two aluminum halves and then clamped together. This clamping action served to seal the four acrylic parts to each other and to seal the acrylic stack to o-rings placed in the base of the bottom aluminum fixture. The bottom fixture also had a hole cross-drilled into it to provide a gas flow path to the acrylic flow channel. The flow channel was plumbed with vacuum on one side and the other side was plumbed to the XeF_2 sublimation chamber that was used in the sublimation dynamics experiments. The vacuum side of the flow channel had a needle valve between vacuum and the setup. This valve was used to regulate the pressure inside the flow channel and, thus, the pressure in the sublimation chamber which ultimately regulated the effluence of XeF_2.

The measurement paradigm of the dynamic etch experiment was based on a multichannel Kelvin (4-point probe) measurement to determine the resistance of the W ribbon at numerous points along its length. The sixteen spring-loaded gold contact pins in the top of the flow channel made contact with the ribbon every 0.5”. The first and last pins were used to inject a current through the entire wire which was measured in real-time by measuring the voltage drop across a

2.2 Ω sense resistor which was placed next to the current source. The rest of the pins were used to measure nodal voltage drops along the wire. These nodal voltage drops were then used to calculate the resistance of the ribbon for every 0.5” segment along its length using the known current. The thickness of the ribbon could then be calculated assuming that the resistivity and width of the wire were constant. This arrangement was controlled and measured by a LabView™ program and a National Instruments data acquisition hardware (DAQ), model NI USB-6216. The temperature was measured via the same hardware as in the sublimation experiments, a K-type thermocouple, a AD595 hermetic thermocouple driver with internal temperature compensation, and NI USB-6002 DAQ, and the pressure was measured via the Baritron™ gauge and MKS 651 controller. A CAD model of the Dynamic Etch Experiment without the sublimation chamber and pressure transducers attached is shown in Figure 3.2. A detailed cross section of the flow channel with W ribbon and contact pins is shown in Figure 3.3.

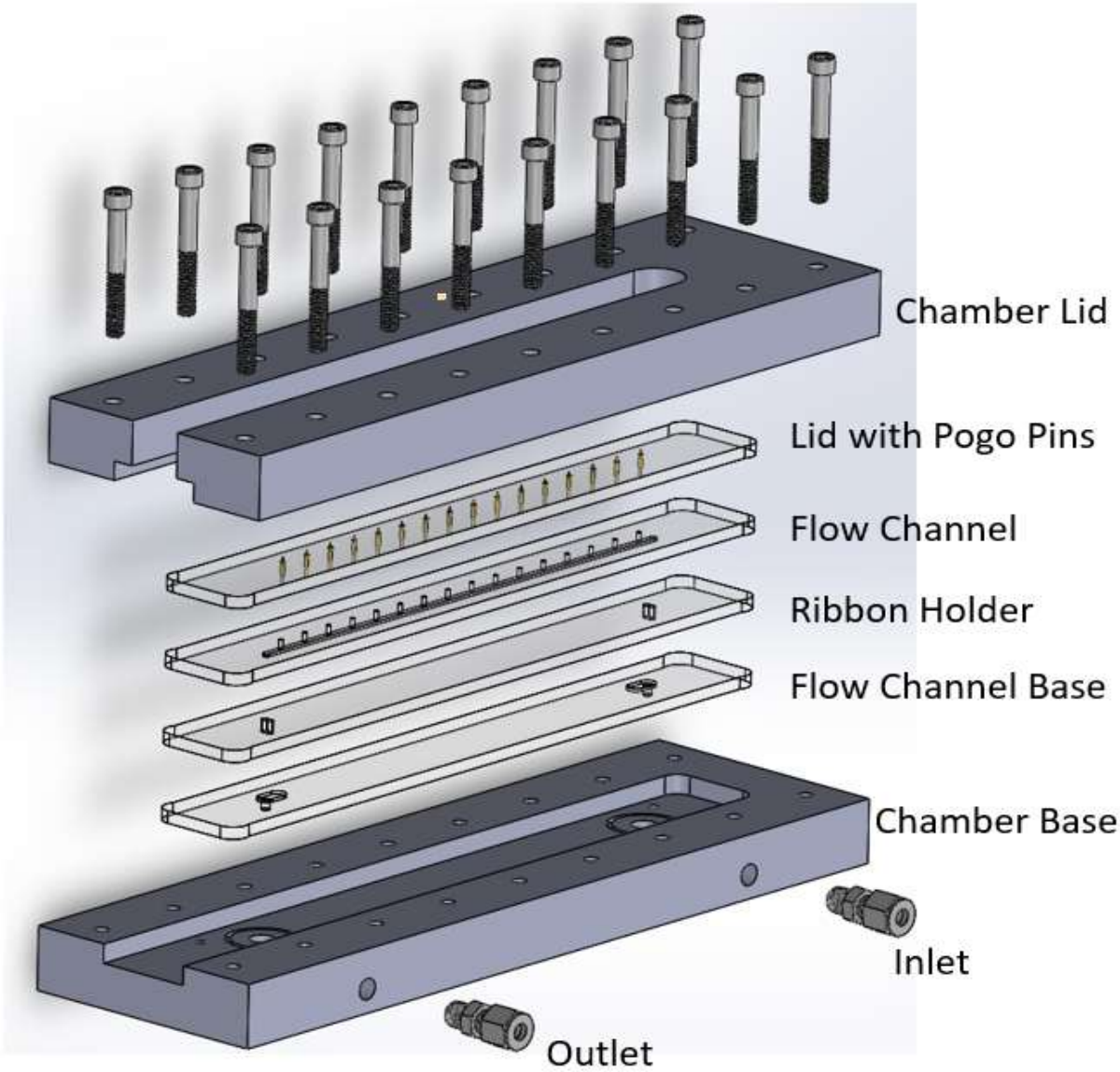

Figure 3.2: Exploded view of the Dynamic Etch flow channel and clamping structure.

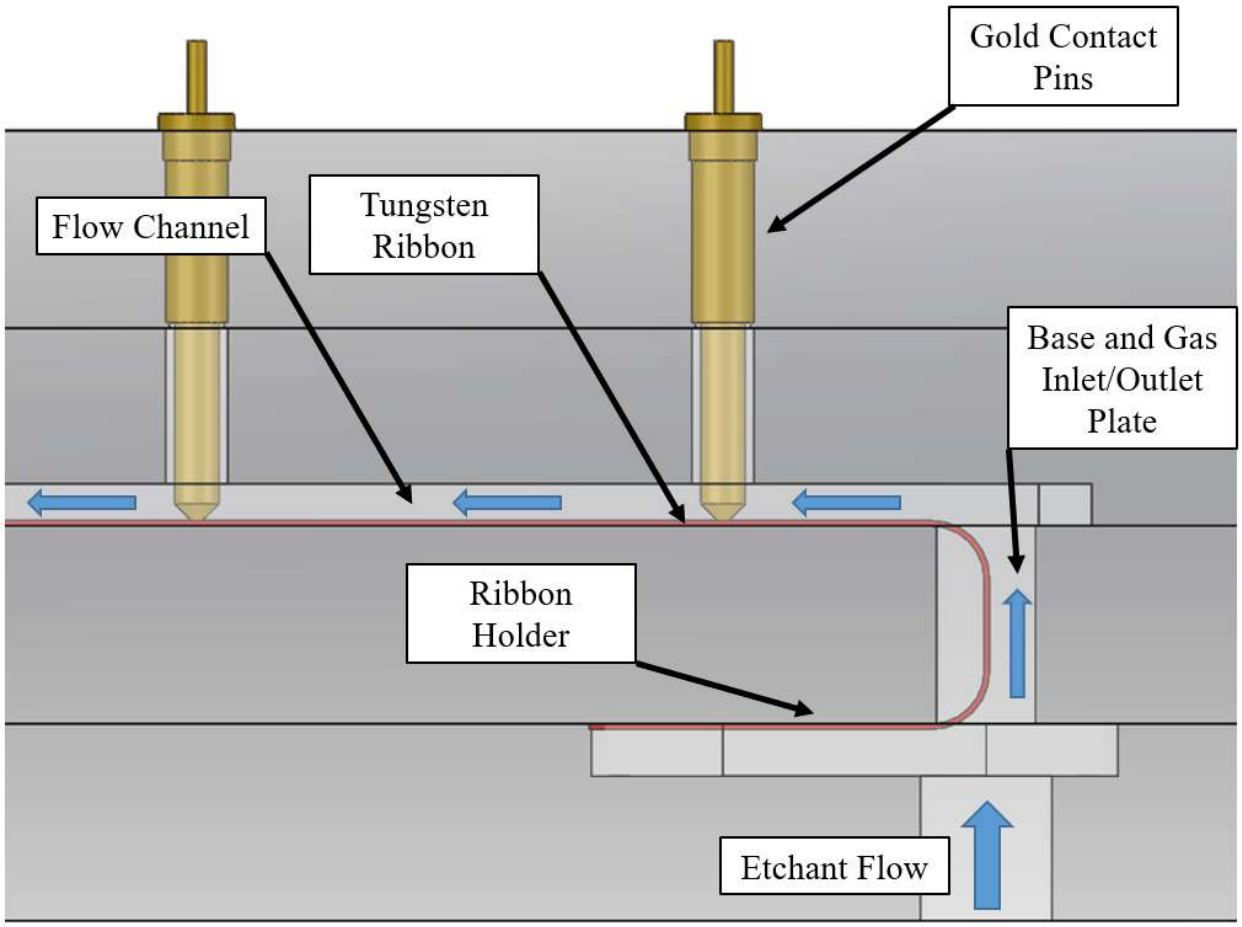

Figure 3.3: Detailed view of the flow inlet to the dynamic etch experiment showing the captured tail of the W ribbon, flow channel, and contact pins.

The process for conducting the dynamic etch experiment was created based on the experience from the sublimation experiments. The W ribbon sample was first cleaned with isopropyl alcohol. The ribbon was then liberated from any surface oxidation and roughed up by buffing the surface with 1000 grit sandpaper. The ribbon was then mounted in the flow channel apparatus and sealed in the mounting fixture. The sublimation chamber was loaded with a sample of XeF_2 crystals and sealed, and entire apparatus was allowed to thermally stabilize at a temperature of 50℃. The experiment was executed by pumping down the system to cause sublimation and this gas was flowed over the W ribbon and the current and nodal voltages

recorded.

A constant current source circuit was built to excite the W ribbon for the Kelvin resistance measurements. A low current of ~0.024 A was used to create a voltage drop across the ribbon while avoiding heating in the ribbon. The constant current circuit used a precision AD 584 5 V reference IC which was fed into the inverting input of an op-amp (OP-27G) which was configured as a voltage follower. This op-amp served as the current source for the entire circuit. Output of the first op-amp was fed into a 220 Ω current control resistor and then into the non-inverting input of a second op-amp. The inverting input of the second op-amp (OP-27G) was tied to ground. A sense resistor and the W ribbon was finally placed in series between the non-inverting input and the output of the second op-amp, which served as a current sink. A schematic of this circuit can be seen in Figure 3.4.

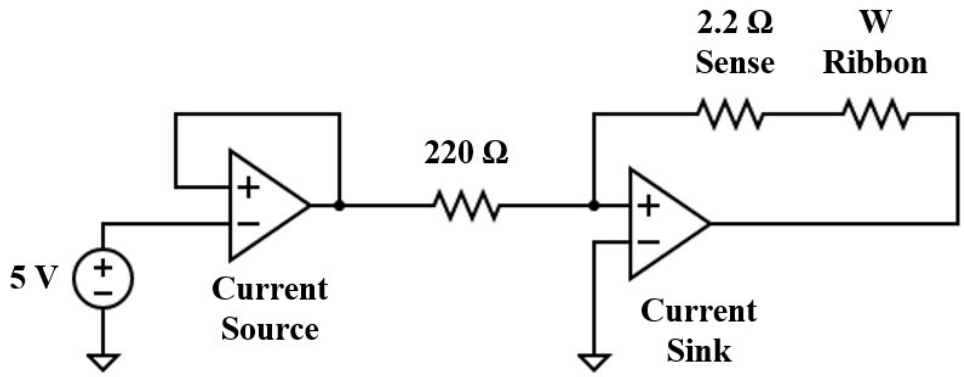

Figure 3.4: Circuit schematic of the constant current source used for the dynamic etch experiments.

The experimental setup for the dynamic etch experiment was plagued with instrumentation challenges due to the low signal level measurements that were needed for the experiment. The linear resistance of the W ribbon was 0.0089 Ω/cm . This meant that the voltage drop between any two adjacent pins in the measurement setup was ~0.27 mV, before etching occurred. To accurately measure this voltage drop it was necessary to collect and average a very large sample of voltage

readings per node. In practice each pin was sampled at 25 kHz over five seconds and then averaged so that each reading of nodal voltage was the average of ~125,000 discrete measurements. The differential resistance and, thus, resistance and thickness measurements, were then composed of ~250,000 discrete measurements. This measurement paradigm was necessary to mitigate noise in the electronics and physical test setup.

A 16 channel op-amp circuit was built with 10X and 100X gain stages to boost the low differential voltage signals. However, this approach had significant issues and was abandoned. The amplifiers suffered from noise as well but the more fatal issue was calibration. It was found that the theoretical value of gain based on the op-amp resistors was not sufficiently accurate for the application. Precise calibration curves were instead generated for each channel of the amplifier to determine the gain. This involved injecting a voltage from the DAQ to the amplifier and directly measuring the input with an Agilent 34410A 6.5 digit benchtop multimeter. The output of the amplifier was then measured with the DAQ. Input voltage was serially swept over the operating range of the amplifier and the linear relationship between input and output voltage was found. This data was fitted with a linear regression to determine the gain and offset errors of the amplifiers which were then applied in software to each of the 14 nodal voltage channels. This still was problematic because the entire circuit was built on a breadboard and simply changing a ground path or the physical location of a power supply wire on the breadboard caused the calibration curves to change. In the end, it was determined that it was more accurate to directly sample the nodal voltages with the DAQ which had a 16-bit resolution and a sensitivity of 59.6 μV in the operating range of ±5 V that was employed.

The final instrumentation configuration used the first and last pins for current injection leaving 14 pins for nodal voltage measurements. The Kelvin measurement is a differential type

measurement so there were ultimately 13 separate measurements of thickness along the length of the W ribbon (one section between each of the 14 node pins).

The dynamic etch test was conducted at 50℃ with a 0.040” deep flow channel and a sublimation chamber pressure of 17 torr. This nominal operating condition was selected to produce a XeF_2 effluence of ~20 μg/s. The W ribbon was prepared and mounted in the test chamber according to the process described above. The mass of the ribbon before etching was measured to be 269.0 mg. A dose of XeF_2 crystals measuring 309.0 mg was loaded in the 0.125” diameter sample holder. The ideal mass of W to be etched by this mass of XeF_2 was calculated to be 112 mg. The Kelvin measurement arrangement was used to measure an average ribbon thickness of 22.7 μm (nominally 0.001”) prior to the experiment running. The experiment was started and proceeded as expected for 63 minutes. The thickness of the ribbon decreased over time, as was expected, which clearly showed that the W was being etched. The end of the ribbon closest to the inlet for the XeF_2 was etched faster than the outlet. At 63 minutes into the experiment the current sense indicated an open circuit and the nodal voltages measured by the DAQ became saturated at -5.3 V. The experiment continued to run for another ~100 minutes until all the XeF_2 had been sublimated and vented from the system. The etch was completed at a time of 145 minutes and was indicated by the pressure falling to 7.25 torr.

This pressure was higher than the finishing pressure observed in the sublimation dynamics experiments because the dynamic etch experimental apparatus was significantly leakier than the sublimation chamber. It was initially thought that the current source circuit or instrumentation had experienced a fault at the 63 minute mark. However, upon further inspection it was discovered that the W ribbon had been etched completely through between the first and second probe pins (current injection pin and first voltage node pin). This resulted in the open circuit behavior. A photograph

of the completely etched W ribbon can be seen in Figure 3.5. Another interesting phenomenon was observed. Prior to etching the surface of the W ribbon was shiny and metallic in appearance as it

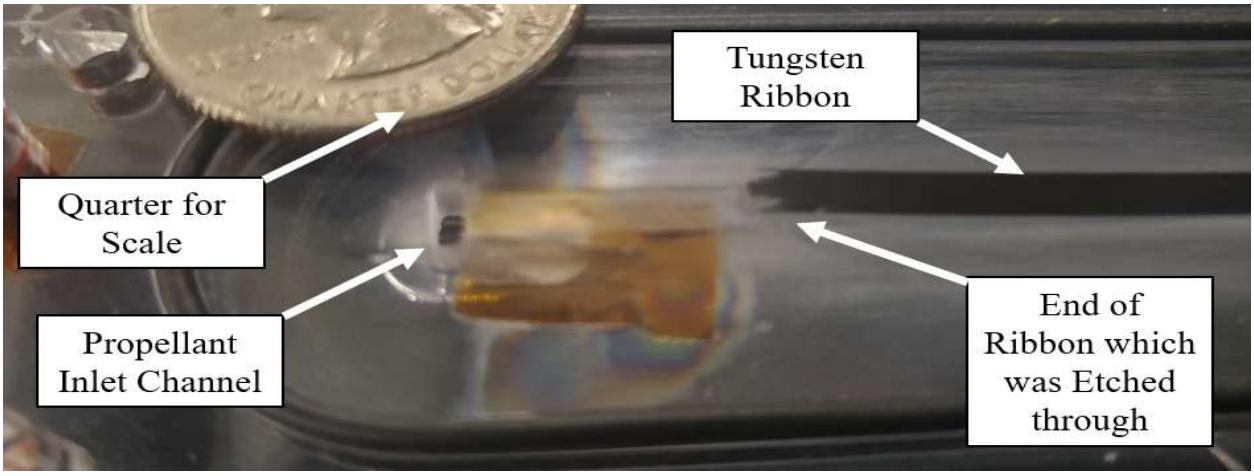

Figure 3.5: Photograph of the completely etched W ribbon at the propellent inlet port.

colored. This is presumably due to the presence of thin-film interference fringes. It is understood was pure W and had been thoroughly cleaned. After the etching experiment, the surface of the W that had not been etched through was multi-that the etching reaction between XeF_2 and W will produce four tungsten fluorides before the final etch product, WF_6 is produced. It is these tungsten fluorides that change the color of the ribbon after etching. A series of photographs of these fringes can be seen in Figure 3.6.

The final mass of the W ribbon was measured and found to be 227.6 mg from which an overall etch efficiency of 37.0% was calculated. The thickness of the 13 sections of ribbon over time are shown in Figure 3.7. A plot of current over time is shown in Figure 3.8. A plot of the sublimation chamber pressure over time is shown in Figure 3.9. A calculation of the etch rate along the length of the ribbon was performed and shown in Figure 3.10 (Section 0 represents the leading edge etch rate).

The results of the dynamic etch experiment had four noteworthy conclusions. First, the peak etch rate that was achieved was in excess of the rate reported in literature [27]. The average ribbon thickness was completely etched through in 63 minutes which resulted in a peak etch rate

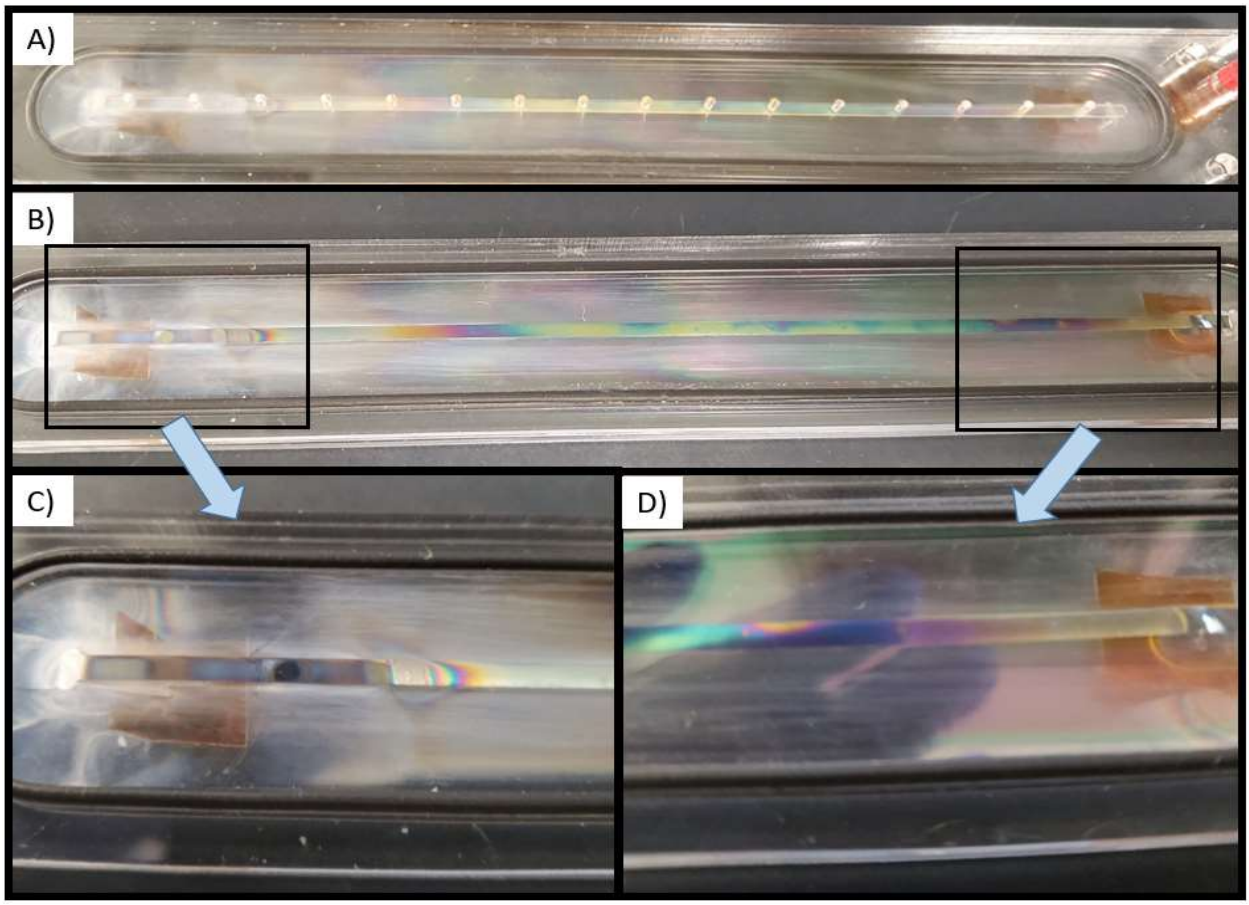

Figure 3.6: Photographs of interference fringes on the W ribbon after etching had occurred. A) Photo showing the etching chamber with the lid still attached (row of holes is lid). B) Photograph of the W ribbon after the lid to the etching channel was removed. C) Detail view of the inlet side of the W ribbon. D) Detail view of the outlet side of the W ribbon.

of 363 nm/min, 4.5 times greater than has been reported. This was an existence proof that under certain conditions the etching action of XeF_2 vapor on W can be very aggressive. Second, the average mass flowrate of tungsten etched was in excess of the target mass flowrate of 1 µg/s. A total of 41.4 mg of W was etched in the 145 minutes that the experiment ran. This yielded an

average overall etch rate of 4.76 µg/s. The surface area from which this material was etched was unknown so the overall etch rate cannot be reported as a linear rate and only as a mass flux. Third, despite the etch rates observed being in excess of that reported in literature, the etch efficiency was still low, meaning that not all the XeF_2 vapor etched any W and some simply passed through the system. It could not be said if the unreacted vapor contacted the surface of the W but didn't etch or if these molecules never interacted with the surface. Fourth, the fact that the leading edge of the tungsten ribbon etched much faster than the trailing end was indicative of the modality of the etching. The average etch rate of the leading edge (over the 63 minutes leading up to the open

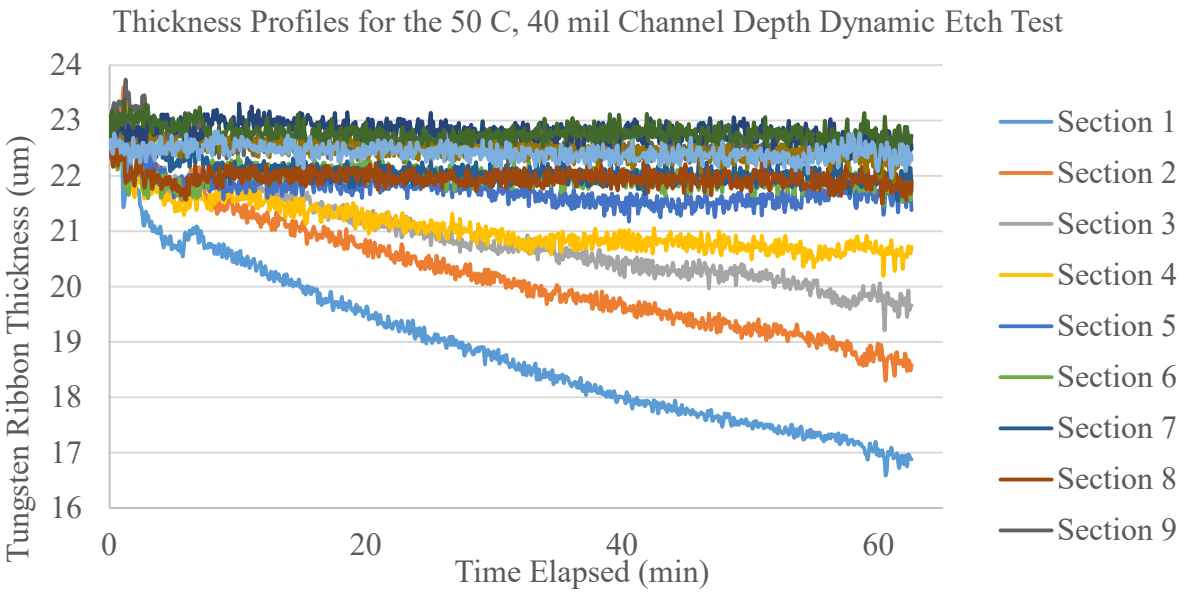

Figure 3.7: Plot of the thickness of the tungsten ribbon over time at 13 locations along its length for the dynamic etch experiment with a 40 mil flow channel depth.

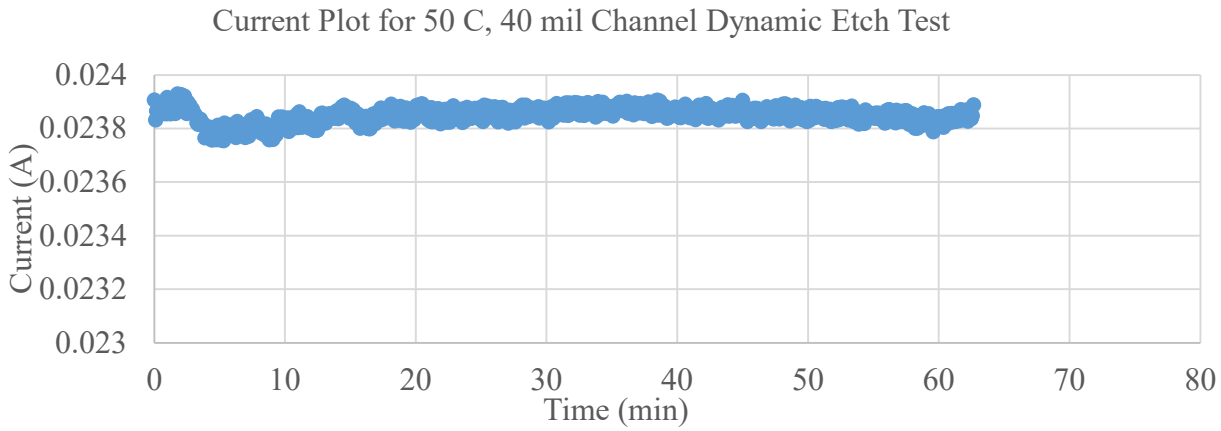

Figure 3.8: Plot of current over time for the dynamic etch experiment with a 40 mil flow channel depth.

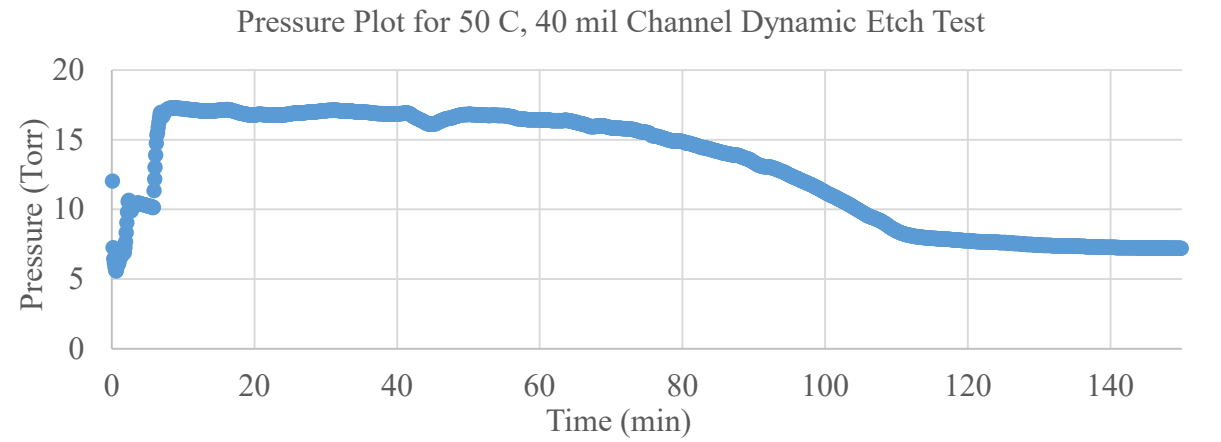

Figure 3.9: Plot of pressure over time for the dynamic etch experiment with a 40 mil flow channel depth.

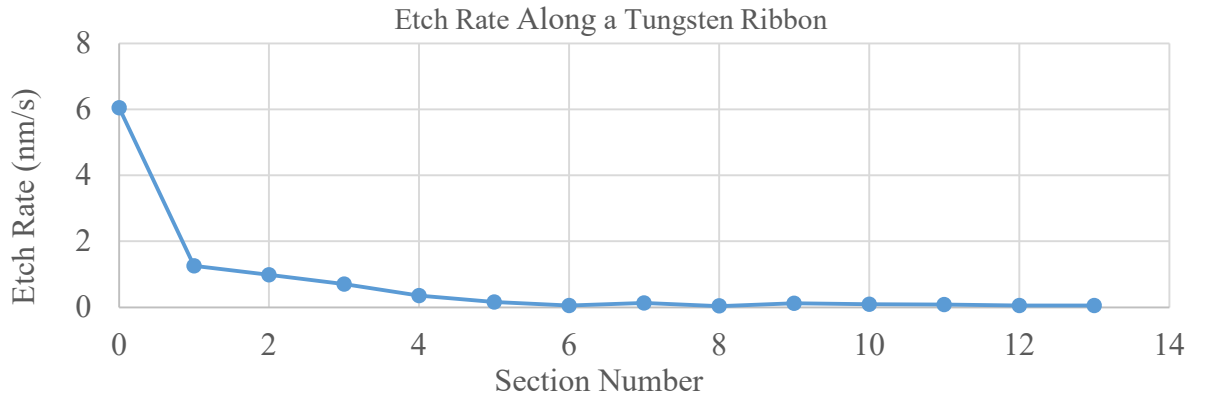

Figure 3.10: Average etch rate along the length of the W ribbon.

circuit condition) was found to be 363 nm/min, the first section measured by the Kelvin arrangement was 87.6 nm/min, and the trailing edge had an average etch rate of 3.35 nm/min. This was interesting because the trailing edge had unreacted XeF_2 vapor pass over (given the etch efficiency), but it etched over two orders of magnitude more slowly than the leading edge.

The most important observation of the dynamic etch test was that the etching action of XeF_2 vapor on W was very aggressive in some areas but there was still unreacted vapor leaving the system as implied by the etch efficiency. There were quantities than could be calculated about the fluid dynamics of the experiment that helped create a picture of what was occurring. It was of note that the following calculations ignore the introduction of WF_6 into the flow stream for the sake of simplicity. The average mass flow rate of the XeF_2 was calculated to be 42.9 μg/s. The pressure of this gas was assumed to be ~17 torr, the pressure of the sublimation chamber. The actual pressure in the chamber would necessarily be less than this, otherwise there would be no flow through the system. However, the flow was controlled by a needle valve between the experiment and vacuum and it was assumed that the vast majority of the pressure was dropped at the valve and the pressure gradient was very low in the flow channel.

This was primarily due to the very low Reynolds number for the flow. Reynold's number is a dimensionless quantity that is used to assess the qualities of a fluid flow such as determining if a flow is laminar or turbulent. The laminar to turbulent transition is generally considered to occur when the Reynold's number is ~3000. Below this value, the flow is laminar and above the value, flow is turbulent. The formula for calculating Reynolds number is shown in Equation 3.2.1 where u is the flow velocity, D is the critical dimension, and υ is the kinematic viscosity of the fluid [74]. For this application the critical dimension was calculated based on the expression for hydraulic

diameter for a rectangular duct and is shown in Equation 3.2.2 where a is the flow channel depth and b is the flow channel width [74].

$$Re = {uD}/{\upsilon} \quad \text{(Equation 3.2.1)}$$

$$Dh = {2ab}/{a + b} \quad \text{(Equation 3.2.2)}$$

Taking the pressure to be 17 torr and the temperature to be 50 °C, the density of the XeF_2 vapor was be found to be 0.143 kg/m^3. From the mass flowrate and density, it was possible to calculate the volumetric flowrate (ignoring the addition of WF_6) which was found to be 0.14 cm^3/s. The cross-sectional area of the flow channel was 0.110" X 0.040" and this was used to calculate an average flow velocity of 4.9 cm/s.

The viscosity of XeF_2 is not reported in literature. Instead, the mass ratio of XeF_2 to Xe, times the viscosity of Xe was taken to be a reasonable approximation of this value, 6.2x10^{-5} Pa•s. The hydraulic diameter of the flow channel was calculated to be 0.00149 m. From these values the Reynolds number was calculated to be 36.4. This calculation confirms the prior assumption that the Reynolds number is low and thus the flow of XeF_2 is in the laminar regime. Furthermore, it is so low that the flow could be considered to be plug flow. This is a specific case of laminar flow where the velocity doesn't vary laterally across the flow path and there is very limited lateral diffusion in the fluid. The entrance length, L_h, was calculated and represents the linear distance down the flow channel where there are changes in the velocity profile of a gas; past the entrance length the velocity profile does not change shape or magnitude. It is calculated according to Equation 3.2.3 where D is the hydraulic diameter and the Re is the Reynolds number [74]. The entrance length was found to be 0.12 cm.

$$L_h = 0.05 * Re * D \quad \text{(Equation 3.2.3)}$$

The conclusion of the flow analysis was that the flow in the channel was laminar, the velocity

profile is uniform along the length of the flow channel, and there is a fully-developed flow at the interface of the flow and the W ribbon.

The flow analysis above ignored the fact that there was WF_6 being generated at the surface of the W ribbon which was diffusing into the stream. From this, claims can be made about the fluid dynamics and etching dynamics. First, there was a zero-slip boundary layer at the surface of the W and this layer was primarily composed of WF_6. There was a zero-slip condition due to the low Reynolds number. Second, the WF_6 was not diffusing into the flow stream to form a homogenous gas in the flow channel. Had this been the case, the etch rate would have been expected to be uniform, however, the etch rate was diminished by over two orders of magnitude along the length of the ribbon. Third, the additional mass flux from the introduction of WF_6 increased the average bulk velocity of the stream. The effect of the additional mass flux was that the velocity of the flow must increase to maintain the constant pressure that was measured in the experiment. However, the Reynolds number was so low that the addition of the extra flux would not change the flow regime from laminar to turbulent. Fourth, spatial composition of the flow could not be calculated along the length of the ribbon with the data collected. The diffusion constant of WF_6 into the XeF_2 and Xe flow was not understood. Developing a model of the surface diffusion and reaction chemistry was deemed to be outside the scope of this work.

The above claims painted a picture of what was happening in the dynamic etch experiment. First, XeF_2 flowed into the inlet of the flow channel. This gas rapidly etched the leading edge of the ribbon as the flow fully developed into a stable, non-mixing and uniform flow. A zero-slip boundary layer formed and was composed of XeF_2, Xe, and WF_6. This concentration of gases was changing as the gas flowed along the length of the ribbon. By the time the gas had traversed approximately a third of the way down the flow channel, there was very little XeF_2 left in the

boundary which led to the etch rate becoming very small. Etching still occurred along the rest of the ribbon but it relied on XeF_2 to diffuse toward the channel walls in order to etch more W. The trailing two thirds of the ribbon had enough interaction with XeF_2 to form some tungsten fluorides, as evidenced by the thin-film interference fringes observed on the tail end of the ribbon. The gas flow exited the flow channel with a significant portion of the XeF_2 remaining unreacted because it never interacted with the W at all.

A change to the experimental setup was made to try and confirm or deny the above analysis. The flow channel depth was reduced from 0.040" to 0.010". This had two effects on the flow dynamics. First, decreasing the channel cross sectional area would make the flow velocity increase, given the same mass flux of XeF_2 entering the system. Simultaneously, the diffusion length that XeF_2 molecules would have to travel through the boundary layer would be quartered. The prediction was that these two effects, higher velocity and lower diffusion length, would have offsetting impacts on the etch efficiency. Decreased channel depth would in tend to decrease the diffusion length for reactants and products leading to increase etching. However, the decreased channel depth would increase the flow rate (constant mass flowrate) and this would decrease the time a reactant would spend in the etching environment which would tend to reduce etching. It was hypothesized that the diffusion length and etch time considerations would counteract and that significant change in etching would occur. However, this was not what was observed. The experiment was conducted as before with all other independent variables remaining the same (only the flow channel geometry was changed).

The result was that the etch efficiency dropped significantly from 37% to 17%. The Reynolds number of this experiment was calculated by the process used formerly and was determined to be 29.7. The calculated etch rates were imperceptibly small and the calculated values

of nearly half of them were less than zero indicating that any etching that occurred was less than the noise floor of the measurement system. The differential mass of the W ribbon before and after the experiment confirmed that there was indeed etching. It was concluded that the etching occurred at the leading edge of the ribbon upstream of the first pair of voltage node measurement pins. Unfortunately, this etch rate could not be measured and only the average mass flux of W could be determined which was 1.7 μg/s. The ribbon showed signs of thin-film interference fringes indicating the presence of tungsten fluorides on its surface so there was some amount of XeF_2 that did reach the ribbon. The prediction was that quadrupling the flow velocity and quartering the diffusion distance for XeF_2 would have offsetting contributions to the etch rate. However, this was not observed and the only conclusion was that there were nonlinear effects of flow velocity and diffusion distance present in the experiment which ultimately effected the etch rate and etch efficiency.

The primary goal of the etch experiment was successfully met under certain conditions. The etch rate of XeF_2 vapor on W was observed to be in excess of the target mass flux of 1 μg/s. The 0.040" etch channel test had an average W mass flux of 5.8 μg/s while the 0.010" etch channel test had a flux of 1.7 μg/s. The secondary goal of demonstrating a best-in-class propellant density was not met because the etching efficiency was too low. The two dynamic etch experiments had an effective propellant density of 4.76 g/cm^3 and 4.52 g/cm^3, respectively. There were three conclusions reached upon completion of the dynamic etch experiments. First, XeF_2 could be used to etch W at a useable rate to render the process suitable for use as a propellant stream in an electric propulsion system. Second, the etch rates measured varied over two orders of magnitude but this range did include the etch rate reported in literature. Third, the fluid dynamics and transport phenomena of reactant and etch products in the dynamic etch test are not sufficiently understood

to yield high etch efficiency.

The lack of understanding of the critical independent variables for good etch efficiency was a serious issue. The dynamic etch experiment employed an interesting measurement technique to observe etching in-situ which was a significant strength. However, the physical experimental setup's significant complexity made the process of data generation challenging. It was determined that a different etch experiment would be useful to deepen the understanding of the etch dynamics and might more readily uncover independent variables that meaningfully affect etch rate and efficiency. For these reasons, a static etch experiment was conducted.

3.3 The Static Etch Experiment

The static etch experiment was a derivative of the sublimation dynamics experiment and used the same experimental setup. The experiment involved placing a W pellet in the sublimation chamber and then running a sublimation experiment. The W was etched by XeF_2 vapor as it sublimated. The reactants were then evacuated out the vacuum vent. This process was repeated cyclically until the XeF_2 loaded in the crystal holder was exhausted. The mass of the W was measured before and after the test and the differential mass of the pellet was the amount of W etched. This process was conducted in an ad-hoc manner at first. After four experiments were conducted a structured data set was collected.

The independent variable considered for the first tests was the sublimation time. The working hypothesis was that if the sublimation time was long, the etching reactants and product would be able to diffuse and mix. This would ensure that all the XeF_2 molecules would have a chance to interact with the surface of the W, and the WF_6 would be able to move away from the surface to uncover additional surface for etching. On the other hand, a very quick sublimation time would lead to worse efficiency because there would be insufficient time for all reactants to interact

with the W. The first four tests were conducted with sublimation times of 1.25, 2.5, 5, and 20 minutes, respectively. The temperature for the tests was 50 °C, the same as the dynamic etch experiment, and the 0.125" diameter crystal holder was employed. After each sublimation cycle the chamber was evacuated and pumped down. The first four tests were pumped down to an arbitrary starting pressure. The next eight tests were pumped down for a specified amount of time, 30 s on the middle four tests and 10 s on the final tests. The fifth through eighth tests were conducted with a sublimation time of 1, 2, 3, and 4 minutes, respectively, as were the final four tests. Each test was conducted with a fresh sample of W which was prepared by cleaning it with isopropyl alcohol and scuffing its surface with 1000 grit sandpaper. The average mass of XeF_2 used per test was 171 mg.

The data collected was comprised of a differential weight measurement of the W pellets, the mass of XeF_2 consumed, and the pressure traces from each sublimation cycle, from which it was possible to calculate numerous quantities from the data. The pressure traces were used to determine the minimum and maximum chamber pressure per cycle, and the number of sublimation cycles for each test. This was used with the sublimation time and the vent time to calculate the total etch time. The average etch depth was calculated based on the nominal surface area of the pellets, the change in mass of the pellets, and the density of W; from this the linear etch rate was calculated. The etch efficiency and hypothetical propellant density was calculated based on the mass of W etched and the amount of XeF_2 consumed. A table of the results of those calculations is shown in Table 3.1. Pressure rate curves for 11 of the static etch tests are shown in Figure 3.11

Table 3.1: Summary table of the Static Etch experiments with independent variables.

Etch Cycle Time (min)	Average Vent Time (s)	Mass of XeF2 Used (mg)	Mass of W Etched (mg)	Average Min Pressure (torr)	Average Max Pressure (torr)	Number of Etch Cycles	Total Etch Time (min)	Average Thickness of Etched W (µm)	Average Etch Rate (nm/min)	Etch Efficiency	Propellant Density (g/cm3)
1.25	189	177.3	27.5	3.19	9.99	13	58.0	7.33	126.3	43%	4.82
2.5	42.1	115.6	29.5	6.21	21.99	14	58.2	6.59	113.3	**70%**	**5.13**
5	139	174.8	32.3	1.37	31.59	16	50.5	7.68	152.1	51%	4.91
20	544	81.1	11.4	1.76	49.82	16	39.5	7.00	177.2	39%	4.78
1	30	170.4	12.7	0.87	8.81	21	89.3	7.52	84.2	21%	4.57
2	30	181.2	25.6	1.55	19.74	14	48.5	6.59	135.8	39%	4.78
3	30	202.5	24.1	1.03	24.55	9	63.5	8.83	139.0	33%	4.71
4	30	212.3	26.8	1.15	30.12	2	49.1	3.12	63.5	35%	4.73
1	10	218.8	20.7	1.37	11.35	15	47.3	8.06	170.4	26%	4.63
2	10	196.8	26.4	1.49	19.59	33	49.0	3.47	70.9	37%	4.76
3	10	180.4	28.1	1.58	26.27	23	26.7	5.66	**212.2**	43%	4.82
4	10	150.5	24.1	1.30	28.36	21	45.3	7.22	159.2	44%	4.84
							Averages				
		171.8	24.1	1.90	23.52	16.4	52.1	6.59	133.7	40.1%	4.79
							Standared Deviation				
		39.8	6.3	1.5	11.3	7.7	15.0	1.7	45	0.13	0.14
							± Error				
		23	3.6	0.8	6.4	4.4	8.6	0.99	26	0.07	0.08

along with the 50 °C, 0.125” sublimation dynamics pressure result for comparison (labeled as Pure XeF_2 Trunc). Pressure rate was chose over an effluence plot because the ideal gas constant changes over the experiment while pressure was a correct result. There were only two cycles of the 20 minute sublimation time static etch experiment so no effluence plot was generated due to

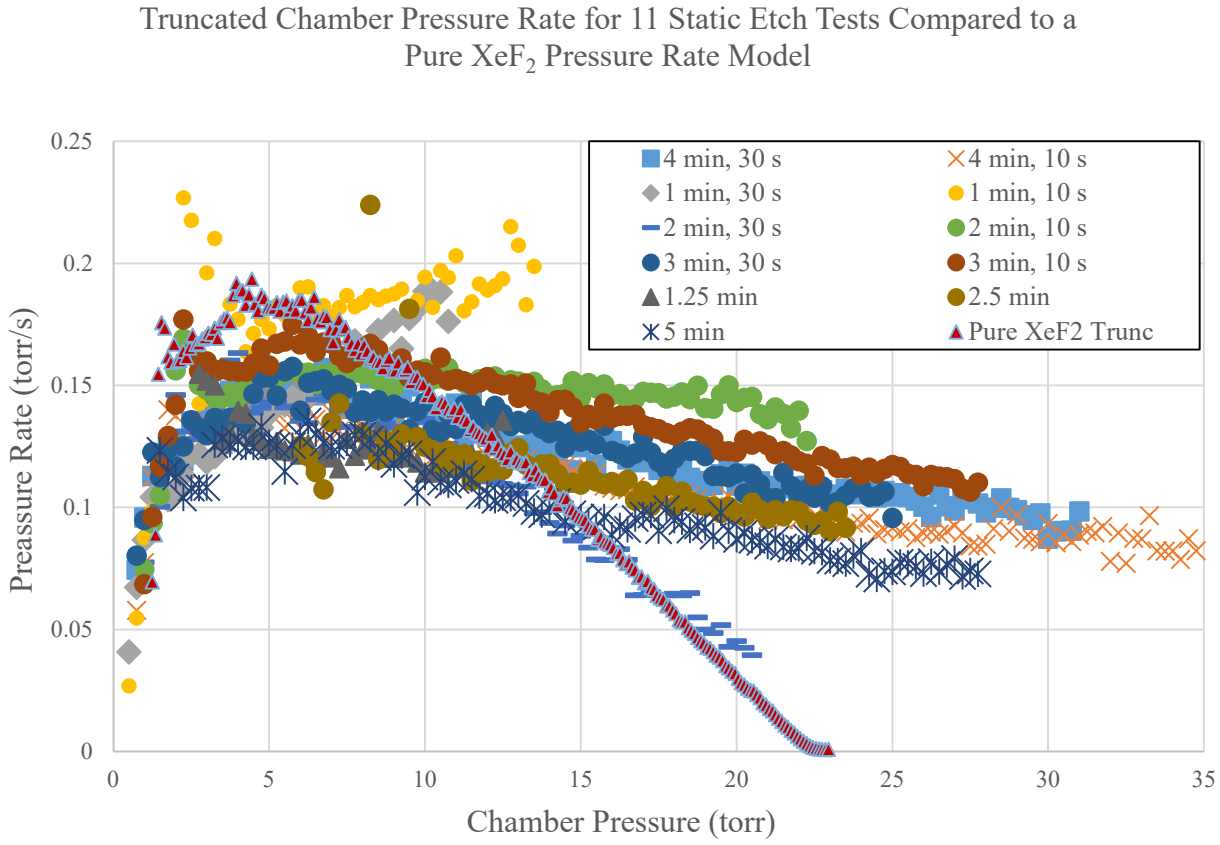

Figure 3.11: Pressure rate plot for 11 static etch experiments and pressure plot for pure XeF2 sublimation at commensurate temperature and effluence area.

insufficient data. The maximum and minimum pressures reached in each cycle of the 12 static etch experiments are shown in Figure 3.12 and Figure 3.13, respectively.

There were several interesting observations from the above figures that should be pointed out. The pressure rate plot, even without the differential W mass data, demonstrated that etching did occur. The 20 min sublimation experiment data on the maximum pressure data set helped produce an analysis of how the static etch method might be useful in a use case propellant delivery system for electric propulsion. Two traces on the minimum pressure plot helped explain the reason why etch efficiency was not ideal.

The first observation was that the pressure rate curves in Figure 3.11 did not approach zero

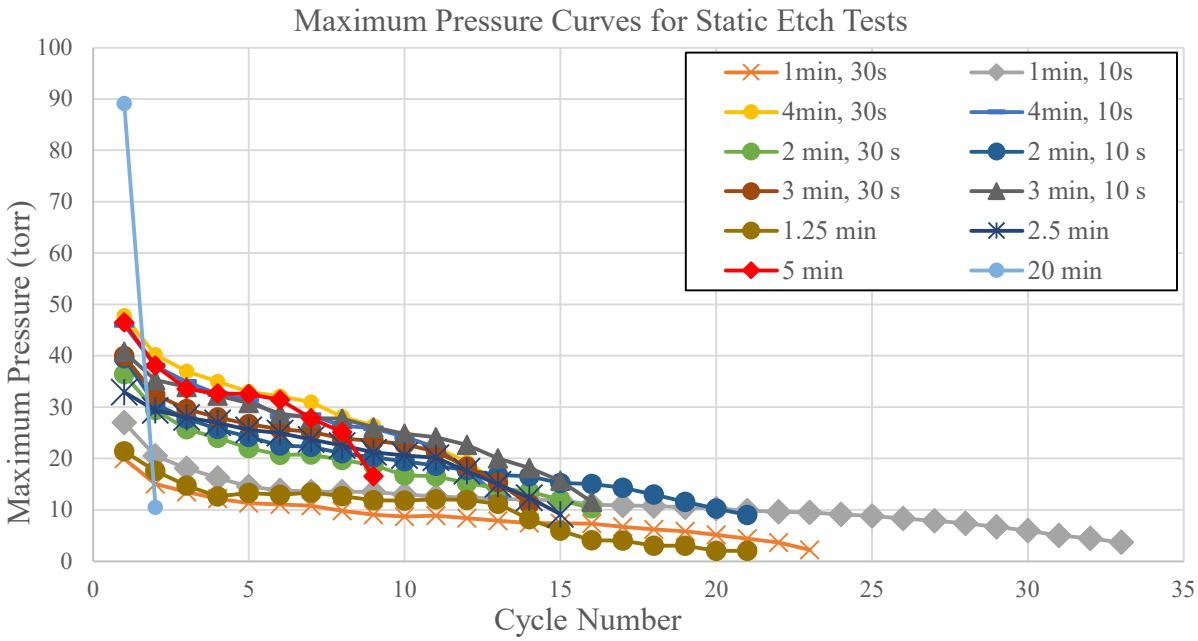

Figure 3.12: Maximum pressure reached during each cycle of each of the 12 static etch experiments.

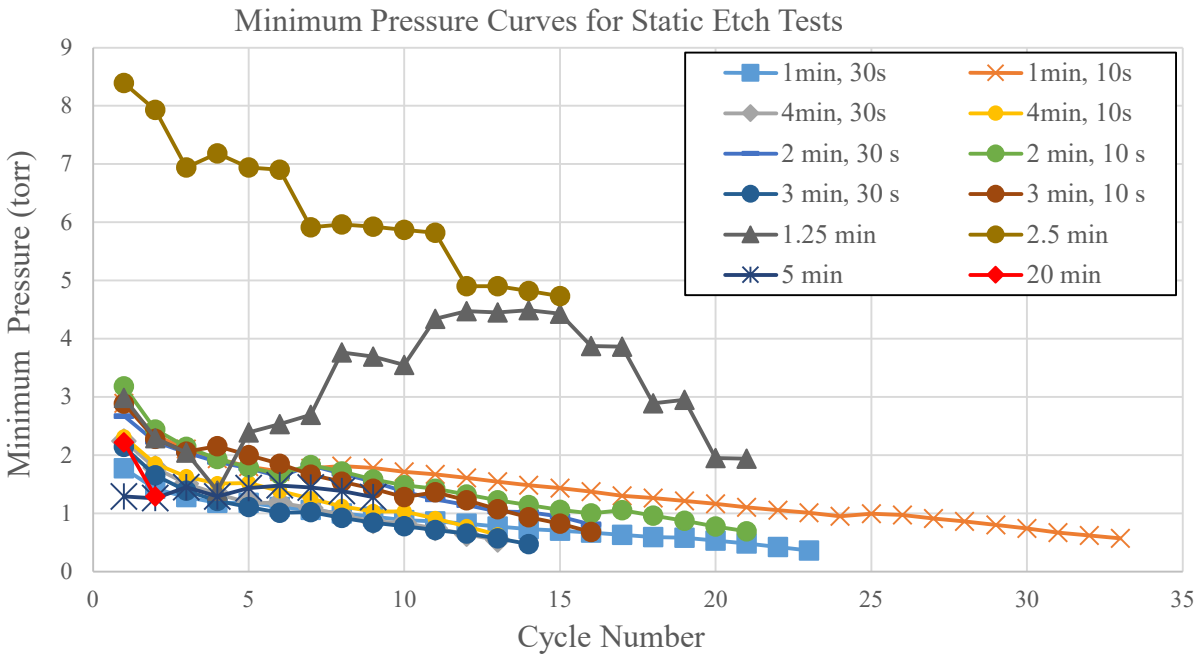

Figure 3.13: Minimum pressure reached during each cycle of each of the 12 static etch

experiments.

pressure change as the pressure became maximum. The effluence curves from the sublimation dynamics study (Figure 2.23 through Figure 2.26), which were derived from pressure rate curves, all showed the same behavior of effluence approaching zero as the maximum pressure was reached. This was because sublimation effectively stopped as the vapor pressure was reached (pressure can continue to rise as was discussed in Chapter 2). The static etch experimental results show different behavior, however, because although sublimation had also stopped (vapor pressure exceeded), the pressure continued to rise due to the etching of W.

The second observation was that the maximum pressure for the 20 minute etch time experiment was nearly double that of any other experiment on its first cycle (89.1 torr) and then dropped to only 12% of that value on the second cycle. The first cycle was also ~4 times higher than the average maximum pressure reached during the sublimation dynamics experiments with the same nominal temperature (it also ran 33% longer than the sublimation test). This significantly higher pressure reached clearly demonstrated that the XeF_2 was indeed reacting with the W to create an environment well in excess of the vapor pressure of the crystals. Indeed, the vapor pressure of WF_6 is in excess of 1 bar at 50 °C [75]. Had the experiment continued indefinitely, one would expect the pressure to continue to rise until a limit was reached. The limit would be dependent on how much XeF_2 could sublimate before the pressure in the chamber caused sublimation to cease. Then, assuming there was sufficient W for complete reaction, the XeF_2 would eventually completely react leaving only Xe and WF_6 gas remaining. The pressure would then be determined by the stoichiometry of the etch reaction and the mass of available F atoms (assuming ideal gas law). This observation gives a glimpse of how the etch reaction might be used in a pulsed flow propulsion system. This modality of propellant delivery would involve dosing an etching

chamber with XeF_2 from a sublimation chamber and then waiting until a complete reaction occurs. At that point, the resulting gases could then be flowed through a metering device to a propulsion system.

The third observation from the static etch plots was that the minimum pressure data was consistently within ±50% from the mean between experiments for all trials except for the 1.25 min and 2.5 min etch time trials. This was initially seen as an unfortunate lack of control of an independent variable but as it turns out these two trials helped formulate an analysis of etching efficiency for the whole experiment. The 1.25 minute experiment showed the fifth best efficiency by a margin of 65 – 104 % as compared to the two experiments conducted with 1 min etch time (most similar with the exception of minimum pressure) which had the two worst efficiencies. The 2.5 minute experiment showed the best efficiency overall and was superior by a margin of 69 – 112 % as compared to the four trials with the closest etch times. The major difference between these five trials was again the minimum pressure. Minimum pressure is effectively a representation of how well the etch products were evacuated from the etching chamber.

It has already been demonstrated that the gas being vented was composed of XeF_2, Xe, F, and WF_6 in unknown ratios. The fact that this vented gas still contained XeF_2 was the fundamental reason that efficiency was not ideal. Limiting the venting between cycles and having high minimum pressure accomplished three important things. First, it increased the amount of XeF_2 and F that stayed in the etch chamber after etching and, thereby, made it available for etching during successive cycles and improved efficiency. Second, it reduced the sublimation rate of XeF_2 that occurred at the start of the cycle. This lead to less XeF_2 being dosed into the chamber per cycle which improved efficiency by using the gas in more sparing amounts. Third, the higher minimum pressure lead to less ‘blow through’, that is, XeF_2 that sublimated while the vent valve was open

and immediately was vented out of the system. Blow through will clearly reduce efficiency by ensuring that some of the XeF_2 vapor will never have the possibility of interacting with the W for etching.

A correlation study was conducted between the six independent variables and the two dependent variables. The independent variables considered were: etch time, vent time, minimum pressure, maximum pressure, number of etch cycles, and total etch time. The two dependent variables considered were average etch rate and etch efficiency. Effective propellant density was a function of etch efficiency, therefore, this variable was not considered in the correlation study. This study resulted in 12 different plots which are shown in Figures 3.14 - 3.25. These results are presented for the sake of being thorough. The only interesting result that was seen from the correlation study between the independent variables and etch efficiency was that minimum chamber pressure was the most significant factor in predicting good etching efficiency which has already been discussed. This correlation had a an R^2 of 0.65 which was weak but the most significant of the 6 correlations. The most significant correlation between the independent variables and etch rate was the etch time which had a weak R^2 of 0.36. This result was not interesting because of how etch rate was calculated. Etch rate was simply the mass of W etched times its surface area and divided by the time and density of W. Simply put, the result shows what was already known which was the faster the etching process, the higher the etch rate.

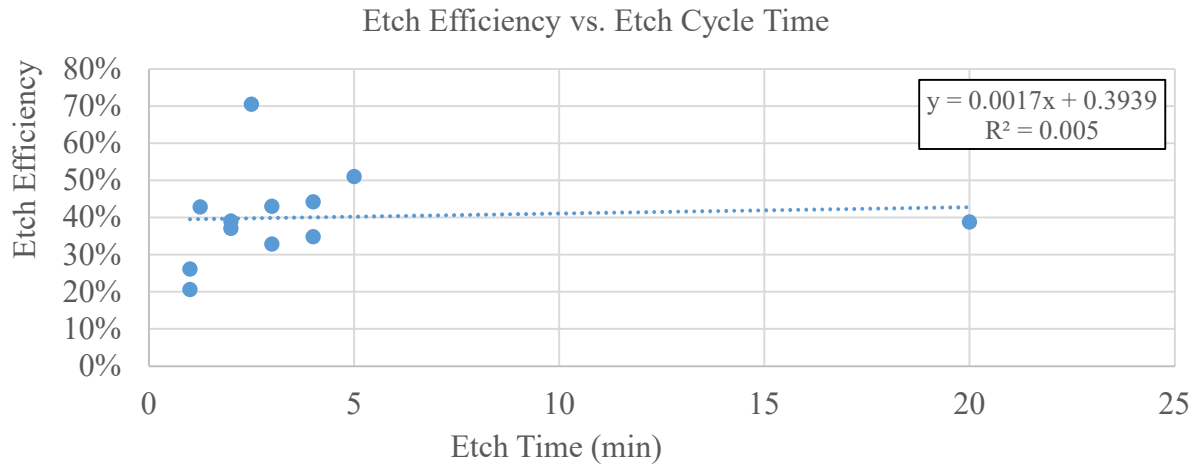

Figure 3.14: Etch efficiency versus etch cycle time.

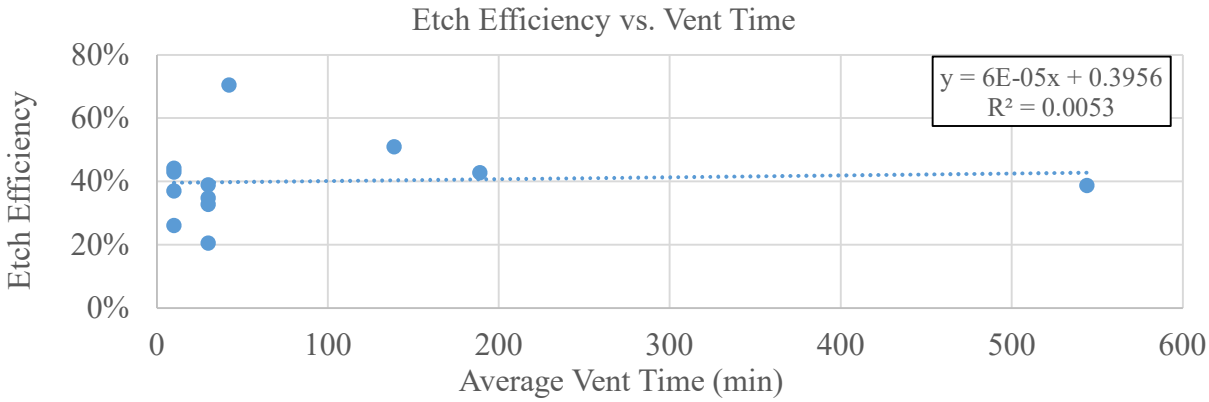

Figure 3.15: Etch efficiency versus vent time.

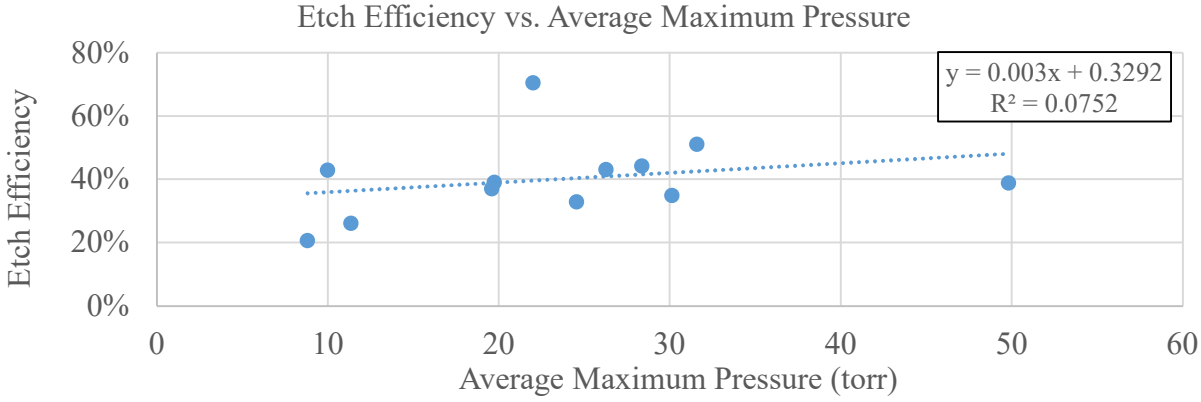

Figure 3.16: Etch efficiency versus average maximum pressure.

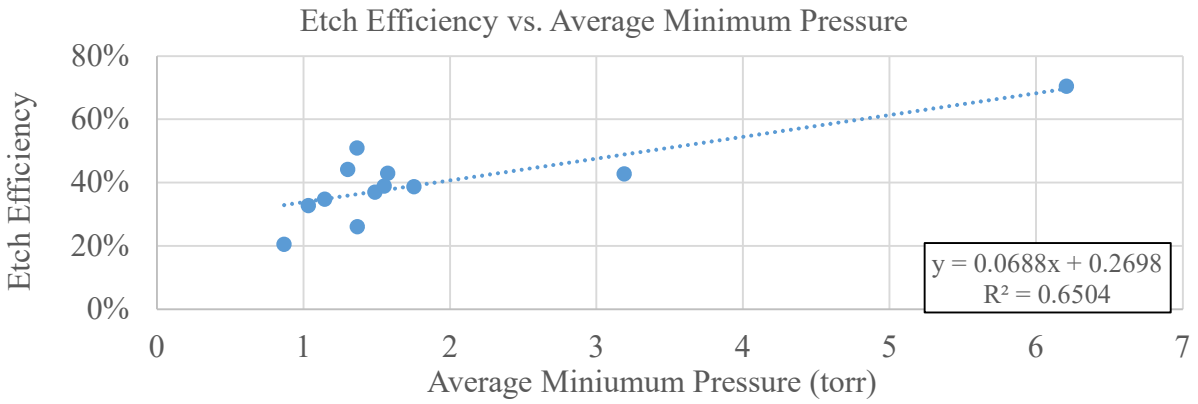

Figure 3.17: Etch efficiency versus average minimum pressure.

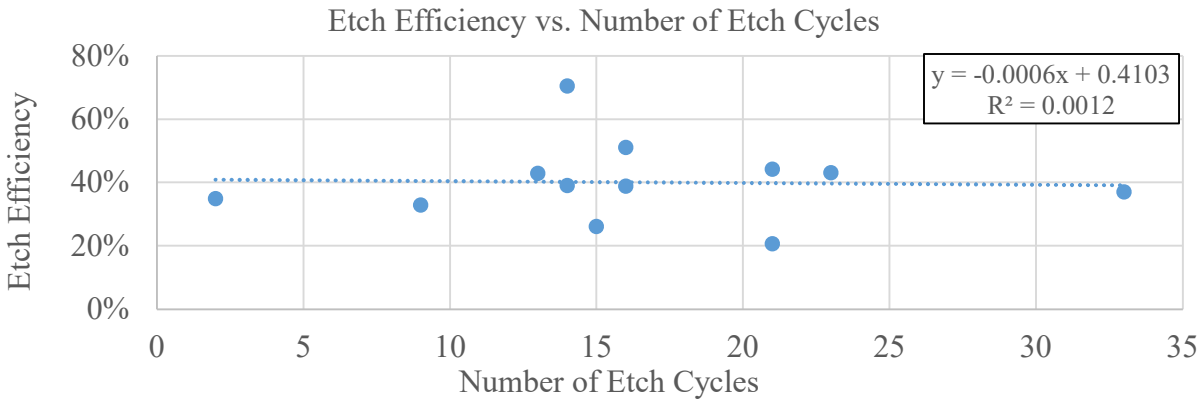

Figure 3.18: Etch efficiency versus number of etch cycles.

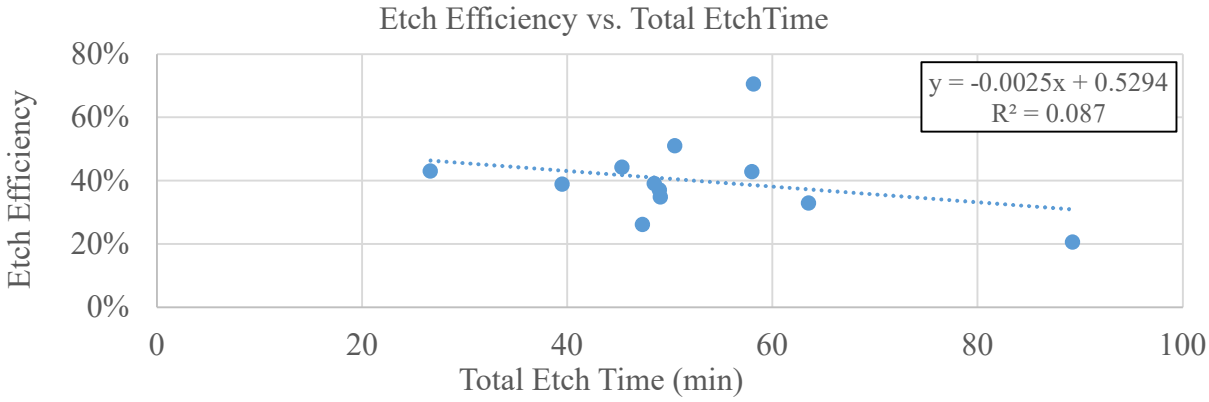

Figure 3.19: Etch efficiency versus total etch time.

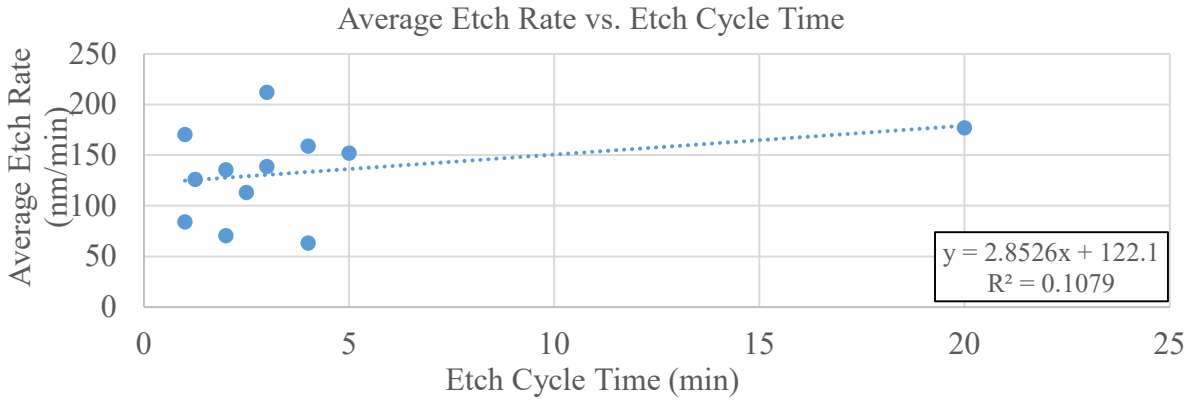

Figure 3.20: Average etch rate versus etch cycle time.

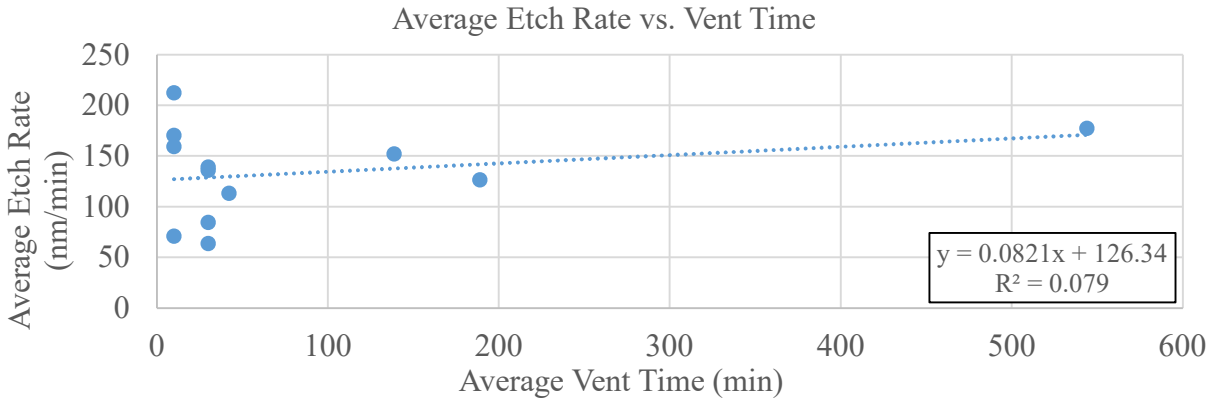

Figure 3.21: Average etch rate versus vent time.

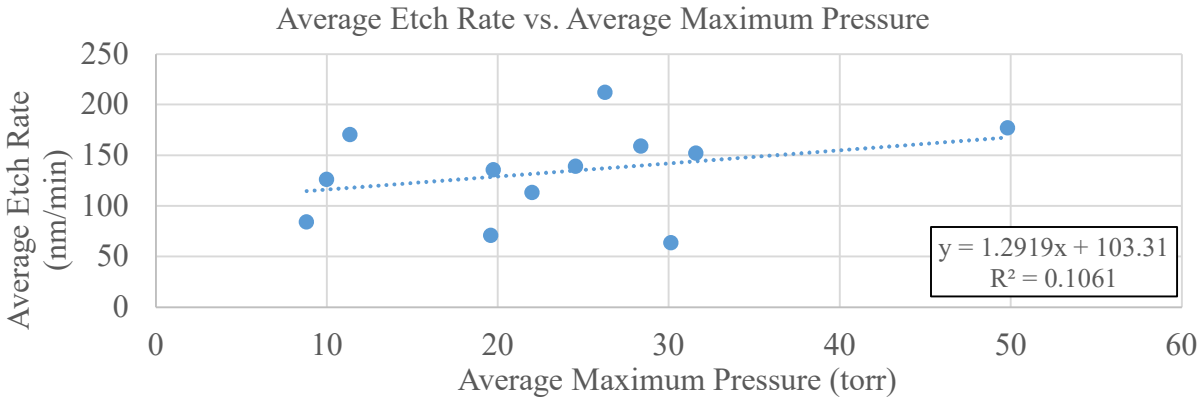

Figure 3.22: Average etch rate versus average maximum pressure.

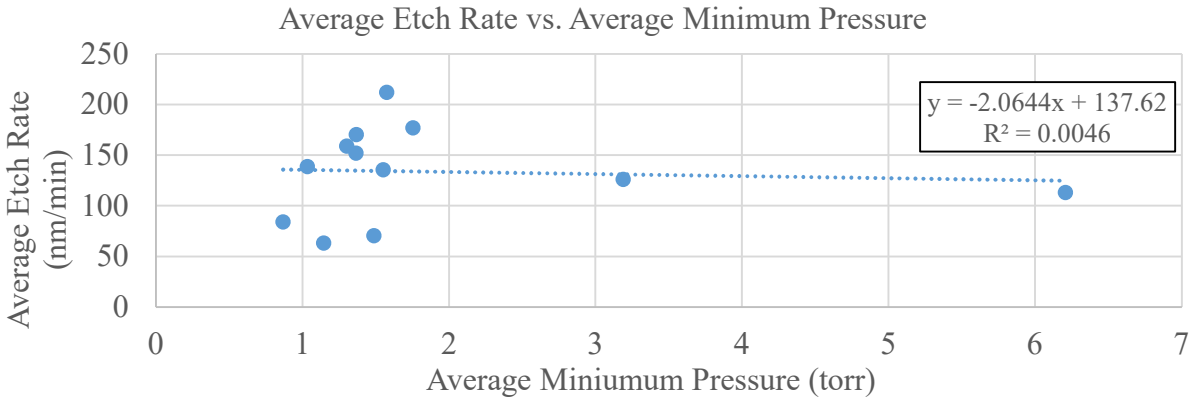

Figure 3.23: Average etch rate versus average minimum pressure.

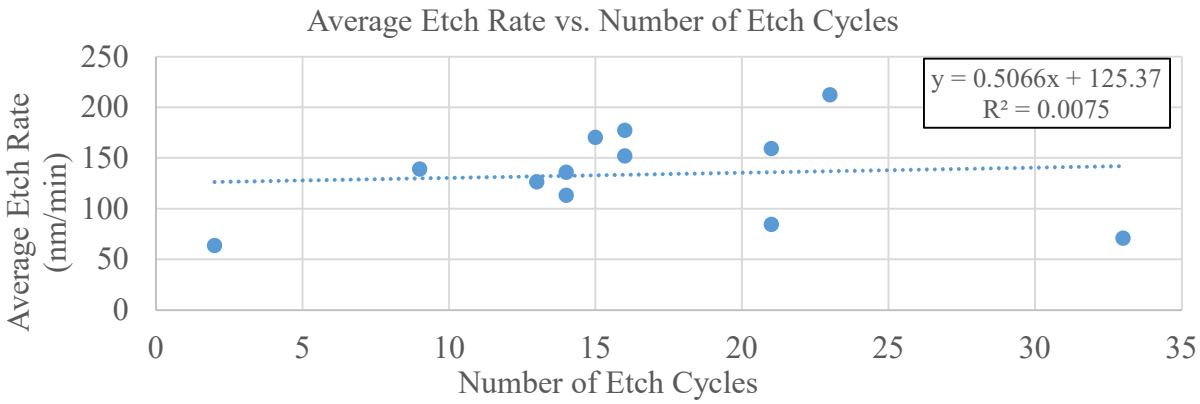

Figure 3.24: Average etch rate versus number of etch cycles.

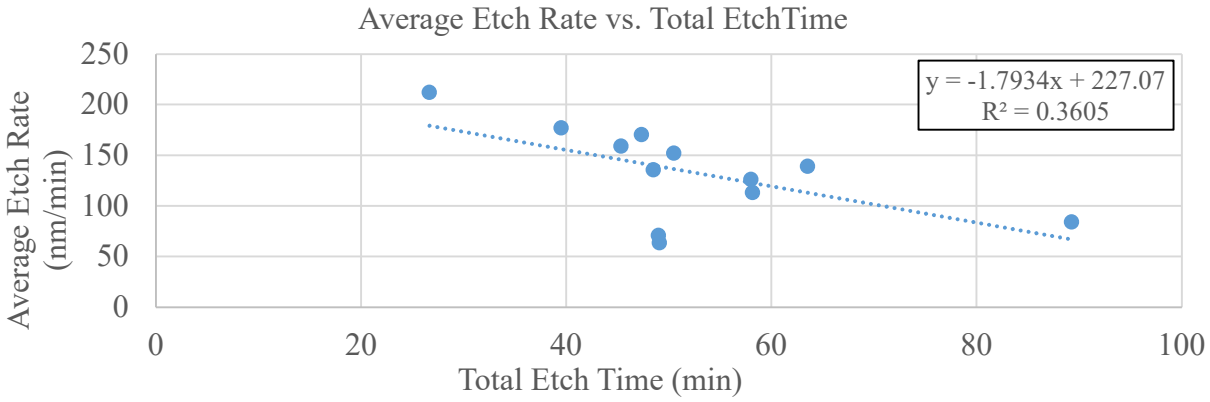

Figure 3.25: Average etch rate versus total etch time.

3.4 Tungsten Etching Conclusions

The objectives of the tungsten etching experiments were threefold. First, to confirm that W could be etched by XeF_2 at a sufficient rate to render the process useful in the proposed propulsion system use case. Second, to investigate the hypothesis that XeF_2 could etch W with sufficient efficiency to realize a storage density of reactants that would be superior to the state-of-the-art. Both of these objectives were successfully met. A third objective that emerged was to develop an understanding of the mechanisms or factors that affect etch rate for the sake of future work. This will be discussed in detail in the future work portion of this dissertation.

The etch rate of XeF_2 on W ranged widely over the experiments performed. However, the results did overlap with the rate reported in literature of 80 nm/min. The rate that was measured during the dynamic etching experiment ranged between 5 – 450 % of the result in literature. The rate measured during the static etch experiments ranged between 79 – 265 % of the result in literature. The very worst etch rate observed, which was too small to measure with the 0.010” flow channel dynamic etch experiment, yielded an average mass flux of W of 1.7 µg/s. The 0.040” flow channel dynamic etch experiment had a mass flux of 4.76 µg/s. The average mass flux for the static

etch experiments was found to be 8.2 ± 1.6 μg/s. All of these results were still in excess of the target mass flux of 1 μg/s. The conclusion of the tungsten etching experiments was that XeF_2 can be used to etch W at more than a sufficient rate to be useful as a propellant stream in an electric propulsion system. Furthermore, physical scale of the apparatus was reasonably small and could, with sufficient development, be made suitably sized for integration with a small spacecraft.

The static etch experiment produced a result that had a hypothetical propellant storage density that was greater than the current state-of-the-art for high density propellant storage which is crystalline iodine (density = 4.933 $g.cm^3$). This was simply based on the fact that the mass of XeF_2 and W that were vaporized were originally stored as solids that had weighted average density in excess of the state-of-the-art. There are, of course, mass and volume overhead that was not accounted for in this calculation. This, however, is no different than on a real spacecraft that would also have mass and volume overhead in their propellant storage and delivery systems. The real result was that the etching of W by XeF_2 was demonstrated at sufficient efficiency to provide an existence proof that this combination of materials exceeds the storage density of iodine under certain conditions. The maximum etching efficiency observed was 70% which yielded a theoretical storage density of 5.13 g/cm^3 (shown in Table 3.1) as compared to iodine (density of 4.93 g/cm^3).

4. LTCC Electrostatic Thruster

The Low Temperature Co-Fired Ceramic Electrostatic Thruster (LTCC-ET) was the first known electrostatic ion thruster prototype based on LTCC manufacturing technology. Its design, materials, and manufacturing selection enabled the parallel fabrication of all the requisite subsystems (internal propellant ionization / plasma cavity, excitation electrodes, and accelerating electrodes) to produce a monolithically-integrated thruster. The successful development of a LTCC-manufactured propulsion system could revolutionize the area of deep-space small satellites by providing a scalable low-cost, low-volume, and high-performance in-space propulsion system architecture. It can enable new capabilities in mobility for small-satellites, especially those at nanosatellite sizes; which are crucial to NASA's goal of utilizing small-satellites for future planetary and deep-space missions. The system could also allow for a new architecture of electric propulsion that could provide thrust vectoring and eliminate the need for a neutralizing spray, thereby reducing overall system complexity.

The first goal in development of the LTCC-ET was to investigate manufacturability and determine if a 'thruster like structure' could be created with the LTCC materials system. The second goal was to investigate the nominal function of prototypes and explore technology feasibility. The first goal was successfully met by creating three functional prototypes and a benchmark fabrication process that could be used to create modified and improved LTCC-ET iterations. The secondary goal was successfully met through a partnership with NASA's Marshal Space Flight Center (MSFC) where prototypes were evaluated in MSFC's electric propulsion testing facilities. This testing provided information on the nominal operational parameters of prototypes and important design feedback for future iterations. The two goals of the LTCC-ET development were successfully achieved and have laid the groundwork for the successful development of future designs.

4.1 Prototype Design and Fabrication

The fabrication of four LTCC-ET prototypes was attempted and three of those attempts were successful. The fourth prototype fractured during fabrication. The physical design of the thruster was not optimized or even studied in terms of its performance as a thruster because the opportunity to attempt fabrication was unforeseen and short-lived. In the summer of 2015, the Huang research group hosted an NSF Research Experience for Undergraduates (REU) intern, Seth Vaughan. At the time, Seth was an undergraduate in Mechanical Engineering at the University of Arkansas. The REU program provided funding for materials and lab supplies, which was matched by the High-Density Electronics Center (HiDEC), and these funds were spent on prototyping the LTTC-ET. The thruster was designed and built over six weeks during this summer program.

The idea to use LTCC technology to create a thruster was already being investigated as part of the research for this dissertation but the hands-on design phase was only afforded one week. This very short design window was the reason there was not more effort put into design or optimization. The criteria for success at the time was to develop a reliable fabrication process that could be used to build a ‘thruster like structure’. The need for such a test was due to the fact that the LTCC-ET was a complicated mechanical structure and it was unknown if it could even be fabricated successfully. The biggest challenge to overcome was to design a plasma cavity structure that would not collapse during the high-pressure lamination process. The embedded electrodes were straight forward to design and the only consideration was how to design them to avoid interlayer delamination of the LTCC structure. The manufacturing experiment was very successful as it led to the creation of three functional prototypes. These prototypes were the largest and most complex LTCC devices ever built at the University of Arkansas at the time (Summer 2015).

The LTCC-ET was conceived to address three specific design constraints. These

constraints were imposed by the intended use case of an interplanetary small satellite with significant delta-V requirements. First, the thruster should be fuel-efficient and have a high specific impulse (I_{sp}). The two factors that affect a spacecraft's delta-V are mass fraction for propellant and the I_{sp}. Because mass fraction for propellant is an independent factor in a spacecraft design, improving the I_{sp} is the only way this work could improve delta-V for the intended use case.

Second, the thruster should be compact to be suitable for integration in a small satellite. Small satellites have allowable volume at a higher premium than mass in their design budgets. This is primarily because small satellites are deployed as secondary payloads on larger spacecraft missions and typically have to conform to a predetermined size or form factor, the most common of which is the CubeSat form factor. For this reason, the goal for the LTCC-ET was to be as dense and compact as possible.

Third, the thruster should be durable in order to survive firing for hundreds or thousands of hours. Small satellites are inherently low powered and don't typically have a large power budget for operating a thruster. This is why chemical or cold gas propulsion is the most common form of propulsion on small satellites. The drawback is that these types of propulsion cannot approach the efficiency of electric propulsion (EP). Spacecraft with EP must operate them at low power levels (relative to the rest of the spacecraft's power consumption) which in turn leads to low thrust. In order to achieve a large delta-V, these spacecraft must burn their engines for a very long time because delta-V is proportional to the product of thrust and burn time. For example, a 10 kg CubeSat with 1 kg of propellant producing 20 μN of thrust at a specific impulse of 1000's could generate 1034 m/s of delta-V but would take ~550 days to do so. This simple calculation illustrates the need for a durable thruster and so the LTCC materials system was chosen for its durable qualities as it is ceramic. Furthermore, the most readily destroyed elements of the thruster, the

ionization antenna and the screen and accelerating electrodes, could be embedded in the ceramic to further protect them and increase thruster lifetime. These constraints led to the LTCC-ET design.

The LTCC-ET thruster's design was based on the work by Goebels and Katz in their book on electric propulsion [63]. There are two major types of electric thrusters, electrostatic and Hall. Broadly speaking, Hall thrusters use magnetic forces to ionize and accelerate propellant and electrostatic thrusters use electric forces. Electrostatic thrusters are more efficient and have higher specific impulse but are less durable than Hall thrusters. However, Hall thrusters are more popular because of their longer operational lifetime and greater amount of flight heritage.

Hall thrusters use magnetic fields that must be generated by magnetic coils which tend to be large and inefficient at generating high magnetic fields because magnetic conductors (high permeability materials) are heavy and inefficient and large currents are needed to generate the fields. Conversely, electrostatic thrusters only need small conductors to generate electric fields and these fields are easy to shield with conductors. The durability of Hall thrusters is because most of the thruster's physical structures are insulated from plasma by a magnetic field and so there is little impingement of ionized species on the thruster itself. Conversely, electrostatic thrusters accelerate propellant by passing them through a charged grid and this grid is regularly impinged upon by ionized species which leads to erosion over time. The selected design architecture was an RF electrostatic ion thruster and was chosen because it is compact. In this architecture, propellant is ionized using RF energy in a cavity and is accelerated with electrostatic forces. The innovation of the LTCC-ET was that it used the more efficient and compact electrostatic architecture but insulated its electrodes from plasma erosion by embedding it in a ceramic material. A schematic of the essential portions of the LTCC-ET as well as how each electrode was wired is shown in Figure 4.1.

The thruster was composed of two fundamental elements: the electrical structures and the physical structures. The entire thruster was composed of numerous green tape sheets, which will become a monolithic ceramic structure after firing, and numerous metallized layers and vertical

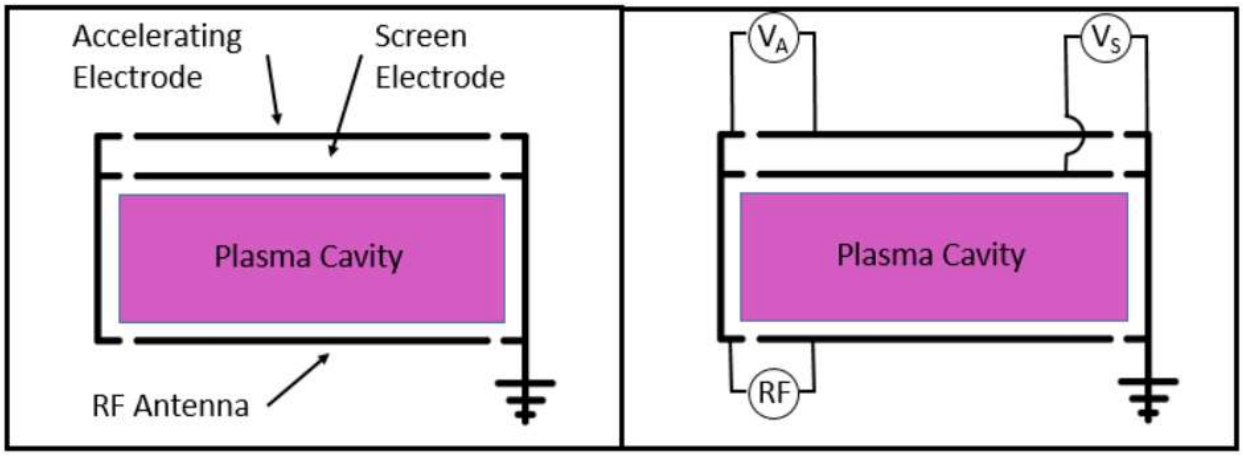

Figure 4.1: Schematics of the LTCC-ET. Left: functional diagram of the primary elements of the thruster. Right: Wiring schematic of the thruster.

interconnects, or vias. Each green tape layer had at least some cavities or holes punched out of it and metal filled vias. There were additionally four layers that had metal paste screen-printed on them which turned into flat conductors after firing. There were seven unique green tape layers that formed the entire structure, electrical and structural, of the LTCC-ET and a schematic of those seven layers is shown in Figure 4.2.

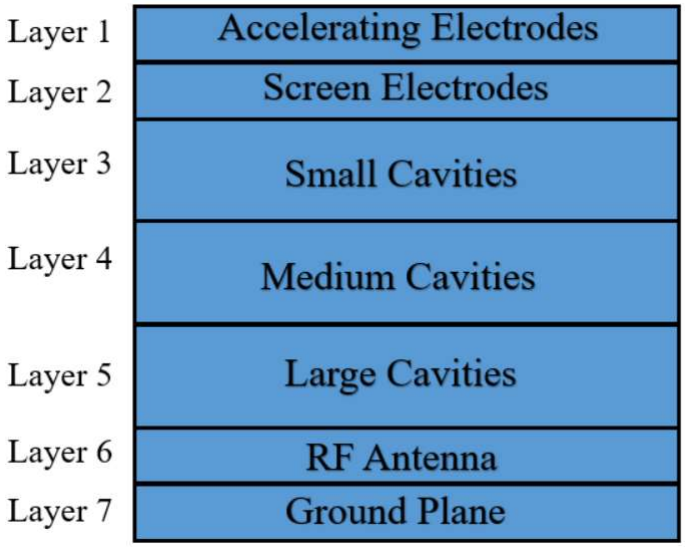

Figure 4.2: Schematic of the 7 distinct layers that together form the LTCC-ET.

The electrical structure of the LTCC-ET was composed of five distinct elements: an RF patch antenna, a screen electrode, an accelerating electrode, a via post-wall, and a ground plane. These elements together formed the plasm cavity and the propellant acceleration stage of the thruster. The plasma cavity was a conductive cage which confined RF energy so that it could be delivered to propellant to form a plasma. The plasma cavity was electrically defined by the RF antenna on the bottom, the screen electrode on the top, and the via post-wall around its perimeter. The post-wall was not a contiguous conductive wall but rather a wall made of vertical grounded conductors that were spaced close enough so that they could effectively contain electromagnetic energy at the desired frequency of operation, in this case 915 MHz was the intended frequency (although the cutoff frequency of this cavity was in excess of 10 GHz).

The post wall, antenna, and screen electrodes were all embedded in the ceramic to form a monolithic structure. The screen electrode was virtually identical to the antenna but had propellant outlet orifices and was held at a positive DC potential during operation. Both of these electrodes spanned the entire thruster structure but were laminated between layers of green tape. Each

electrode had numerous voids cut out of it so that the ceramic on top and bottom could bond together and avoid delamination at these discontinuities in the ceramic stack.

The second stage of the thruster was the accelerating stage and was composed of propellant outlet orifices and an accelerating electrode. The orifices were simply holes in the green tape. The accelerating electrode lay on the top of the entire thruster and did not need voids cut out of it because there was no issue of ceramic delamination on the top. The bottom of the thruster had a ground plane, which also did not need delamination voids and propellant inlet holes. The electrode was virtually identical to the antenna and screen electrode but was held at a negative DC potential during operation. A CAD model depicting the electrical boundaries of the plasma cavity is shown in Figure 4.3. Renderings of the four metallized layers in the LTCC-ET are shown in Figure 4.4.

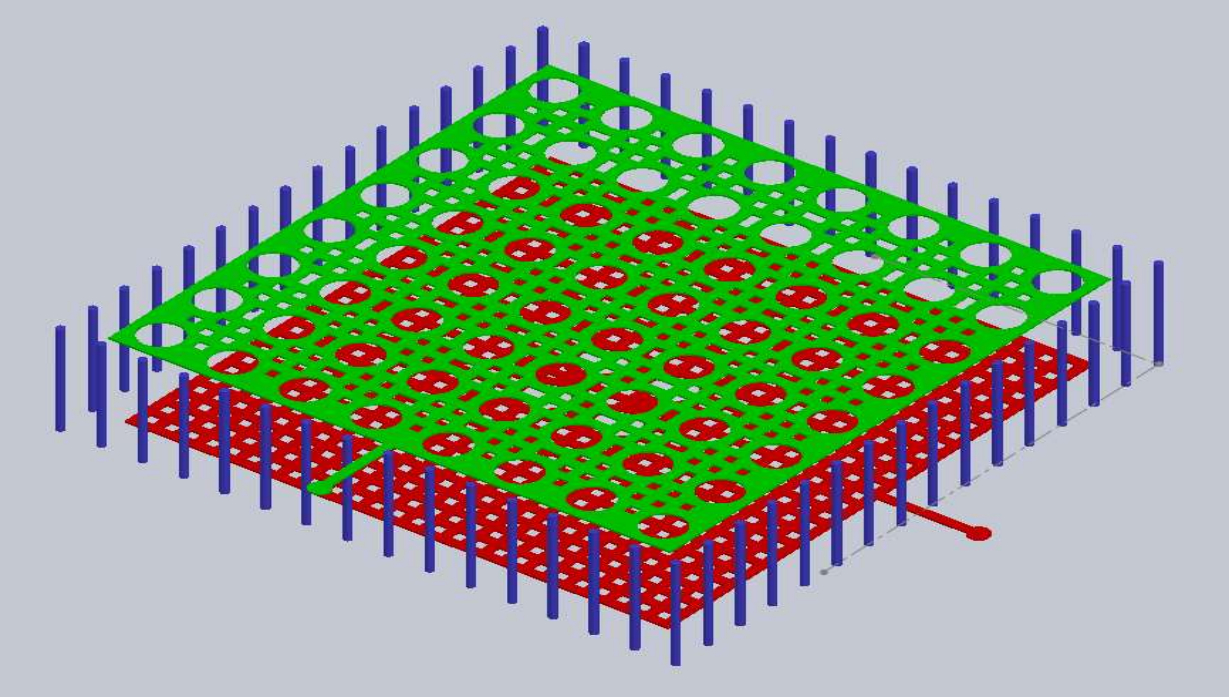

Figure 4.3: CAD model of the plasma cavity with ceramic removed and color added for visual clarity. The red structure is the RF antenna, the green structure is the screen electrode, and the blue structures are the via post-wall.

The physical structure of the LTCC-ET was composed of four primary elements: the

thruster structure, the propellant inlet ports, the propellant outlet ports, and the plasma cavity. The thruster structure was simply the agglomeration of all of the peripheries of all of the layers in the thruster which created a frame around the thruster. The propellant inlet and outlet ports were simply holes into and out of the internal cavity of the thruster. The inlet port was composed of four 0.090" diameter holes. The outlet ports were composed of an 8X8 array of 0.090" orifices. The plasma cavity served two functions. First, the cavity provided a space for the propellant to be ionized. Second, the cavity provided a gas distribution manifold to direct propellant to each of the outlet orifices. The gas distribution manifold was created by numerous interdigitated cavities or voids of varying sizes that were punched into the green tape. The arrangement, shape, and size of those voids was conceived to try to maximize the open internal volume of the plasm cavity while still

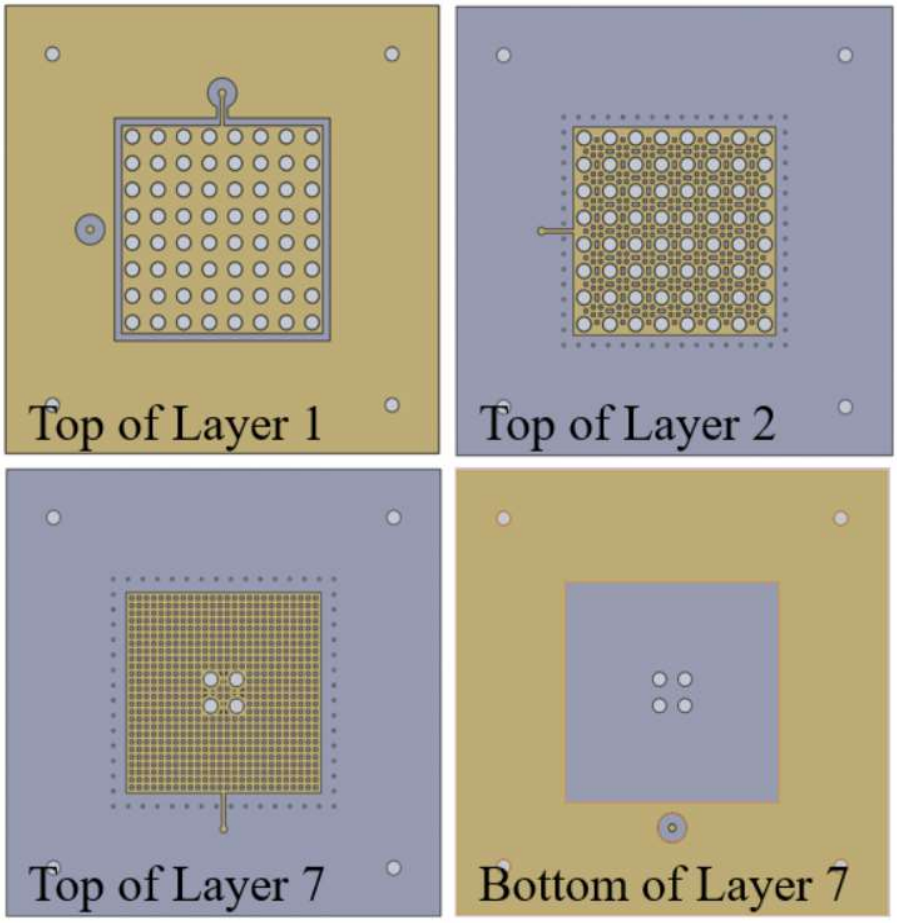

Figure 4.4: Renderings of all metallized layers in the LTCC-ET. Upper left is the accelerating

electrode and interconnect for the screen electrode with propellant outlet holes. Upper right is the screen electrode with propellant outlet holes. Lower left is the RF antenna with propellant inlet holes. Lower right is the ground plane, RF interconnect for the RF antenna and propellant inlet holes.

maintaining structural integrity to prevent collapse during manufacturing. All seven layers of LTCC had holes punched out which all contributed to the internal voids of the structure. The summation of these voids collectively formed all of the thruster's internal structures. A CAD rendering of the contribution of all seven layers of the LTCC-ET for the internals is shown in Figure 4.5. Renderings of the physical hole / void layout of all seven layers are shown in Figure 4.6.

Prototype fabrication was conducted at the LTCC lab at the University of Arkansas High

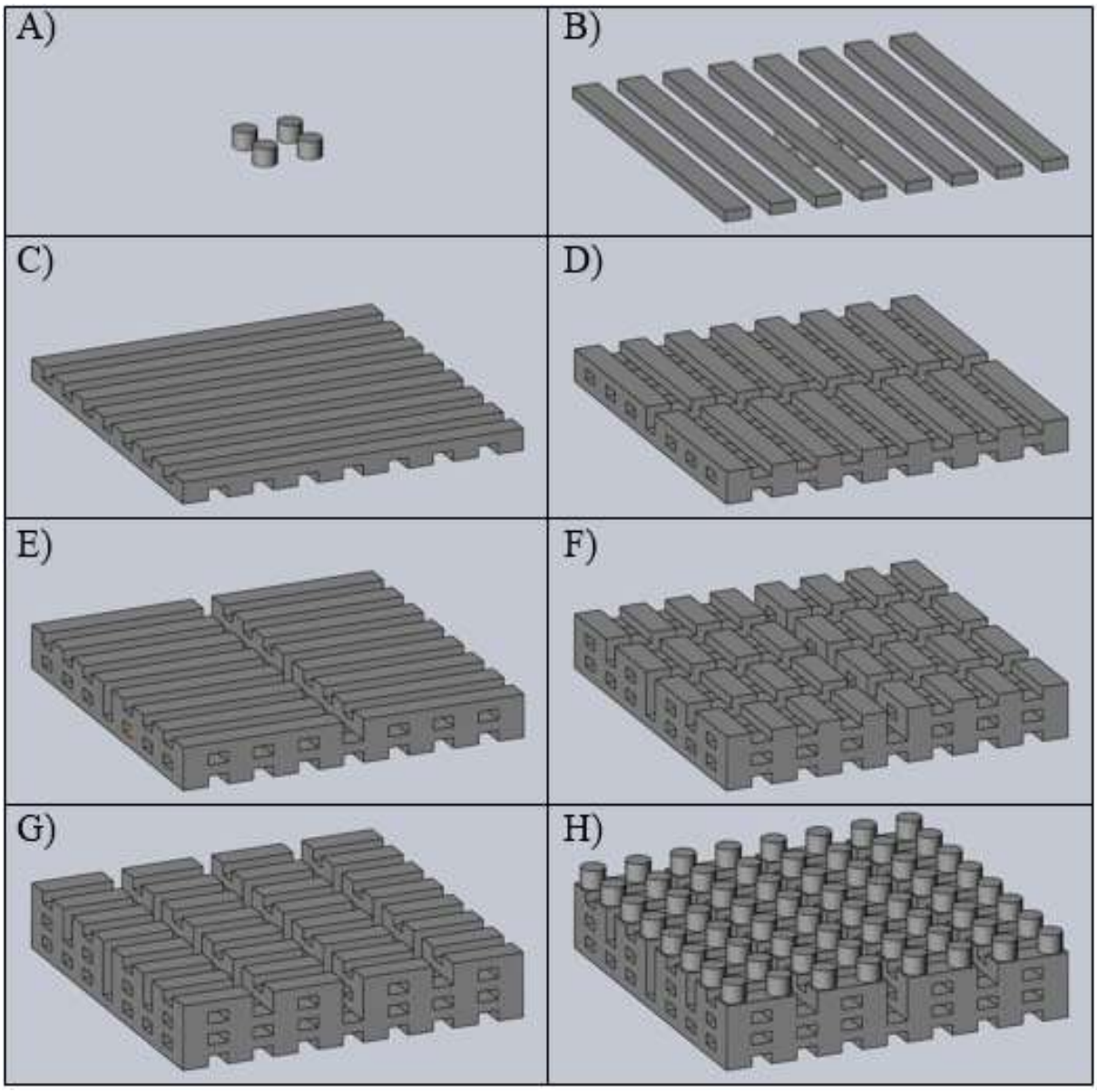

Figure 4.5: CAD visualization of how the internal cavities in the LTCC-ET add up to form a propellant manifold, plasma cavity, and propellant outlet ports. A) Start with propellant inlet ports B) Add the first Layer 5 C) Add the second Layer 5 D) Add the first Layer 4 E) Add the second Layer 4 F) Add the first Layer 3 G) Add the second Layer 3 H) Add the propellant outlet ports

Density Electronics Center (HiDEC) in the summer of 2015. Four prototypes were built in the

pursuit of a successful fabrication process. The first prototype cracked after it was fired and was used to test soldering methods for attaching RF and high voltage connectors. The LTCC-ET design contains seven distinct layers of green tape. There were multiple sheets of each layer. There were

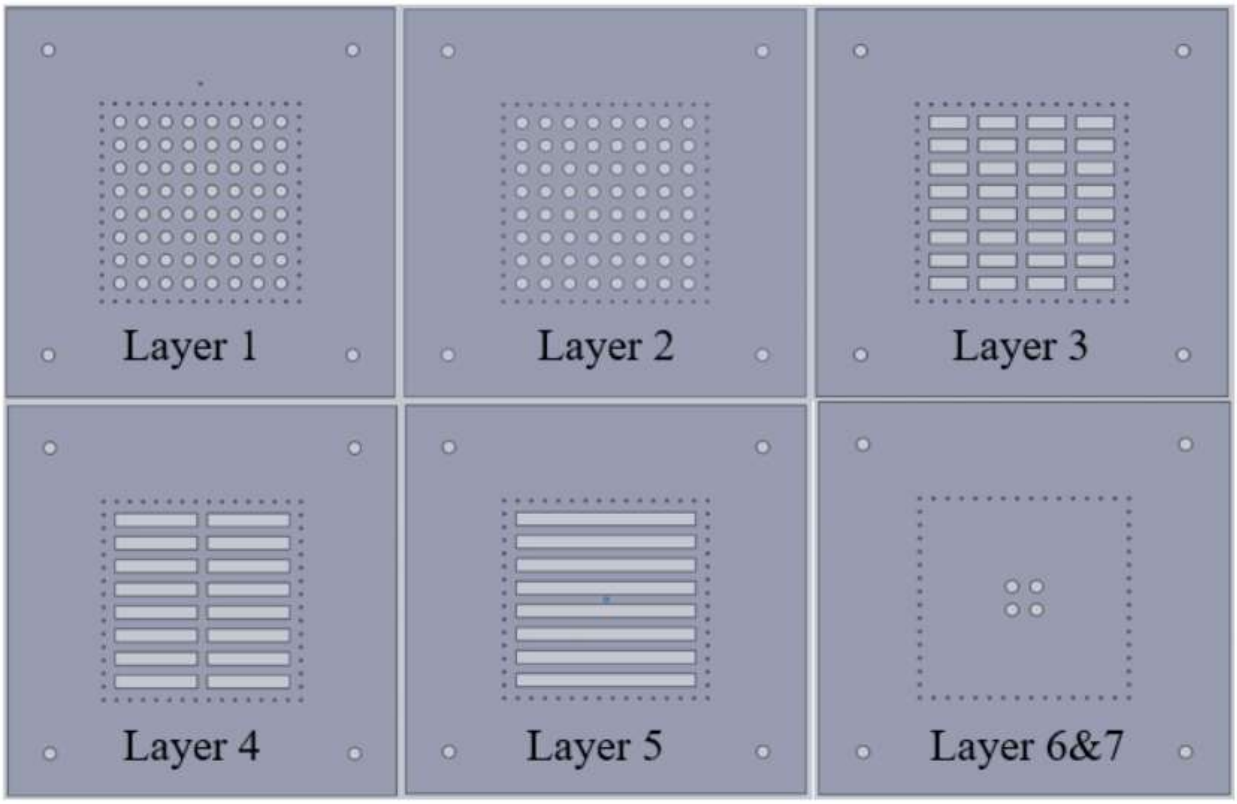

Figure 4.6: CAD renderings of all seven structural layers in the LTCC-ET.

also four distinct metallization layers. Additionally, every layer contained the same layout of vertical interconnects (this created the via post-wall through the entire device), but only a single metallized sheet per layer. The sequential stack-up was as follows. Layer 1 contained an accelerating electrode, discharge orifices for propellant, and an interconnect via to make connection to Layer 2. There were six 10 mil thick instances of Layer 1, the topmost of which contained the screen-printing for the accelerating electrode. Best results were obtained when the accelerating electrode was screen-printed and fired after the co-fire process. There was a single 10 mil thick instance of Layer 2 containing the screen electrode and propellant discharge orifices. The

screen electrode also served as an RF ground for the ionization chamber. Those seven layers were laminated to form a sub assembly.

Layers 3-5 formed a structure comprised of the ionization chamber and a propellant gas manifold. Each layer had different cavities built into them which, when stacked together, formed an interconnected cavity but all had the post-wall vias. The cavities consisted of interdigitated channels. There were two sets of Layer 3 composed of four 10 mil sheets of green tape. These were each laminated to realize two Layer 3 subassemblies. The same was true of Layers 4 and 5; two subassemblies of each Layer composed of four sheets of 10 mil green tape. The stack-up of the six subassemblies formed the plasma cavity and propellant manifold.

Layer 6 was composed of a single layer of 5 mil thick green tape and contained the via post-wall, the RF patch antenna, and propellant inlet channels. This layer served to isolate the antenna from direct exposure to the RF plasma. Layer 7 contained the propellant inlets, the RF patch antenna, an RF ground, the via post-wall, and an additional interconnect via to make electrical connection to the antenna. The Layer 7 stack-up was composed of six 10 mil layers of green tape. The topmost layer contained the antenna and the bottommost layer contained an RF ground and the RF interconnect via solder pad. Layers 6 and 7 were laminated to form the final subassembly. All subassemblies were then aligned and laminated to form the final device stack. The structure was then co-fired. All prototypes were manufactured using DuPont 9k7 LTCC Green Tape.

The final fabrication process was broken down into nine steps. First, all sheets and layers were punched out using a CNC punching tool to create cavities, orifices, and vias. Second, all via holes were filled with DuPont LL601 silver paste. Third, the internal metallized layers (Layer 2 and Layer 7 topside) were screen printed with DuPont LL612 silver conductor paste to form the

screen electrode and antenna, respectively. Fourth, all subassembly stack-ups were laminated at 3000 psi. Fifth, the eight subassemblies were stacked together and laminated at 2500 psi. It was critical to the design of the device that the the two instances of Layer 3, 4 and 5 had a 90 degree rotation between each of them. Sixth, the laminated stack-up was co-fired at 900℃ for 18 hours. Seventh, the accelerating electrode and ground plane conductors were screen-printed on Layers 1 and 7, respectively, using DuPont 6277 silver / palladium paste. Eighth, the final conductors were cured and sintered at 850 ℃ for 1 hour.

A summary in schematic form of the entire LTCC-ET stackup, including layer count, thickness, orientation, co-fire paste, post-fire paste, and lamination pressures, is shown in Figure 4.7. The first prototype attempt was successful but sagging was observed in the top layer (layer 1) and so more layers were added in subsequent designs. The second prototype had these extra layers but fractured during firing. This was determined to be due to built-in stresses caused by the use of

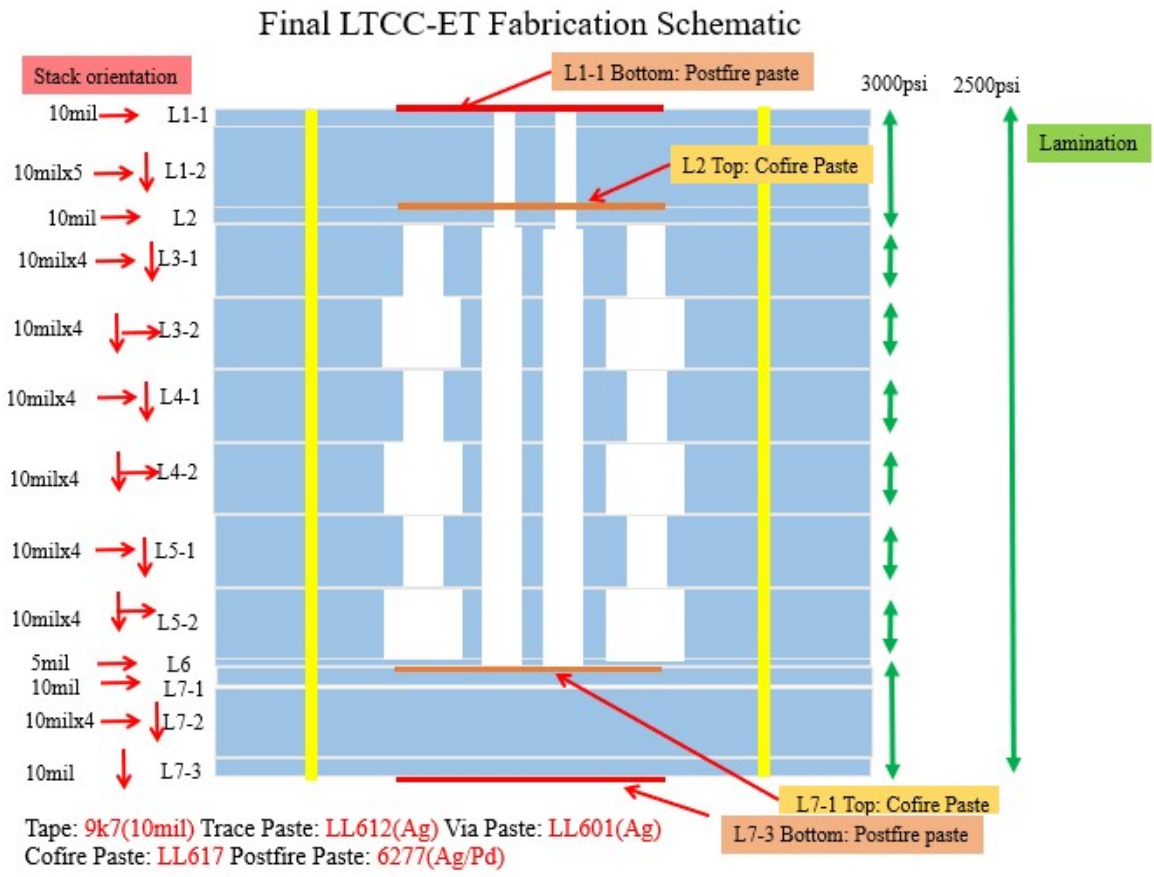

Figure 4.7: Final LTCC-ET lamination stack-up and fabrication schematic.

co-fire paste, that is metal paste that is fired with the ceramic material. The first successful device used post-fire paste and this was believed to be the most substantial difference between the two prototypes. To mitigate this fracturing issue the subsequent prototypes used a post-fire metallization method. This was the method used to create the final two prototypes, named Test Article 3 and Test Article 4.

The final device measured 2.75” on each edge, was 0.340” thick, weighed ~110 g, and had a volume of ~45 cm^3. This mass and volume could be reduced with design optimization. The LTCC thruster was not only the thickest device ever fabricated at the HiDEC labs but was also the first to incorporate internal cavities. Photographs of the LTCC-ET during fabrication and after firing

and final metallizationo are shown in Figure 4.8. A schematic of the prototype with the sagging issue is shown in Figure 4.9 and a schematic of the prototype that fractured during firing is shown in Figure 4.10.

In summary, the LTCC-ET design posed two unique challenges. First was the challenge to incorporate a plasma cavity in the design without having the device collapse under the extreme pressure of the lamination process involved in its manufacture. This was achieved by including additional sheets in Layers 1, 2, 6, and 7. Functionally speaking, those layers did not require

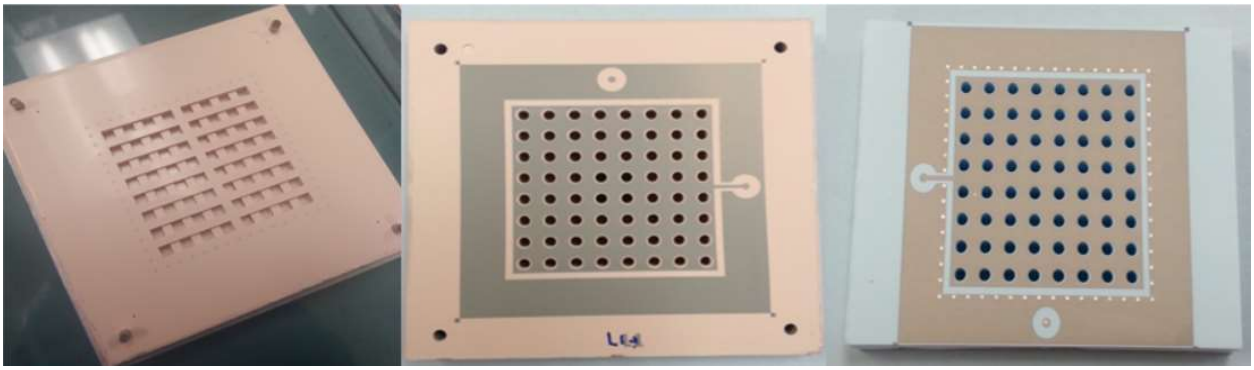

Figure 4.8: Photographs of the LTCC-ET during fabrication. Right: partially completed thruster stack showing internal cavities. Center: fully laminated device before co-firing of the ceramic. Right: fully complete device after co-firing.

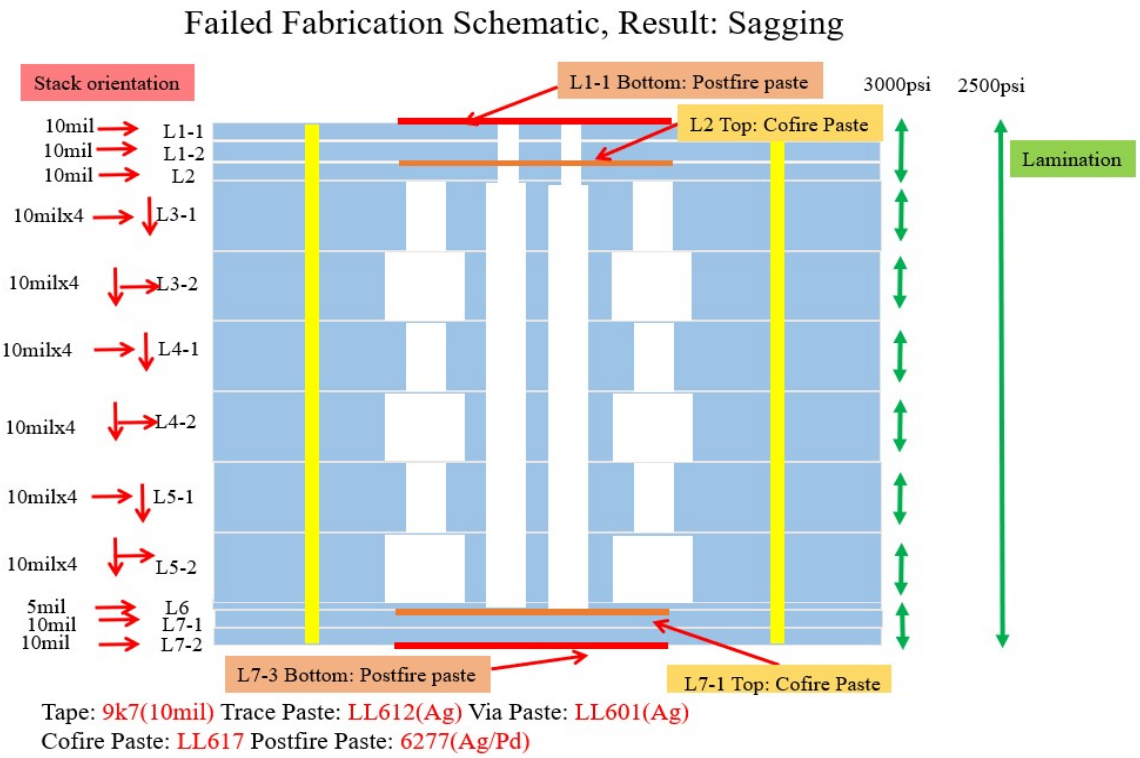

Figure 4.9: Lamination stack-up and fabrication schematic that led to failure by means of sagging of the topmost layers.

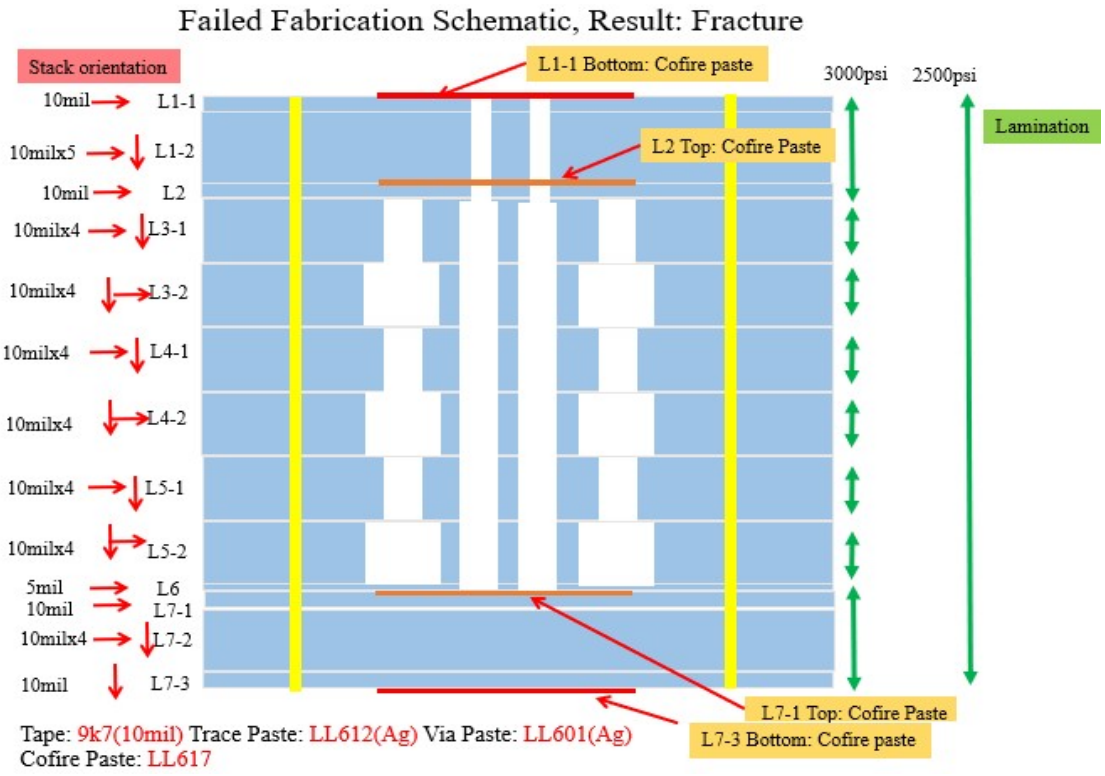

Figure 4.10: Lamination stack-up and fabrication schematic that led to failure by means of fracture.

multiple sheets, but eight sheets were incorporated during assembly to add structural integrity. Also, the interdigitated cavity design shown in Figure 4.1.5 allowed for 'pillars' of LTCC material to exist in the cavity to provide added support and prevent collapse. The second challenge was to minimize the thermal stresses in the device. Excess thermal stress was identified as the reason for the fracture during the assembly of the first prototype. For this reason, post-fire metallization was used to reduce thermal coefficient of expansion mismatch between the external conductors and the ceramic stack during firing. The fabrication process has been documented and may be used as design guidelines for successful manufacturing of future devices.

4.2 Thruster Testing

Prototype testing was conducted at the High-Power Plasma Propulsion and Diagnostics Laboratory at NASA's Marshall Space Flight Center (MSFC) in Huntsville, Alabama in June 2018. A cooperative agreement partnership (CAN), a type of cooperative grant funded by MSFC, was

established with MSFC because there were no facilities with sufficiently large vacuum chambers at the University of Arkansas to test electric propulsion systems. Additionally, MSFC lent their expertise to help plan and conduct testing activities. The testing activities were limited to only one week of work due to time and funding constraints. A work plan was established to try to achieve the testing goals. The plan was to first attempt to ignite a plasma in the thruster. This was done in an ad-hoc manner until nominal setpoints could be established to reliably ignite and maintain a plasma. The next part of the plan was to integrate the thruster on the thrust stand and instrument with thermocouples and Langmuir probes. The final part of the plan was to conduct characterization experiments. Unfortunately, the testing did not progress past the first step of determining nominal setpoints during the week of testing. While a plasma was successfully ignited, it would not reliably stay lit for reasons to be discussed.

The detailed goals of testing the LTCC-ET were threefold. The first goal was to determine the power requirements to ignite a plasma as a function of propellant flowrate. Flowrate has an impact on the power requirements because it affects the plasma chamber pressure. The test setup involved having propellant flow from the inlet ports, through the plasma chamber / gas distribution manifold, and out to the propellant outlet orifices into a vacuum chamber. The vacuum chamber's background pressure was on the order of $1x10^{-5}$ – $1x10^{-6}$ torr. As propellant flowed at higher and higher flowrates, the propellant outlet orifices restricted flow and this led to a rise in the chamber pressure. At too low of a pressure, it becomes difficult (takes very large electric fields) to strike a plasma because propellant species recombine after being ionized before they collide with other gas species and cause a cascade effect of mutual ionization leading to plasma ignition. At too high of pressure, it is difficult to strike a plasma because of the energy density required to sustain a plasma. Those were the bounding cases of plasma generation and there was an ideal (although

unknown) pressure for plasma ignition for the LTCC-ET.

The species used for most testing was argon which has a minimum ignition voltage of 214 V at a pressure distance product of 0.8 torr·cm for an electrode separation of 1 cm. The effective electrode separation was unknown because the plasma chamber was not uniform and the electrodes were buried in ceramic, both of which prevented calculating an ideal chamber pressure. Furthermore, there was no instrumentation on the LTCC-ET test articles to measure chamber pressure directly and if there was, it would not be uniform throughout the plasma cavity. For all of these reasons, it was determined that the first step in evaluating the LTCC-ET would be to first try to determine a flowrate (and thus chamber pressure) and input RF power combination that would lead to plasma ignition.

The second goal for testing was to measure thrust as a function of accelerating grid voltage (V_A) which is the voltage applied to the accelerating electrode relative to ground. This is related to the effective accelerating voltage (V_{eff}) which is the actual potential that the ionized propellant is accelerated through. V_{eff} is an important quantity because this is easily related to the I_{sp} of the thruster by the Equation 4.2.1, where T is thrust, $\dot{m}_p$ is the propellant mass flowrate, and g is the acceleration due to gravity on Earth, 9.81 m/s^2.

$$I_{sp} = {}^{T}/_{\dot{m}_p * g} \qquad \text{(Equation 4.2.1)}$$

The relationship between V_{eff} and V_A is dependent on several factors including thruster geometry, the screen voltage (V_s), the plasma density, propellant flowrate, and others. This relationship could be calculated by developing a multiphysics model of the entire thruster system. However, this process would be well beyond the scope of this research. By measuring thrust as a function of V_A and knowing the propellant mass flowrate ($\dot{m}_p$), a relationship between the primary independent variables of thruster operation ($\dot{m}_p$ and V_A) and the primary dependent variables of

operation (thrust and I_{sp}) could be determined. The link between V_A and V_{eff} is the ion exit velocity (v_{exit}) and this evident by Equation 4.2.2 and Equation 4.2.3, where q is the fundamental electron charge, and M is the molecular weight of the propellant. Solving these two equations for V_{eff} results in Equation 4.2.4 which is the link between V_A and V_{eff}.

$$I_{sp} = {v_{exit}}/{g} \quad \text{(Equation 4.2.2)}$$

$$v_{exit} = \sqrt{{2 * q * V_{eff}}/{M}} \quad \text{(Equation 4.2.3)}$$

$$V_{eff}(V_A) = {{v_{exit}}^2 * M}/{2q} \quad \text{(Equation 4.2.4)}$$

Substituting Equation 4.2.1 into Equation 4.2.4 yields the final expression of V_{eff} and the measurable parameters, thrust and flowrate, and independent variable, V_A, and as shown in Equation 4.2.5.

$$V_{eff}(V_A) = {T^2 * M}/{2q{\dot{m}_p}^2} \quad \text{(Equation 4.2.5)}$$

This empirical model would represent a 'holy grail' model of thruster operation and could then be used to study how the thruster could be incorporated into a mission context.

The third goal for testing was to determine if it was possible to accelerate electrons and positive ions in an alternating fashion. This was the most interesting testing goal due to its significant implications. The fact that the sides of the plasma cavity and the DC electrodes were insulated from the plasma by a layer of ceramic give them more durability. However, this fact also means that as positive ions are accelerated out of the thruster there is negative charge buildup as the electrons in the plasma have no path to ground. This could lead to 'poisoning' the plasma by making it too negative. Eventually, the plasma would extinguish if negative charge cannot be discharged. It was theorized that this could be avoided by periodically switching the polarity of screen and accelerating electrodes to expel electrons instead of positive ions. This had a significant

impact on the usefulness of the thruster for more than the obvious reason that the thruster wouldn't turn itself off periodically.

As a thruster pushes out positive heavy ions to generate thrust, the electrons stripped from the ions remain behind. This is true for all EP systems and, if not properly addressed, will lead to the spacecraft becoming negatively charged which can cause serious problems for the electronics, instruments, and payloads. More critically is that if a spacecraft is negatively charged, the positively charged propellant that is expelled will become attracted to the spacecraft and return and stick to it which would bring with it momentum and, thus, ruin the ability to generate delta-V. This problem is typically solved by using what is referred to as a neutralizing spray composed of an electron gun that fires electrons at the exhaust plume to neutralize the exhaust as well as the spacecraft. This method has been used for decades and works well. An innovation of the LTCC-ET is that it may be able to eliminate the need for a neutralizing spray if it could operate in the hypothesized mode of reversing its grid polarity periodically. The third goal was to investigate this hypothesis. These three test goals for the work done at MSFC were not met during testing due to issues with the test articles. However, significant insight into the design weaknesses of the LTCC-ET were identified and recommendations for future improvements were compiled. In the end, the progress made and the insights gained by the effort of the CAN certainly satisfied the overall goal of this research which was to evaluate the LTCC-ET and determine if the technology had sufficient merit to warrant further investment and development.

The LTCC-ET had to be packaged for testing before evaluation at MSFC. A custom package was designed and built to serve several key functions. First, the package provided a way to mechanically attach test articles to test fixtures such as a thrust stand. This structure was made of machined 6061-T6 aluminum and was a clam-shell design where the ceramic was sandwiched

between two halves that were bolted together. The contact surfaces between the ceramic and aluminum were padded by Grafoil™ high-temperature graphite gasket material. The package also provided structural support for RF, high-voltage, and propellant connectors.

Second, a propellant injection port provided a means to plumb test articles with gas. This port was also machined out of 6061-T6 aluminum. It sealed to the back of the ceramic thruster body with a custom laser-cut, 30 mil thick, buna-N rubber gasket. The port mounted to the main structure and was threaded to accept a ¼" NPT to compression connector. Third, there was Teflon plug in the front of the thruster that blocked the four center propellant outlet orifices to help increase the chamber pressure. This feature was added because the propellant injector delivered fuel straight into the plasma chamber which had propellant outlet orifices directly in front of the injectors. A photograph of the propellant injector is shown in Figure 4.11. This is a design flaw that was not considered initially as the prototypes were designed for a manufacturing experiment, not designed for test. Without this feature, propellant would simply flow with line-of-sight trajectories directly through the thruster and not build up enough pressure to light a plasma. The Teflon plug was sized so that the distance between it and the end of the injector was 0.005".

Figure 4.11: Photo of the propellant injection manifold.

Lastly, the test articles had electrical connectors soldered to the interconnects on the thrusters. The RF antenna was connected with an SMA connector and the screen and accelerating electrodes used MHV connectors. The completed LTCC-ET thruster packaging is shown in Figure 4.12. In total, three prototypes were packaged for testing and were referred to as Test Article 1 (TA1), Test Article 3 (TA3), and Test Article 4 (TA4). The enumeration of these test articles was based on their fabrication order.

The initial setup for ignition testing consisted of a signal generator, a RF amplifier, an isolator, a directional coupler, two spectrum analyzers, a matching network, and the test article. Inspection of the test articles determined that the spectrum analyzers and the matching network were not necessary because the thruster had good impedance match near the desired operating frequency of 915 MHz. The intended use of the spectrum analyzers was to observe the forward and reflected RF power going to, and coming from, the test articles and the matching network would be used to minimize reflected power, as measured by one of the spectrum analyzers. A schematic of the RF wiring scheme is shown in Figure 4.13. A photograph of the two spectrum analyzer displays

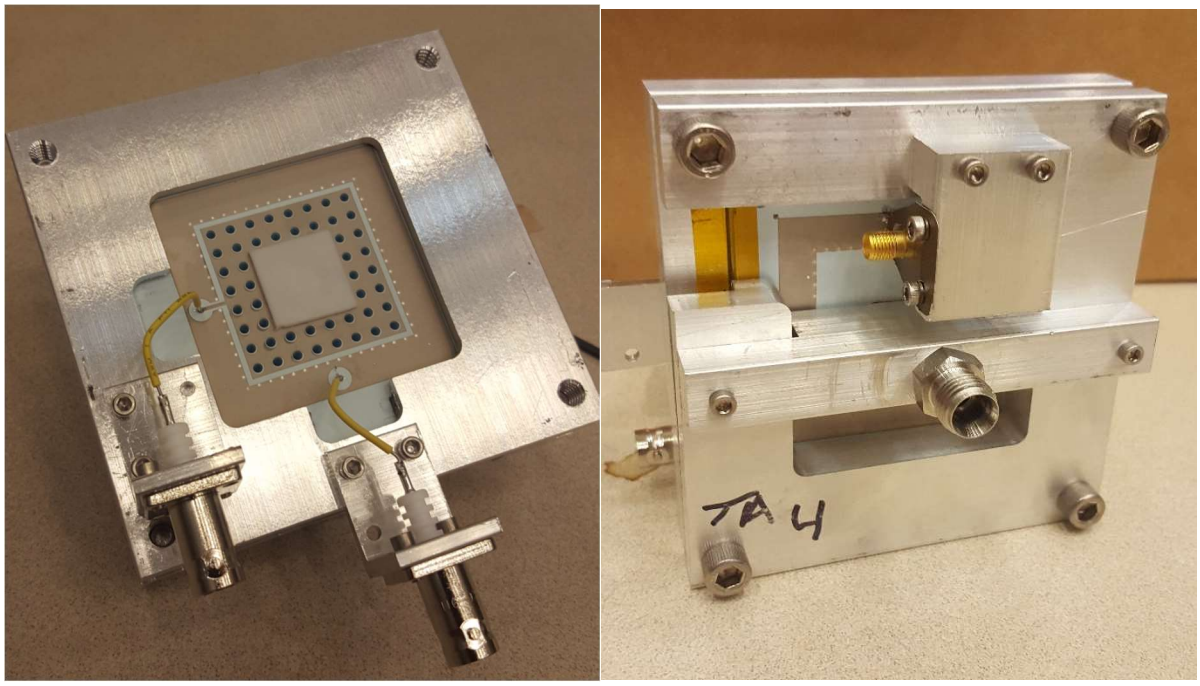

Figure 4.12: Photographs of the LTCC-ET TA4 packaged for testing. Left, the front of the test article showing the two MHV connectors and the Teflon plug. Right, the back of the test article showing the SMA RF connector and the propellant inlet fitting.

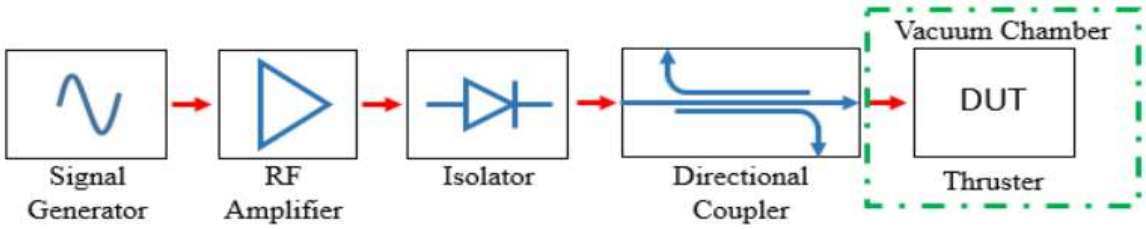

Figure 4.13: RF wiring schematic for thruster evaluation.

showing transmitted power of +35.91 dBm and a reflected power of +3.37 dBm during testing is shown in Figure 4.14. The magnitude of these numbers was not important but rather the difference between them which demonstrated excellent impedance matching. During ignition testing, the accelerating and screen electrodes were grounded to remove any issues that might arise from floating electrically conductive surfaces. It is also important to note that the

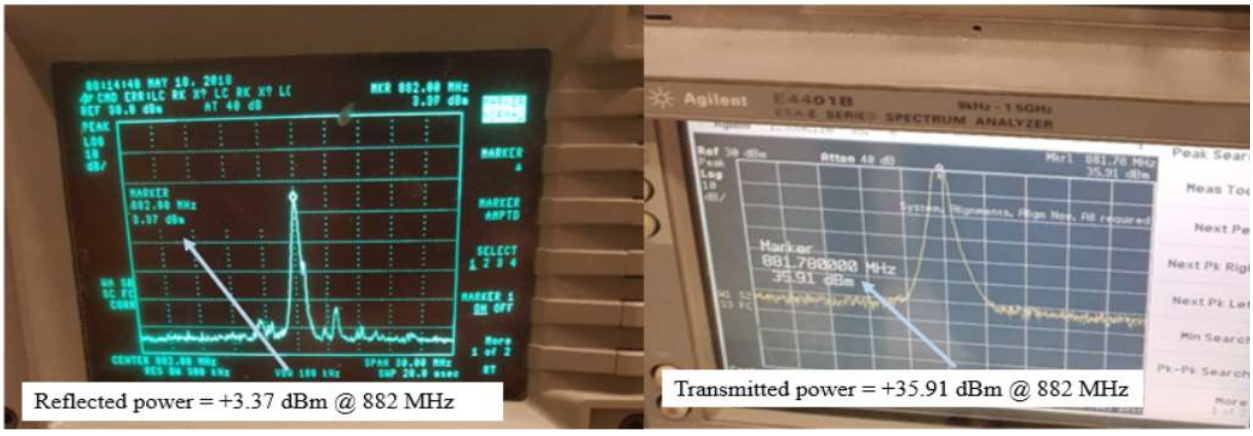

Figure 4.14: Spectrum analyzer traces of reflected and transmitted power.

impedance measurements and antenna matching were performed with the accelerating and screen

electrodes in this configuration. All elements of the signal path were outside of the vacuum chamber with only the test articles inside the chamber. A photograph of the physical setup and the vacuum chamber is shown in Figure 4.15. The impedance of the test articles was measured with a Vector Network Analyzer (VNA) to determine the S11 parameter for each device. The benchmark for being impedance matched was to have an S11 parameter less than -10 dB. A photograph of the S11 for TA1 is shown in Figure 4.16 which showed that there were two frequencies that had good

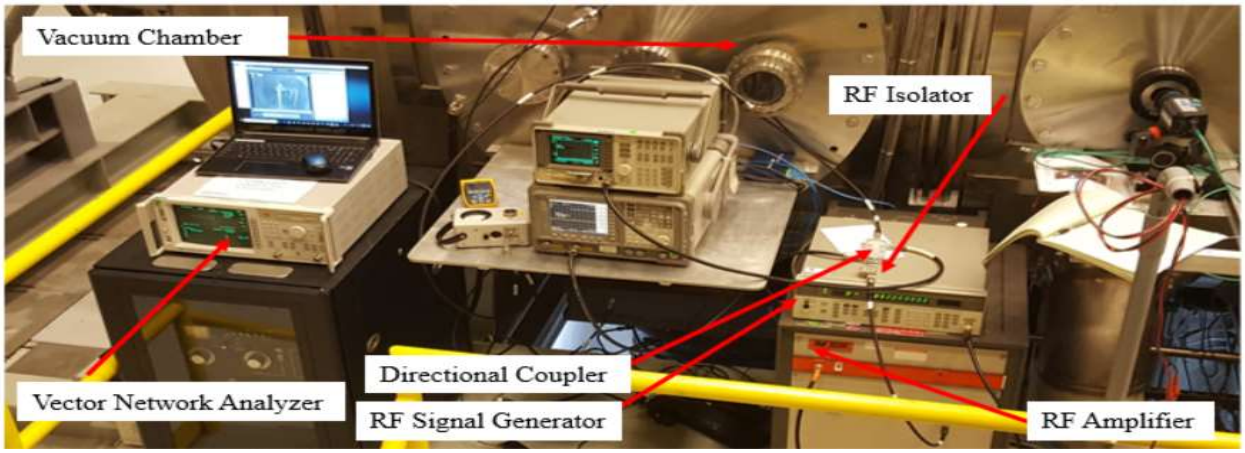

Figure 4.15: Photograph of the test setup on the exterior of the vacuum chamber at MSFC

matching, 858.757 MHz and 871.854 MHz. A photograph of the S11 curve for TA4 is shown in Figure 4.17 which showed that there was good matching at 884.420 MHz.

Figure 4.16: S11 for Test Article 1.

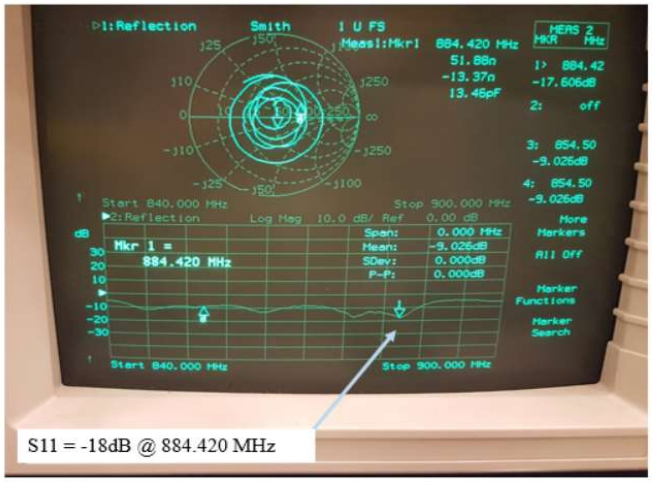

Figure 4.17: S11 for Test Article 4.

The evaluation of the LTCC-ET test articles was conducted with argon gas as a propellant. This gas was selected based on the experience of the staff at MSFC for its traditional relative ease in breaking down at RF frequencies to form a plasma and reasonable cost as compared to more common propellants such as xenon. Propellant was flowed to the device at a controlled flowrate by a calibrated mass flow controller. The investigation process involved flowing gas and then ramping up the RF power to see if a plasma could be ignited. The initial flowrate was low, and

when a plasma would not form up to the maximum RF power of the system (50 W), the flowrate was increased to a new value and the RF power was again ramped up to the maximum value. This process was repeated until a plasma was ignited. No ignition was achieved for argon flowrates of 1, 3, 10, and 33 sccm. Ignition was repeatably achieved at an argon flowrate of 95 sccm and an input power of 22 W. Photographs of Test Article 1 are shown before and during plasma ignition in Figure 4.18. The plasma was maintained for 20 – 60 seconds before it would self-

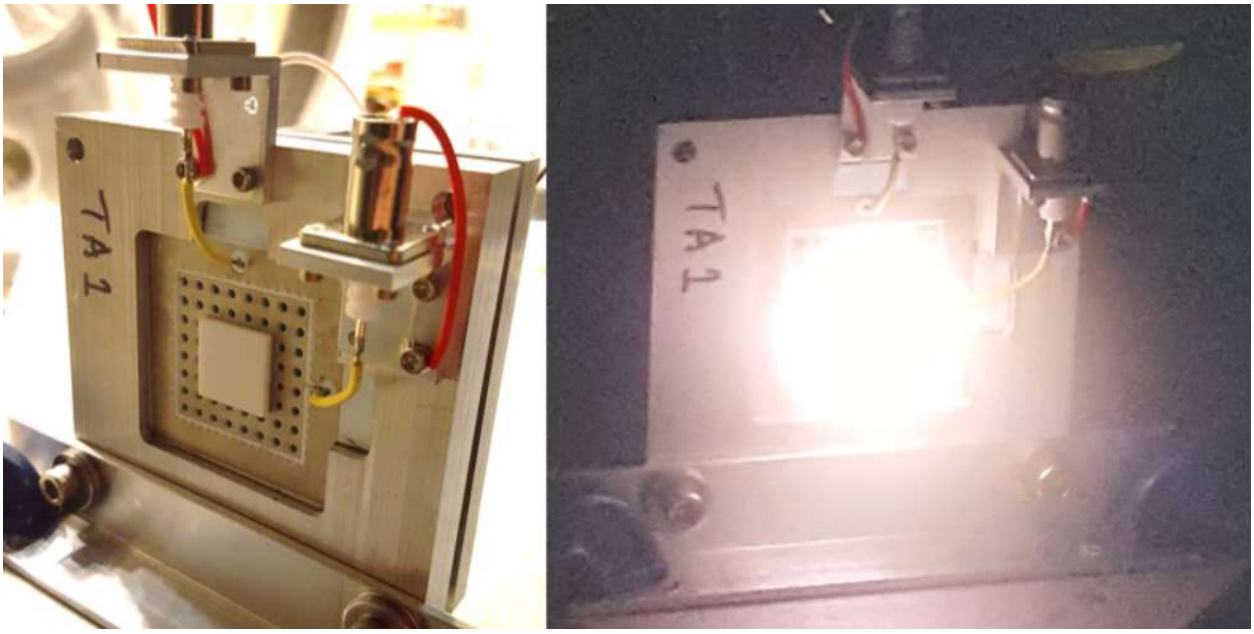

Figure 4.18: Photograph of Test Article 1 in the test chamber.

extinguish. The extinguishing of the plasma was determined to be due to inefficient RF power delivery to the test article. The RF load (antenna) was well matched to a 50 ohm impedance between 858 – 884 MHz across the test articles measured when there was no plasma present. However, upon ignition the RF load presented to the amplifier changed resulting in significantly

less power being delivered to the test article.

This issue was exacerbated as the entire test setup would heat during operation. Heating was a major issue because the pressure in the plasma cavity was far lower than what would be ideal which necessitated high power to be used for plasma ignition. Eventually, the plasma extinguished as it was no longer receiving enough power to sustain the discharge due to the impedance drift in the antenna. Unfortunately, the impedance change could not be quantitatively measured in-situ. If the forward and reflected power had been measured over time by the spectrum analyzers during the ignition testing, then an ad-hoc scalar network measurement could have been taken to determine the extent to which the impedance became mismatched. However, there was not sufficient time to implement this technique during the test campaign at MSFC. Increasing the propellant flowrate to 400 sccm marginally reduced the input power needed for ignition. A plasma was ignited, if only briefly, in all three of the test articles that were brought for testing at this flowrate. All of them suffered the same issues of impedance mismatch, inefficient RF power delivery, and excessive heating.

After initial ad hoc testing, each test article stopped working entirely, exhibiting open circuit behavior when observed with a vector network analyzer. A photograph of the VNA showing high S11 (reflection) and ripple indicative of an open circuit is shown in Figure 4.19. Visual inspection revealed that the heating caused the SMA connectors to desolder, cutting the RF antenna off from the amplifier. The test articles could be re-soldered and would operate briefly, but they would again suffer the same desoldering issue after a brief period of operation. An additional

Figure 4.19: VNA measurement of a test article after it suffered desoldering showing impedance mismatch and ripple indicative of an open circuit.

attempt was made to improve the performance of the test articles by switching to krypton gas as the propellant. This gas was selected because it has a higher molecular weight and more weakly bound valence electrons than argon and it was hypothesized that it would lead to a higher chamber pressure relative to argon and require less field strength to ignite a plasma, both of which would reduce power consumption and possibly improve the aforementioned issues with testing. This attempt led to a successful plasma ignition but with an unwanted side effect. The krypton could not be pumped out of the vacuum chamber by the pumping system as quickly as the argon was. This led to a higher background pressure in the chamber. When plasma was ignited, the plasma caused the thin atmosphere around the test article to also be ignited outside of the device. While this certainly looked ‘cool’, it more importantly demonstrated the extent to which the under pressured plasma chamber was leaking out into the test chamber and adversely affecting performance. The reason the plasma was centralized on the back of the test article was because the SMA connector used to deliver RF power was unshielded. A photograph of the final krypton test is shown in Figure 4.20. A photograph of the unshielded SMA connector is shown in Figure 4.21.

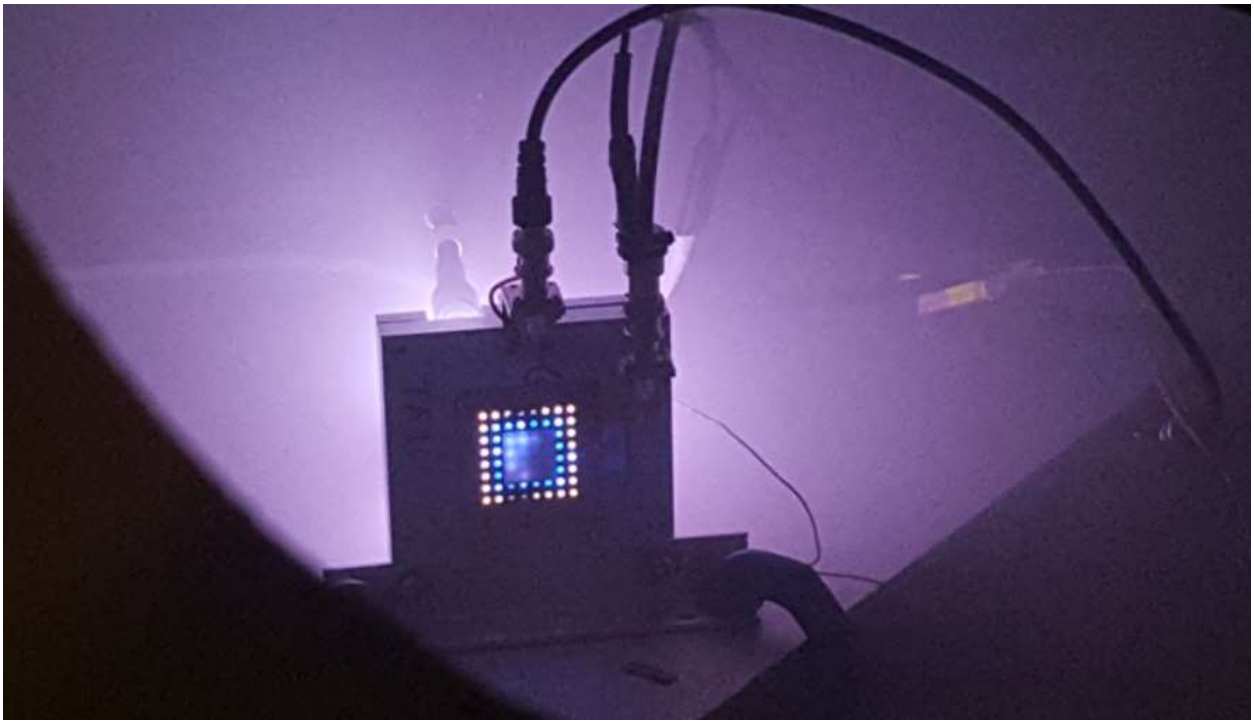

Figure 4.20: Photograph of TA1 igniting a krypton plasma out of the back of the thruster body.

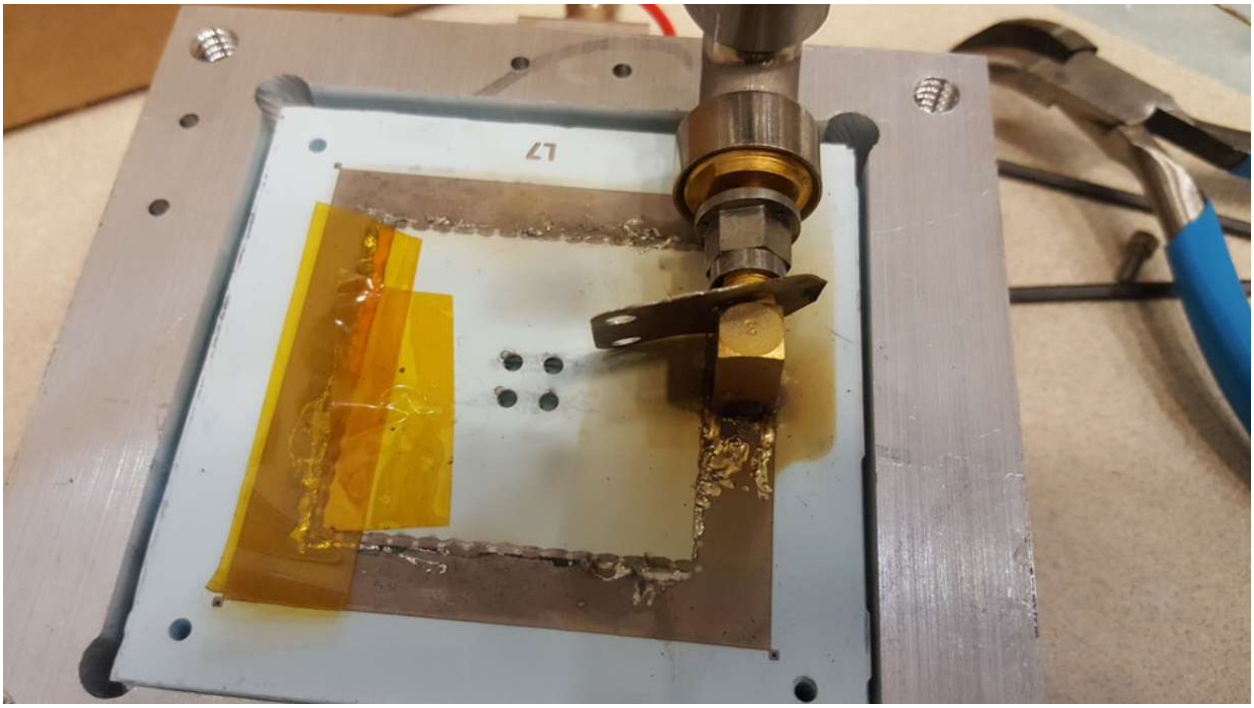

Figure 4.21: Photograph of the backside of TA1 after krypton plasma ignition. Scorching marks

can be seen under the ‘shadow’ of where the propellant inlet manifold was mated to the device.

4.3 LTCC-ET Conclusions

The LTCC-ET showed promise but still needs further development to realize something that can be truly characterized as a thruster. A more defensible description is that a plasma generator was successfully demonstrated. There are three major issues that must be addressed before new test articles can be fabricated. First, the antenna matching needs to be improved. The antenna needs to be modeled to ensure good impedance matching at the intended operating frequency, in this case 915 MHz in the ISM band. The prototypes tested were relatively close to this goal but, by mere coincidence, because they were not modeled and studied before their manufacture. Most importantly the antenna needs to be matched when plasma is being created. The presence of plasma changes the electrical characteristics of the antenna by changing the design. If matching cannot be achieved during normal operation, then a matching network must electrical properties of the environment around the antenna and these must be considered in the be created for efficient and reliable operation.

Second, cavity pressure must be increased by decreasing the propellant outlet orifice size and number. The ideal pressure can be obtained by examining the Paschen’s curve for the selected propellant and taking into account the antenna / screen electrode spacing, and electric displacement caused by the presence of ceramic in the plasma cavity [9]. The pressure of the cavity can then be calculated as a function of orifice size via CFD or other means. The proper orifice size and number can be determined by matching the design to the desired cavity pressure. Third, the thruster structure should be improved. The primary improvement would be to increase the operating temperature of the RF and high voltage connectors for higher reliability. This can be achieved by using higher temperature solder and larger connectors which are better at dissipating heat and are rated for higher power levels.

In conclusion, this work has realized functional prototypes of the LTCC-ET. The test articles were successfully fabricated and demonstrated that the LTCC materials system could be a viable way of creating an electric thruster. The primary benefit of this was that designs can add significant complexity while not increasing cost in a commensurate way. The ultimate application of this technology would be to create an entirely monolithic thruster that has multiple quadrants whose accelerating grids could be controlled independently to realize a solid-state thruster that could electrically thrust vector with no moving mechanical parts or actuators. Additionally, regions could be built in to accelerate negative ions / electrons and, thereby, have an electric thruster that does not require a neutralizing spray. These two technological possibilities make the LTCC-ET design concept well suited to deep space small satellite missions, the use case for this research, due to low volume, long-lifetime, and high I_{sp} properties.

5. Conclusions and Future Work

The research presented in this work has confirmed critical hypotheses and provided insight into logical approaches to continuing development of a new propulsion system. First, it was confirmed that the effluence rate of XeF_2 is sufficient to supply the needed mass flow rate of propellant to a small satellite / CubeSat scale electric thruster and at reasonable temperatures. The threshold for success on this dimension was to exceed 1 μg/s of effluence and this was measured to range from 1 – 90 μg/s. Second, the etch rate of XeF_2 on W was rapid enough that the reaction could be used to supply sufficient propellant to a thruster. The average etch rate of W ranged from 4 – 13 μg/s in static etch tests and rates two orders of magnitude greater were observed in the dynamic experiment. Third, a propellant storage density in excess of the current state of the art was demonstrated. The theoretical maximum storage density for the materials investigated was 5.40 g/cm^3 and a maximum storage density of 5.17 g/cm^3 was observed. Fourth, the LTCC materials and manufacturing process can be used to create a monolithic thruster body with all the functional elements of an electrostatic thruster. The prototypes demonstrated that LTCC approach is viable and should be further developed. Additionally, the insights gathered in this research effort are important in defining the next steps in propulsion system development. These will be discussed in detail in the future work section of this chapter.

There were five important insights learned that should be recognized in order to best plan future work. First, sublimation dynamics of XeF_2 did not adhere to simple first order kinetics. The crystal size and surface area effects sublimation rate on a macro and micro scale. There was a range of pressures and temperatures over which the effluence of XeF_2 is repeatable. This repeatable effluence region should be the target operating area for any future propulsion system based on this technology. Third, the etching of W by XeF_2 vapor was most significantly affected by the desorption of WF_6 from the surface of the solid W. The biggest challenge for incorporating W

etching into a propellant stream is to address this limiting factor. This could be addressed in a number of ways including: changing the flow regime of the gas stream or increasing the surface area of the W by using pellet or power based W samples. Fourth, the gas flow dynamics and the chamber pressure of the LTCC thruster are critical items to study before the thruster design can be iterated. The challenges of testing the prototype thruster would be best addressed by increasing chamber pressure and reducing mass flow rate of propellant. Fifth, the manufacturing process of the LTCC-ET opens the door for incorporating more internal elements, most notably, multiple isolated accelerating grid sections for thrust vectoring. This is perhaps the most innovative part of the LTCCE-ET because this would lead to a solid-state steerable thruster. This has been proposed and demonstrated on other platforms such as the S-iEPS [57], however, that functionality requires multiple discrete thrusters. The LTCC-ET could achieve this with a single monolithic thruster body. These five insights will be extremely valuable in steering the future development of this technology.

5.1 Future Work

There are a number of follow-on studies that would be beneficial to conduct. These studies would serve to investigate effects that were not predicted in the original conception of this research topic. They could be possible topics for future graduate student work or grant-based research projects. The studies make a logical starting point for picking up where this work leaves off.

The dissociation rate of XeF_2 to Xe and F should be quantified. It was observed in this study, and described in the literature, that XeF_2 breaks down into its constituent elements spontaneously. However, there has not been any study to quantify the half-life of XeF_2 under various pressure and temperatures. The application of this knowledge would be useful in designing the proposed propulsion system because it would provide more information of how to store and

handle the XeF_2 in an efficient manner.

The desorption rate of WF_6 from W is not presently quantified. It was understood that this compound is volatile but there is more that needs to be understood. The vapor pressure was known to be 1 atm at 17.8 °C [75]. However, WF_6 is also one of the heaviest gasses known to exist at room temperature. Weight is not important in space, but, it can be critical factor in conducting laboratory studies on W etching. Simply inverting the experiment could have possibly led to better etching results, however, this was not explored due to various constraints. The desorption factors that should be explored are W surface temperature, pressure, orientation of gravity with respect to the W surface, surface roughness, and fluid dynamics of the environment. These are important questions to explore for gaining a greater understanding of how to optimize etching of W by XeF_2 vapor.

The in-depth analysis of the tradeoff space between thrust and specific impulse that was presented in the background section of this work identified power as a key system variable. This was the power delivered to the exhaust plume as measured by accelerating voltage multiplied by beam current. The true power that a thruster consumes is significantly greater than just the beam power and is affected by the efficiencies of all the support components of the propulsion system; including heaters, valves, and power supplies. The calculations made in the background assumed that 10 W of power was a reasonable value for a small satellite / CubeSat application. This assumption needs to be tested. Therefore, it would be beneficial to conduct a power budget study to determine practical operating efficiency to determine what a practical beam power level should be as a function of the spacecraft propulsion power budget. This information is critical in doing mission analysis of any possible candidate missions that may benefit from the proposed propulsion system. Such studies are also critical to conduct in order to competitively propose grant projects

for future development because NASA heavily favors proposals that have a thorough mission concept, even if the proposal is only for hardware development and demonstration. Mission context is key to win grants and a power budget analysis and propulsion requirement analysis both depend on having an idea of the efficiency of the proposed thruster.

A prerequisite to further prototyping of the LTCC-ET is to conduct computational fluid dynamics (CFD) studies to determine ideal propellant outlet orifice size and locations. The testing of the LTCC-ET was successful in demonstrating that the manufacturing approach was valid and brought value to the design. However, the other key aspects of the design could not be tested because of the issue with low chamber pressure, excessive propellant flow demands, and high power required for plasma ignition. Important metrics that should be tested are: thrust, specific impulse, and transfer function between accelerating voltage and grid voltage. The testing issues can be avoided in the future by addressing the known issues with the design, namely insufficient chamber pressure and too high of propellant flow rate. Furthermore, a well-designed CFD study will bring the LTCC-ET design much closer to having operating power in a regime that is commensurate with typical small satellite / CubeSat examples.

A prototype of the proposed thruster should be designed in CAD. The prototype propulsion system should incorporate the XeF_2 sublimation chamber, W etch chamber, the LTCC-ET, thermal control systems, plumbing, and drive electronics. This CAD model should be targeted to consume no more than a 1 U CubeSat block, ideally smaller. The development of this model will be critical to reference as the constituent elements are developed. A successful propulsion system prototype must have a high degree of integration and this will require each component to be co-designed as much as possible.

5.2 Impacts on the Field

This dissertation represents a body of work that is in support of future development of a new type of propulsion system intended for use on Small Satellites and CubeSats. The work has demonstrated two key features that can have an impact in the field of in-space propulsion. First, it provided a new approach to generating propellant from solids. Second, it demonstrated feasibility of a new compact, durable, and scalable electrostatic thruster manufacturing process. These features collectively represent the technical contributions to the field and primary results of this work.

This dissertation has presented a novel way of generating propellant. There are propulsion systems currently in development that rely on sublimation of solids such as the iodine-based thruster under development by Busek Inc. and NASA. However, there has never been a proposed propulsion system which generated propellant by subliming a gaseous etchant from a solid that is then used to gasify dense materials. Additionally, no heavy metals have been considered for use as propellant (heavy gases such as krypton have). The demonstrated subliming etchant approach could have a major impact on the propulsion field because this method could be used to gasify other materials than tungsten, such as asteroid regolith. The process of using asteroids or other materials that can be sourced in space is called ‘in-situ resource utilization’ or ISRU. ISRU has long been considered as a powerful technique for deep space exploration but has been limited to planetary applications. An example of this is SpaceX’s plan to harvest water ice from the surface of Mars to produce methane for rocket fuel. Future development of the work presented in this dissertation could lead to a practical way of applying ISRU to electric propulsion.

This dissertation presented a new approach to manufacturing an electrostatic thruster. These devices are traditionally made with subtractive manufacturing technology. Furthermore,

electrostatic thrusters typically have numerous parts in their bill of materials. The demonstration of using LTCC to create the thruster body significantly reduces the assembly complexity of this category of thruster. The other major benefit of the approach is the ability to integrate added complexity into the thruster design with minimal additional cost. The thruster body itself can be fitted with additional electrodes and functionality while still maintaining its monolithic structure.

The overarching impact of this work has been to establish TRL 3 status to the conceptual propulsion system proposed in this dissertation. The definition of TRL 3 is: “Analytical and experimental critical function and/or characteristic proof-of-concept”. The impact of this is that there is now a foundational work that can serve as the basis for future grant and other funding proposals. Prior to this dissertation there was insufficient data or work in the area to secure any substantial funding. This is the reason that this dissertation was conducted on a limited budget as there was no grant funding available. Future researchers can now seek funding to significantly accelerate the progress of this work.

References

[1] C. D. Brown, Elements of Spacecraft Design, American Institute of Aeronautics and Astronautics, Reston, VA, 2002, p. 167.

[2] "Alternatives for Future U.S. Space Launch Capabilities," Congressional Budget Office, Washington, DC, 2006, p. 2.

[3] 115th Congress of the United States, *House Resolution 6910 - Leading Human Spaceflight Act,* 2018.

[4] "Lockheed Satellite Products," Lockheed Martin, [Online]. Available at: https://www.lockheedmartin.com/en-us/products/satellite.html, Accessed Sept 10, 2019.

[5] "1300 Series Platform," Space Systems Loral, [Online]. Available at: http://sslmda.com/html/1300_series_platform.php, Accessed Sept 10, 2019.

[6] "Satellite Family Overview," Boeing, [Online]. Available at: https://www.boeing.com/space/boeing-satellite-family/, Accessed Sept 10, 2019.

[7] "James Webb Space Telescope," NASA, [Online]. Available: https://jwst.nasa.gov/content/about/index.html, Accessed Sept 10, 2019.

[8] Mission Design Division , "Small Spacecraft Technology State of the Art," NASA/TP-2015-216648/Rev1, Ames Research Center, Moffett Field, California, 2015, pp. 40-60.

[9] Small Spacecraft Systems Virtual Instsitute, "State of the Art – Small Spacecraft Technology," NASA/TP-2018-220027, Ames Research Center, Moffett Field, California, 2018, pp. 53-80.

[10] I. Nelson, M. Creedon and N. Johansen, "CUBESAT P-POD Deployer Requirements," CalPoly, 2002, Avaliable at: http://www.oh1sa.net/data/satellite/cubesat/P-POD-mk1/ppod_mk1_icd.pdf, Accessed June 27, 2020.

[11] NanoRacks. LLC, 18100 Upper Bay Rd, Suite 150, Houston TX, 77058 "NanoRacks CubeSat Deployer (NRCSD) Interface Definiton Document," Available at: http://nanoracks.com/wp-content/uploads/Current_edition_of_Interface_Document_for_NanoRacks_Smallsat_Customers.pdf. Accessed Jul 14, 2020.

[12] "NanoSats Database," October 2019, Available at: https://www.nanosats.eu/database, Accessed Jun 27, 2020.

[13] H. H. Claassen, H. Selig and J. G. Malm, "Xenon Tetrafluoride," *Journal of the American*

Chemical Society, vol. 84, no. 18, 1962, pp. 3593.

[14] D. F. Smith, "Xenon Difluoride," *The Journal of Chemical Physics,* vol. 38, no. 1, 1963, p. 270.

[15] S. I. Morrow and A. R. Young, "The Reaction of Xenon with Dioxygen Difluoride. A New Mehtod for the Synthesis of Xenon Difluoride," *Inorganic Chemistry,* vol. 4, no. 5, 1965, pp. 759-760.

[16] F. Schreiner, G. N. McDonald and C. L. Chernick, "Vapor Pressure and Melting Poings of Xenon Difluoride and Xenon Tetrafluoride," *Journal of Physical Chemistry,* vol. 72, no. 4, 1968, pp. 1162-1166.

[17] S. Reichman and F. Schreiner, "Gas-Phase Structure of XeF2," *The Journal of Chemical Physics,* vol. 51, no. 6, 1969, pp. 2355-2358.

[18] J. Jortner, E. G. Wilson and S. A. Rice, "The Heats of Sublimation of XeF2 and XeF4 and a Conjecture on Bonding in the Solids," *Journal of the American Chemical Society,* vol. 85, no. 6, pp. 814-815, 1963.

[19] H. F. Winters and J. W. Coburn, "The Etching of Silicon with XeF2 Vapor," *Applied Physics Letters,* vol. 34, no. 70, 1979, pp. 70-73.

[20] F. I. Chang, R. Yeh, G. Lin, P. B. Chu, E. Hoffman, E. J. Kruglick, K. S. Pister and M. H. Hecht, "Gas-Phase Silicon Micromachining with Xenon Difluoride," *SPIE,* vol. 2641, no. 117, 1995, pp. 110-128.

[21] I. W. Chan, K. B. Brown, R. P. Lawson, A. M. Robinson, Y. Ma and D. Strembicke, "Gas Phase Pulse Etching of Silicon for MEMS with Xenon Difluoride," in *IEEE Canadian Conference on Electrical and Computer Engineering*, Edmonton, Alberta, Canada, May 9-12, 1999.

[22] A. Bensaoula, A. Ignatiev, J. Strozier and J. C. Wolfe, "Low-Temperature Ion Beam Enhanced Etching of Tungsten Films with Xenon Difluoride," *Applied Physics Letters,* vol. 49, no. 24, 1986, pp. 1663-1664.

[23] A. Bensaoula, A. Grossman and A. Ignatiev, "Etching of Tungsten with XeF2: An X-ray Photoelectron Spectroscopy Study," *Journal of Applied Physics,* vol. 62, no. 11, 1987, pp. 4587-4590.

[24] J. D. Dagata, D. W. Squire, C. S. Dulcey, D. S. Hsu and M. C. Lin, "Chemical Processes Involved in the Etching of Silicon by Xenon Difluoride," *Journal of Vacuum Science and Technology B,* vol. 5, no. 5, 1987, pp. 1495.

[25] K. R. WIlliams and R. S. Muller, "Etching for Micromachining Processing," University of

California Berkeley Electronics Research Laboatory M96/37, Berkeley, California, 1996, p. 30.

[26] K. R. Williams and R. S. Muller, "Etch Rates for Micromachining Processing," *IEEE Journal of Microelectromechanical Systems,* vol. 5, no. 4, 1996, pp. 256-269.

[27] K. R. WIlliams, K. Gupta and M. Wasilik, "Etch Rates for Micromachining Processing - Part II," *IEEE Journal of Microelectromechanical Systems,* vol. 12, no. 6, 2003, pp. 762-778.

[28] M. R. Gongora-Rubio, P. Espinoza-Vallejos, L. Sola-Langua and J. J. Santiago-Aviles, "Overview of Low Temperature Co-Fired Ceramics Tape Technology for meso-System Technology (MsST)," *Sensors and Actuators,* vol. 89, 2001, pp. 222-241.

[29] A. R. Tummala and A. Dutta, "An Overview of Cube-Satellite Propulsion Technologies and Trends," *Aerospace,* vol. 4, no. 58, 2017, pp. 1-30.

[30] K. Lemmer, "Propulsion for CubeSats," *Acta Astronaut,* vol. 134, 2017, pp. 231-24,.

[31] N. E. S. T. Office, "TRL Definitions," [Online]. Available at: https://esto.nasa.gov/files/trl_definitions.pdf, Accessed October 2, 2019.

[32] D. T. Schmuland, R. K. Masse and C. G. Sota, "Hydrazine Propulsion Module for CubeSats," in *25th Annual AIAA/USU Conference on Small Satellites/SSC11-X4*, Logan, UT, Aug 10-14, 2011.

[33] Busek Space Propulsion Systems, "Buske BGT-X5 Datasheet," 2016, Available: http://www.busek.com/index_htm_files/70008517E.pdf, Accessed November 5, 2019.

[34] M. Tsay, C. Feng and J. Zwahlen, "System-Level Deomonstration of Busek's 1U CubeSat Green Propulsion Module,"AMAC"," in *53rd AIAA/SAE/ASEE Joint Propulsion Conference*, Atlanta, GA, Jul 15-17, 2017.

[35] C. B. Carpenter, D. Schmuland, J. Overly and R. Masse, "CubeSat Modular Propulsion Systems Product Line Development Status and Mission Applications," in *49th AIAA/ASME/SAE/ASEE Joint Propulsion Conference*, San Jose, CA, Jul 14-17, 2013.

[36] R. A. Spores, R. Masse, S. Kimbrel and C. McLean, "The GPIM AF-M315E Propulsion System," in *49th AIAA/ASME/SAE/ASEE Joint Propulsion Conference*, San Jose, CA, Jul 14-17, 2013.

[37] P. Friedhoff, A. Hawkins, J. Carrico, J. Dyer and K. Anflo, "On-Orbit Operation and Performance of Ammonium Dinitramde Based High Performance Green Propulsion Systems," in *53rd AIAA/SA/ASEE Joint Propulsion Conference*, Atlanta, GA, Jul 10-12,

2017.

[38] VACCO Industries, "VACCO X14102000-01 Dat Sheet," 2018. [Online]. Available: https://www.cubesat-propulsion.com/wp-content/uploads/2015/11/X14102000-01_2019update.pdf. [Accessed 5 November 2019].

[39] C. I. Underwood, G. Richardson and J. Savignol, "In-Orbit Results from the SNAP-1 Nanostatellite and Its Future Potential," *Philosophical Transactions: Mathematical, Physical, and Engineering Sciences,* vol. 361, no. 1802, pp. 199-203, 2003.

[40] G. Bonin, N. Roth, S. Armitage, J. Newman, B. Risi and R. E. Zee, "CanX-4 and CanX-5 Precision Formation Flight: Mission Acomplished," *29th Annual AIAA/USU Small Satellite Conference/SSC11-I-4*, Logan, UT, Aug 8-13, 2015.

[41] G. Manzoni and Y. L. Brama, "Cubesat Micropropulsion Characterization in Low Earth Orbit," in *29th Annual AIAA/USU Conference on Small Satellites/SSC15-IV-5*, Logan, UT, Aug 8-13, 2015.

[42] S. Wu, Z. Mu, W. Chen, P. Rodrigues, R. Mendes and L. Alminde, "TW-1: A CubeSat Constellation for Space Networking Experiments," in *6th European CubeSat Symposium*, Estavayer-le-Lac, Switzerland, Oct 14-16, 2014.

[43] J. Bowen, M. Villa and A. WIlliams, "CubeSat Based Rendezvous, Proximity Operations, and Docking in the CPOD Mission," in *29th Annual AIAA/USU Conference on Small Satellites/SSC15-III-5*, Logan, UT, Aug 8-13, 2015.

[44] P. Davies, P. Whittaker, R. Bird, L. Gomes, B. Stern, M. Sweeting, M. Cohen and D. Hall, "NovaSAR - Bringing Radar Capability to the Disaster Monitoring Constellation," in *AIAA/USU Small Satellite Conference/SSC12-I-7*, Logan, UT, Aug 10-14, 2012.

[45] D. L. Carroll and R. Cardin, "Propulsion Unit for CubeSats," in *62nd JANNAF Propulsioon Meeting / 7th Spacecraft Propulsion Conference*, Nashville, TN, Jun 1-5, 2015.

[46] K. I. Parker, "State-of-the-Art for Small Satellite Propulsion Systems," in *Biennial Aerospace Systems Conference of the National Society of Black Engineers*, Arlington, VA, Aug 24-27, 2016.

[47] M. Robin, T. Brogan and E. Cardiff, "An Ammonia Microrestojet for Micro Satellites," in *44th AIAA/ASME/SAE/ASEE Joint Propulsion Conference*, Hartford, CT, Jul 26-28, 2008.

[48] R. H. Lee, A. Bauer, M. D. Killingsworth, T. Lilly, J. Duncan and A. Ketsdever, "Free-Molecule-Microresistojet Performance Using Water Propellant for Nanosatellite Applications," *Journal of Spacecraft and Rockets,* vol. 56, 2008, pp. 302-307.

[49] Busek Space Propulsion Systems, "Buske BmP-220 Datasheet," 2019, Available at: http://busek.com/index_htm_files/70008502G.pdf, Accessed Nov 5, 2019.

[50] J. B. Robinson and D. J. Richie, "Stabilization and Attitude Determination Methods for FalconSAT-3," *Journal of Spacecraft and Rockets,* vol. 53, pp. 507-519, 2016.

[51] R. Joseph, W. Cassady and M. Andrew-Hoskins, "A Micro Pulsed Plasma Thruster (PPT) for the "Dawgstar" Spacecraft," in *IEEE Aerospace Conference*, Big Sky, MT, Mar 6-11, 2000.

[52] J. Kolbeck, J. Lukas, G. Teel, M. Keider, E. Hanlon, J. Pittman, M. Lange and J. Kang, "uCAT Micro-Propulsion Solution for Autonomous Mobile On-Orbit Diagnostic System," *30th Annual AIAA/USU Conference on Small Satellites*, Logan, UT, Aug 10-14, 2016.

[53] I. Kronhaus, M. Pietzka, K. Schilling and J. Schein, "Pico-Satellite Orbit Control by Vacuum Arc Thrusters as Enabling Technology for Formations of Small Satellites," in *5th International Conference on Spacecraft Formation Flying Missions and Technologies*, Munich, Germany, May 29-31, 2013.

[54] "AeroCube-8 (IMPACT) Flight Summary," Nanosats Database, 2016, Available at: https://www.nanosats.eu/sat/aerocube-8, Accessed Nov 5, 2019.

[55] D. Krejci, F. Mier-Hicks, C. Fucetola, P. Lozano, A. H. Schouten and C. Martel, "Design and Characterization of a Scalable ion Electrospray Propulsion System," in *Joint Conference of 30th ISTS, 34th IEPC and 6th NSAT*, Hyogo-Kobe, Japan, Jul 4-10, 2015.

[56] R. S. Legge, E. B. Clements and A. Shabshelowitz, "Enabling Microsatellite Maneuverability: A Survey of Microsatellite Propulsion Technologies," in *IEEE MTT-S International Microwave Symposium*, Honololu, HI, Jun 6-8, 2017.

[57] D. Spence , E. Ehrbar, N. Rosenbald, N. Demmons, T. Roy, S. Hoffman, W. D. WIlliams, M. Tsay, J. Zwahlen and K. Hohman, "Electrospray Propulsion Systems for Small Satellites and Satlets," in *AIAA Space Conference and Exposition*, San Diego, CA, Sep 10-12, 2013.

[58] N. Z. Warner, "Theoretical and Experimental Investigation of Hall Thruster Miniaturization," Dissertation for Partial Fulfillment of the degree Doctor of Philosophy, Massachusetts Institute of Technology, Cambrage, MA, 2007, p 3.

[59] S. Y. Cheng and M. Martinez-Sanchez, "Hybrid Particle-in-Cell Erosion Modeling of Two Hall Thrusters," *Journal of Propulsion and Power,* vol. 24, no. 5, pp. 987-996, 2008.

[60] L. Biagioni, U. Cesari, M. Saverdi and M. Andrenucci, "Deveopment Status of the HT-100 Miniaturized Hall Effect Thruster," in *41st AIAA/ASME/SAE/ASEE Joint Propulsion*

Conference, Tuscon, AZ, Jul 10-13, 2015.

[61] V. Salvatore, F. Battista, D. Ricci and M. Invigorito, "Development Activities in Electric Propulsion Testing," in *66th Internation Astronautical Congress*, Jerusalem, Israel, Oct 12-16, 2015.

[62] C. E. Pigeon, G. Nathan and B. Orr, "A Low Power Cylindrical Hall Thruster for Next Generation Microsatellites," in *29th Annual AIAA/USU Conference on Small Satellites*, Logan UT, Aug 8-13, 2015.

[63] I. Katz, D. M. Goebel, Fundamentals of Electric Propulsion: Ion and Hall Thrusters, Jet Propulsion Laboratory Space Sciene and Technical Series, 2008, pp 91-239.

[64] D. G. Fearn, E. Solutions and C. Crookham, "The Future Development of Gridded Ion Engines," in *39th Annual AIAA/ASME/SAE/ASEE Joint Propulsion Conference*, Huntsville, AL, July 20-23, 2003.

[65] D. M. Goebel, J. E. Polk and I. G. Mikellides, "Ion Thruster Perforamance Impmacts Due to Cathode Wear," *Journal of Propulsion and Power,* vol. 27, no. 4, 2011, pp. 768.

[66] D. Brinza, J. Wang, J. Polk and M. Henry, "Deep Space Measurements of Ion Propulsion Contamination," *Journal of Spacecraft and Rockets,* vol. 38, 2001, pp. 426-432.

[67] I. G. Mikellides and I. Katz, "Wear Mechanisms in Electron Sources for Ion Propulsion, 1: Neutralizer Hollow Cathode," *Joural of Propulsion and Power,* vol. 24, no. 4, 2008, pp. 992-999.

[68] R. D. Kolasinski and J. E. Polk, "Characterization of Cathode Keeper Wear by Surface Layer Activation," *Journal of Propulsion and Power,* vol. 20, no. 6, 2004, pp. 855-865.

[69] P. J. Wilbur, M. Wilson, K. Hutchings and J. D. Williams, "Emissive Membrane Ion Thruster Concept," *Journal of Propulsion and Power,* vol. 23, no. 5, 2007, pp. 992-999.

[70] P. Knauth and H. L. Tuller, "Solid-State Ionics: Roots, Status, and Future Prospects," *Journal of the American Ceramics Society,* vol. 85, 2002, pp. 1655-1680.

[71] M. Tsay, J. Frongillo and J. Zwahlen, "Maturation of Iodine Fueled BIT-3 RF Ion Thruster and RF Neutralizer," in *52nd AIAA/SAE/ASEE Joint Propulsion Conference*, Salt Lake City, UT, Jul 25-27, 2016.

[72] N. Bosanac, A. Cox, K. C. Howell and D. C. Folta, "Trajectory Design for a Cislunar Cubesat Leveraging Dynamics Systems Techniques: The Lunar Icecube Mission," in *AAS/AIAA Space Flight Mechanics Meeting*, San Antonio, TX, Aug 20-24, 2017.

[73] A. GmbH, "Electric Ion Space Propulsion and Thrusters," 2019, Available at:

http://www.space-propulsion.com/spacecraft-propulsion/propulsion-systems/electric-propulsion/index.html, Accessed Nov 5, 2019.

[74] NIST, "Physical Properties of Tungsten Hexafluoride," National Institute of Standards and Technology, 2018, Available at: https://webbook.nist.gov/cgi/cbook.cgi?ID=C7783826&Mask=4&Type=ANTOINE&Plot=on, Accessed Nov 5, 2019.

[75] H. Leiter, "Evolution of the AIRBUS DS GmbH Radio Frequency Ion Thruster Family," *30th International Symposium on Space Technology and Science / 34th International Electric Propulsion Conference / 6th Nano-satellite Symposium*, Hyogo-Kobe, Japan, Jul 4-10, 2015.

[76] H. Kawahara, J. A. Yaginuma, H. Koizumi, R. Funase and K. Komuraski, "Ground Experiment for the Small Unified Propulsion System: I-COUPS Installed on the Small Space Probe: PROCYON," *30th International Symposium on Space Technology and Science / 34th International Electric Propulsion Conference / 6th Nano-satellite Symposium*, Hyogo-Kobe, Japan, Jul 4-10, 2015.

[77] Enpulsion, "IFM Nano Thruster Product Data Sheet," 2019, Available at: https://www.enpulsion.com/wp-content/uploads/ENP2018-001.F-IFM-Nano-Thruster-Product-Overview.pdf, Accessed Nov 5, 2019.

Appendix A: Description of Research for Popular Publication

Imagine you live in a far-away land and must go on a great journey that will take many months. Now, imagine you also live in a time without many conveniences and once you begin your journey, there is no going back to grab something you forgot. A smart person would probably want to plan very carefully so as not to be without anything they may need on the journey. That may sound very difficult, but this is the job that scientists and engineers who work on spacecraft must do every single day. After satellites designed to explore moons on other planets are launched into space, they must carry every single thing they may need over a mission that could last many years.

Spacecraft are always designed with a specific mission in mind. This is very different from what we usually experience. Imagine if you had a car that was only good for going to the grocery store and had to have a different car to go to school. That would be very impractical for everyone! The reason that this works for spacecraft is because we only send very few spacecraft out into the solar system. All of mankind has only ever sent a few dozen spacecraft away from the Earth. Each one of these had a very specific job to do, such as observe Saturn's rings, look at Jupiter's Great Red Spot, or fly through the tail of Halley's comet. This is the sort of job where the mission is so important that it makes sense to have a special custom spacecraft.

Spacecraft must be designed so that they can do a very good job of conducting a mission but not have any extra parts that are not critical to the goal. The first job of designing a spacecraft then is to make a list of capabilities it must have for the jobs it is intended to do. One of the big jobs on any spacecraft is maneuvering or changing course along the mission. There are many reasons for this. A spacecraft might need to adjust its course to avoid hitting an asteroid. Or it may just need to turn and point in a new direction. The propulsion system is the part of the spacecraft that must handle this very important job. Propulsion systems therefore are built very specially so that they can do all the maneuvering for an entire mission. Remember that great journey that you

imagined before? Imagine how difficult it must be to plan every single amount of fuel that a spacecraft might need over its lifetime! This is the job of the propulsion engineer and it is a difficult job indeed.

The propulsion engineer has a tough job because they must figure out how to get the most maneuverability while using up the smallest amount of room on the spacecraft. As the need for maneuvering grows, so does the amount of the spacecraft that is taken up with a propulsion system. Designers must be very clever to maximize how well the propulsion system works and not have a negative impact on the rest of the spacecraft. A collection of technologies that is currently being developed at the University of Arkansas can help designers be clever and produce the best propulsion systems.

Okay, remember that journey that keeps coming up? Consider now just the food you would have to take with you on your journey, so you don't starve. Remember, there aren't any fuel stops on the way to Jupiter (unless you are very very clever), so you too have to be efficient. Now let's say you only have one wheelbarrow to carry all of your food for a year long trip. How about Lunchables? That would take 2000 – 3000 Lunchables, depending on your appetite, and they wouldn't all fit in the wheelbarrow anyway! Even if you decided to bring something more practical such as a military style ration kit like an MRE or HDR, that will still be several hundred pounds of food that won't fit either! So, what would a propulsion engineer do with this predicament? They would figure out how to make the food smaller so they could fit more in their wheelbarrow. They would also try and plan for eating the smallest amount of food per day so their food lasts longer. The propulsion engineer's job is to deal with this precise issue in their task to make propulsion systems work better: bring as much fuel as possible and use that fuel as efficiently as possible.

Research by Morgan Roddy at the University of Arkansas has sought to improve propulsion

systems in two ways. The thought experiment journey has two parallel ideas with this research. The issue of needing a denser way to carry food is analogous to the way the work has demonstrated best-in-class storage density of propellant. The issue of eating less food is addressed by a new compact form of super-efficient thruster design.

The first half of the work revolves around conducting studies on a new kind of propellant that is very dense. The propellant comes in two parts; a heavy metal called the 'target' material and a very corrosive crystal material called the 'etchant'. The two materials are stored in separate chambers. When propellant is needed, the etchant crystals are sublimated and turn into a vapor. This vapor flows then to the chamber with the target material which gets attacked by the vapor. The result of this reaction is a gas that can be used for propellant. The important work that Roddy conducted was to study how fast the materials react. This was important to understand because it helps propulsion engineers to figure out how large to make the propellant system, or how much thrust can be achieved with the available fuel. Most importantly, it showed that propellant can be stored as a dense solid and this is very important for spacecraft. Solids are always the densest way to store any material and so this approach to generating propellant from solids is very space efficient.

The second half of the work was to make a well-known kind of ultra-efficient thruster, the Ion Engine, more compact and more durable. The ion engine works by taking a gas and turning it into a plasma in a chamber. One side of the chamber is filled with tiny holes so that some of the plasma leaks out. When ionized gas atoms (that's all a plasma is, very angry gas) leak through the holes, they get pushed out very quickly by a series of electrical grids that surround the holes. The ions get shot out the back of the spacecraft at high velocity which results in thrust. The thruster built by Roddy works in the same manner but what is new is how the thruster was manufactured.

Typically, an ion thruster would be machined out of many pieces of exotic space-grade metal alloys. This is an expensive and time-consuming process. The new work uses a process that is closer to how circuit boards are built to make a functioning prototype of the ion engine. This was made possible with assistance from the University of Arkansas's Low Temperature Co-Fire Ceramics (LTCC) manufacturing facility. The thruster was made with the LTCC process which results in a thruster that has all of the wires and grids needed to operate which are all embedded into ceramic material. This makes the design very compact and durable. The thruster was tested by Roddy at NASA's Marshall Space Flight Center in Huntsville, Alabama, and is shown in the photos below.

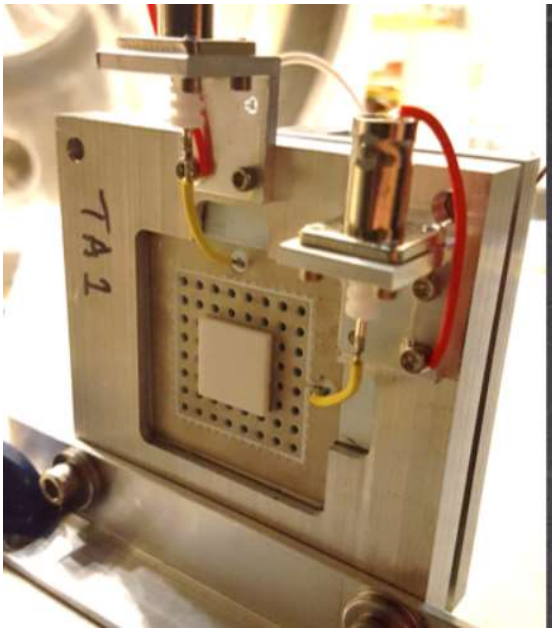

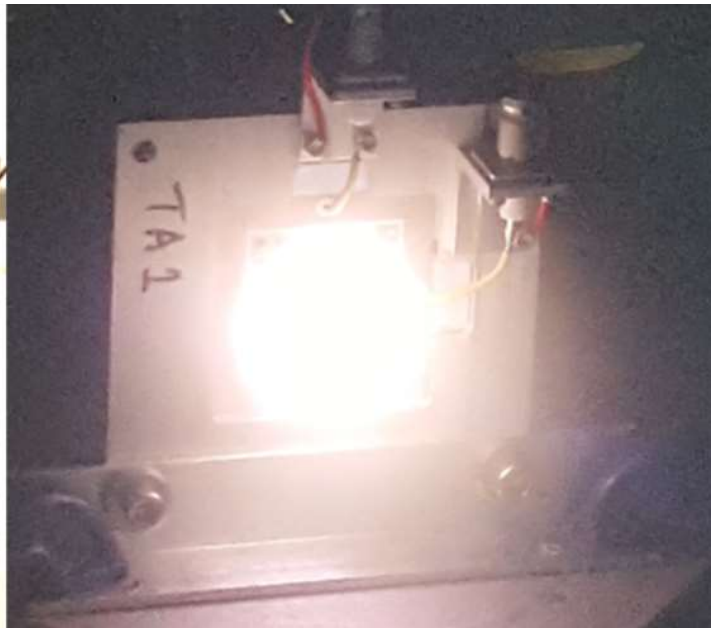

So, if you are planning a great space journey of your own, you should consider using some of the ideas that Roddy was working on. His work showed two great ways to improve interplanetary exploration by introducing some new propulsion technologies. First, have best-in-class propellant density so you can carry the most amount of fuel possible. Second, have a compact,

durable, and high efficiency thruster so that you can use your space and fuel efficiently. Stay Curious!

Appendix B: Executive Summary of Newly Created Intellectual Property

The use of solid subliming corrosive materials to etch dense materials for the purpose of generating a propellant flow is a novel concept that has first been proposed in this research. This singular contribution is the primary intellectual property produced by this research. The essence of the IP is that propellant can be stored in a dense form, as a solid. When the propellant is needed, the right combinations of controllable environmental conditions (pressure, temperature, etc) will cause the selected combination of propellant materials to naturally react and form a gas phase which can be used in an electric propulsion system. This approach allows for best-in-class propellant storage density which is an important design metric for propulsion systems.

The method of using numerous Kelvin measurements along the length of the tungsten ribbon during the dynamic etching experiment is a novel method that has not been found in literature. This measurement technique was developed by Morgan Andrew Roddy and Po-Hao Adam Huang as part of this research. The value of this technique is that it can be used to measure the thickness of a conductive material in-situ while it is being etched by a gas-solid interfacial etching reaction. This electrically-based approach allows for measuring material thickness that would be impossible to measure without vastly more sophisticated techniques.

Appendix C: Potential Patent and Commercialization Aspects

C.1 Patent Prospects IP (can each be patented)

There are two newly created IP blocks developed in this work: sulid subliming etching dense propellants, and multi-probe Kelvin measurements for etch rate analysis. As there is no known prior work on both of these topics, it both should be possible to receive a patent for both of them. Furthermore, the two methods that were developed are each composed of disparate technical elements and it should not be considered 'obvious to someone in the field' that these methods are possible. The use of solid subliming etching materials is well known to the semiconductor industry as XeF_2 is used in commercial etching tools. While the use of this method is known to be capable of etching dense metals, it would not be obvious to someone working on such etch tools that the technology could be applicable to space propulsion systems. Additionally, the use of a Kelvin measurement to measure very small resistances is a method know for over 100 years. However, it would not be obvious to an electrical engineer that using an array of these measurements could yield a technique to study real-time in-situ etch rates of pure metals. For these reasons, it is understood that it would be possible to submit a justified patent application for both pieces of IP.

C.2 Commercialization Possibilities of IP (should each be patented)

There are potential commercialization prospects for the solid subliming etching propellant method. The entire propellant generation technique could be a single patent. The entire process is made up of well-known elements but putting them together in a single system is new. High density propellants have been studied for many years, so this is not a new approach. Tungsten has been known to be etched by xenon difluoride for decades and this is not new. Solid subliming etchants have been in use in commercial semiconductor processing equipment for decades as well. The novel and patentable IP from this work is bringing together disparate technological elements to form a single system to create bring new value. There are no technical barriers to patenting this

technology and it could be deserving of IP protection. The patentability is not in question, however, the potential commercialization opportunities are very limited. While the technology has significant merit, there is no established market for this IP. The space propulsion market has shifted away from focusing on high-density propellant as a major area of interest and shifted to compressed gas based propellant systems for Hall thrusters. These are well understood systems and the commercial markets value reliability and flight heritage over innovation in high-risk applications. The market where this could be of value is in the academic or governmental research arenas. Neither of these make good customers of this IP as academics do not typically engage in IP licensing to empower their work and governmental researchers do not directly license IP themselves, but, rather through defense contractors. The limited potential market for the IP is to license the technology to a federally funded research laboratory, or a defense contractor. This coupled with the fact that the technology is still many years away of being commercializeable leads to my conclusion: there is no significant motivation to protect this IP with a patent.

There are no significant commercialization prospects for the multi-Kelvin method. This technique is of academic interest as it could be used for materials science investigations, as it was used in this work. A possible application of the technology would be to monitor the health of a sacrificial element that was designed to fail in a specified amount of time. Such a device could be used to deploy an end-of-life design feature to a system. Examples of this would be a buoy could be deployed from an underwater sensor when the system had finish data collection to identify its location and aid in data recovery. The buoy could be released by the complete etching of a wire by seawater corrosion. The rate at which this corrosion occurred to could be monitored in real-time by the mult-Kelvin method. However, there are much more simple technical solutions that would have the same effect of deploying a buoy at a predetermined time. In short, the few potential

applications where the method could have commercial value are well served by other technologies. Therefore, there is not significant commercial potential for the IP.

C3. Possible Prior Disclosure of Intellectual Property

There has been no prior public disclosure of the intellectual property generated during this research.

Appendix D: Broader Impact of Research

D.1 Applicability of Research Methods to Other Problems

The methods used in this research have only limited tangential applicability to other similar problems. The static sublimation method could be used to investigate the sublimation dynamics of other materials. The multi-Kevin probe approach could be useful in the study of the etch rates of other conductive solids by corrosive gases. The application of LTCC manufacturing and materials could be used for devices other than thrusters. LTCC has been widely reported to be used for a vast and diverse set of applications including solid state fuel cells and microfluidics devices. The versatility of LTCC was indeed illustrated by many of these other applications which helped inspire the LTTCC-ET developed in this research.

D.2 Impact of Research Results on US and Global Society

The broader impacts of this work to the US and global society are admittedly quite limited, insofar as the technology is useful. The work is largely esoteric as it could only be useful to an extremely small category of technologies, small satellites. However, the work is exciting because it has 'cool factor' by being sci-fi techy. Heavy Metal Monolithic Ceramic Ion Thruster has a pretty cool ring to it. This means that the subject is kind of fun to talk about and makes for a better story than anything. If this work has a cool factor and is something that you could tell kids about to get them excited about the STEM field, then there could be a real impact greater than the marginal technological gains it may provide. Educating children about how an ion thruster works and showing them some prototypes would be worth weeks of time spent just reading a book. This work can be impactful because it shows how to think outside the box, be creative, and use imagination to create new things. For these reasons, this work is a greater social tool than a technological tool because of the potential impact it could have on education.

D.3 Impact of Research Results on the Environment

There are no significant impacts of this work on the environment. The material xenon difluoride is toxic and can decompose into hydrogen fluoride, a very dangerous acid, when contacted with moisture form the air. However, the entire research effort described in this dissertation only consumed ~14 g of XeF_2 over a span of ~1.5 years. The waste products of using the material were handled and disposed of in accordance with all federal, state, and local regulations, as well as the health and safety policies of the University of Arkansas. Furthermore, additional efforts were made to safely handle this material that was not specified in official guidelines. The material was only handled in a sealed glove-box with a positive pressure nitrogen environment. This prevented moisture from causing unwanted and dangerous reactions to occur during handling. The byproducts of the sublimation and etching experiments were vented via vacuum pump and mass air handler system to a roof-top mounted fume vent.

The results of this research could possibly lead to the adoption of XeF_2 or XeF_4 based propellant systems. There are two reasons that even major adoption of this technology would not pose significant negative or positive impact on the environment. First, there is no scenario where the results of this work would encourage large scale industrial production of XeF_2 or XeF_4. The application of this technology only requires small amounts (on the order of kilograms) of these chemicals which, if adopted widely for space applications, would still be insignificant compared to present industrial demand. Second, the XeF_2 or XeF_4 would be consumed outside of the Earth's atmosphere so the byproducts of consumption would pose no risk to our planet.

Appendix E: Microsoft Project for PhD Microelectronics-Photonics Degree Plan

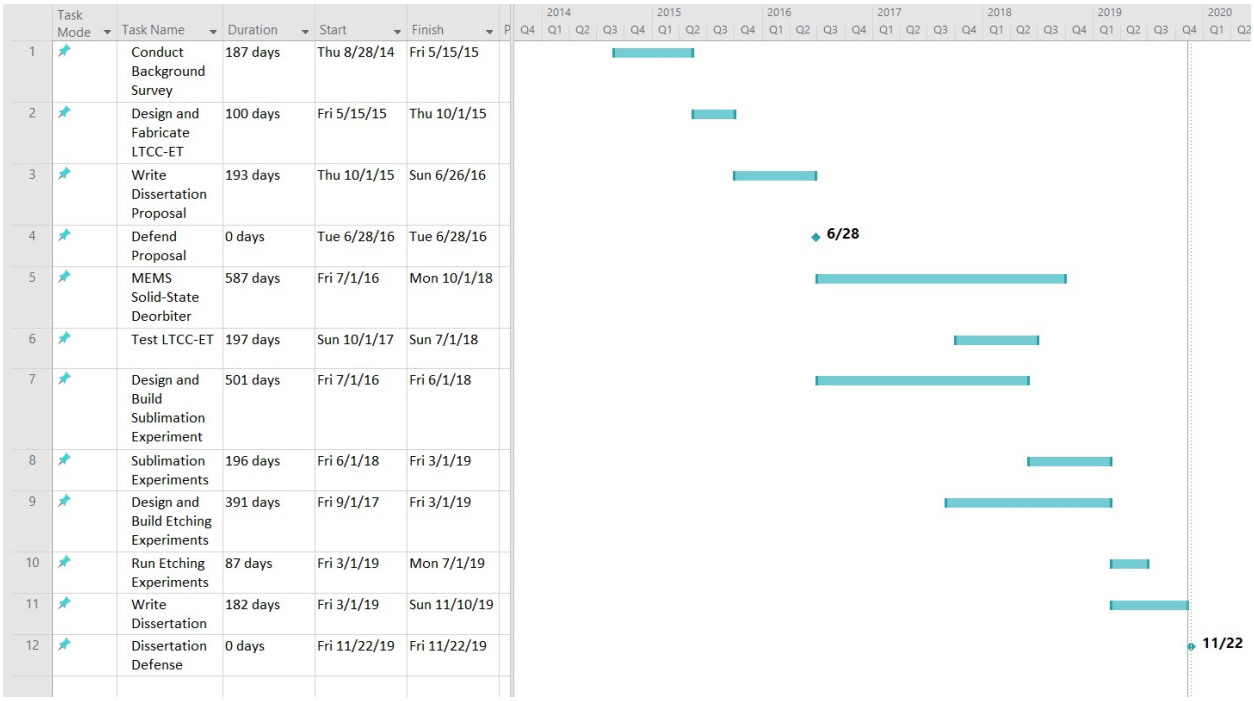

	Task Mode	Task Name	Duration	Start	Finish
1		Conduct Background Survey	187 days	Thu 8/28/14	Fri 5/15/15
2		Design and Fabricate LTCC-ET	100 days	Fri 5/15/15	Thu 10/1/15
3		Write Dissertation Proposal	193 days	Thu 10/1/15	Sun 6/26/16
4		Defend Proposal	0 days	Tue 6/28/16	Tue 6/28/16
5		MEMS Solid-State Deorbiter	587 days	Fri 7/1/16	Mon 10/1/18
6		Test LTCC-ET	197 days	Sun 10/1/17	Sun 7/1/18
7		Design and Build Sublimation Experiment	501 days	Fri 7/1/16	Fri 6/1/18
8		Sublimation Experiments	196 days	Fri 6/1/18	Fri 3/1/19
9		Design and Build Etching Experiments	391 days	Fri 9/1/17	Fri 3/1/19
10		Run Etching Experiments	87 days	Fri 3/1/19	Mon 7/1/19
11		Write Dissertation	182 days	Fri 3/1/19	Sun 11/10/19
12		Dissertation Defense	0 days	Fri 11/22/19	Fri 11/22/19

Morgan Roddy's PhD Project Plan for the Microelectronics-Photonics Graduate Program at the University of Arkansas

Appendix F: Identification of Software used for Research

Computer:	Home Laptop
Owner:	Morgan Roddy
Model:	Dell Inspiron 15 7000
Software 1:	Solid Works
Software 1 License:	Student License
Software 2:	Microsoft Office 2016
Software 2 License:	Student License
Computer:	Office Computer
Owner:	Adam Huang
Model:	Dell Optiplex
Software 1:	Solid Works
Software 1 License:	University License
Software 2:	Microsoft Office 2016
Software 2 License:	University License
Software 3:	Labview
Software 3 License:	DX-47K01PQ3
Software 4:	Matlab
Software 4 License:	University License
Computer:	Lab Computer
Owner:	Adam Huang
Model:	Dell Optiplex
Software 1:	Solid Works
Software 1 License:	University License
Software 2:	Microsoft Office 2016
Software 2 License:	University License
Software 3:	Labview
Software 3 License:	DX-47K01PQ3
Software 4:	Matlab
Software 4 License:	University License
Computer:	Lab Laptop
Owner:	Adam Huang
Model:	Dell Optiplex
Software 1:	Microsoft Office 2016
Software 1 License:	University License
Software 2:	Labview
Software 2 License:	DX-47K01PQ3

Appendix G: All Publications Published, Submitted and Planned

G.1 Published Work

[1] **M. Roddy**, A. Huang, "A Solid-State Gas Generator Actuated Deorbiter For CubeSats", Accepted for Publication: IEEE Journal of MEMS, Reference Number: JMEMS-2019-0069, 2019

[2] A. Huang, K. A. Polzin, **M. Roddy**, "Characterization of LTCC-Manufactured Electrostatic Thruster (LTCC-ET)", NASA Technical Memorandum, NASA/TM-2019-220126, February 2019

[3] **M. Roddy**, K. A. Polzin, A. Huang, "Development of a Monolithic Ceramic Electrostatic Ion Thruster for Interplanetary SmallSat Missions", 29th AIAA/USU Conference on Small Satellites, Logan, UT, 2018

[4] **M. Roddy**, H. Hodges, L. A. Roe, A. Huang, "Demonstration of a Solid-State Inflation Balloon Deorbiter" Proceedings of the ASME 2017 International Mechanical Engineering Congress and exposition, IMECE 2017-71998, November 2016, Tampa, FL

[5] **M. Roddy**, H. Hodges, L. A. Roe, A. Huang, "Solid State Gas Generator For Small Satellite Deorbiter" ASME NEMS Conference Paper

[6] **M. Roddy**, A. Huang, "Development of a Solid-State Inflation Balloon for Aerodynamic Drag Assisted Deorbit of CubeSats" International Academy of Astronautics 2017, Book Chapter (In Press)

[7] **M. Roddy**, A. Huang, "Development of a Solid-State Inflation Balloon for Aerodynamic Drag Assisted Deorbit of CubeSats" UNISEC Conference Proceedings (In Press)

[8] **M. A. Roddy**, A. Cassell, K. Hines, R. Beck, B. Yost. L. A. Roe, A. Huang, "Development of a Solid-State Inflation Balloon Deorbiter", Proceedings of the ASME 2016 International Mechanical Engineering Congress and exposition, IMECE 2016-67467, November 2016, Phoenix, AZ

[9] **M. Roddy**, A. Huang, "Development of a Solid-State Inflation Balloon for Aerodynamic Drag Assisted Deorbit of CubeSats", Presentation at the University Nanosatellite Engineering Consortium Conference, Varna, Bulgaria, October 2016

[10] **M. Roddy**, L. A. Roe, A. Huang, "Development of a Solid-State Inflation Balloon Deorbiter", Poster Presentation, 30th Annual AIAA/USU Conference on Small Satellites, Logan, Utah, August 2016

[11] **M. Roddy**, A. Huang, "Progress on the Development of an Active Deorbiter Subsystem for Small Satellites", Arkansas Academy of Sciences 100th meeting, 2016, Fayetteville, AR

[12] **M. A. Roddy**, M. O. El-Shenawee, "Computational Design of Steerable Broadband MEMS Antennas", 29th Annual Review of Progress in Applied Computational Electromagnetics, March 25, 2013, Monterey, CA

[13] **M. A. Roddy**, “Computational Design of the Electrical and Mechanical Performance of Steerable MEMS Antennas”, MS Thesis, Microelectronics-Photonics Graduate Program, University of Arkansas, 2012

[14] C. Schenk, **M. Roddy**, R. Sleezer, R. Turner, M. Ware, G. Salamo, “Inquiry Based Learning in Materials Science at the Micro/Nano Scale in Arkansas Middle Schools”, MRS Spring 2011 Symposium SS, In review

[15] **M. A. Roddy**, E. M. Kirkpatrick, S. R. Kirkpatrick, “Novel Top-Down Fabrication Technique for Metallic Nanoparticles Using Nanosphere Self-Assembly and Oblique Angle Thin Film Deposition” American Vacuum Society Fall 2009 Conference, San Jose, CA October 2009

[16] **M. Roddy**, M. Fiedeldey, M. Fuson, J. Turpen, E. Wheeler, A. Siahmakoun, “Improving Radiation Efficiency of Electrically Small Antennas Using Metamaterials”, Presentation at four symposia. 2009 and 2010 RF Alliance meetings in Rolla, MO and Lafayette, IN respectively

[17] A. Horvath, **M. Roddy**, M. Syed, A. Siahmakoun, “Contrast Reversal on Surface Plasmon Resonance Reflectivity in Nickel and Nickel Alloy Films,” SEM 2010 Conference: MEMS and Nanotechnology Symposium, Indianapolis, IN, June 7-11 2010

[18] **M. Roddy**, S. Zohar, W. E. Bailey “Low Temperature Magnatization Dynamics: A Cryogenic Ferromagnetic Resonance Study of Terbium Doped Permaloy and Fe2O3 Nanoparticles”. Public Presentation at Columbia University’s MRSEC, August 2008

Appendix H: Author Paper: Characterization of LTCC-Manufactured Electrostatic Thruster (LTCC-ET) – Close-out Report

The following paper was written and published at NASA's request based on the testing work conducted at NASA's Marshall Space Flight Center. It was published as a NASA Technical Memorandum, NASA/TM-2019-220126, February 2019. Format alone has been modified from the final memorandum submission.

Characterization of LTCC-Manufactured Electrostatic Thruster (LTCC-ET) – Close-out Report

NASA MSFC Cooperative Agreement Notice-Dual Use Technology Development at MSFC NNM17AA15A

Po-Hao A. Huang (PI)
University of Arkansas, Fayetteville, Arkansas

Kurt Polzin (NASA Tech Lead/POC)
George C. Marshall Space Flight Center, Huntsville, Alabama

Morgan Roddy (Key Personnel)
University of Arkansas, Fayetteville, Arkansas

Acknowledgments

The work presented in this end-of-project report for the Cooperative Agreement Notice (CAN) Dual use Technology Development at NASA/Marshall Space Flight Center include work performed by the team's PI, NASA POC, and Key Personnel. Additionally, acknowledgement for the University of Arkansas High-Density Electronics Center (HiDEC) senior staff Mrs. Karou Porter for assisting in conceiving the first successful manufacturing process of the LTCC-ET and undergraduate research student Seth Vaughan for his assistance in fabrication. The team also

acknowledges the administrative support and technical advice provided by MSFC Chief Technologist John Dankanich.

I. Project Goal and Summary

The goal of the project was to evaluate prototypes of an experimental thruster developed by the University of Arkansas. The design under evaluation is an RF electrostatic thruster that was fabricated using the low temperature co-fired ceramic (LTCC) materials and fabrication process. This materials system is analogous to printed circuit board technology with the most significant difference being that the laminate is replaced by a ceramic material and the copper layer is replaced by printed sinterable silver paste. LTCC designs are baked after fabrication and assembly to realize an entirely monolithic structure with internal conductors, vias, and cavities. In this process, the LTCC electrostatic thruster (LTCC-ET) that is the subject of the present work becomes is a monolithic ceramic thruster capable of withstanding temperatures in excess of 500ºC. The University of Arkansas and MSFC jointly performed prototype testing on the LTCC-ET under a NASA Cooperative Agreement Notice (CAN) award. The LTCC-ET was tested at MSFC in May 2018 over a one week period. There were two goals for the test program. The first goal of testing was to determine the operating parameters required to create plasma ignition in the test articles. This was explored by setting a propellant flow rate and increasing RF power until plasma ignition was observed. Testing was conducted with both argon and krypton. The second goal was to investigate the thrust and specific impulse performance of the thruster as a function of propellant flowrate and grid voltage. This goal was not met during the project as technical challenges in maintaining stable plasma ignition arose due to stress and heating of the RF feed.

In summary, a prototype thruster design (consisting of 3 packaged units) was fabricated by

the University of Arkansas and tested for the first time under vacuum conditions at MSFC to experimentally determine basic performance metrics and functionality. It was found that the design was not sufficiently optimized or robust enough in its initial iteration to support a significant test campaign or characterization program. It was concluded that the propellant outlet channels must be reduced in size with the flowpaths adjusted to increase propellant residence time in the thruster, and that the RF connector must be replaced with a version capable of handling higher power throughput and heating. However, even in its unoptimized form a plasma could be produced in the LTCC-ET, demonstrating the validity of the design approach. The design is especially compelling due to its low cost to manufacture and, more importantly, its scalability of size and power throughput. Low cost and scalability are also important in that additional functionalities, such as thrust vectoring and plume charge neutralization, can be integrated into future designs. This project has matured the LTCC-ET development TRL from 1 to 2. The low-cost RF plasma source portion of the LTCC device was matured from TRL 2 to 4 through the demonstration of RF plasma ignition under vacuum conditions.

II. Project Description

The LTCC manufacturing technology enables the parallel fabrication of all the requisite subsystems (internal ionization / plasma cavity, excitation electrodes, and accelerating electrodes) required to produce a monolithically-integrated electrostatic ion thruster. The successful development of a LTCC-manufactured propulsion system has the potential to revolutionize the use of SmallSats by providing a scalable low-cost, low-volume, high-specific impulse in-space propulsion system capability. High performance propulsion on SmallSats can enable new capabilities in small-satellite mobility, especially for CubeSats and nanosatellites. Mobility is crucial to NASA's goal of utilizing small satellites for future planetary and deep-space missions.

The LTCC manufacturing process could also allow for new electric propulsion designs that can provide thrust vectoring and eliminate the need for a separate beam neutralization component.

The impetus for the LTCC-ET arose from considering what features a propulsion system specifically designed for interplanetary CubeSats would contain. The ever growing capabilities of and technologies for CubeSats give rise to more and more ambitious mission concepts. This is evidenced by missions such as the 6U MarCo CubeSats, designed to serve as communications relays for a Mars flyby, and the 13 CubeSats manifested on NASA's Space Launch System (SLS) inaugural EM-1 flight. These missions demonstrate that CubeSats are maturing and their capabilities are expanding far beyond low Earth orbit. Indeed, 12 of these 14 missions include some form of propulsion including: cold gas, water electrolysis, monopropellant, solid rockets, electrospray, and ion engines [1 – 4]. All of these propulsion systems are commercial or custom solutions developed and tailored for each mission. The goal of the research described in this TM is to present a generic alternative propulsion system, rather than a custom solution, that was capable of addressing a wide range of interplanetary mission needs.

The primary focus of the work was on the thruster portion of such a propulsion system, as opposed to the propellant storage and delivery system or power generation and conditioning. The authors see several key performance factors that need to be met to realize a generic solution for interplanetary CubeSats. First, the system would need to have a high specific impulse, I_{sp}, so as to be capable of imparting significant delta-V to the spacecraft. This led to an RF electrostatic ion propulsion architecture. Second, the limited sunlight and solar panel area constraints interplanetary CubeSats face lead to a system that has low power requirements with compact, low-loss power transmission pathways. Third, the system must be compact to integrate within the limited mass and volume envelope of CubeSats. A consequence of the limited power and compact size is a low

thrust level. At low thrust, this system must operate over a long time to impart significant delta-V to the spacecraft. The electrodes were embedded in the ceramic for maximum durability. Additionally, the durability afforded by the ceramic makes the thruster compatible with corrosive propellants such as solid subliming iodine, which is of significant interest due to its high propellant storage density [5]. A significant benefit of the manufacturing process is its scalability. The LTCC process enables batch fabrication of highly complex structures for relatively low cost, allowing for the manufacture of complex thruster geometries at low relative cost. These considerations, in conjunction to the unique fabrication facilities and capabilities at the University of Arkansas, lead to the adoption of the LTCC materials system and ultimately the LTCC-ET design.

The use of LTCC in manufacturing is analogous to printed circuit board (PCB) fabrication, except that LTCCs use ceramic structural layers instead of glass-epoxy laminates [6 – 7]. Designs are created by stacking individual thick film layers of soft ceramic-polymer called 'green tape'. Each layer can have patterned geometries and vias (vertical interconnects), much like PCBs, which are then filled with electrically conductive pastes (i.e. silver particles). Once all layers are completed, they are stacked together and subjected to high pressures ranging from 2000 – 4000 psi to laminate the layers together. The entire stack is then co-fired at 850 – 1000 °C to fuse all the layers and burn off the polymer binders. The value of using LTCC technology is that it is extremely durable, can operate at very high temperatures, has a very low dielectric loss tangent (0.001 at 10 GHz), and does not exhibit mechanical and voltage leakage until ~450℃ [6]. Additionally, designs using this manufacturing process are scalable in complexity. That is, they can have a wide range of complexity without significantly increasing cost. This is similar to PCB fabrication technology where the cost for three conductors on a layer is the same as for a thousand. The most significant cost driver is the number of unique layers, not the complexity they contain. This feature is

important to the LTCC-ET because device complexity is scalable. The typical applications for LTCC technology are packaging for high power electronics or extremely high frequency devices (>10 GHz). In the present work, LTCC technology was selected for the thruster design due to ease of manufacturing (parallel and scalable), mechanical properties (durability of ceramics in plasma environment), and electrical properties (insulator and low RF losses).

RF ELECTROSTATIC ION THRUSTER

Although the operating principle of an electrostatic thruster is straightforward, the actual device can be quite complex [8]. There are three primary elements: a cavity, a screen electrode, and an accelerating electrode. Propellant is fed into the cavity and a plasma is produced through the application of DC or RF power. The screen electrode is perforated with holes to allow propellant to emerge from the cavity and it is at a potential to draw ions out of the cavity while repelling electrons. The accelerating electrode downstream of the screen electrode is held at a high DC voltage to accelerate the ions as they enter the gap between the screen and accelerating electrodes. A secondary device called a neutralizer is typically included in propulsion systems in the downstream region. This device injects electrons into the positively-charged exhaust beam, allowing the spacecraft to remain charge neutral. The I_{sp} of such a device is directly related to the square root of the applied voltage divided by the molecular mass of the propellant ($\sqrt{V/M}$), while the thrust directly scales with this quantity times the propellant flowrate. If the thruster is operating in the space-charge limited regime, the thrust per unit area simply scales with the square of the applied voltage divided by the electrode spacing ($[V/\Delta x]^2$).

LTCC-ET PROTOTYPE FABRICATION

An opportunity arose in the summer of 2015 that started the development of the LTCC-ET.

The research group at the University of Arkansas (UA) hosted an NSF Research Experience for undergraduate students over a period of 10 weeks. These limited financial resources of this program were used in the fabrication of LTCC-ET prototypes. At the time of that effort, the concept had already been conceived but no significant design work had been performed. Due to time constraints, none of the functional elements were able to be optimized through design, simulation, and calculation before manufacturing took place. Instead, the primary goal of the effort was to demonstrate that a monolithic ion thruster could be fabricated using LTCC, with an additional goal of developing design guidelines for future iterations. The biggest challenge was to design a plasma cavity structure that would not collapse during the high-pressure lamination process.

The specific design was quickly assembled, containing all the functional elements of an electrostatic RF ion thruster including propellant inlet ports, a propellant distribution manifold, RF antenna, plasma cavity, screen and accelerating electrodes, RF and high voltage connections, propellant discharge orifices, and overall supporting structure. The embedded electrodes for all the interactions with the plasma were relatively easy to incorporate into the LTCC structure. These efforts resulted in the fabrication of four (4) prototype thrusters, one of which shattered during high-temperature processing due to internal stresses. The manufacturing experiment was successful as it led to the creation of three (3) functional prototypes representing the largest and most complex LTCC devices ever fabricated by at the University of Arkansas.

The LTCC-ET thruster design was based on the work of Goebels and Katz [9]. The thruster is composed of two distinct stages, each composed of numerous green tape sheets. The first stage of the thruster is the plasma cavity. This stage has a gas distribution manifold, an RF patch antenna, a plasma cavity, and a screen electrode. The plasma cavity must be a conductive cage and in the thruster it is defined around its perimeter by a via post-wall, at the bottom by the RF antenna, and

at the top by the screen electrode. The post-wall is not a contiguous conductive wall but rather a wall of vertical grounded conductors that are spaced close enough so that they can effectively contain electromagnetic energy at the frequency of operation, in this case, 915 MHz (although the cutoff frequency of this cavity would be in excess of 10 GHz). The post-wall, antenna, and screen electrode are all embedded in the ceramic so as to be part of the monolithic structure after high-temperature processing. The screen electrode is virtually identical in size to the antenna, but it has propellant outlet orifices and is held at a fixed DC potential during operation. A positive or negative DC potential could be employed to accelerate negative or positive ions respectively. The cavity and gas distribution manifold are created by numerous interdigitated cavities or voids that are punched into the green tape. The arrangement, shape, and size of these voids were designed in an attempt to maximize the open internal volume of the plasm cavity while still maintaining structural integrity to prevent collapse during manufacturing and high-temperature, high-pressure processing. The second stage of the thruster is the accelerating stage. This is composed of propellant outlet orifices and an accelerating electrode. The orifices are simply holes in the green tape. The electrode is again virtually identical to the antenna and screen electrode but is held at a negative DC potential relative to the screen electrode during operation.

Prototype fabrication was conducted in the LTCC lab at UA's Hi-Density Electronics Center (HiDEC) in the summer of 2015. Four prototypes were fabricated in the pursuit of a successful fabrication process. The first prototype cracked after it was fired, and the scrap pieces of this unit were used to test soldering methods for attaching RF and high voltage connectors.

All prototypes were manufactured using DuPont 9k7 LTCC Green Tape. The LTCC-ET contains seven distinct layers of green tape and there are multiple sheets comprising each layer. There are also 4 distinct metallization layers. Additionally, every layer contains the same layout of

vertical interconnects (this creates the via post-wall through the entire device). The sequential stack-up is as follows. Layer 1 contains an accelerating electrode, discharge orifices for propellant, and an interconnect via to make a connection to layer 2. There were six 10 mil thick instances of Layer 1, the topmost of which contained the screen-printing for the accelerating electrode. Best results were obtained when the accelerating electrode was screen-printed and fired after the co-fire process. There was a single 10 mil thick instance of Layer 2 containing the screen electrode and propellant discharge orifices. The screen electrode also serves as an RF ground for the ionization chamber. These seven layers were laminated to form a sub assembly. Layers 3-5 form the ionization chamber and a propellant gas manifold structure. Each layer has different cavities built into them which, when stacked together, form an interconnected cavity, but all have the same post-wall vias. The cavities consist of interdigitated channels. There were two sets of Layer 3 composed of four 10 mil sheets of green tape. These were each laminated to realize two Layer 3 subassemblies. The same was true of Layers 4 and 5; two subassemblies of each Layer composed of 4 sheets of 10 mil green tape. The stack-up of these six subassemblies forms the plasma cavity and propellant manifold. Layer 6 was composed of a single layer of 5 mil thick green tape and contained the via post-wall and propellant inlet channels. This layer served to electrically insulate the antenna from direct exposure to the RF plasma. Layer 7 contains the propellant inlets, the RF patch antenna, an RF ground, the via post-wall, and an additional interconnect via for the electrical connection to the antenna. The Layer 7 stackup was composed of six 10 mil layers of green tape. The topmost layer contained the antenna and the bottommost layer contained an RF ground and the RF interconnect via solder pad. Layers 6 and 7 were laminated to form the final subassembly. All subassemblies were then aligned and laminated to form the final device stack. The structure was then co-fired. Figure 1 shows a negative of the cavities in the LTCC-ET for better visualization

of the shape and distribution of voids which comprise the internals of the thruster. Figure 2 shows the seven unique layers and the electrode silk-screenings, as well as a circuit diagram of the thruster. Figure 3 shows photographs of the LTCC-ET during fabrication while Figure 4 shows the arrangement of the via post-wall, RF antenna, and screen electrode which forms the plasma cavity.

The final fabrication process can be separated into nine steps. First, the hole patterns in all sheets and layers were punched using a CNC punching tool to create cavities, orifices, and vias. Second, all via holes were filled with DuPont LL601 silver paste. Third, the internal metallized layers (Layer 2 and Layer 7 topside) were screen printed with DuPont LL612 silver conductor paste to form the screen electrode and antenna, respectively. Fourth, all subassembly stack-ups were laminated at 3000 psi. Fifth, the eight subassemblies were stacked together and laminated at 2500 psi. It was critical to the design of the device that the two instances of Layers 3, 4 and 5 had a 90 degree rotation between each of them. Sixth, the laminated stack-up was co-fired at 900℃ for 18 hours. Seventh, the accelerating electrode and ground plane conductors were screen-printed on Layers 1 and 7, respectively, using DuPont 6277 silver / palladium paste. Eighth, the final conductors were cured and sintered at 850 deg C for 1 hour.

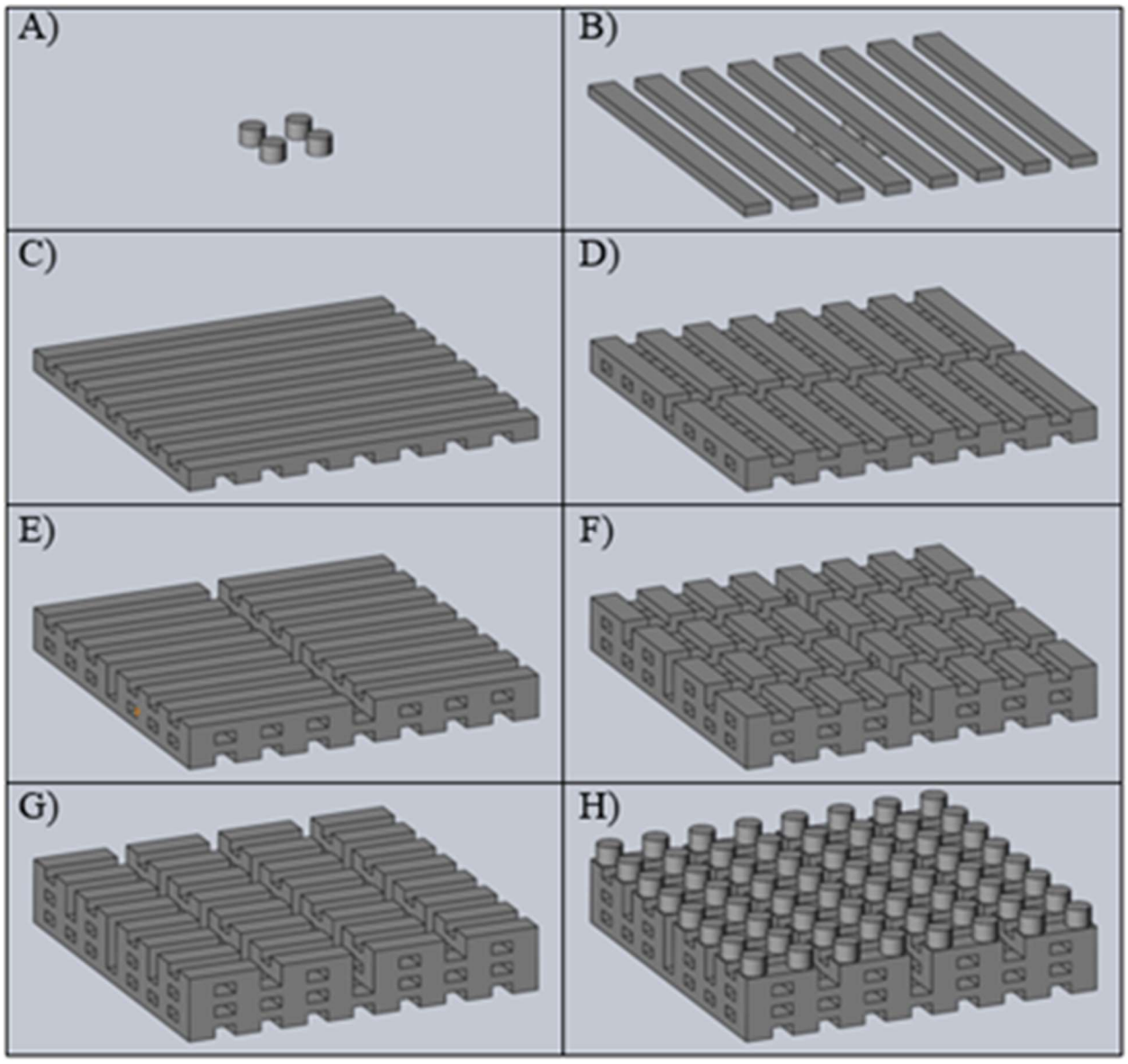

Figure 1: Negative-space layer-by-layer CAD model showing the internal cavities in the LTCC-ET that form the propellant manifold, plasma generation cavity, and propellant outlet ports. A) propellant inlet ports, B) first copy of Layer 5, C) second copy of Layer 5 (rotated 90°), D) first copy of Layer 4, E) second copy of Layer 4 (rotated 90°), F) first copy of Layer 3, G) second copy of Layer 3 (rotated 90°), H) propellant outlet ports.

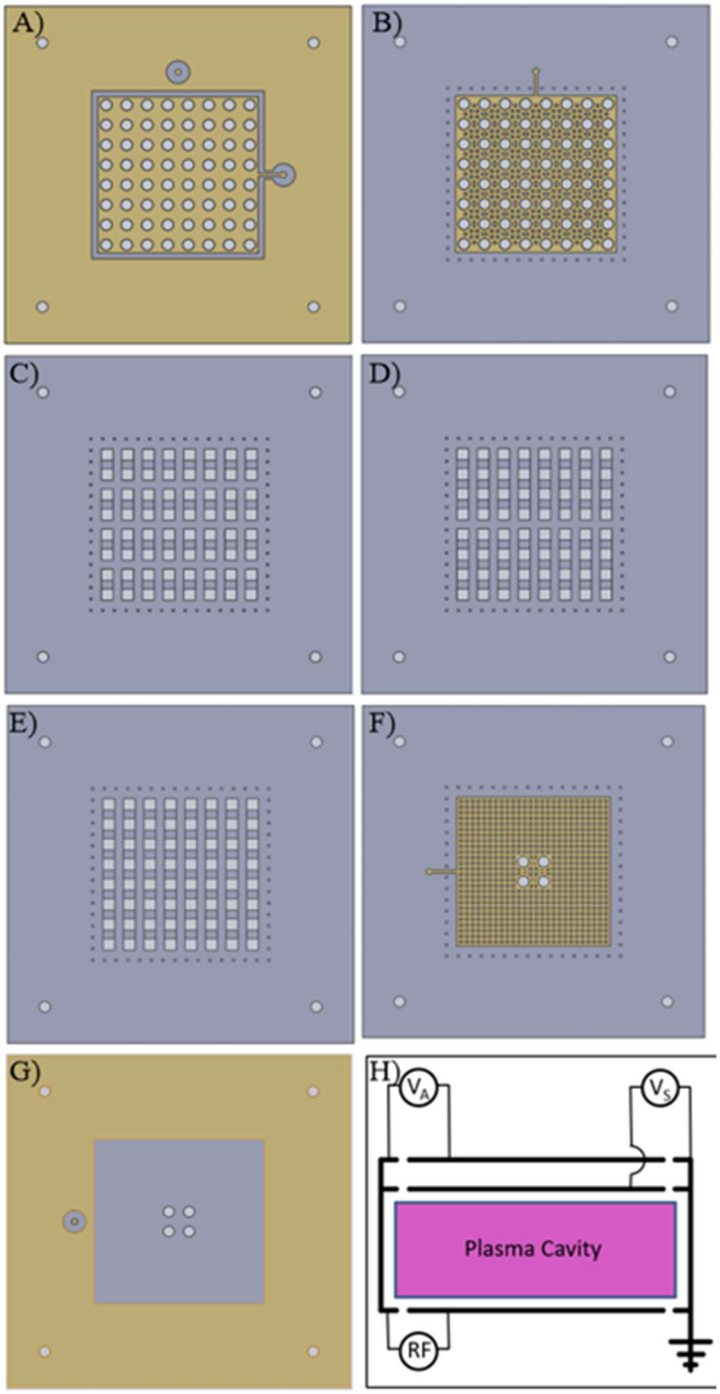

Figure 2: CAD renderings of the seven unique layers in the LTCC-ET showing vias and silkscreen printed conductors. A) Layer 1, propellant outlet ports and accelerating electrode. B) Layer 2, propellant outlet ports and screen electrodes. C) Layer 3, small cavities. D) Layer 4, medium

cavities. E) Layer 5, large cavities. F) Layer 6 propellant inlet port and RF antenna. G) Layer 7, propellant inlet port and ground plane. H) Electrical schematic of the LTCC-ET showing the plasma cavity, RF antenna, screen voltage, V_s, and accelerating voltage, V_a.

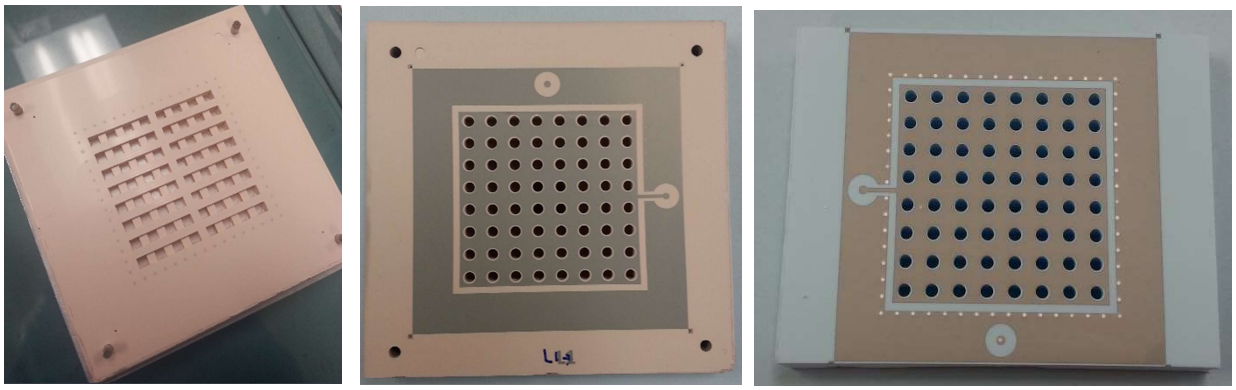

Figure 3: Photographs of the LTCC-ET during fabrication. (Left) Partially completed thruster stack showing internal cavities. (Center) Fully laminated device before co-firing of the ceramic. (Right) Fully complete device after co-firing

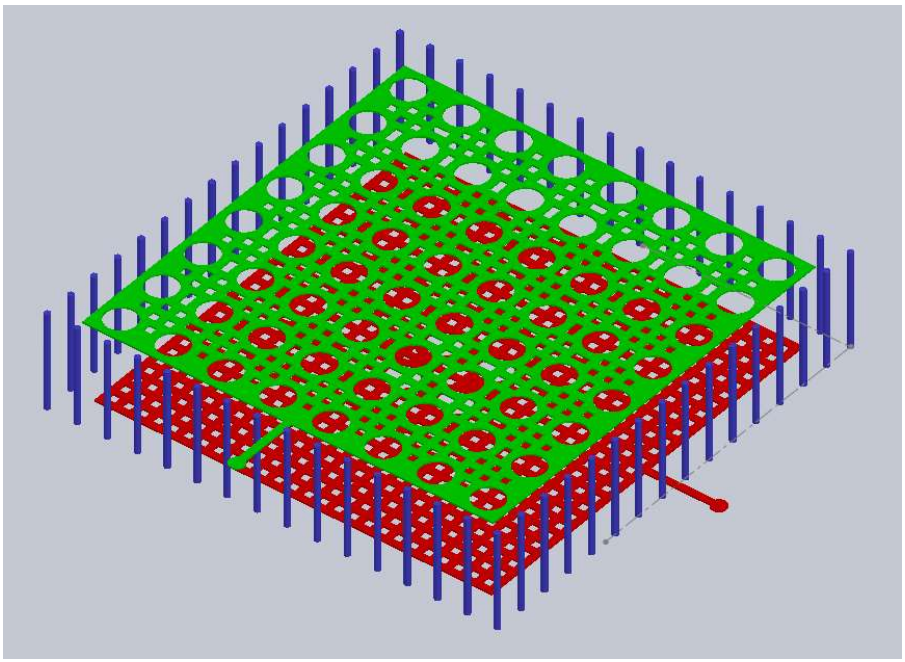

Figure 4: CAD model of the plasma cavity with ceramic removed and color added for visual

clarity. The red structure is the RF antenna, the green structure is the screen electrode, and the blue structures comprise the via post-wall.

The final device measures 2.75-in on each edge. It is 340 mils thick, masses ~110 g, and has a volume of ~45 mL. It is thought that the size and mass could be reduced in the design optimization process. The LTCC thruster was not only the thickest device ever fabricated at the HiDEC labs, but it was also the first to incorporate internal cavities.

The LTCC-ET design posed two unique challenges. First was the challenge to incorporate a plasma cavity in the design without having the device collapse under the extreme pressure of the lamination process. This was achieved by including additional sheets in Layers 1, 2, 6, and 7. Functionally speaking these layers did not require multiple sheets, but eight sheets were incorporated during assembly to add structural integrity. Also, the interdigitated cavity design shown in Fig. 1 allowed for 'pillars' of LTCC material to exist in the cavity to provide added support and prevent collapse. The second challenge was to minimize the thermal stresses in the device. Excess thermal stress was identified as the reason for the fracture during the assembly of the first prototype. For this reason, post-fire metallization was used to reduce thermal coefficient of expansion mismatch between the external conductors and the ceramic stack during firing. The fabrication process has been documented and will be used as design guidelines for successful manufacturing of future devices.

THRUSTER TESTING

The LTCC-ET had to be mounted in a 4" X 3.8" planar cross-section test fixture (see Fig. 5) to permit further evaluation. A custom fixture serving several key functions was designed and fabricated. The fixture provided a way to mechanically attach the test articles to larger structures,

such as a table or thrust stand. The structure was machined from 6061-T6 aluminum and consisted of a clam-shell design where the ceramic apparatus was sandwiched between the two halves that were bolted together. The contact surfaces between the ceramic and aluminum were padded by Grafoil® high-temperature graphite gasket material. The fixture provided support for RF, high-voltage, and propellant connectors. The propellant injection port feeding the test article with gas was also machined from 6061-T6 aluminum. This connection was sealed at the back of the ceramic thruster body with a custom laser-cut, 30 mil thick, buna-N rubber gasket. The gas port was a threaded ¼" NPT connection, which was connected to a flexible gas line by a male-to-male ¼" NPT to ¼" Swagelok compression fitting. A square Teflon plug installed on the front side of the thruster in the middle of the grid blocks the center outlet orifices, increasing the chamber pressure by ensuring the injected neutral gas could not freestream through the device. This plug was added when a visual inspection caused a realization that there was a straight-line path from the propellant injection holes through the plasma chamber and out of the thruster. Since the LTCC-ET was initially a manufacturing experiment, this aspect of test operation was not considered in the design phase. Future designs will have these freestreaming exit paths blocked by the internal structure of the device, without the need for an additional plug. The Teflon plug was sized so that the distance between it and the end of the injector was 0.005". The test fixtures contained the electrical connectors for the LTCC-ET. The RF antenna was connected with an SMA connector and the screen and accelerating electrodes used MHV connectors.

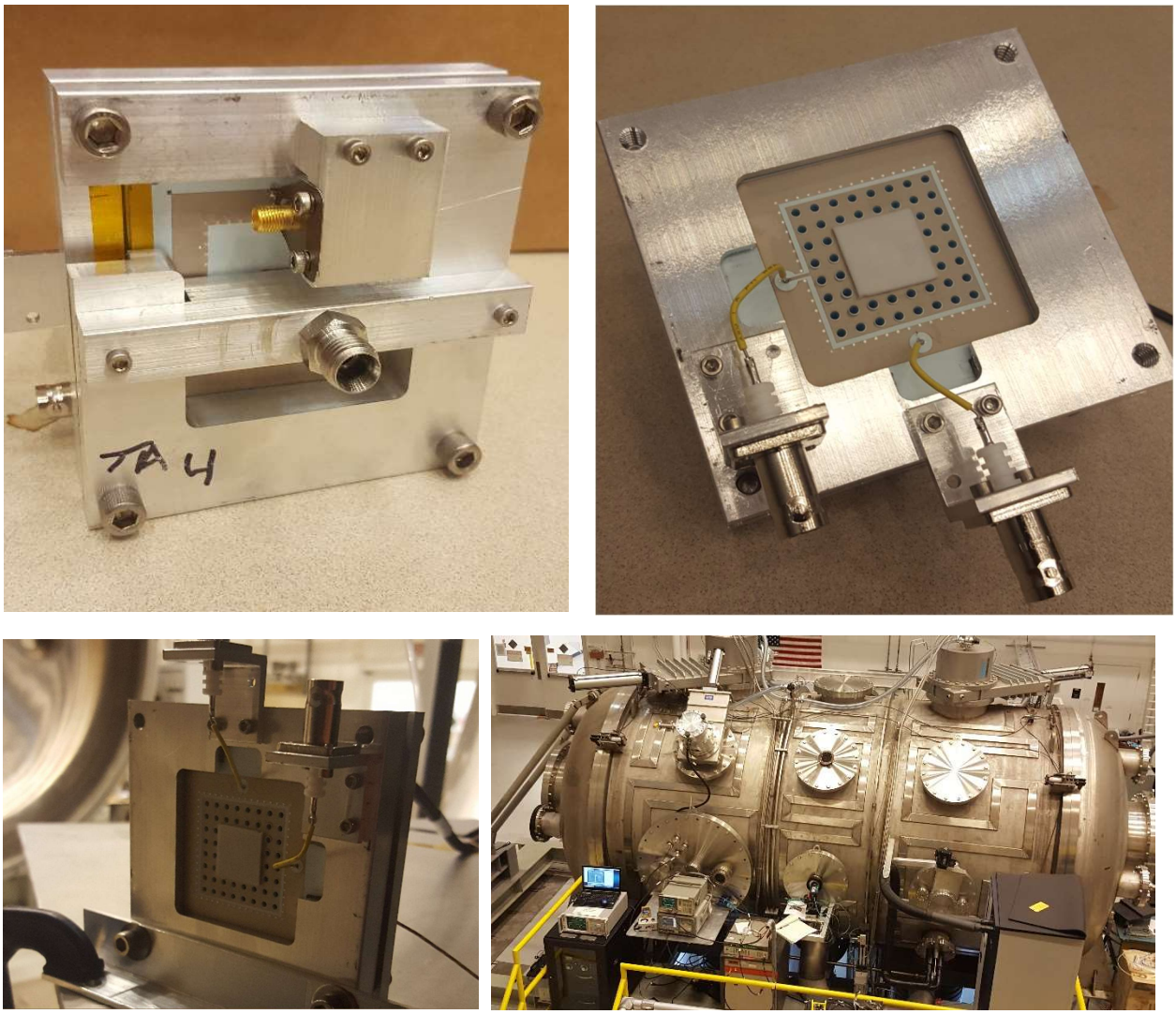

Figure 5: Photographs of the LTCC-ET mounted in the test fixture. (Left) The back of the test article showing the SMA RF connector and the propellant inlet fitting. (Right) The front of the test article showing the two MHV connectors for the screen and accelerating electrodes and the Teflon plug in the center of the device blocking a 4x4 grid of holes.

The goal of testing the LTCC-ET was threefold. The first goal was to determine the RF power required to ignite a plasma in the device as a function of propellant flowrate. The second goal was to measure thrust as a function of applied accelerating voltage. The third goal was to

determine if it was possible to accelerate electrons and positive ions in an alternating fashion by modulating the applied voltage between positive and negative. This was the most interesting testing goal due to its potential to remove a neutralizing cathode from the thruster design. In addition, while the plasma cavity sidewalls are insulated from the plasma by a layer of ceramic give them more durability, this insulation removes any possible path to circuit common for the electrons, permitting negative charge to accumulate on the sidewalls as positive ions are accelerated out of the thruster. This could lead to 'poisoning' the plasma by making it too negative. Eventually the plasma may self-extinguish as the accumulated negative charge screens the applied RF fields. During the present effort, goal one was met. Goals two and three were not attempted as issues with the RF connection to the antenna arose during testing.

Figure 6: (Left) Test article installed in the vacuum chamber at MSFC. For plasma ignition testing, the screen and accelerating electrodes were grounded (grounding wires not shown). (Right) 9-ft diameter large vacuum chamber at MSFC used for testing.

Testing was conducted at the Propulsion Research and Development Laboratory at NASA's Marshall Space Flight Center (MSFC) in Huntsville, Alabama in June 2018. This testing was performed under a NASA cooperative agreement notice (CAN) contract (NNM17AA15A). The use of the facilities at MSFC were required because there are no sufficiently large vacuum chamber facilities at the University of Arkansas that would be suitable for testing electric propulsion systems. Additionally, MSFC personnel have significant expertise in the planning and conduction of electric propulsion testing activities. The testing activities at MSFC were limited to one week due to time and funding constraints. While not all tasks were accomplished (or attempted), the initial work plan is given here for completeness. Step one of the plan was to ignite the RF plasma

in the thruster. Since this type of device had never been operated in the past, this was accomplished in an ad-hoc manner until nominal setpoints could be established to reliably ignite and maintain a plasma. While a plasma was successfully ignited several times, it was unreliable and would extinguish for reasons to be discussed. Had the plasma demonstrated reliable ignition, the next step was to integrate the thruster on the thrust stand and instrument it with thermocouples and a Langmuir probe in the thruster plume. Once instrumented, a matrix of varying parameters (inlet gas flow rate, RF input power, acceleration grid voltage) would have been devised and systematically tested. Finally, if all that had been completed, the voltage on the grids would have been modulated to attempt electron extraction from the device.

Hardware used for ignition testing consisted of a signal generator, an RF amplifier, an isolator, a bi-directional coupler, two spectrum analyzers, and the test article. During ignition testing, the accelerating and screen electrodes were grounded to remove any issues that might arise from floating electrically-conductive surfaces. Testing was conducted with argon gas as a propellant, selected for its traditional relative ease in breaking down at RF frequencies. A photograph of a test article setup for ad-hoc ignition testing, and a second photograph of the test facilities at MSFC, are shown in Figure 6. The propellant to the device was provided at a controlled flowrate. The initial flowrate was low, and when a plasma would not form up to the maximum RF power of the system (50 W), the flowrate was increased to a new value and the RF power was again ramped up to the maximum value. This process was repeated until a plasma was ignited. No ignition was achieved for argon flowrates of 1, 3, 10, and 33 sccm. Ignition was repeatably achieved at an argon flowrate of 95 sccm and an input power of 22 W. The plasma was maintained for 20 – 60 seconds before it would self-extinguish. The extinguishing of the plasma was determined to be due to inefficient RF power delivery to the test article. The RF load (antenna)

was well matched to a 50 ohm impedance at 985 Mhz when there was no plasma. However, upon ignition the RF load presented to the amplifier changed resulting in significantly less power being delivered to the test article. This issue was exacerbated as the entire test setup would heat during operation. Eventually, the plasma extinguished as it was no longer receiving enough power to sustain the discharge. Increasing the propellant flowrate to 400 sccm marginally reduced the input power needed for ignition. A plasma was ignited, if only briefly, in all three of the test articles that were brought for testing. All of them suffered the same issues of impedance mismatch, inefficient RF power delivery, and excessive heating. After initial ad-hoc testing each test article stopped working entirely, exhibiting open circuit behavior when observed with a vector network analyzer. Visual inspection revealed that the heating caused the SMA connectors to desolder, cutting the RF antenna off from the amplifier. The test articles could be re-soldered and would operate briefly, but they would again suffer the same desoldering issue after a brief period of operation. A photograph of one test article with an RF plasma in it is shown in Figure 7.

Figure 7: Photograph of the Test Article 1 of the LTCC-ET prototype with an RF-driven argon plasma.

III. Future Work and Challenges

The LTCC-ET exhibits promise but still requires further development before it becomes something that can be rigorously tested. There are major issues that must be addressed before new test articles can be fabricated. The antenna matching needs to be improved. The antenna should be modeled to ensure good impedance matching at the operating frequency, which in the present case was 915 MHz (placing it in the industrial, scientific, and medical (ISM) radio band). Most importantly, the antenna needs to be matched when a plasma is present to reduce reflected power owing to impedance mismatches in the system. If matching cannot be achieved, then a matching network should be implemented to promote more efficient and reliable operation. The cavity pressure must be increased by decreasing the propellant outlet orifice size and number, and by designing the cavity so there are no exits for freestreaming gas entering the thruster. The ideal pressure can be estimated by examining a Paschen curve for RF breakdown of a selected propellant, taking into account both the spacing between the RF antenna and the screen electrode and electric displacement caused by the presence of ceramic in the plasma cavity [9]. The pressure of the cavity can then be calculated as a function of orifice size via computational fluid dynamics or other means. The proper orifice size and number can be determined by matching the design to the desired cavity pressure. Finally, the thruster structure should be improved. The primary improvement would be to design the system so the RF and high voltage connectors will remain reliably-connected even at higher temperatures. This can be achieved by redesigning the connection points to reduce insertion losses and improve heat dissipation. A mechanical connection, as opposed to a soldered joint, may be more useful and robust in this instance.

IV. Publications

This work represents part of the Ph.D. Dissertation for Mr. Morgan Roddy, which is expected to be completed and published in the summer of 2019. In addition, there will be a journal article submission based on the following Small Satellite Conference oral presentation citation: M. Roddy, K. Polzin, and A. Huang, “Development of a Monolithic Ceramic Electrostatic Ion Thruster for Interplanetary SmallSat Missions,” 2018 Small Satellite Conference, SCC18-WKVII-02, Logan, Utah, August 8-13, 2016. (Oral Presentation; Pre-Conference Workshop Session 7: Advanced Concepts 2)

V. References

[1] B. A. Cohen, R. G. Sellar, R. Staehle, N. Toomarian and D. A. Piage, "Lunar Flashlight: Mapping Lunar Surface Volatiles Using a Cubesat," in Annual Meeting of the Lunar Exploration Analysis Group, 2013.

[2] H. Heidt, J. Puig-Suari, A. Moore, S. Nakasuka and R. Twiggs, "CubeSat; A new generation of picosatellite for education and industry low-cost space exploration," in *14th Annual USU Conference on Small Satellites*, 2000.

[3] J. W. Dankanich, K. A. Polzin, D. Calvert and H. Kamhawi, "The Iodine Satellite (iSat) Hall Thruster Demonstration Mission Concept and Development," in *50th Joint Propulsion Conference*, Cleveland, OH, 2014.

[4] L. McNutt, L. Johnson, D. Clardy, J. Castillo-Rogez, A. Frick and L. Jones, "Near-Earth Asteroid (NEA) Scout," in *AIAA Space 2014 Conference and Exposition*, San Diego, CA, 2014.

[5] A. R. C. Mission Design Stff, "Small Spacecraft Technology State of the Art, Vol. TP-20140216648, Rev 1," NASA, 2014.

[6] M. R. Gongora-Rubio, P. Espinoza-Vallejos, L. Sola-Langua and J. J. Santiago-Aviles,

"Overview of Low Temperature Co-Fired Ceramics Tape Technology for meso-System Technology (MsST)," *Sensors and Actuators*, vol. 89, pp. 222-241, 2001.

[7] L. J. Golonka, "Technology and applications of Low Temperature Co-fired Ceramic (LTCC) based sensor and microsystems," *Bulletin of the Polish Academy of Sciences*, vol. 54, no. 2, 2006.

[8] D. M. Goebel and I. Katz, *Fundamentals of Electric Propulsion: Ion and Hall Thrusters*, Jet Propulsion Laboratory Space Science and Technical Series, 2008.

[9] J. M. Meek, "A theory of Spark Discharge," *Physics*, vol. 57, pp. 722 - 728, 1940.